Three-dimensional thermometry and velocimetry in fluid flows using thermographic phosphor tracer particles

Dissertation
zur Erlangung des akademischen Grades

Doktoringenieur
(Dr.-Ing.)

von M.Sc. Moritz Stelter

geb. am 11. September 1994 in Hannover

genehmigt durch die Fakultät für Verfahrens- und Systemtechnik
der Otto-von-Guericke-Universität Magdeburg

Gutachter/innen:

Prof. Dr.-Ing. Frank Beyrau

Prof. Dr. Friedrich Dinkelacker

Dr. Benoît Fond

Promotionskolloquium am 22. September 2025

Abstract

In turbulent fluid flows, heat and mass transfer are coupled over a wide range of time and length scales. Considering their three-dimensional (3D) nature, their investigation requires simultaneous 3D temperature and velocity measurements. While the latter are readily possible, combined thermometry is difficult. To measure both quantities, several techniques have been developed using seeded tracer particles, for example thermographic phosphors. Due to their thermal and chemical stability, they can be used over a wide temperature range and in various environments.

In this thesis, a technique for instantaneous 3D fluid flow thermometry and velocimetry is developed based on individual seeded phosphor tracer particles (ZnO). Upon volumetric illumination of a flow seeded with these particles using green and UV lasers, both their temperature dependent luminescence emissions and scattered light are recorded from multiple camera perspectives. Each particle acts as a discrete sensor for flow velocity through 3D position tracking and temperature by ratiometric phosphor thermometry. The technique is demonstrated in a turbulent gas jet heated to 433 K at a bulk velocity of 34 m/s (Re $\sim$ 4600). After the applicability of the developed technique is proven, the number of discrete 3D measurement points is increased by introducing cutting edge algorithms for processing macroscopic images of microscopic particles. This includes volume self-calibration, iterative particle reconstruction, and Shake-The-Box for camera calibration, 3D particle position reconstruction, and tracking. Eight different image segmentation schemes are explored to retrieve imaged luminescence signals from individual particles for ratiometric phosphor thermometry and a 3D flat field correction is implemented to correct calculated intensity ratios. Single-shot results with a spacing of 900 µm and time-averaged results exceeding 30 points/mm^3 are obtained with an estimated temperature precision of 6 % and velocity precision of 13 %. This technique will be especially useful for investigations of non-isothermal turbulent gas flows and for the validation of simulation submodels.

Kurzfassung

In turbulenten Fluidströmungen sind die Wärme- und Stoffübertragung über viele Zeit- und Längenskalen miteinander gekoppelt. Zu ihrer Untersuchung sind daher gleichzeitige dreidimensionale (3D) Temperatur- und Geschwindigkeitsmessungen erforderlich. Während Letztere mittels einiger partikelbasierter Techniken möglich sind, ist eine gleichzeitige Temperaturmessung herausfordernd. Kürzlich entwickelte Techniken nutzen zur Messung beider Größen spezielle Partikel, wie thermografische Phosphore. Dank hoher thermischer und chemischer Beständigkeit lassen sich diese über einen weiten Temperaturbereich und in vielen Umgebungen einsetzen.

In dieser Arbeit wird eine Technik zur gleichzeitigen 3D-Messung von Strömungstemperatur und -geschwindigkeit entwickelt, welche auf in die Strömung eingebrachten Phosphor-Partikeln (ZnO) basiert. Nach Beleuchtung mittels grünen und UV Lasern wird die von den Partikeln emittierte temperaturabhängige Lumineszenz und das an ihnen gestreute Licht aus mehreren Kameraperspektiven aufgenommen. Durch die Verfolgung der 3D-Position und ratiometrischer Phosphorthermometrie fungiert jeder Partikel als diskreter Geschwindigkeits- und Temperatursensor. Die Technik wird in einem auf 433 K geheizten Gasjet bei einer mittleren Geschwindigkeit von 34 m/s (Re $\sim$ 4600) demonstriert. Anschließend werden neue Algorithmen zur Verarbeitung der makroskopischen Bilder mikroskopischer Partikel eingeführt. Dies umfasst *Volume Self-Calibration*, *Iterative Particle Reconstruction* und *Shake-The-Box* zur Kamerakalibrierung, 3D-Rekonstruktion von Partikelpositionen und ihrer Verfolgung. Zudem werden acht Algorithmen zur Segmentierung einzelner Partikelbilder getestet und ein 3D-Korrekturfeld für die Lumineszenzauswertung eingeführt. Es werden instantane Ergebnisse mit Abständen einzelner Messpunkte von 900 µm und zeitgemittelte Ergebnisse mit mehr als 30 Messpunkten/mm^3 mit Messunsicherheiten von 6 % (Temperatur) und 13 % (Geschwindigkeit) erreicht. Diese Technik wird für Untersuchungen turbulenter und insbesondere nicht-isothermer Gasströmungen und zur Validierung von Simulationsmodellen nützlich sein.

Contents

List of Figures

List of Tables

Chapter 1

Introduction and thesis structure

Fluid flows coupled with heat transfer processes are present and important in everyone's daily life. For example, large scale flows in the atmosphere and oceans govern the weather we are all exposed to. To create reliable weather forecasts, powerful computers are needed to run simulation models (Quarteroni 2022). To ensure their smooth operation, they have to be sufficiently air- or water-cooled (Mytton 2021), involving small scale heat and mass transfer processes. To cope with the weather, we use devices such as gas heaters, boilers, heat pumps, heat exchangers and air conditioning units, where coupled heat and mass transfer flows are also present on small scales. To run many of these devices we need electricity, that is commonly generated using gas and steam turbines, where heat and mass transfer processes govern the efficiency and safety of operation on small and intermediate scales (Martin et al. 2012; Straußwald et al. 2020).

Within these flows, some degree of turbulence is widely prevalent. As turbulence enhances heat and mass transfer processes, it helps to increase the power density of combustors, to increase the efficiency of turbines, and to reduce the pollutant production by combustion processes, as it improves the mixing of fuel and oxidizers, leading to a more complete combustion (Bray 1979; Sadykova et al. 2021). However, turbulence is a complex and inherently three-dimensional (3D) phenomenon (Pope 2015). Therefore, its exact modelling is challenging, especially for large spatial domains. At the same time, improving our understanding of turbulence is crucial to improve the efficiency of many devices and machines, contributing to a preservation of resources and reduction of pollutant production.

Experimental data has been indispensable to build our understanding of turbulence as flow visualization techniques using dyes or shadowgraphy and Schlieren methods allow insights into transparent flows and turbulence basics for many decades (Settles 2001). In general, optical measurement techniques continue to provide contactless and often nonintrusive measurements of various flow properties today. This predestines them for measurements in harsh environments or when investigating moving objects, as they do not require a wired connection to the sensor (Steinberg 2023). Promoted by the availability of ever more computational power, numerical models are nowadays a great complement to experimental methods. Still current numerical models reach limits if the modelled domain exceeds a few cubic centimetres in case of turbulent flow of low density fluids coupled with heat transfer and potentially chemical reactions. In these cases, the computational complexity of direct numerical simulations (DNS, Pitsch 2020) becomes very high due to the wide time and length scales involved in the processes, and it is necessary to resort to submodels such as large eddy simulations which require additional validation (Zhiyin 2015). Tremendous potential lies in the combination of experimental data and numerical models by data assimilation (DA). Originating from the area of earth and planetary sciences, DA is a standard measure in weather forecasting where sensor data is combined with numerical predictions (Le Dimet et al. 1986). Nowadays, it is used in smaller scale technical experiments with isothermal flows, too, to increase the spatial resolution and derive additional quantities from flow measurements (Jeon et al. 2018; Mons et al. 2022). For it to work reliably, there must be a minimum number of samples measured per unit volume, otherwise its solution becomes unstable (Schneiders et al. 2017). Advancements in particle based velocimetry methods, such as in tomographic particle image velocimetry and Shake-The-Box (Elsinga et al. 2006; Schanz et al. 2013), allow tracking of seeded tracer particles with great spatial and temporal resolution. Their results are used as input to recently developed advanced DA schemes such as FlowFit or VIC# to further increase the spatial resolution of the results (Zhou et al. 2024).

For the development of DA schemes that include coupled heat and mass transfer, as well as the validation of numerical models applicable to non-isothermal flows, measured temperature data is needed with spatial resolution matching the velocimetry results. This demand is driven by the realisation that scalar quant-

ities such as temperature might be advected by the flow with its velocity, but turbulent fluctuations of scalar and vector quantities show dissimilarities (Warhaft 2000; Pasinato 2011; Hara et al. 2020). Hence, simultaneous measurements or reliable simulations of both temperature and velocity distributions are required with high spatial resolution. However, obtaining such data is challenging, especially in turbulent non-isothermal gas flows. For two-dimensional (2D) measurements, several techniques were developed in recent decades, building upon advancements in laser and camera technology. They allowed insights into previously unknown flow structures and gradients, and the validation of numerical simulations (Pfadler et al. 2009). These techniques often rely on some kind of small tracer particles being seeded into the flow. By monitoring different emissions and/or scattered light signals of them, simultaneous and potentially time-resolved temperature and velocity information can be extracted (Abram et al. 2013; Massing et al. 2018; Schiepel et al. 2021).

In recent years, there has been a push for instantaneous 3D measurement techniques to simultaneously resolve the temperature and velocity flow fields (Li et al. 2023). For liquid flows, where particles larger than a few micrometers in size follow the flow faithfully, 3D measurement techniques using dyed plastic particles or thermochromic liquid crystals were developed (Massing et al. 2018; Schiepel et al. 2021). While these techniques excel in microscopic flow investigations or investigations of narrow temperature ranges, they are challenged when macroscopic, non-isothermal, and turbulent flows of low density fluids such as gases are to be investigated. This is due to long temperature and velocity response times of their particles in such flows and a limited thermal stability, especially at temperatures exceeding 378 K (Kaiser 2011). The present thesis aims to close this gap by providing a measurement technique that is capable of simultaneous and instantaneous 3D temperature and velocity measurements in turbulent gas flows by using individual micrometer sized thermographic phosphor particles as seeded flow tracers. By using scattered light and luminescence emissions of the same particles, both temperature and velocity values can be extracted with identical temporal and spatial resolution. As the full 3D velocity- and temperature-gradient tensors will be accessible, it allows investigations of coupled conductive and convective heat transfer, and the interplay of coherent turbulent and thermal flow structures. To this end, the present thesis is structured as follows.

Thesis structure

Chapter 2 provides an overview of the current state of the art of multidimensional thermometry techniques, that are compatible with simultaneous flow velocity measurements. Their basic modes of operation are described and their applicability to turbulent gas flows is evaluated. This is followed by a more in-depth description of phosphor thermometry as selected temperature measurement component for the present thesis in **chapter 3**, including an overview of thermographic phosphor material properties and luminescence thermometry strategies. As the current thesis aims to provide 3D measurements, **chapter 4** introduces the necessary background on the calibration of cameras to create 3D reconstruction of particles distributed in space and how to obtain velocity values from particle displacements. As flow properties are measured using seeded tracer particles, equilibrium between particles and surrounding fluid elements must be assumed. The validity of this assumption is investigated in **chapter 5** by discussing desired particle properties for flow velocity and temperature tracing, before characterising the phosphor particles selected for the present thesis, and how to seed them into the flow. In **chapter 6**, the developed measurement setup for the implementation of simultaneous 3D flow temperature and velocity measurements is thoroughly described. Important components such as lasers, cameras, and spectral filters are characterised, and details on the data processing are provided. Results of a demonstration experiment using this setup and data processing scheme are presented in the following **chapter 7**, including a discussion of factors limiting the current measurement performance. To increase the number of individual temperature and velocity samples and improve the measurement precision, advanced algorithms for nearly all steps of the data processing are introduced in **chapter 8** and their effect on the results is quantified. Finally, **chapter 9** provides a summary of the present work, draws conclusions on the developed measurement technique, and provides an outlook for specific steps that would further increase its capabilities.

Chapter 2

Simultaneous flow thermometry and velocimetry

As discussed in the preceding introduction, there is a need for simultaneous multidimensional measurements of flow temperature and velocity. To satisfy this demand, several concepts have been developed and implemented over the years, often improved or even enabled by technological advancements in light sources, imaging detectors, and computational power needed for evaluation of multidimensional data. This chapter provides an overview of some of these concepts. They share that optically transparent flows are made visible to detectors for velocity measurements by adding small tracer particles. Assuming that these particles follow the flow truthfully, its velocity can be inferred from observed particle motion, as detailed in chapter 4, using techniques like particle image velocimetry (PIV, section 4.3.1) or particle tracking velocimetry (PTV, section 4.3.2). These techniques can be combined with methods for simultaneous flow thermometry that either measure the fluid temperature directly or use the seeded particles not only for velocimetry but also as flow thermometers. In the following sections, different flow thermometry methods and sensor particles that are compatible with particle based flow velocimetry are discussed.

The first method is filtered Rayleigh scattering in **section 2.1**, in which the elastic scattering of light on gas molecules is used for temperature measurements. This is followed by laser induced fluorescence in **section 2.2**, where a fluorescent dye is

dissolved or dispersed in a flow, emitting a temperature dependent fluorescence. In **section 2.3**, such dyes are bound to polymer particles to act as discrete temperature and velocity sensors. In **section 2.4**, thermochromic liquid crystals are introduced as temperature and velocity tracers that reflect different parts of the visible spectrum depending on their temperature. Finally, thermographic phosphor tracer particles are introduced in **section 2.5** that emit a temperature dependent luminescence upon excitation.

2.1 Filtered Rayleigh scattering

Filtered Rayleigh scattering (FRS) is a laser-optical and nonintrusive technique capable of quantitative gas-phase temperature, velocity, density, pressure, and species concentration measurements, that was first implemented for planar velocity measurements (Miles et al. 1990). It relies on light scattered by individual gas atoms or molecules present within a flow without the need for additional seeded tracers. At its core, FRS is a variant of conventional Rayleigh scattering (Dyer 1979; Miles et al. 2001). In this technique, a laser is used to illuminate the flow region of interest, where gas atoms or molecules much smaller than the wavelength scatter light proportional to the species number density and its scattering cross-section. Due to the Doppler shift of the scattering signal resulting from motion of the gas molecules, information about the aforementioned flow quantities is encoded in the Rayleigh signal intensity and spectrum (Ground et al. 2023). As the Rayleigh scattering cross-section of gas atoms and molecules is low compared to geometric scattering from surfaces or Mie scattering from larger particles (Hecht 2017), its intensity is low and easily obscured by interfering signals. This makes combined gas phase thermometry using Rayleigh scattering with simultaneous velocimetry using seeded tracer particles close to impossible. FRS was developed to overcome this limitation by using a narrow notch filter that stops Mie-scattered light from reaching the detector. For this, the laser wavelength is precisely tuned to the absorption line of an atomic or molecular species, while its spectral bandwidth is reduced by means of injection-seeding, to be narrower than the bandwidth of the targeted absorption line. If a cell filled with the selected species is then placed in front of the

detector, it acts as a molecular filter that strongly attenuates stationary scattering signals at the laser wavelength while permitting most of the more broadband and Doppler-shifted Rayleigh scattering signal to pass as summarised in Steinberg 2023. This leads to a strong increase in signal-to-noise ratio (SNR) as background signals at the laser wavelength are effectively attenuated (Forkey et al. 1996). Iodine cells have been widely adopted as filters owing to their compatibility with widely available high-power frequency-doubled Nd:YAG lasers (Miles et al. 1990).

Initial 2D temperature measurements using FRS have been reported in Hoffman et al. 1996 and Elliott et al. 1997. In both studies combustion environments have been investigated, and temperature information was extracted from recorded FRS signal intensities. If simultaneous information about the flow velocity is desired, FRS can be combined with particle based velocimetry techniques such as PIV. This was implemented by Most et al. 2001 and applied for turbulent flow research in Most et al. 2002. Since then, this has been expanded to 2D thermometry using planar FRS combined with stereoscopic PIV for simultaneous 3D velocity information within a 2D plane (McManus et al. 2020). Interest in FRS development continues to date, leading to performance improvements and time-resolved FRS measurements (Doll et al. 2016; Doll et al. 2022; Ground et al. 2023).

However, 3D-FRS temperature measurements integrated with simultaneous 3D velocimetry remain challenging. This is due to the already complex data evaluation for planar FRS (Dinkelacker et al. 2009), the added complexity when integrating it with simultaneous velocimetry (McManus et al. 2020), and technical limitations for volumetric illumination. Already for planar FRS temperature measurements in a 30 $\times$ 0.36 mm^2 light sheet, initial laser pulse energies of 800 mJ were required McManus et al. 2020. For volumetric measurements, this would need to be multiplied to maintain an adequate laser fluence for sufficient Rayleigh scattering signal strengths. This prevents FRS from being implemented in the present thesis.

2.2 Laser induced fluorescence

Laser induced fluorescence (LIF) is a technique for scalar measurements, such as temperature or species concentration, in liquid and gas flows with a high spatial resolution (Hanson 1988; Cruyningen et al. 1990). It is based on the excitation and subsequent fluorescence of tracers added or naturally present in the investigated flow, for example, as a combustion product. These tracers can be categorised into small molecules, such as OH, CH, CO, and NO_x (Kohse-Höinghaus et al. 2002); larger molecules, such as formaldehyde, acetone, and biacetyl (Bäuerle et al. 1994; Schulz et al. 2005; Böhm et al. 2010); or dyes, such as fluorescein or different rhodamine variants (Crimaldi 2008).

For planar LIF (PLIF), a thin light sheet is formed to excite tracer fluorescence in a well-defined plane. It is important that the tracer has a high absorption cross-section at the utilised laser wavelength which regularly requires tunable dye lasers if small molecule tracers are used, while large molecule tracers are commonly excited using frequency tripled or quadrupled Nd:YAG lasers (Hanson 1988; Böhm et al. 2010). The subsequently emitted fluorescence signal is then recorded using a camera, and temperature information is inferred from it using suitable intensity calibration. As the fluorescence signal imaged by a camera is also dependent on tracer concentration and excitation energy, a ratiometric two-colour approach is commonly implemented. It counters these cross-dependencies by employing two different tracers with unique emissions, for example, implemented using two different dyes for liquid thermometry in Natrajan et al. 2008. Currently, 2D LIF measurements are state of the art and have been successfully applied in micro- (Natrajan et al. 2008; M. Kim et al. 2010) and macroscopic (Sakakibara et al. 1999; Shafii et al. 2009) flows.

In recent years, 3D-LIF measurements were developed, either using a scanning approach where multiple 2D planes are imaged in rapid succession (Krug et al. 2014; Kashanj et al. 2023) or using a tomographic approach where fluorescence intensities are reconstructed from multiple views (Gomez et al. 2023). Of these two approaches, the latter offers very high temporal resolution, limited only by the light source and detector capabilities. However, there is a compromise between

spatial resolution, measurement volume size, and the number of cameras required. Typically, eight different views are used to provide the necessary information to solve the tomographic reconstruction problem of continuous intensity distributions (Halls et al. 2018). While using eight separate cameras would allow the highest spatial resolution or measurement volume size, it requires wide optical access to the flow and the availability of enough cameras. Special imaging optics such as quadscopes can be used to reduce the number of cameras to two by imaging a different view of the measurement volume on each quarter of an image sensor at the expense of effective sensor resolution per view (Gomez et al. 2023).

While the combination of LIF with tracer particles for simultaneous particle based velocimetry has been demonstrated by combining scanning stereo PTV with scanning PLIF in Krug et al. 2014, there are complications when trying to combine tomographic PTV or PIV with LIF for full 3D measurements. One major concern is the attenuation of the laser light by seeded particles as it travels through the measurement region. Krug et al. 2014 developed a correction scheme for this effect for planar measurements. However, no equivalent correction scheme has been reported to date for 3D measurements. As two-colour LIF is insensitive to local excitation fluence changes, this could be countered by implementing a two-colour 3D-LIF approach. This would double the number of views required for the reconstruction of the fluorescence signal though, in addition to the tomographic imaging system for simultaneous velocimetry (cf. chapter 4). In light of the resulting high setup complexity other thermometry methods that use particles for both thermometry and velocimetry are considered for the present thesis.

2.3 Dye-filled polymer particles

One approach to reduce the number of views required for the tomographic reconstruction of dye fluorescence compared to classical LIF is to bind the dye to a small particle. Not only does this shield the dye against influences from the flow chemistry (Schulz et al. 2005), it also creates distinct emitters that can serve as both temperature and velocity tracers. Velocity is measured from particle displacement and temperature is inferred from particle luminescence, resulting in combined measurements at the exact same location.

In Massing et al. 2016 such a technique was developed, where polymethylmethacrylate (PMMA) particles were dyed with perylene and europium (III) thenoyltrifluoroacetonate (EuTTA) for two-colour LIF temperature measurements on a per-particle basis. Particles with a nominal diameter of 10 µm were produced, seeded into a water droplet, and monitored using an imaging microscope. A temperature precision of 4.4 K was achieved over a range of 293 K and 333 K and a combination with PIV or PTV for simultaneous velocimetry is readily possible. A challenge for two-colour fluorescence measurements with micrometer-sized dye particles is that the emission intensity ratio between both dyes is a function of particle size due to partial reabsorption of emitted fluorescence , especially for small particles (Labergue et al. 2010). While this can be compensated for in microscopic imaging, where the particle image size is not diffraction-limited, it is not possible for macroscopic imaging targeted in the present thesis. If higher temperatures or (turbulent) gas flows are to be investigated, the glass transition temperature of PMMA (378 K, Kaiser 2011) and the size of dyed PMMA particles used so far (Massing et al. 2016; Deng et al. 2022) would set certain limits as the particles would melt and have long temperature and velocity response times (cf. chapter 5).

In summary, it seems attractive to use seeded tracer particles that act as combined temperature and velocity sensors from a setup point of view, but dyed PMMA particles are not ideal for the planned application in turbulent gas flows at temperatures exceeding 400 K. Therefore, other particles are explored.

2.4 Thermochromic liquid crystals

Thermochromic liquid crystals (TLCs) are complex organic compounds that belong to the group of thermotropic liquid crystals. As such, they exhibit an intermediate phase in addition to the pure solid and liquid phases. If the TLC temperature is below a compound-dependent limit, it solidifies, forming a crystal phase, whereas it completely liquifies if the upper temperature limit is exceeded (Abdullah et al. 2010). In addition, thermochromism refers to the temperature dependent and reversible change in colour of a compound (Gulati et al. 2021) and is the basis for the application of TLCs as temperature tracers (Kimura et al. 1988).

If TLCs are seeded into a fluid flow, velocity can be inferred from monitoring their displacement over time, while their temperature can be inferred from their colour after careful calibration, as described in detail in Abdullah et al. 2010. Flashlights or white LEDs are commonly used as light sources, and the temperature dependent colour of the light reflected by TLCs is used as a temperature measure (Hiller et al. 1993). Using colour cameras as sensors, TLCs have been used for 2D flow visualisation and thermometry for several decades (Smith et al. 2001). Recently, this has been expanded to combined 3D flow temperature and velocity measurements using particle tracking (Segura et al. 2012; Segura et al. 2015; Käufer et al. 2023) or cross-correlation (Schiepel et al. 2021) based approaches in micro- and macrofluidic contexts. As the TLC colour is very sensitive to temperature changes, temperature precisions on the order of 0.2 K are commonly achieved (Käufer et al. 2023). Another advantage of TLCs is that only white LEDs and no lasers are required as light sources, making the technique more economically affordable than laser-optical alternatives. The main drawbacks of TLCs for application in a broader range of (turbulent) flows are their limited absolute temperature range and physical size. Commonly, TLCs can measure temperature only over a range of 0.5 to 4 K with an upper limit at 333 K (Li et al. 2023). To scatter enough light for reliable imaging, the TLCs also must be rather large, regularly exceeding 40 µm (Schiepel et al. 2021) which severely limits their applicability in turbulent gas flows due to high temperature and velocity response times (cf. chapter 5).

2.5 Thermographic phosphor particles

Thermographic phosphors are ceramics often produced in powder form with particle sizes ranging from nano- to micrometers (Abram et al. 2018). Upon excitation using continuous or pulsed light sources, such as LEDs or widely available lasers, they emit a temperature dependent luminescence that can be exploited for temperature measurements using phosphor thermometry (Allison et al. 1997). These inorganic compounds frequently have a high melting point on the order of 2000 K (Takahashi 2007; Nilsson et al. 2023) and are often highly chemically stable. As their luminescence emission is regularly insensitive to the surrounding atmosphere, they

are suitable for application in harsh and reactive environments (Aldén et al. 2011; Sposito et al. 2021). Potentially interfering signals such as blackbody radiation, chemiluminescence, or background scattering can be filtered efficiently (Mendieta et al. 2019). Driven by the lighting industry, a vast variety of phosphor materials are known to date and new materials are regularly synthesised which allows a material selection tailored to the respective measurement task (Shionoya et al. 2006). These properties made seeded thermographic phosphor particles an attractive option for fluid thermography as reviewed in Abram et al. 2018. As these particles also scatter green light commonly produced by double-pulse or high-speed lasers for particle based velocimetry, their integration with such techniques is straightforward by observing the same particle in different spectral regions for combined temperature and velocity measurements. Such has been reported for point (Ojo et al. 2015; Ojo et al. 2017) and 2D measurements (Omrane et al. 2008; Fond et al. 2012; Neal et al. 2013; Abram et al. 2013; Witkowski et al. 2013).

After comparison with the other identified options (sections 2.1 to 2.4), thermographic phosphors are selected as the basis for the presently developed 3D temperature and velocity measurement technique. In chapter 3, available phosphor thermometry strategies are discussed in more detail, before introducing the specifics of 3D camera calibration, reconstruction, and particle based flow velocimetry in chapter 4 to enable their combination.

Chapter 3

Particle based phosphor thermometry methods

Phosphor thermometry is a remote, optical, and emissivity-independent temperature measurement technique that relies on thermographic phosphors as luminescent sensors (Allison et al. 1997). Upon excitation, thermographic phosphors emit a temperature dependent luminescence that can be captured using point detectors or cameras to provide spatially and temporally resolved temperature measurements up to the kHz range with temperature precisions of a few Kelvin (Abram et al. 2013; Schreivogel et al. 2016; Straußwald et al. 2020). Even better precision has been reached ($< 1\,\mathrm{K}$) when resorting to a lower measurement rate, depending on the used phosphor (Abram et al. 2020). Phosphor thermometry has been demonstrated for a broad range of temperatures, from cryogenic (Beshears et al. 1990) to almost 2000 K (Nilsson et al. 2023). As the emitted luminescence of phosphors is often short-lived and spectrally distinct from black-body radiation, it is applicable to combustion environments where both spectral separation and temporal discrimination of black-body radiation and other background signals, such as fluorescence, is possible (Aldén et al. 2011; Mendieta et al. 2019). As phosphor luminescence is often emitted in the visible spectrum, many substances, such as standard windows, water, or air, are transparent. Hence, measurements through these media are generally possible, which is an advantage over other remote temperature measurement techniques such as infrared thermography. As many phosphors are also insensitive to the chemical composition and pressure of the

local environment (Abram et al. 2018), phosphor thermometry can be more robust than for example temperature-sensitive paints (T. Liu et al. 2021) and is suitable for application in harsh environments such as nuclear decommissioning facilities (Sposito et al. 2021). Initially developed for solid surface thermometry (Bradley 1953), phosphor thermometry is currently applied in fluid flows as well (Abram et al. 2018).

In the following sections, thermographic phosphors are introduced as a class of luminescent materials (**section 3.1**) and specific phosphor thermometry strategies are presented (**section 3.2**).

3.1 Thermographic phosphors

Thermographic phosphors are a group of materials that emit luminescence upon excitation using radiation (x-rays, electron beams, gamma rays, or light in the visible or UV range) where the lifetime or spectrum changes with temperature. Visually, they often appear as white powders of nano- to micrometer-sized particles, but larger solids can also be produced. The majority of phosphors in use are inorganic compounds consisting of a ceramic host material deliberately doped with small amounts of rare earth or transition metal ions to modify their electronic band structures (Allison et al. 1997; Abram et al. 2018). Rare earth ions act as luminescent centres where irradiating energy, provided for example by a short laser pulse, lifts electrons from a ground state to an excited state from where they deplete back to the ground state using radiative and non-radiative processes (Fond 2014). As the rate of non-radiative processes increases with temperature, the luminescence lifetime tends to be temperature-sensitive (Brübach et al. 2013). Another class of phosphors are semiconductors, where luminescence reportedly originates from lattice defects (Rodnyi et al. 2011) or emissions close to the absorption edge (Gong et al. 2007), ultimately originating from exciton states (Abram 2014). Neglecting upconversion phosphors, where the energy of multiple lower-energy photons is combined to emit a photon with higher energy (S. Liu et al. 2023), the emitted photon will have a lower energy (longer wavelength) than the exciting photon owing to the Stokes shift (Albani 2004).

Driven by the lighting and display technology industries and enabled by the close-to infinite number of host-dopant combinations, thousands of different phosphor materials have been synthesised and characterised over the past decades (Shionoya et al. 2006; Ropp 2004; Ropp 2010). For this thesis, the semiconductor ZnO was chosen as a suitable phosphor as detailed in section 5.2.

3.2 Thermometry strategies

As stated above, the luminescence emission of thermographic phosphors is temperature dependent. This can affect both the lifetime and spectrum of the phosphor and allows for multiple thermometry strategies to be implemented by calibrating the luminescence response to temperature. Two main groups are defined: temporal and spectral methods. For temporal methods, one approach is to calibrate the luminescence lifetime as a function of temperature (section 3.2.1). If a modulated light source is used, the phase shift between the excitation and emission signals can also be calibrated against temperature (section 3.2.2). For the spectral methods, either a shift of the emission spectrum or a change in its shape, such as a change in relative intensity of different emission peaks within the spectrum, are monitored (section 3.2.3). In the following subsections, these strategies are discussed.

3.2.1 Lifetime method

Once the excitation energy ceases, the luminescence emission intensity decays over time. As temperatures rise, higher energy vibrational modes become populated within the phosphor, which increases the probability of non-radiative de-excitation mechanisms, which in turn leads to a quicker depletion of excited states, reducing the luminescence lifetime (Abram et al. 2018). As non-radiative de-excitation mechanisms are significantly influenced by the host-dopant combination, their complex interactions are subject of ongoing research (Dorenbos 2005; Makhov et al. 2016; Bai et al. 2024). Over the years, several phosphors have been identified that show a temperature dependent luminescence lifetime in temperature ranges from 200 K to almost 2000 K (Aldén et al. 2011; Nilsson et al. 2023). Figure 3.1a shows an

example for increasingly fast luminescence decay with rising temperature. Using a pulsed light source, such as a pulsed laser, the phosphor can be excited periodically to monitor the subsequent luminescence decay for thermometry applications.

For a given phosphor showing a temperature dependent luminescence lifetime, the time dependent luminescence emission intensity can often be described using a single exponential function

$$I = I_o \exp -t/\tau, \tag{3.1}$$

where the luminescence intensity at time t depends on the intensity after the excitation source ceases I_0 and the luminescence lifetime τ. The lifetime is then defined as the time until the emission intensity decreases to $1/e$ of its initial value. However, for some phosphors, the luminescence decay does not follow a single exponential function which requires a more complex expression (Aldén et al. 2011). Once a suitable model is found, τ can be calibrated over the temperature range of interest to allow subsequent temperature measurements. In fig. 3.1b such a calibration is shown as computed from the luminescence decay in fig. 3.1a.

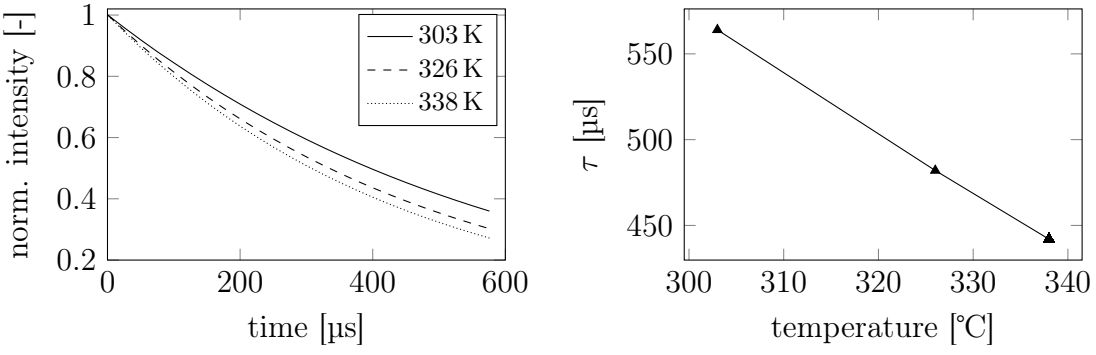

(a) (b)

Figure 3.1: Luminescence emission decay of the $^5D_4$ energy level of $Gd_2O_2S{:}Tb^{3+}$ (a) and lifetime τ derived from it (b). Reproduced from Stelter 2019.

To acquire the intensity decay, several approaches can be adapted. Point sensors such as photodiodes or photomultiplier tubes (PMT, Brübach et al. 2009; Fond et al. 2019b) can be used to directly resolve the intensity decay over time. If planar measurements are needed, either high-speed cameras can be used where the luminescence decay can be fitted using the decaying pixel intensity values

over time (Kissel et al. 2009; Cai et al. 2021; Khodsiani et al. 2024) or a double-frame camera can be used to acquire temporal intensity ratios which allows 2D lifetime-based thermometry without the need for high-speed cameras (Abram et al. 2020). Recently, other methods to obtain luminescence lifetime information from low-speed imaging systems have also been introduced (Cai et al. 2017; Sutton et al. 2019).

While the lifetime method is generally applicable to fluid flows (Abram et al. 2020), it is not the preferred thermometry strategy for the present thesis for two main reasons. First, the developed measurement technique is demonstrated in a turbulent gas jet where particles move at speeds of multiple meters per second. Therefore, particles would move between the recording of individual camera frames, which complicates even the double-frame lifetime method. Second, the phosphor selected for the present implementation features a very fast decay (<1 ns, cf. section 5.2) to prevent motion blur in recorded particle images, which makes a reliable measurement of the luminescence lifetime generally very challenging, especially using imaging detectors needed for spatially resolved measurements.

3.2.2 Phase shift method

If the pulsed light source is replaced by a continuous-wave light source, where the intensity is modulated to follow a periodic function, the emission decay of the phosphor will follow this excitation with a delay proportional to its luminescence lifetime τ (Aldén et al. 2011). If a mono-exponential decay of the luminescence is assumed, this phase shift $\Delta\phi$ is related to the lifetime discussed before via the modulation frequency f as described in López Bonilla et al. 2024 by

$$tan(\Delta\phi) = 2\pi f\tau. \tag{3.2}$$

Therefore, the phase shift between excitation and emission decreases with decreasing luminescence lifetime. As light sources, LEDs or diode lasers are commonly used because their continuous light output is easily modulated (Ojo et al. 2017; López Bonilla et al. 2024). The detector must be able to trace the phase-shifted luminescence emission precisely, which requires a fast sensor response from a PMT,

readout by an oscilloscope, facilitating point measurements, as demonstrated for surface thermometry (McCormack 1981) and in flows (Ojo et al. 2017). This was expanded to 2D measurements using LEDs for excitation and high-speed cameras for luminescence recording (Schreivogel et al. 2015; López Bonilla et al. 2024). Both the LEDs and high-speed camera were triggered synchronously, and the phases of the excitation and luminescence emission signals were calculated from an oscilloscope trace and decaying pixel intensities, respectively, using digital Fourier transforms. In López Bonilla et al. 2024 a spatial resolution of 1 mm and a temperature precision of 0.13 K were achieved for measurements with a temporal resolution of 0.25 s. While appealing, implementing such measurements for 3D flow thermometry would be challenged by the requirement of computing the emission phase shift from moving particle images in turbulent flow (temporal resolution, transient heat transfer), the limited spatial sensor resolution of fast high-speed cameras, and by the lack of light sources that can provide modulated continuous wave volume illumination with absolute intensity levels comparable to pulsed Nd:YAG lasers.

3.2.3 Spectral intensity ratio method

In addition to the time-domain approaches discussed above, it is also possible to exploit a change in the luminescence emission spectrum for thermometry applications. For every phosphor, the emission spectrum can be described by at least one emission line, defined as the localised luminescence emission intensity maximum at a specific spectral location and with spectral width commonly defined by the full width at half maximum (Allison et al. 1997). Both the position and width of these lines can change with temperature, depending on the phosphor. If multiple emission lines that originate from different energy level transitions are present, then their relative intensities can also change with temperature (Stelter 2019). In fig. 3.2, both a change in relative emission intensity and a spectral shift are shown using normalised emission spectra recorded from two phosphors in liquid dispersion. Figure 3.2a shows the change in relative emission intensity for lines originating from ${}_5D^3$ ($<$ 480 nm) and ${}_5D^4$ ($>$ 480 nm) energy levels in $Gd_2O_2S{:}Tb^{3+}$ (Popovici et al. 2004; Yap et al. 2009) using emission spectra normalised to the ${}_5D^3$ emission at 416.6 nm

(Stelter 2019). With increasing temperature, the $_5D^4$ emissions gain relative to those from the $_5D^3$ level. By separately monitoring the intensity emitted from both energy levels, a temperature dependent luminescence intensity ratio (LIR) can be defined intuitively. In fig. 3.2b, the red-shift of normalised ZnO emission spectra with increasing temperature is shown. By selecting filters that monitor, for example, the blue and red half of the spectrum, a temperature dependent LIR can be defined.

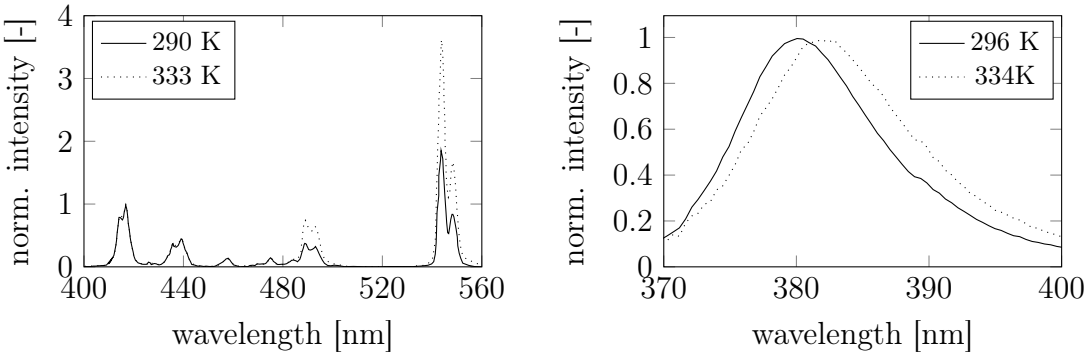

Figure 3.2: Normalised luminescence emission spectra for (a) $Gd_2O_2S:Tb^{3+}$ and (b) ZnO showing a temperature dependent change in emission line intensity or spectral shift, respectively. Reproduced from Stelter 2019.

To facilitate thermometry measurements based on spectral LIR, two separate detectors are commonly used (Abram et al. 2018). Each detector observes a different part of the emission spectrum as governed by distinct interference or coloured glass filters mounted in front of the detectors. The filter selection is tailored to the specific phosphor emission spectrum as detailed in section 6.1.3 from page 82 for the present implementation. Unless point measurements are desired, cameras are most commonly used as detectors and often challenged by low luminescence emission signal levels. It has been shown in multiple studies that low luminescence image signal levels can become a limiting factor for practical thermometry (Lawrence et al. 2013; Jenkins et al. 2012; Lipzig et al. 2013). This aggravates if the emissions of individual phosphor particles are used for thermometry instead of the combined emissions of multiple particles. This warrants a more detailed exploration of ways to quantify and predict the performance of ratiometric phosphor thermometry measurements. Adopting the nomenclature from Abram

et al. 2018, the LIR as basis for such measurements is defined as

$$\varphi(T) = \frac{I_B}{I_A} = \frac{\int_0^\infty E(\lambda, T)\tau_B(\lambda)d\lambda}{\int_0^\infty E(\lambda, T)\tau_A(\lambda)d\lambda} \tag{3.3}$$

where the integrated intensity I_i per channel $i = A, B$ results from the luminescence spectral flux $E(\lambda, T)$ and transmission function τ_i. Following Abram et al. 2018, this transmission function includes the transmissivity of the spectral filter, imaging optics, and the quantum efficiency of the sensor. To quantify the LIR's temperature dependency the normalised sensitivity is defined as

$$\psi(T) = \frac{1}{\varphi(T)}\frac{d\varphi(T)}{dT}. \tag{3.4}$$

Normalising the sensitivity makes it independent of the absolute LIR, allowing an easier comparison among different phosphors or filter combinations. From this it might seem attractive to tune the sensitivity to extremely high values, for example by selecting spectral filters that are at the edges of the luminescence emission spectrum. While ψ would indeed increase, the available signal per channel would be severely limited. According to Abram et al. 2018, this would strongly increase the random temperature uncertainty σ, that is directly related to the integrated intensity and the estimated random uncertainty in these values via

$$\sigma = \frac{1}{\psi}\sqrt{\left(\frac{\sigma_{I_A}}{I_A}\right)^2 + \left(\frac{\sigma_{I_B}}{I_B}\right)^2}. \tag{3.5}$$

Here, σ_{I_i}/I_i is understood as approximation of the inverse SNR in channel $i = A, B$. While the intensities I_i are inferred from spectrally separated camera images, the uncertainties in these values σ_i can be approximated by considering the readout- and shot-noise contributions, given that non-intensified cameras are used for particle luminescence image recording (Fond et al. 2015). Based on Fond et al. 2015, the total gray level noise in individual particle images covering a region of m pixels with gray level intensities I_{p_k} for pixel k and a resulting total intensity of $I_i = \sum_{k=1}^{m} I_{p_k}$

is approximated as

$$\begin{aligned}\sigma_{I_i} &= \sqrt{\sum_{k=1}^{m}\left(\sqrt{\left(\frac{\sigma_r}{K}\right)^2+\left(\sqrt{\frac{I_{p_k}}{K}}\right)^2}\right)^2} \\ &= \sqrt{\sum_{k=1}^{m}\left(\left(\frac{\sigma_r}{K}\right)^2+\frac{I_{p_k}}{K}\right)} \\ &= \sqrt{m\left(\frac{\sigma_r}{K}\right)^2+\frac{I_i}{K}}.\end{aligned} \tag{3.6}$$

In this equation, σ_r is the readout noise of the camera in electrons, and K is the camera conversion factor in electrons per count. It is then possible to compute the random uncertainty in measured LIR as

$$\eta = \sqrt{\left(\frac{\sigma_{I_A}}{I_A}\right)^2+\left(\frac{\sigma_{I_B}}{I_B}\right)^2}. \tag{3.7}$$

Using these equations together with information from recorded particle images, one can estimate the signal limited LIR and temperature precisions, to assess potential performance improvements directly related to imaged signal levels (cf. section 7.2.3).

Using the spectral LIR approach, phosphor thermometry point measurements (Ojo et al. 2015) and 2D measurements (Särner et al. 2008; Fond et al. 2012; Abram et al. 2013; Straußwald et al. 2020) have been reported in the literature. As this method allows instantaneous 2D temperature measurements using low-noise, non-intensified, and low-speed sCMOS cameras as luminescence detectors, together with low-lifetime phosphors to omit image motion blur, it is well suited and selected for the 3D measurements developed in the present thesis.

To obtain 3D temperature measurements from 2D camera recordings of individual phosphor particle luminescence emissions, the 3D position of these particles must be reconstructed and associated with the luminescence images. The reconstruction of these 3D particle locations from multiple 2D views of an illuminated measurement volume is discussed in the following chapter.

Chapter 4

Particle based 3D reconstruction and flow velocimetry methods

This chapter provides an overview of the fundamentals of particle based flow velocimetry and state of the art implementations for 3D measurements. Although holographic methods have been applied for 3D flow velocimetry (Chen et al. 2021), they entail several technical constraints, such as limited spatial resolution, measurement volume size restrictions, and setup complexity (Schäfer et al. 2011; Scarano 2013). Therefore, this thesis focuses on photogrammetric velocimetry techniques that use an array of cameras to record images of tracer particles seeded into a flow from different views. To use these recordings for quantitative 3D flow measurements, camera calibration models must be computed. These models establish a mathematical relationship between the 3D world space, where the particles are located, and the 2D camera image space, where the images of the particles are recorded. **Section 4.1** introduces the pinhole camera model and its computation for real cameras based on target images and its refinement using particle images. Once the cameras are calibrated, images of tracer particles seeded into a flow are simultaneously recorded from multiple views. From these views, 3D particle positions are reconstructed using either optical tomography or triangulation (**section 4.2**). By recording the particle images in quick succession, the displacement of the 3D particle positions reconstructed from these recordings can be evaluated over time. Considering the time delay between individual particle image recordings, this displacement yields velocity information. In **section 4.3**, three different methods for computing velocity information from particle displacements are presented.

4.1 Camera calibration

Perspective camera calibration is a prerequisite for volumetric multicamera measurement techniques, such as those presented in this thesis. Its aim is to establish a mapping between the 3D world space of the measurement volume and the 2D image space of each camera observing this volume, enabling the reconstruction of voxel intensities (tomography, section 4.2.1) or particle locations (triangulation, section 4.2.2) from multiple views of a measurement volume filled with tracer particles, and the determination of image coordinates of 3D particle positions. Over the years, two main groups of mapping functions have been developed: polynomial and pinhole camera-based mapping functions. Polynomial models such as those introduced by Soloff et al. 1997 and Prasad 2000 directly connect image with volume coordinates using second- or third-order polynomials. They require recordings of target planes translated precisely to typically three to seven positions at well-defined intervals within the measurement volume (C. E. Willert 2006). While polynomial functions are very flexible in accounting for refractive index changes within the optical path between the camera and measurement volume, not all of the numerous parameters are relevant (Wieneke 2005). Compared with these polynomial mapping functions, pinhole camera-based models are easier to interpret and require fewer parameters to be fitted. While the most basic pinhole camera model does not account for lens distortions (Hartley et al. 2019), variants with distortion parameters (Tsai 1987; Z. Zhang 2000; C. E. Willert 2006) and Scheimpflug adapters (Fournel et al. 2004; Louhichi et al. 2007; Cornic et al. 2016; Yin et al. 2019) have been developed. Although both polynomial and pinhole model mapping functions can be used with the presented measurement concept, a pinhole-based mapping function was chosen for its good interpretability and easy inversion of the mapping function for reconstruction using both tomography and triangulation. The mathematical basics for pinhole models considering Scheimpflug conditions (section 4.1.1) are introduced next.

4.1.1 Pinhole camera model

For the formulation of pinhole models, the following notation is used. Bold letters such as $\boldsymbol{P}$ are used for vectors and matrices, points in 3D space are denoted by capital letters such as X, and points in 2D space use lower-case letters such as c. At its core, a basic pinhole camera model consists of a 3×4 projection matrix $\boldsymbol{P}$ that relates image points $\boldsymbol{x} = (x, y, 1)^T$ to corresponding world points $\boldsymbol{X} = (X, Y, Z, 1)^T$ both noted in homogeneous coordinates as formulated by Hartley et al. 2019 as

$$\boldsymbol{x} = \boldsymbol{P}\boldsymbol{X}. \tag{4.1}$$

Following Hartley et al. 2019, the projection matrix $\boldsymbol{P}$ can be decomposed into an intrinsic matrix $\boldsymbol{K}$ and an extrinsic matrix $[\boldsymbol{R}|\boldsymbol{t}]$. The intrinsic matrix contains information about the *internal* parameters of the modelled camera, such as its focal length along the vertical and horizontal image sensor axes (f_x, f_y), the skew s to account for non-perpendicular image coordinate system axis (normally 0 for rectangular pixels), and the location of the principle point (x_0, y_0) as intersection of the image plane with the image plane normal that passes through the camera projection centre.

In general, points such as particle positions are referenced in a 3D Euclidean space referred to as the world coordinate system (WCS). Therefore, it is necessary to determine the position and pose of the camera within this reference frame. This information is stored in the extrinsic matrix $[\boldsymbol{R}|\boldsymbol{t}]$ where $\boldsymbol{R}$ represents the rotation of the camera about the WCS axes and $\boldsymbol{t}$ is the translation of the camera centre with respect to the origin of the WCS (C. E. Willert 2006). Combining internal and external matrices one can write the projection matrix as

$$\boldsymbol{P} = \boldsymbol{K}[\boldsymbol{R}|\boldsymbol{t}] = \begin{bmatrix} f_x & s & x_0 \\ 0 & f_y & y_0 \\ 0 & 0 & 1 \end{bmatrix} \left[\begin{array}{ccc|c} r_{11} & r_{12} & r_{13} & t_x \\ r_{21} & r_{22} & r_{23} & t_y \\ r_{31} & r_{32} & r_{33} & t_z \end{array}\right] \tag{4.2}$$

where the parameters for camera rotation and translation of the extrinsic matrix are conventionally separated by a vertical bar.

In multi-camera setups for 3D measurements, it is common that the camera image sensor plane is not aligned with the main plane of the measurement volume. Hence, the plane of focus does not coincide with the measurement plane which leads to out-of-focus effects in parts of the imaged volume (cf. fig. 6.11 on page 76). To compensate for this, lens tilt adapters are commonly mounted between the camera body and lens. Thus, the plane of focus can be aligned with the measurement volume by satisfying the Scheimpflug principle (cf. fig. 6.12 in page 77). The basic pinhole model described above does not account for this which may lead to inaccuracies when used to model cameras equipped with such adapters. Cornic et al. 2016 extended the pinhole model to account for a Scheimpflug adapter that tilts the lens plane relative to the image plane by τ_x and τ_y (rotation about camera coordinate system x- and y-axes) by augmenting the projection matrix by two additional matrices $\boldsymbol{R_\tau}$ and $\boldsymbol{S}$ to modify the intrinsic and extrinsic parameters of the camera. For further details, including the complete derivation of the augmented camera model, refer to (Cornic et al. 2016).

It is the task of the calibration process described in the next section to find good approximations for the camera parameters in eq. 4.2, and if applicable, $\boldsymbol{R_\tau}$ and $\boldsymbol{S}$, to obtain the mapping function for every camera.

4.1.2 Target image based perspective calibration

Target plates displaying a known pattern are commonly used to estimate the camera-mapping function. These target plates can have either a single plane where all target marks are coplanar or multiple levels presenting a 3D calibration marker pattern (Scarano et al. 2005). Images of the calibration target are recorded while changing the orientation of the target within the measurement volume, as proposed by Z. Zhang 2000. In this thesis, a target showing a regular pattern of black dots on a white background was used. It was translated through the volume using a micrometer translation stage and images of the target were recorded using all cameras while it was placed at multiple locations within the volume (cf. section 6.1.5). From the collection of imaged target points at known WCS locations obtained in this manner, the mapping function was calculated either by fitting a

simple pinhole model (Tsai 1987; Calluaud et al. 2004) or the Scheimpflug camera model (Cornic et al. 2016) using custom MATLAB implementations or commercial software such as LaVision DaVis 11 (LaVision 2025).

4.1.3 Particle image based volume self-calibration

Once camera models based on calibration target images are obtained, they can be used for the reconstruction of 3D particle locations from multiple 2D views (cf. section 4.2). However, initial models are typically subject to at least two types of errors. First, the coordinate system defined by the calibration target can disagree with the illuminated measurement volume. Second, the mapping function from the 3D world to the 2D image space can be flawed. The first type of error is normally caused by a rotational or translational mismatch between the $z = 0$ plane position of the calibration target and the laser beam plane. As this error has a large impact on the results produced by velocimetry techniques that measure 2D velocities and compute the third velocity component perpendicular to the measurement plane, such as stereoscopic particle image velocimetry (PIV), this sparked the creation of various correction schemes (C. Willert 1997; Coudert et al. 2001; Wieneke 2005). However, as pointed out by Wieneke 2008, this type of error is much less important for true 3D velocity measurement techniques. For such techniques, the second type of error of a flawed mapping function is much more important. Already apparently low mapping errors from 3D to 2D space of 0.4 pixel cause heavily degraded reconstruction results, as investigated for tomographic PIV by Elsinga et al. 2006. A flawed mapping function can be generated by different mechanisms, such as finite manufacturing accuracy of the calibration target (surface flatness, size, and position of the target markers), instabilities in the camera mounts, or the presence of optical distortions in the recorded particle images that are not accounted for by the mapping function. To correct for these types of errors, a volumetric self-calibration scheme was introduced (Wieneke 2008) and refined (Wieneke 2018).

Volume self-calibration (VSC) uses the initial camera models provided by a target image-based calibration as initial input and gradually corrects it using information

from recorded particle images. Following Wieneke 2008 and Wieneke 2018, this is achieved by applying an iterative correction scheme depicted in fig. 4.1. While the figure shows three cameras, the process works analogously with any camera number ≥ 2. First, particle images are detected in the recordings of all cameras i as local intensity maxima (x_i, y_i). From these image positions, the 3D position (X, Y, Z) of every particle is computed using triangulation (cf. section 4.2.2). As the cameras' lines of sight (LOS) do not intersect in a single point due to calibration inaccuracies, the particle 3D location is approximated as the point in 3D space with minimum distance to all LOS (least-squares estimation). Using the mapping function $\boldsymbol{P_i}$ each triangulated particle location is projected back to the camera image space. There, the disparity d_i as difference between projected (x_i', y_i') and actually found image locations are computed according to

$$d_i = ((d_{xi}, d_{yi}) = (x_i', y_i') - (x_i, y_i). \tag{4.3}$$

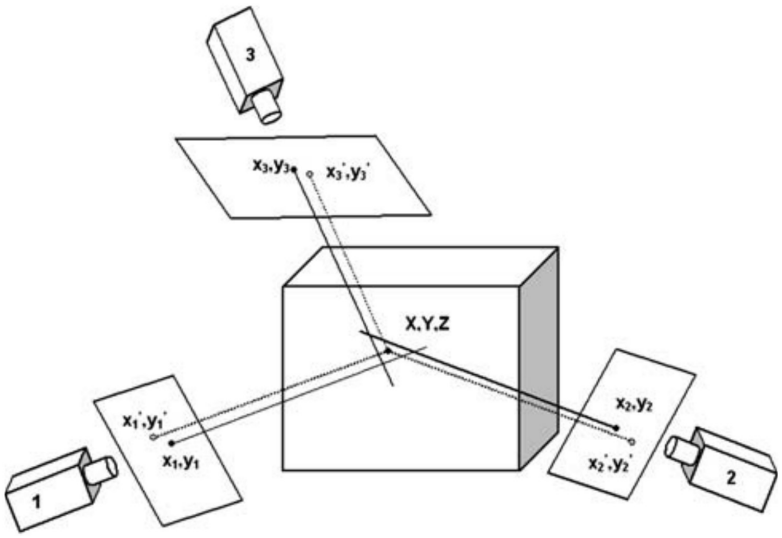

Figure 4.1: Disparity estimation from detected and projected particle locations. Reproduced from Wieneke 2008 with permission from Springer Nature.

To make the disparity estimation more robust, the disparity obtained from multiple particles is combined. All disparities are plotted as identical 2D Gaussian distributions with uniform intensities on a 2D map. By summing the disparity results from individual particles, a strong peak is formed, as shown in fig. 4.2.

The position of this peak is used as an estimate of the true disparity. To account for spatial non-uniformities in the calibration function of each camera (for example due to distortions), the measurement volume filled with triangulated particle locations is divided into n_x, n_y, n_z sub-volumes, and the disparity is calculated separately for each of them. The number of sub-volumes should be sufficiently high to account for spatial non-uniformities in the mapping function while maintaining sufficient particles within each sub-volume for robust disparity estimation. Disparity information is then either used to correct the original mapping function directly by manipulating the camera model parameters to minimise the disparity, or indirectly by computing a correction field that is applied to mapping function outputs. This allows flexible integration of classical pinhole camera-based models with higher-dimensional correction functions. In the present thesis, the correction field approach for correcting the camera pinhole models was applied. The VSC cycle and its enhancements to suppress ghost particles (reconstruction artefacts) are described in detail in (Wieneke 2008) and (Wieneke 2018).

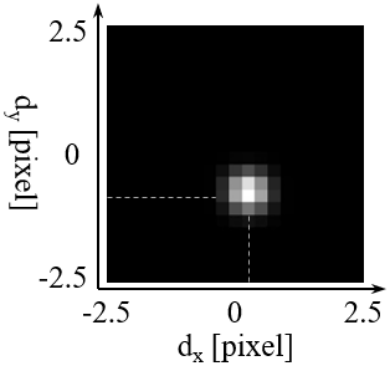

Figure 4.2: Disparity peak obtained from VSC. Dashed lines indicate its x- and y-axis components.

By running the VSC cycle three to six times, the remaining maximum calibration errors are typically reduced to below 0.1 pixel, as required by tomographic PIV or particle tracking at higher particle image seeding densities (Elsinga et al. 2006). In section 8.2, the VSC implementation of LaVision DaVis 11 (LaVision 2025) was integrated into the measurement concept presented in this thesis. Compared to the standard use of using only Mie scattering imaging cameras for VSC, this required the inclusion of luminescence imaging cameras in the VSC cycle, even though their images are not used for later particle 3D position reconstruction. This is critical

for the present technique, as the VSC process can lead to a subtle shift of the WCS origin, as investigated by Cornic et al. 2016. If VSC were applied to only a part of the cameras, then the camera mapping functions would no longer share the same WCS.

Within the present thesis, the VSC described above is referred to as global VSC, as it uses the disparity information gathered from multiple single-shot recordings to create a global correction for the calibration model. Besides this global mode of operation, VSC can also be used to correct for small camera vibrations noticeable from single-shot to single-shot, introduced for example by active cooling elements of the cameras. To detect and correct such variations in camera pose, disparity information is obtained from individual single-shot recordings and used to apply an additional correction to the global VSC (see fig. 8.4 on page 147).

As the final step of VSC in DaVis 11, the optical transfer function is commonly calibrated (Schanz et al. 2012) to correctly model particle images in later iterative reconstruction schemes introduced in sections 4.2.2 and 4.3.3.

4.2 Particle position reconstruction

To enable 3D velocity and temperature measurements using individual phosphor tracer particles, the positions of these particles within a measurement volume must be known. By imaging particles from different views, in combination with the mapping functions obtained in the preceding camera calibration, their 3D locations can be reconstructed using different approaches. A 2D sketch of the general reconstruction principle is shown in fig. 4.3, where three particles *A, B, and C* located within the measurement volume (green area) are imaged from different views of cameras *P2* and *P3*. Neglecting out-of-focus effects, all particles are imaged as identical narrow-intensity peaks. By inverting the mapping function of each camera, the image locations or particle image intensities are projected into the measurement volume along the LOS of each particle. This allows the implementation of two reconstruction principles: Either a volumetric particle intensity distribution is reconstructed using tomography (section 6.2.2), or particle

locations are obtained directly using triangulation (section 4.2.2). In the following section, both principles and exemplary implementations are discussed.

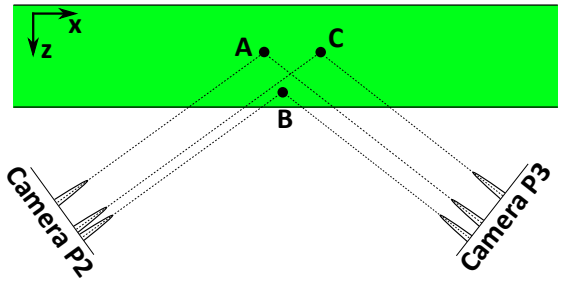

Figure 4.3: 2D representation of the basic reconstruction principle using three particles illuminated within a measurement volume (green) imaged by two cameras P2 and P3.

4.2.1 Tomography

In general, tomography is a 3D reconstruction technique that creates a 3D representation of an object or volume from a series of 2D projections. Therefore, instead of directly measuring the 3D shape, it is inferred from how it appears from different angles. In the context of particle position reconstruction for 3D velocimetry, optical tomography was introduced in Elsinga et al. 2006. The physical measurement volume in the (X, Y, Z) world space is discretised into a 3D array of voxels (N_x, N_y, N_z) with gray level intensities $\boldsymbol{E}(X, Y, Z)$ calculated from the camera image pixel intensities $I_i(x_k, y_k)$ using algebraic methods, as proposed by Herman et al. 1976. Following Elsinga et al. 2006, the relationship between 2D pixel space and 3D voxel space intensity distributions can be written using a linear equation

$$\sum_{m \in L_{k,i}} W_{k,m,i} \boldsymbol{E}(X_m, Y_m, Z_m) = I_i(x_k, y_k), \tag{4.4}$$

where the intensity of voxel m, which is a part of all voxels $L_{k,i}$ intercepted by (or close to) the LOS of pixel k in camera i, is linked to the image intensity distribution via a weighting function with coefficients $W_{k,m,i}$. The weighting function coefficients are calculated as the volume fraction of the LOS with each voxel. Hence, they depend on the pixel size relative to the voxel size, the distance between each pixel's

LOS and the voxel centre, and the shapes of the LOS and voxel. Several methods for calculating the weighting function have been proposed, either using geometric shapes (Lamarche et al. 1990; Thomas et al. 2010; Thomas et al. 2014) or modelling the point spread function of particles (Delbracio et al. 2011; Schanz et al. 2012), to avoid the computationally expensive and non-trivial calculation of an intersection of a frustum projected from each pixel with a cubic voxel. Figure 4.4 shows the tomographic reconstruction principle where the LOS are modelled as cylinders and the voxels are approximated as spheres as proposed by Lamarche et al. 1990.

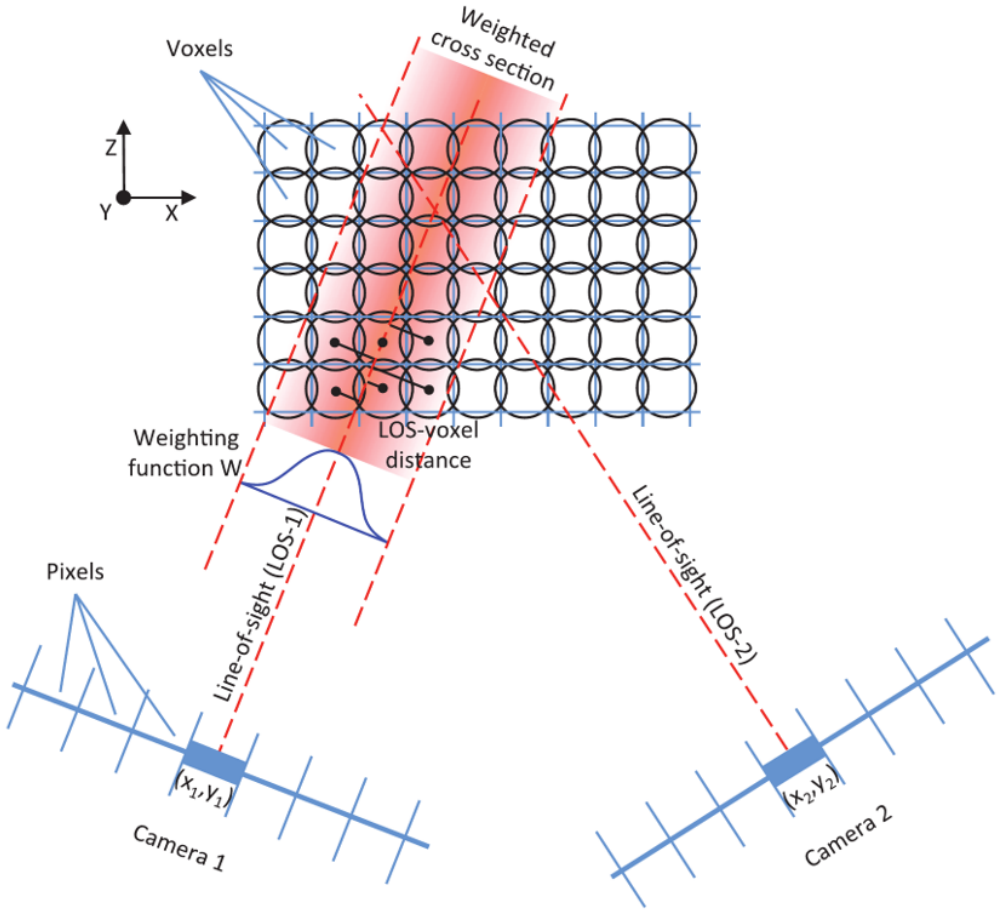

Figure 4.4: World space discretised into voxels and weighted contribution of voxel to pixel intensities via the weighting function W centred on the LOS of each pixel for tomographic reconstruction.

Many algorithms have been proposed to solve eq. 4.4 for practical tomographic reconstruction applications (Martins et al. 2015), including multiplicative LOS

(MLOS, Worth et al. 2008; Atkinson et al. 2009), minimum LOS (MinLOS, Putze et al. 2008; H.-G. Maas et al. 2009), and various algebraic reconstruction techniques (ART, Gordon et al. 1970) such as multiplicative ART (MART, Elsinga et al. 2006; Novara et al. 2010; Lei et al. 2025), simultaneous MART (SMART, Atkinson et al. 2009; Thomas et al. 2014), and block-iterative MART (BIMART, Censor et al. 1987; Byrne 2009). Most of these algorithms implement an iterative reconstruction scheme to improve an initial guess. As shown by Michaelis et al. 2010, the non-iterative and, therefore, much quicker MinLOS algorithm, which is often used to provide this initial guess, is sufficient when the particle image seeding density n_{ppp}, as number of imaged particles relative to the number of pixels in the region of interest of the camera image, is limited to a maximum of 0.02 particles per pixel (ppp). In this algorithm, each voxel is assigned the minimum intensity contributed by all camera views. This means that a voxel is only assigned a high intensity (indicating the presence of a particle), if all cameras see the particle (Putze et al. 2008). Particles are then identified by setting voxel intensities below a threshold to zero, producing isolated structures in 3D space. For the initial demonstration of the proposed measurement concept, a custom solver for this algorithm was implemented in MATLAB (chapter 6).

4.2.2 Triangulation

Unlike tomography, triangulation does not reconstruct the 3D intensity distribution from which the particle positions can be retrieved. Instead, it computes 3D particle locations directly. The triangulation process can be summarised in four main steps.

1. Find particle images in all camera recordings as local intensity maxima.
2. Determine the centre location of each particle image with sub-pixel accuracy using one of various methods (Ouellette et al. 2005; Dabiri 2020), including fitting 2D Gaussian functions (Mann et al. 1999; Kähler et al. 2012a), using weighted averaging (H. G. Maas et al. 1993), or convolutional neural networks (Godbersen, Schanz et al. 2024)).

3. Project the LOS of particle centre locations in each camera into the volume using the inverse mapping function from camera calibration (section 4.1).

4. Approximate the 3D particle location. If the camera models had zero uncertainty, the LOS would match at a single point. This is not the case for real camera models; hence, the 3D particle location is approximated as a point in world space with the minimum distance to all LOS, as shown in fig. 4.1.

In practice, epipolar geometry is commonly employed to implement the triangulation process (H. G. Maas et al. 1993; Hartley et al. 1997). The triangulation procedure using four cameras is visually summarised in fig. 4.5. For every particle detected in the image of camera 1, the LOS within the measurement volume is calculated and projected onto the image of camera 2 (blue line) using epipolar geometry (Z. Zhang 1998). A tolerance ϵ is defined to span a search area around the projected LOS to identify candidates for corresponding particle images (green area). For each combination of particle image (from camera 1) and pairing candidate (from camera 2), a 3D location is triangulated. To eliminate incorrect pairing, the 3D position is projected into the image space of cameras 3 and 4, where candidates are searched within ϵ (green circles). Only if a pairing of particle images can be established in all the images, the 3D location is kept. Here, four potential 3D locations are obtained (for example one true and three ghost particles). The rate of ghost particles scales with ϵ^5 and n_{ppp}^3 (Wieneke 2008). Hence, the particle image seeding densities used with triangulation are normally lower than those used with tomography schemes (H. Kim et al. 2012).

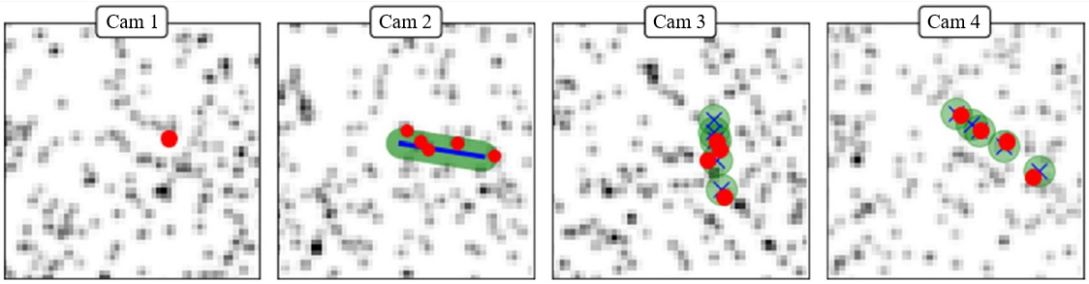

Figure 4.5: Triangulation scheme using epipolar geometry and four camera views. Selected intensity peaks (red) within a tolerance ϵ (green) around a given LOS (blue). Adapted from Jahn et al. 2021 (CC-BY 4.0).

The iterative particle reconstruction (IPR) scheme was recently developed to deal with higher particle image seeding densities in triangulation (Wieneke 2012; Jahn et al. 2021). It allows precise triangulation at higher particle image seeding densities of for example 0.05 ppp in Wieneke 2012 and Jahn et al. 2021 that were not usable with triangulation before. The key to IPR is the iterative execution of triangulation steps with the optimisation of reconstructed 3D particle locations using information from the recorded particle images, similar to MART.

A graphical overview of the IPR procedure is presented in fig. 4.6. Particle images are detected in the camera recordings as local intensity peaks. From these peaks, initial 3D particle locations are triangulated and stored in a state vector. Due to reconstruction inaccuracies, it will contain both true (green) and ghost (red) particle locations. An inner cycle (small arrows in fig. 4.6) is used to refine true particle locations and remove ghosts. To optimise reconstructed particle locations, they are slightly shifted in each direction. Each of these positions is projected back into camera image space using the mapping function and optical transfer function obtained from camera calibration (Schanz et al. 2012). By subtracting the projection from the actual camera recording a residuum is created. By minimising this residuum the optimal 3D position is found for every particle (Wieneke 2012). After executing the inner optimisation loop for a prescribed number of iterations, residual images are computed for all cameras using the surviving 3D particle position candidates in the state vector. From these residual camera images triangulation is attempted again to recover additional 3D particle locations. The whole cycle is repeated until a specified number of outer iterations is reached. Typically, 10 to 20 inner and outer iterations are performed (Jahn et al. 2021).

As the number of free parameters in the 3D reconstruction problem with triangulation is orders of magnitudes lower than for tomography (Wieneke 2012), the computational cost of IPR is much lower than for iterative tomographic reconstruction algorithms (Worth et al. 2008; Michaelis et al. 2010; Lynch et al. 2015). The effect of using IPR implemented in LaVision DaVis 11 (LaVision 2025) instead of a custom single-pass tomographic reconstruction using MinLOS was benchmarked in section 8.3.

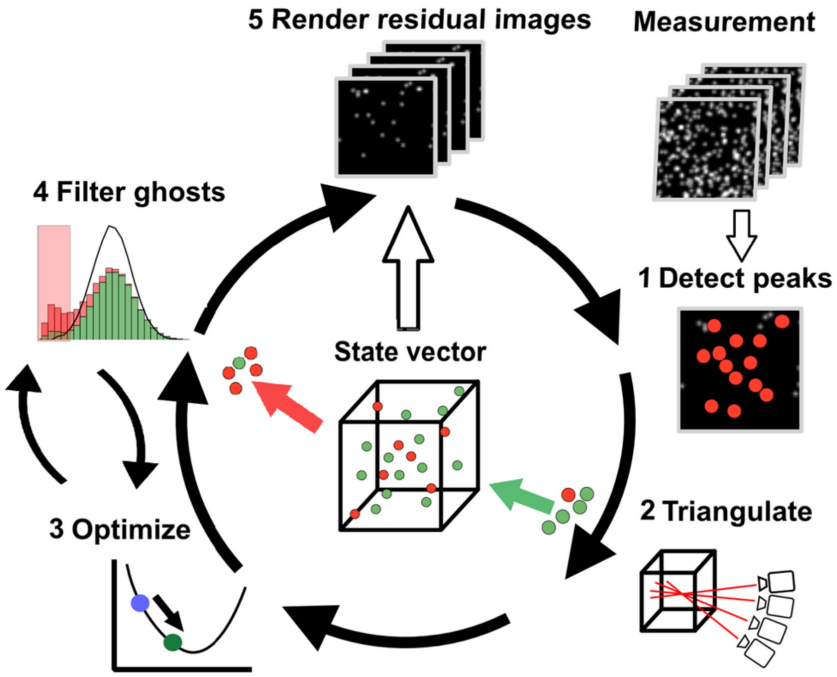

Figure 4.6: IPR schematic showing the outer and inner loops using large and small arrows. Reproduced from Jahn et al. 2021 (CC-BY 4.0).

4.3 Particle image based flow velocimetry

Measuring flow velocity is possible in a variety of ways. Once it is known, other variables including gradients, vorticity, rortex, and turbulence statistics are readily derived from it, to help identify and investigate various flow structures (Scarano et al. 2009; Violato et al. 2011; Lemos 2012; Guyon et al. 2015; C. Liu et al. 2018). To determine how to measure the flow velocity in a specific experiment, an overview and understanding of the available methods is desirable. One class of velocity measurement techniques relies on seeded particles to track and visualise transparent flows. Within the scope of this thesis, only such techniques are implemented and discussed. The same particles can then be used for flow velocimetry and thermometry. As volumetrically distributed 3D velocity (and temperature) measurements are required, point measurement techniques, such as laser Doppler velocimetry (Stein et al. 1969; Adrian 1991; Tropea 2007), are excluded. Hence, we arrive at three velocimetry techniques introduced below and used within the scope of this thesis: particle image velocimetry (PIV, section 4.3.1), particle tracking

velocimetry (PTV, section 4.3.2), and the recent addition Shake-The-Box (STB, section 4.3.3).

Although all three techniques are applicable to high-resolution 3D velocimetry, their modes of operation and strengths differ. PIV and PTV are well-established techniques that are constantly being developed and have been compared several times over the past decades (H. G. Maas et al. 1993; Doh et al. 2012; Cierpka et al. 2012; Scarano 2013). The key difference between the two is the manner in which the velocity information is extracted from the particle images. Whereas PIV relies on window-based cross-correlation to follow particle groups (Raffel et al. 2018), PTV tracks individual particles (Adrian 1991). Consequently, PIV returns velocity vectors on a regular grid, whereas PTV results in an unstructured vector field corresponding to Eulerian and Lagrangian results (Schröder et al. 2010). Often, the particle image seeding density n_{ppp} governs the decision for or against one of these contestants. While PIV requires a sufficiently high n_{ppp} to achieve accurate cross-correlation results, n_{ppp} must not exceed an upper limit for PTV, as otherwise tracking individual particles becomes impossible (Schneiders et al. 2017). The value of this upper limit ranges between 0.005 ppp and 0.025 ppp, depending on the 3D reconstruction approach used for 3D-PTV (Schneiders and Scarano 2016). STB is a much more recent development that enables particle tracking at n_{ppp}, which were previously inaccessible (Schanz et al. 2013). In the following sections, the three techniques are compared.

4.3.1 Particle image velocimetry

PIV development started already before the widespread availability of digital cameras (Burch et al. 1968) and profited greatly from the automated evaluation of digital images (Kimura et al. 1987) with increasing accuracy (C. E. Willert et al. 1991). A modern 2D-PIV setup utilising a double-frame single-exposure scheme is shown in fig. 4.7, where a thin light sheet is formed from a double-pulse laser and directed into a flow with seeded tracer particles whose scattered light is imaged at two time instants t_0 and $t_0 + \Delta t$ on the first and second image frame of a double-frame camera (Raffel et al. 2018).

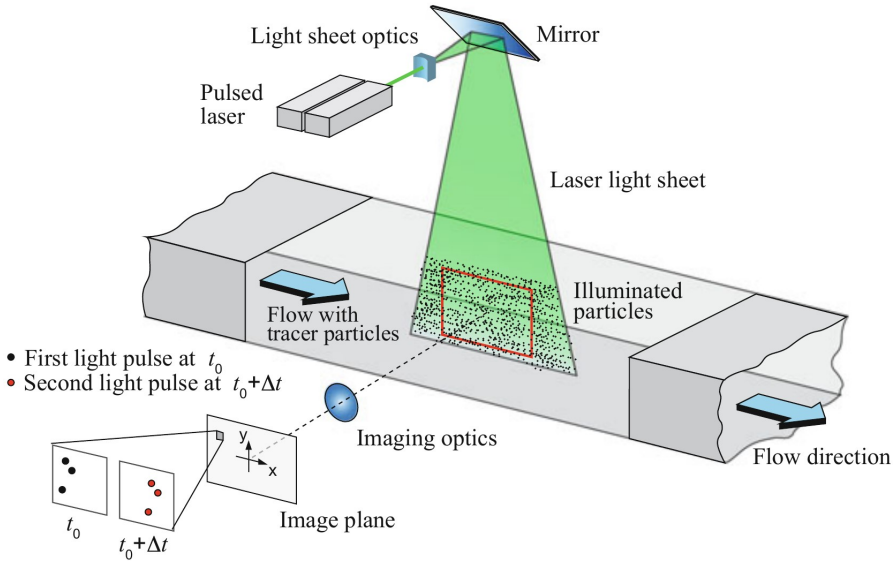

Figure 4.7: 2D-PIV setup schematic where a thin laser light sheet is directed into a flow with seeder tracer particles imaged at two time instants t_0 and $t_0 + \Delta t$. Reproduced from Raffel et al. 2018 with permission from Springer Nature.

The time delay Δt between both laser pulses is chosen to allow a displacement of 8-12 pixel between the camera image frames (Westerweel 1997). Recorded double-frame image pairs are evaluated using a cross-correlation algorithm. For this, the camera images are divided into windows to which the cross-correlation algorithm is applied. This yields the average displacement of all particle images within each window. Using the camera calibration, pixel units are converted to world units and displacement to velocity values considering the known Δt (Raffel et al. 2018).

These 2D measurements were expanded to investigate 3D flow features by either implementing a scanning approach in which multiple 2D planes are recorded in rapid succession (Brücker 1997; Rousseau et al. 2020) or a stereoscopic imaging setup in which the third velocity component is computed from two 2D images (C. Willert 1997; Prasad 2000; Wieneke 2005). These measurements are commonly referred to as 2D3C, indicating that all three velocity components are accessible, while measurements are recorded in two dimensions. Although stereoscopic PIV remains a valuable tool (Patil et al. 2023), the demand for 3D three-component measurements is high. Nowadays, these are readily possible using tomographic PIV, where seeded tracer particles are imaged from multiple views in a volumetrically

illuminated flow, and using tomographic reconstruction to obtain 3D particle volumes, to which a 3D cross-correlation is applied for displacement evaluation, making the full velocity gradient tensor available (Elsinga et al. 2006; Novara et al. 2010; Silva et al. 2012; Scarano 2013; Champagnat et al. 2014; Lei et al. 2025).

The advantages of PIV as an Eulerian measurement technique, compared to Lagrangian contestants, include other quantities, such as vorticity, often being defined as Eulerian quantities, allowing a straightforward computation from velocity results. In addition, grid-based data can be compared directly with numerical results for validation or data assimilation (He et al. 2022). However, because PIV relies on window-based cross-correlation, it applies an inherent low-pass filter to the velocity results by providing the average particle velocity per cross-correlation cell. Velocity differences at smaller scales cannot be resolved (Kähler et al. 2006). Considering that the present thesis provides a joined measurement capability for flow velocity and temperature, where each particle acts as a distinct thermometer, obtaining velocity information directly on a per particle-level without interpolation of grid-bound data is appealing.

4.3.2 Particle tracking velocimetry

Using the same measurement setup as for PIV (fig. 4.7), it is also possible to perform PTV. In results from PTV, velocity vectors are scattered within the measurement area instead of being bound to a regular grid. This allows exceptionally low uncertainties in measured particle displacements (and hence velocities) and little modulation of rapid velocity changes (Kähler et al. 2012a; Kähler et al. 2012b).

The basic principle of 2D-PTV measurements can be summarised in a few steps, starting with the detection of individual particle images in camera images. This is commonly achieved by removing background signal and searching for local intensity maxima (Raffel et al. 2018). Then, the particle image location is determined with sub-pixel accuracy, as described above in section 4.2.2, before pairing particle images between subsequently recorded camera images belonging to the same physical particle. This last step is critical in PTV evaluation because incorrect pairing results in spurious velocity vectors. This is the main reason for the requirement of

a reduced particle image seeding density compared to PIV evaluations, as discussed above in section 4.3. For 3D-PTV, the processing is similar and depends mostly on the employed 3D reconstruction scheme of triangulation (section 4.2.2; H. G. Maas et al. 1993) or optical tomography (section 4.2.1; Schneiders, Caridi et al. 2016; Stelter et al. 2023) extended by a particle pairing scheme. In general, the extension of PTV to 3D measurements started already in the 1990s (Dinkelacker et al. 1992; H. G. Maas et al. 1993) and since then 3D-PTV has been continuously improved (Pereira et al. 2006; Barker et al. 2011; Fuchs et al. 2016; Cornic et al. 2020; Wu et al. 2021).

To achieve reliable pairing, several methods have been explored for 2D and 3D particle tracking applications. The most straightforward is nearest neighbour pairing, where each particle recorded at time t_0 is paired with the closest particle at $t_0 + \Delta t$ (Pereira et al. 2006). This can be combined with a displacement predictor, obtained, for example, from *a priori* knowledge of the flow field or ensemble cross-correlation, as implemented in section 6.2.3 (Stelter et al. 2023). Other pairing strategies augment nearest neighbour pairing using additional constraints to resolve pairing ambiguities. Examples include minimum acceleration or minimum change in acceleration criteria along tracks of at least three and four time-correlated particle recordings (Virant et al. 1997). Cardwell et al. 2011 provides an overview of more (double-frame) particle pairing schemes for PTV application, including some not reliant on velocity predictors but on similar particle image size and intensity at both time instants (Mikheev et al. 2008). In general, the pairing of 3D particles over successive time steps is subject of ongoing research. (Mercier et al. 2024).

Once 2D or 3D particle locations are paired between time steps t_0 and $t_0 + \Delta t$, Δt is used to convert displacements to velocities, resulting in Lagrangian velocity tracks. Because they are not bound to predefined grid locations, they are free of spatial smoothing (Kähler et al. 2012a). Because the velocity must be combined with the temperature information obtained from the same particles, PTV is advantageous for the measurement capability developed in this thesis. Potential disadvantages, such as the need for interpolation of the scattered data to a regular grid to compute velocity-derived quantities such as vorticity, have been addressed in the literature already (Cierpka et al. 2012). In addition, although not the primary concern of the present thesis, significant progress has been achieved in data assimilation from

scattered velocity data (Jeon et al. 2018; Mons et al. 2022; Godbersen, Gesemann et al. 2024), alleviating the advantage that PIV had over PTV and STB in this area. Finally, STB was introduced in recent years as new particle tracking approach that mitigates the main drawback of a limited particle image seeding density that classic particle tracking processing could handle (cf. section 4.3.3).

4.3.3 Shake-The-Box

The latest tracer particle based flow velocimetry technique is Shake-The-Box (STB). It is a particle tracking method similar to, yet more advanced than, classic PTV. This iterative particle-tracking scheme is implemented solely for 3D measurements. It relies on iterative particle reconstruction (IPR, Wieneke 2012; Jahn et al. 2021) for 3D particle position reconstruction and utilises temporal information to enhance the number of tracked true particles while reducing the number of ghost particles and the computational cost (Schanz et al. 2013). The process of time-resolved STB (TR-STB) is illustrated in fig. 4.8. Particle images are recorded from three to six different camera views at high sampling rates to ensure sufficient temporal correlation between subsequent recordings, which is comparable to tomographic PIV. From the first four recordings, particle volumes are reconstructed using IPR (section 4.2.2) and tracked over time to initialise the method with short tracks (yellow). From these tracks, the position of every particle at the next time step is predicted by fitting the tracks with a polynomial or spline (red). The predicted position is optimised by 'shaking' as known from IPR (Schröder et al. 2022). The tracked particles (green) are then projected into camera image space using the calibration models from VSC and the spatially calibrated optical transfer function (Schanz et al. 2012). This allows the computation of residual images by subtracting projected particle locations from the original camera images, forming images with a lower particle image seeding density. The remaining particles within these images are reconstructed using IPR and tracking is attempted. Particles leaving the measurement volume are removed, and those entering it are initialised using four IPR steps (purple) as for the initial initialisation (Schröder et al. 2022). Using this method, synthetic data with very high seeding levels of 0.125 ppp were processed, recovering 99.65 % of all true particles while creating only 0.13 % ghost particles,

clearly outperforming iterative tomographic reconstruction and tracking of the same data (Schanz et al. 2016). Applied to real camera image data, TR-STB is superior to other evaluation methods available to date (Wolf et al. 2024).

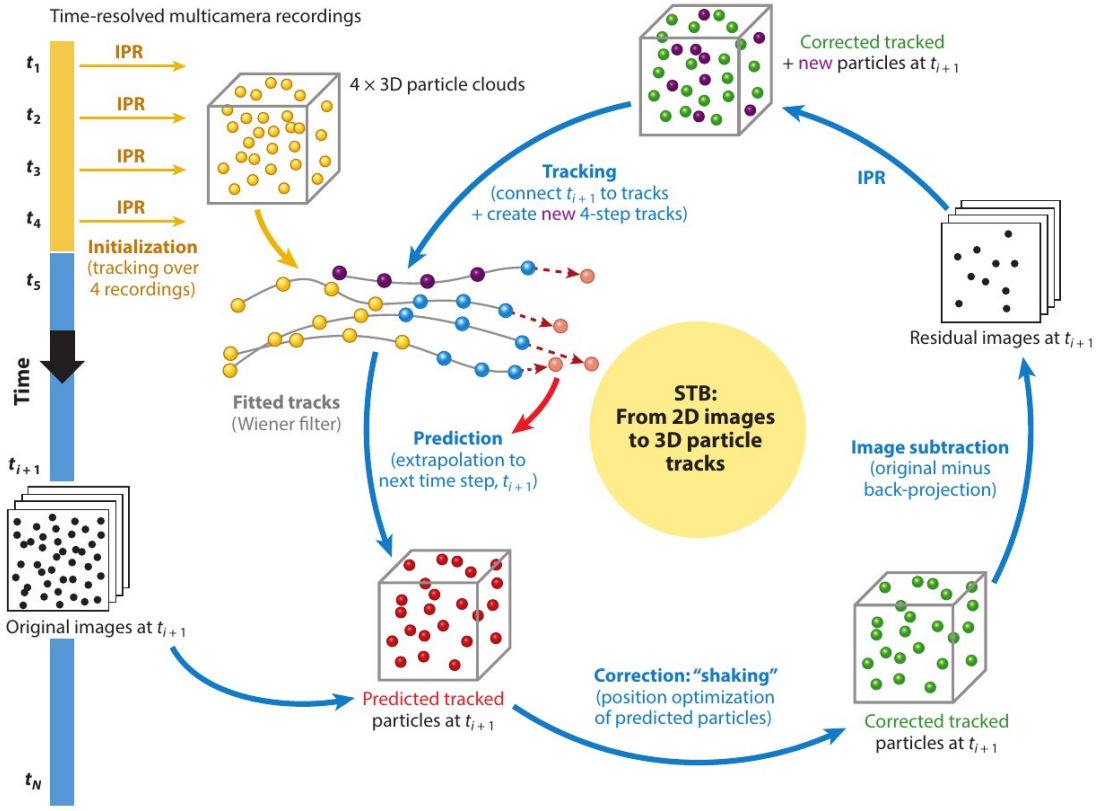

Figure 4.8: Processing scheme for TR-STB, reproduced from Schröder et al. 2022 (CC-BY 4.0).

For investigations of very fast flows where currently available high-speed cameras are not sufficiently fast or high-speed lasers and cameras are not available, STB was extended by a multi-pulse variant. Depending on the implementation, four time-correlated particle images are recorded using either a double-frame single-exposure scheme with two tomographic camera setups (Novara et al. 2016) or a single tomographic camera setup with a double-frame double-exposure imaging scheme (Novara et al. 2018; Novara et al. 2019). By optimising the relative timing of the four recordings (Fenelon et al. 2023), velocity and acceleration are available without the need for or limitations of high-speed lasers and imaging equipment. It was shown that the reduced temporal context is still sufficient to suppress ghost

particles when processing image data with 0.046 ppp.

Particle based flow velocity measurements are often conducted using double-frame single-exposure schemes with a single tomographic camera setup. This is also the case in the present thesis. The recent development of two-pulse STB (TP-STB) enables STB processing also with data acquired using such setups (Novara et al. 2023). At its core, it uses IPR (section 4.2.2) for reconstruction and an iterative particle-tracking scheme (optionally aided by a velocity predictor), as shown in the 2D representation in fig. 4.9 (left). From particle images typically recorded from four camera views, corresponding volume pairs are reconstructed (one for each double-frame image quartet). Particles are tracked between these volumes, and the position of successfully tracked particles is refined by 'shaking'. The optimised positions are then projected into camera image space using the camera mapping functions and optical transfer functions from VSC, as for TR-STB above. Residual images are computed by subtracting these projections from the original camera images. Reconstruction is attempted from remaining local image intensity maxima using IPR again. Subsequently, tracking is attempted again. The entire loop is executed a specified number of times (often between 5 and 11, Novara et al. 2022) to reconstruct and track all imaged particles. To track the particles between both time steps (corresponding to first and second green laser pulse times of double-frame recordings) and suppress ghost particles in the process, a cost function is defined. Track candidates are defined by pairing each particle of the first time step with particles of the second time step within a search area δ_{2p} (right part of fig. 4.9). If a velocity predictor is available (orange arrow, fig. 4.9), the search area is reduced. The cost function for finding the correct pairing uses two factors: First, the reconstructed particle intensity along the track should be constant, and second, the deviation from the velocity predictor (if available) should be minimal (Novara et al. 2023). The velocity predictor can be obtained from multiple sources, for example, by specifying a constant velocity from *a priori* knowledge about the flow, or from coarsely cross-correlating the volumes either in the voxel or particle space, that is, by applying either tomographic PIV (Scarano 2013) or particle space correlation (Novara et al. 2023).

The performance of TP-STB was benchmarked against that of TR-STB for both synthetic and experimental data in Novara et al. 2022. Synthetic data were obtained

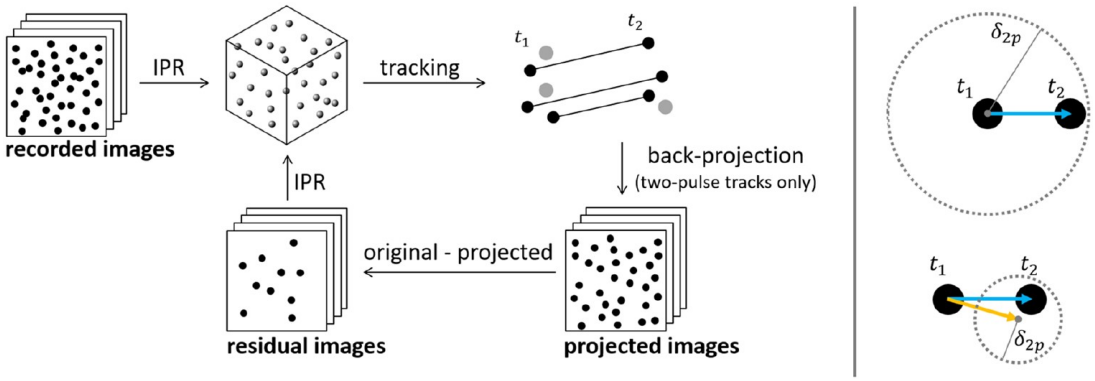

Figure 4.9: TP-STB processing scheme (left) and particle tracking scheme with and without velocity predictor (right) as reproduced from Novara et al. 2023 (CC-BY 4.0).

from the HOMER database (Sciacchitano et al. 2021) for two seeding levels of 0.05 and 0.12 ppp. While TR-STB yielded 52000 and 114 000 tracks, respectively, TP-STB yielded 46700 and 93 600 tracks or 89 % and 81 %, respectively, while maintaining the number of ghost particles below 3 %. Using experimental data with a particle image seeding density of 0.075 ppp, TP-STB retrieved more than 87 % of the data obtained using TR-STB with fewer than 1 % ghost particles (Novara et al. 2022). These results highlight the benefit of time-resolved data when evaluating image data with high seeding levels, but underlines the applicability of TP-STB to these data.

After the initial implementation and demonstration of the combined temperature and velocity measurement capability developed in the present thesis was achieved using an in-house tomographic reconstruction and cross-correlation-aided PTV in chapters 6 to 7, the TP-STB algorithm implemented in LaVision DaVis 11 (LaVision 2025) was utilised in chapter 8 for 3D particle position reconstruction and tracking.

Chapter 5

ZnO particle characterisation as turbulent flow tracer

As for any particle based flow diagnostic, it is important to recognise that the present concept is not probing the flow directly. To infer the flow temperature, luminescence emissions depending on the particle temperature are recorded. To retrieve the flow velocity, the particle positions are monitored using Mie-scattered light (see section 6.1.2 for details on Mie scattering). Because we are interested in flow rather than particle properties, one needs to ensure that the differences between the temperature and velocity of the particle and the flow element around it are negligible. In the following sections, the ideal flow tracer ensuring this crucial condition is described (**section 5.1**) before investigating the selected phosphor particles for the present implementation of the concept (**section 5.2**) and how they can be seeded into the investigated gas flow (**section 5.3**).

5.1 The ideal thermographic flow tracer particle

As outlined above, an ideal flow tracer truly represents the state of its surrounding fluid elements. This means that its response times to local flow temperature and velocity changes must be low compared to the monitored fluid timescale. The characteristics of the ideal flow velocity and temperature tracer are described below.

5.1.1 Velocity tracing

To actually monitor the flow velocity by observing seeded particles, minimal slip velocity between particles and fluid and a fast response of the particles to local changes in flow velocity are required. A central metric for quantifying this response is the velocity response time τ_u. According to Raffel et al. 2018, it is calculated for small particles typically used for flow measurements as

$$\tau_u = d_p^2 \frac{\rho_p - \rho_f}{18\mu_f} \approx d_p^2 \frac{\rho_p}{18\mu_f}. \tag{5.1}$$

It depends on the diameter of the seeded particle d_p, density difference between particle ρ_p and fluid ρ_f, and dynamic viscosity of the fluid μ_f. If the density difference between particle and flow is large, a good approximation of the response time is possible without considering the fluid density.

However, the velocity response time τ_u alone is not sufficient to judge whether particles follow a flow faithfully. Instead, a comparison with the relevant characteristic timescale of the flow τ_f is required, as facilitated by the Stokes number (Raffel et al. 2018).

$$St = \frac{\tau_u}{\tau_f} \tag{5.2}$$

If the Stokes number is below 0.1, the particles follow the flow with little slip velocity, as shown for example by Samimy et al. 1991 and Elliott et al. 1990 using direct numerical simulations in subsonic and laser Doppler velocimetry measurements in supersonic flows. Therefore, a low Stokes number is required. In practice, however, the fluid timescale is often not directly accessible which complicates the estimation of the Stokes number. Instead, one can approximate the attenuation of fluid flow fluctuations measured by particles with certain properties, as done for the zinc oxide (ZnO) particle samples investigated below (eq. 5.4 and fig. 5.3 on page 51).

Some more particle properties are favourable when used as flow velocity tracers. A narrow size distribution of the tracer particles is advantageous, as each particle then follows the flow with the same accuracy. Considering a constant illumination laser fluence, this would also result in a constant Mie scattering signal, promoting equal image registration probability across the entire measurement volume. For this

to hold true, the particle should also be spherical. If the particles are non-spherical, their scattering cross-section would depend not only on the camera angle relative to the laser propagation direction, but also on the particle orientation within the laser beam. Finally, neutral buoyancy must be mentioned even if it cannot be attained by solid phosphor tracer particles in atmospheric gas flow. If particles are neutrally buoyant, their velocity response time would be greatly reduced as the density difference between particle and fluid in eq. 5.1 would diminish.

5.1.2 Temperature tracing

Monitoring the flow temperature using luminescence emissions of particles warrants the dissemination of the influencing particle properties. As for velocity tracing, the temperature response time of the particles to changes in local flow temperature must be low to allow measurements without strong attenuation. Using the approach introduced by Abram et al. 2018, the temperature response time τ_T can be calculated as

$$\tau_T = d_p^2 \frac{c_{p,p}\,\rho_p}{12 k_f}. \tag{5.3}$$

In addition to the particle diameter d_p and density ρ_p, it depends on the specific heat capacity of the particle $c_{p,p}$ and the thermal conductivity of the fluid k_f. If this time is comparable to the characteristic time of the flow, a good correspondence between particle and flow temperature is ensured.

In addition to the particle temperature behaviour, there are several desired properties regarding its luminescence. First, the absorption cross-section and quantum efficiency of the particle should be high, as it translates to an efficient excitation of the luminescence emission. To record particle images with a high signal-to-noise ratio (SNR), strong luminescence emissions are desired. It should be recognised that luminescence emissions cannot be scaled ad infinitum by increasing the irradiating laser fluence, compared to Mie scattering, where this is theoretically possible, as phosphors commonly show a saturation behaviour (Abram et al. 2016). Moreover, the luminescence emissions should be spectrally well separated from the excitation wavelength and green light used for particle position reconstruction and tracking. This allows for the rejection of these signals using spectral filters to ensure that only the signal of interest is recorded by each camera.

When imaging particles in turbulent flow, the luminescence lifetime should be short compared to fluid motion in the camera reference frame. Otherwise, the particle images are subjected to motion blur for long camera exposure times. For 2D measurements, the velocity information encoded in this blur can be exploited for velocimetry as demonstrated in Fan et al. 2021. However, for the present 3D measurement concept it is detrimental as it would increase the number of pixels covered by individual particle images, which would increase the probability of them overlapping. In addition, the peak intensity in the luminescence particle images would be reduced if the signal is spread across multiple pixels, reducing image SNR.

Furthermore, the particle material must be chosen such that it is suitable for the investigated temperature range. This includes both its chemical stability and its luminescence emissions. The absolute signal emitted by the particle must be high enough for sufficient image SNR, and the change in emission spectrum or lifetime per Kelvin temperature difference must be strong enough, expressed as temperature sensitivity. Finally, the luminescence emissions should not be cross-dependent on anything but the temperature. Otherwise, these parameters must be either controlled precisely in the experiment or corrected for in data processing.

5.2 ZnO particle characterisation

For the present implementation of the measurement concept, ZnO was chosen as the thermographic phosphor based on its material and luminescence properties outlined below. Three particle samples from two manufacturers were compared to select the best option for combined turbulent gas flow thermometry and velocimetry.

ZnO material properties

ZnO (CAS number 1314-13-2) is an inorganic direct wide-bandgap semiconductor with a bandgap of approximately 3.3 eV (Özgür et al. 2005), a molar mass of 81.41 g/mol, a density of 5.6 g/cm^3, and a thermal conductivity of 17 W/(m K) (Haynes et al. 2010). It is practically insoluble in water (Wiberg 1995), has a

refractive index of 2.2, and a high melting point of 2250 K (Takahashi 2007). Owing to its white colour and chemical robustness, it is widely used in many industries, such as zinc white colour pigment (Bohnet et al. 2003), in medical pastes for topical application (Gupta et al. 2014), as a vulcanisation activator in the rubber industry (Wiberg 1995), and, due to its strong absorption in the UV, also in sun blockers (Mitchnick et al. 1999). It forms colourless hexagonal crystals (Klingshirn 2007) that appear white due to refraction if small particles are formed, such as in powders. ZnO is also useful in optical applications, where it is used in LED manufacturing (Jiao et al. 2006), and since at least 2008, the temperature dependent luminescence emitted by ZnO is used for phosphor thermometry upon UV excitation (Särner et al. 2008; Abram et al. 2015; Abram et al. 2016).

The luminescence spectrum of ZnO consists of two bands. First, a broad green emission at 510 nm with a lifetime of approximately 1 µs originating from local crystal structure variations ('defects') that stem from zinc and oxygen vacancies or added copper ions within the crystal lattice (Rodnyi et al. 2011). Second, an edge luminescence close to the absorption edge of ZnO (Gong et al. 2007), as shown in fig. 5.1b. With increasing excitation fluence, the intensity of the defect luminescence decreases compared to the edge luminescence. Therefore, in applications where powerful lasers are used, the edge luminescence is considerably stronger (Abram et al. 2015).

Hence, the edge luminescence is commonly used in thermometry applications. It decays very fast with a lifetime below 1 ns (Rodnyi et al. 2011) which is well suited to avoid motion blur when imaging fast-moving particles in turbulent flows. Compared to the emission of other commonly used thermographic phosphors, the emissions of ZnO are also very bright, which is desirable when imaging individual particles (Fond et al. 2019a). As investigated in Abram et al. 2016, edge luminescence can be excited using both 355 nm and 266 nm, corresponding to the 3rd and 4th harmonics of Nd:YAG lasers, respectively. This is reflected in the normalised excitation spectrum of ZnO in fig. 5.1a. At 296 K, the emission peaks at 381.3 nm, as shown in fig. 5.1b. With increasing temperature, the emission spectrum redshifts further and becomes broader. It is spectrally well separated from the excitation and green light used for particle tracking. A temperature sensitivity of 0.6 to 2 %/K is reported by Abram et al. 2015 over a temperature range of 295 K to 473 K, resulting in a

temperature precision of approximately 5 K, using the luminescence intensity ratio (LIR) approach with 387-11 nm and 425-50 nm filter channels. Above 500 K the luminescence intensity becomes very weak, which makes temperature measurements increasingly difficult.

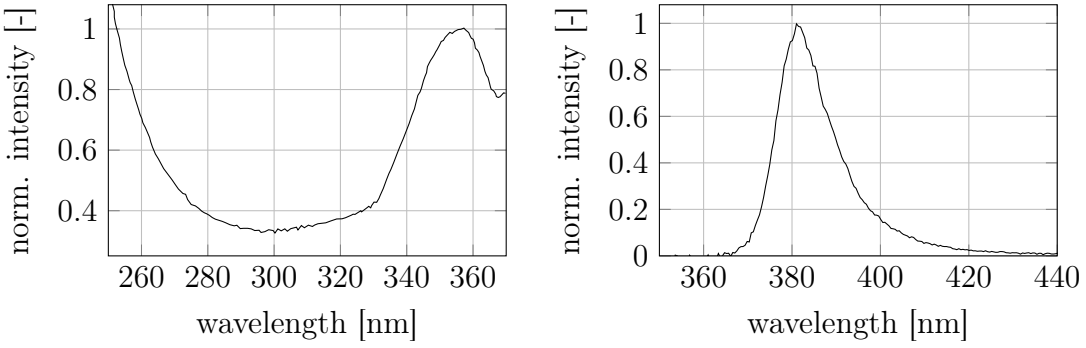

Figure 5.1: Normalized excitation spectra (a) of ZnO reproduced from Abram et al. 2016 (CC-BY 4.0) and edge luminescence emission spectra (b) recorded in liquid dispersion reproduced from Stelter 2019.

5.2.1 ZnO particle selection

After establishing the general suitability of ZnO as a particle material for temperature sensing and flow tracking in turbulent gas flows, the available ZnO samples were compared to identify the best particle specimen. The investigated samples were supplied by Sigma Aldrich (product code 96479) and Phosphor Technology (product codes GK30/UF-X and GK30/F-F1). Two critical parameters for their application in turbulent gas flows are the particle temperature and velocity response times, as discussed above in section 5.1. To obtain good estimates of these response times, knowledge of the particle diameter is essential. Scanning electron microscopy (SEM) images of all particle samples were recorded to investigate their particle diameters. The results are shown in fig. 5.2. Particles supplied by Sigma Aldrich were the smallest of all the samples. While these flake-like particles span 1-2 µm in their largest dimensions, their volume-equivalent sphere diameter was estimated as 600 nm by Fond et al. 2018. Both samples provided by Phosphor Technology (PT) showed much more spherical but larger particles with diameters of 1.5 µm and 10 µm. Following eq. 5.1 and eq. 5.3, these particle diameters result in response

times between a few microseconds and more than a millisecond, as summarised in table 5.1.

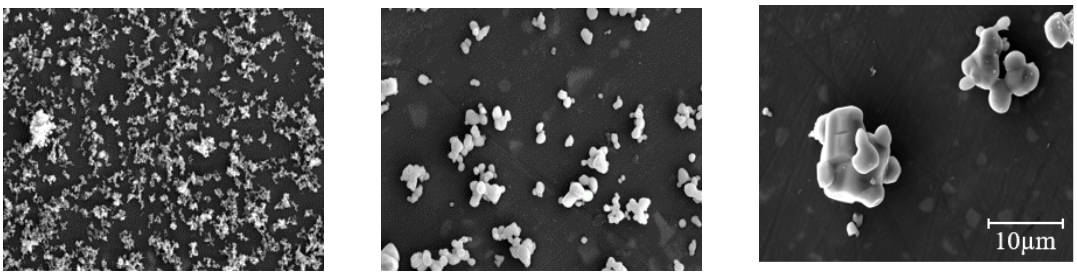

(a) (b) (c)

Figure 5.2: SEM images of three ZnO particle samples: (a) Sigma Aldrich # 96479, (b) PT GK30/UF-X, and (c) PT GK30/F-F1. Reproduced from Stelter et al. 2023 (CC-BY 4.0).

Table 5.1: Sphere-equivalent particle diameters and corresponding temperature and velocity response times for three ZnO samples. Reproduced from Stelter et al. 2023 (CC-BY 4.0).

Sample	d_P [µm]	τ_T [µs]	τ_u [µs]
Sigma Aldrich # 96479	0.6	2.42	4.90
PT GK30/UF-X	1.5	15.10	30.59
PT GK30/F-F1	10.0	670.99	1359.75

As per Melling 1997, the velocity response time τ_u enables calculation of the ratio of time-averaged particle and fluid velocities $\bar{u}_p$ and $\bar{u}_f$, to estimate the tendency of particles following an unsteady flow at fluctuation frequency f_c.

$$\frac{\bar{u}_p^2}{\bar{u}_f^2} = \frac{1}{(1 + 2\pi f_c \tau_u)} \tag{5.4}$$

Equation 5.4 was solved for all ZnO samples, and the results are plotted in fig. 5.3 as calculated over a wide frequency range. In particular, the particles provided by Sigma Aldrich are suitable for tracking turbulent gas flows. While PT UF-X can be used in gas flows with moderate turbulence, PT F-F1 particles strongly attenuate any gas flow motion. Applying the Basset-Boussinesq-Oseen equation of small particles in unsteady flow to the present particles allows the calculation of a cut-off frequency where the particles follow the true gas motion with $-3\,\mathrm{dB}$

attenuation. For the Sigma Aldrich particles, this is 32.5 kHz, underpinning their suitability for application in turbulent gas flows. Their fast response is further aided by their non-spherical shape, as such particles tend to align their major axis perpendicular to the flow to maximise drag forces (Wachem et al. 2015). As this minimises the slip velocities between them and the flow, the presented estimations for the Sigma Aldrich sample are considered conservative.

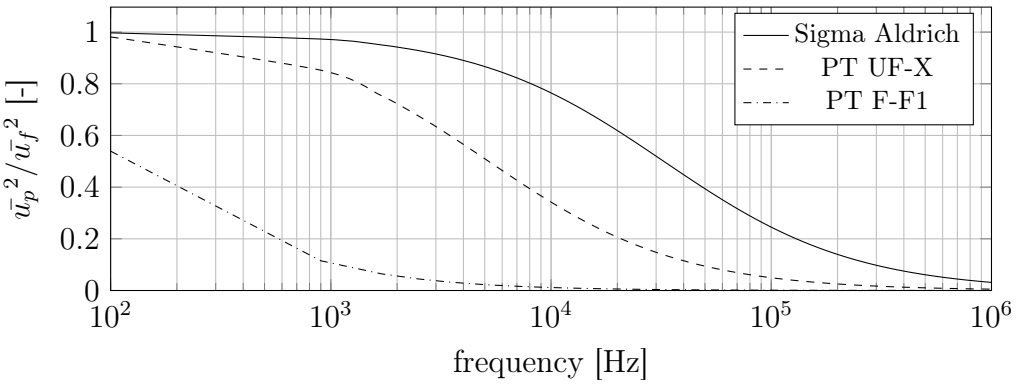

Figure 5.3: ZnO particle response to air flow velocity fluctuations at different frequencies.

However, larger particles could emit more luminescence photons, providing higher-intensity particle images, which would improve signal limited temperature precision. To investigate the luminescence signal emitted by individual ZnO particles, dilute particle dispersions were prepared in a fused silica cuvette using distilled water as the dispersant. A thin light sheet of 300 µm thickness and a fluence of 105 mJ/cm^2 was formed from a 266 nm laser to avoid Raman scattering of water molecules, and images of the particles were recorded with a sCMOS camera at 10 Hz. A high magnification of 0.66 aided particle image detection by increasing particle image peak intensities. The luminescence emission of individual particles was obtained by fitting each particle image with a 2D Gaussian fit and summing all pixel intensities, where the fit was above 5 % of its maximum. A minimum of 5000 individual particle images were evaluated for each sample. The resulting probability density functions of the particle intensities per ZnO sample are shown in fig. 5.4. For all samples, these distributions peak at 240 counts, regardless of particle size. For particles from Sigma Aldrich and PT UF-X, the distribution of particle intensities is very similar over the entire intensity range, while for larger PT F-F1 particles, the probability

for recording particle signals above 450 counts is increased.

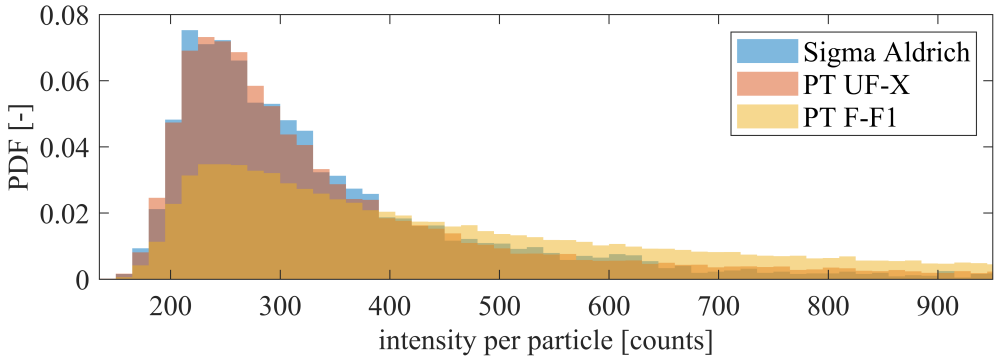

Figure 5.4: Luminescence image intensity histograms for three different ZnO samples obtained from a minimum of 5000 samples each. Reproduced from Stelter et al. 2023 (CC-BY 4.0).

Based on these investigations, the ZnO particles provided by Sigma Aldrich were selected as thermographic tracer particles in this thesis. Their luminescence intensity is on par with that of PT UF-X particles while being considerably smaller, leading to six times shorter velocity and temperature response times.

5.2.2 Excitation wavelength selection

In general, ZnO luminescence emissions can be excited using either the 3rd or 4th harmonic of a Nd:YAG laser. Depending on the excitation wavelength, the luminescence response differs regarding its dependency on the excitation fluence and the intensity of the luminescence emission (Abram et al. 2016).

First, the luminescence emission spectrum of ZnO shows a cross-dependency on the excitation laser fluence, in addition to the desired temperature dependency. This was investigated in Abram et al. 2015, where the LIR between the 387-11 nm and 425-50 nm filter channels was monitored versus excitation laser fluences ranging from 3 to 90 mJ/cm^2. Until 60 mJ/cm^2, the LIR shows a non-linear dependency on the excitation fluence before it becomes independent of it. While these results were obtained under 355 nm excitation, another study using excitation at 266 nm confirmed the qualitative trend but showed a weaker dependency of the computed LIR on the excitation fluence (Abram et al. 2016). To avoid temperature

uncertainties related to fluence variations within the measurement volume, the laser was operated at high pulse energies leading to average fluences exceeding $100\,\mathrm{mJ/cm^2}$, and a flat field correction in the laser cross-section was applied to compensate the remaining inhomogeneities, as described below in section 6.4.

Second, the absolute emission signal intensity of the ZnO particles differs depending on the excitation wavelength. This was first investigated for 2D measurements by Abram et al. 2016, where ZnO particles were excited using both 266 nm and 355 nm, and the imaged luminescence signal per camera image was compared to the laser fluence. For both wavelengths, the imaged signal increases over the investigated range of approximately 1 to $50\,\mathrm{mJ/cm^2}$. At $40\,\mathrm{mJ/cm^2}$, the recorded emission signal for 355 nm excitation was twice as high as that for 266 nm excitation.

Compared to the study of Abram et al. 2016, in the present thesis, the excitation laser fluence was two to four times higher to deliberately exceed the saturation threshold of ZnO, mitigating fluence cross-dependencies of the calculated LIR, as discussed above. In addition, the emissions of individual ZnO particles were evaluated rather than computing them from camera image-level intensities. Therefore, a comparison of imaged particle luminescence signals using the same conditions as for the 3D measurements presented in this thesis was necessary. Hence, ZnO particles were seeded into an airflow at ambient temperature of 298 K and illuminated by 266 nm and 355 nm laser beams at $200\,\mathrm{mJ/cm^2}$ each. The resulting particle image intensity distributions are shown in fig. 5.5, obtained by summing the signal recorded in both 387-11 nm and 425-50 nm filter channels for individual particles. The average particle image intensity is 1467 counts for 266 nm excitation and 2546 counts for 355 nm excitation, while the highest probability is reached for intensities of 450 counts and 1250 counts, respectively, which is in good agreement with the results provided by Abram et al. 2016.

In conclusion, both 266 nm and 355 nm excitations have their advantages and were used in the 3D measurements below, as indicated individually. For earlier measurements, 266 nm was used before moving to 355 nm for later measurements to favour higher luminescence signal levels.

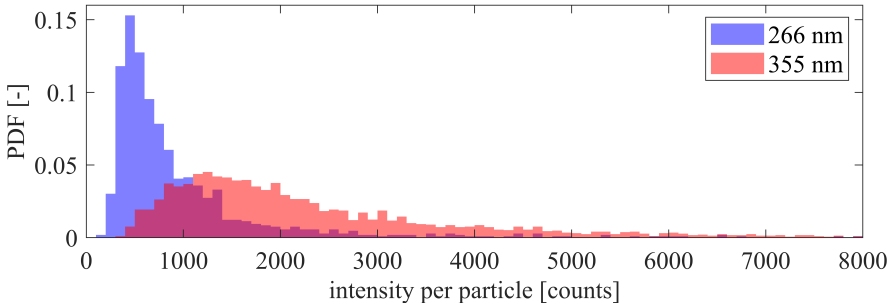

Figure 5.5: Probability density functions of measured particle image intensities under 266 nm and 355 nm laser excitation. Reproduced from Stelter et al. 2023 (CC-BY 4.0).

5.3 Particle seeding

Only those regions of the flow where tracer particles are present can be investigated using the developed technique. Hence, particle seeding into the flow was very important. However, achieving time-invariant homogeneous seeding of a gas flow, with solid tracer particles from bulk powder, is challenging (Self et al. 1976). In general, seeding success is governed by the kind of seeder, particle characteristics, and handling of the particles prior to seeding them into a gas flow. A straightforward approach for seeding solid particles to gas flows is using a fluidised bed seeder (Melling 1997). Here, the bulk powder rests on a porous plate, and a gas flow passes through it from the bottom. The gas fluidises the powder and entrains the particles into the flow, creating an aerosol. However, phosphor particles with particle sizes useful for gas flow measurements belong to class C of the Geldart classification system (Geldart 1973), meaning their Sauter mean diameters (Sauter 1926; Scala 2013) are below 20 µm and the density difference between particles and gas is large. Hence, such particles form cohesive powder beds that are difficult to fluidise because the interparticle binding forces are stronger than the forces exerted by the passing gas. In this case, the gas forms small channels in the powder bed through which it passes without entraining many particles, instead of generating a stable fluidised bed. Powder cohesion is further increased by the irregular, nonspherical shapes of many phosphor particles (Cocco et al. 2023). Compared to other phosphors, this is especially severe for ZnO as reported by Abram et al. 2022. As other factors, such as moisture, also increase powder cohesion, the phosphor particles were dried in an electric oven at 110 °C for 8 h before they were filled into a seeder.

As an alternative to fluidised bed seeders, two different types of seeders were utilised, depending on the volume flow rate of the gas that had to be seeded. For smaller flow rates a cyclone seeder (Glass et al. 1977) as shown in fig. 5.6 was employed. A wiggling tube seeder was used for larger gas volume flow rates. Both seeders were equipped with a bypass to control the fraction of the total gas flow that passed through the seeder, effectively controlling the seeding. For the cyclone seeder, the feed gas arriving from a mass flow controller passes through the inlet tube into a distribution ring at the bottom of the seeder. From there, it ejects through angled boreholes at the bottom of the ring, creating a swirling gas flow within the seeder. This entrains particles from the bulk powder placed in the distribution ring centre into the flow and carries them through the outlet towards the measurement volume. Owing to centrifugal forces within the seeder vortex flow, this seeder favours seeding smaller particle sizes while rejecting agglomerates. However, this seeder works only for smaller gas flow rates. The boreholes in the distribution ring are only a millimetre wide. The resulting pressure drop limits the maximum flow rate that can pass through it.

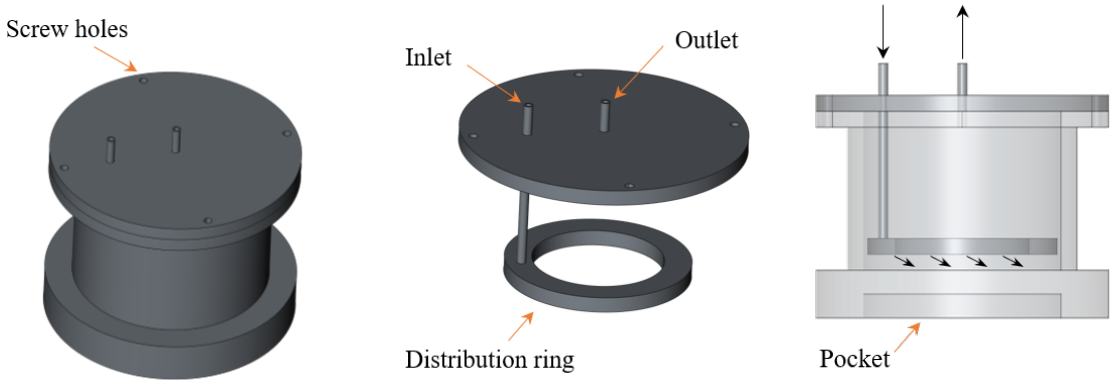

(a) 3D view (b) Seeder inset (c) Side view

Figure 5.6: Rendered 3D representations of the cyclone seeder used in this thesis (a). In (b) only the lid with the inlet/outlet part of the seeder is shown including the distribution ring. In (c), the seeder is depicted from side view with increased transparency. The outer body is illustrated in light gray, whereas the inset featured in (b) appears dark gray. Black arrows indicate gas flow.

One approach to reduce the pressure drop introduced by the seeder is to replace the distribution ring with a flexible silicone tube. When passing gas through the tube,

its momentum leads to movement of the tube, preventing a pileup of phosphor powder in certain areas of the seeder. Such a design was proposed in Abram et al. 2022 specifically for phosphors that tend to form cohesive beds. They studied the tube movement depending on the gas volume flow. With increasing volume flow, the tube starts to move regularly before reaching a threshold upon which the movement becomes chaotic. These volume flow thresholds depend heavily on the tube parameters, as detailed in Abram et al. 2022. Using this seeder, flows of 30 L/min or more were successfully seeded. For smaller flow rates up to 30 L/min and below, a cyclone seeder was employed.

Chapter 6

Development of imaging setup and data processing procedures

A setup was conceived to provide an implementation of the developed measurement concept. It served as a practical proof of concept and provided data for algorithm development and optimisation. For this purpose, measurements were performed in two gas jets of different nozzle exit diameters. As such flows are well described in literature, they were ideal test beds for this first implementation of the concept.

The physical implementation of the setup, timing considerations, and procedure for joined camera calibration are described in **section 6.1**. The subsequent **sections 6.2 to 6.3** describe the processing of Mie scattering and luminescence image data. This includes their combination, to provide simultaneous velocity and temperature measurements. As the presented concept targets non-isothermal gas flows, the effect of temperature dependent gas refractive index changes on the applicability of tomographic reconstruction algorithms was investigated. Considering the beam profiles of the lasers used, a 2D flat field correction was necessary to correct the computed luminescence intensity ratios (LIR), as described in **section 6.4**, to provide accurate 3D temperature results. Finally, the first calibration measurements from a temperature controlled gas jet are presented in **section 6.5** to provide an *in situ* calibration of the phosphor thermometry system. The result of this chapter is a functioning measurement system that can be applied to measurements in isothermal and non-isothermal gas flows (cf. chapter 7). Parts of this chapter are based on the author's publication (Stelter et al. 2023).

6.1 Setup implementation

The following setup was implemented for simultaneous 3D measurements of gas flow temperature and velocity. It provided a seeded gas flow as research object, light sources to illuminate the measurement volume, and an array of cameras to record particle image data. To provide 3D temperature and velocity results, three superordinate steps were required. First, the positions of the seeded tracer particles were reconstructed from four views of particle Mie scattering camera images. These were then tracked over time to retrieve the velocity of each particle. Finally, the luminescence response of the same particles was recorded using two additional cameras to retrieve their temperature. Consequently, simultaneous temperature and velocity measurements were provided at each particle location within the flow. For each volumetric single-shot measurement, four double-frame images of particle Mie scattering and two single-frame images of particle luminescence were recorded.

A turbulent non-isothermal gas jet was selected as research object for the first demonstration as it is well described in literature (Corrsin 1943; Ribeiro et al. 1975; Chant 2005; Nieuwstadt et al. 2016). This allowed a comparison of measurement results with literature to access the measurement's performance. To create the gas jet, the setup shown in fig. 6.1 was conceived. The gas jet was generated from a circular cross-section steel nozzle of either 4 mm or 9.5 mm diameter. Its supply line was wrapped with a fibreglass heater tape (Omegalux STH102-080) to allow heating of the jet flow. As the supply line had a straight section of ≥ 40 nozzle diameters in length before the nozzle outlet, the flow profile was assumed to be fully developed (Pope 2015). A co-flow at ambient temperature of 300 K was used to provide a controlled environment around the jet. To maintain uniformity of the co-flow, the feed gas passed through a chamber filled with glass marbles of 15 mm in size and then channelled through a layer of honeycombs made from Aluminium to straighten the flow. To reduce jet flow recirculation at the nozzle exit, the nozzle was conically shaped and extended slightly above the co-flow honeycombs. Nitrogen was used as feed gas for practical reasons of available bottle storage and could be replaced by compressed air without influencing the luminescence emission of the selected phosphor. To control the flow rates of jet and co-flow, precision

thermal mass flow controllers (MFCs; Bronkhorst EL-Flow Select F-201AV and F-203AV) were used, and phosphor particles were seeded into the flow(s) using reverse cyclone or wiggling tube seeders, as described in section 5.3. While MFCs measure and control the mass flow of gas, they indicate a volume flow in software. This requires a factory calibration of each MFC to a reference gas and temperature. When operating the MFC with another gas or at different temperatures, the set volume flow rate $\dot{V}_{set}$ must be adjusted to actually achieve the desired volume flow rate $\dot{V}$ using

$$\frac{\dot{V}}{\dot{V}_{set}} = \frac{G_{real}}{G_{cal}} * \frac{T_{real}}{T_{cal}}, \tag{6.1}$$

where G_{real} and G_{cal} are gas conversion factors available from the MFC manufacturer or can be estimated from the product of specific heat capacity and normal density of the gases (Bronkhorst High-Tech B.V. 2025), and T_{real} and T_{cal} are the actual temperature of the gas (considering any active heating) and the calibration temperature of the MFC.

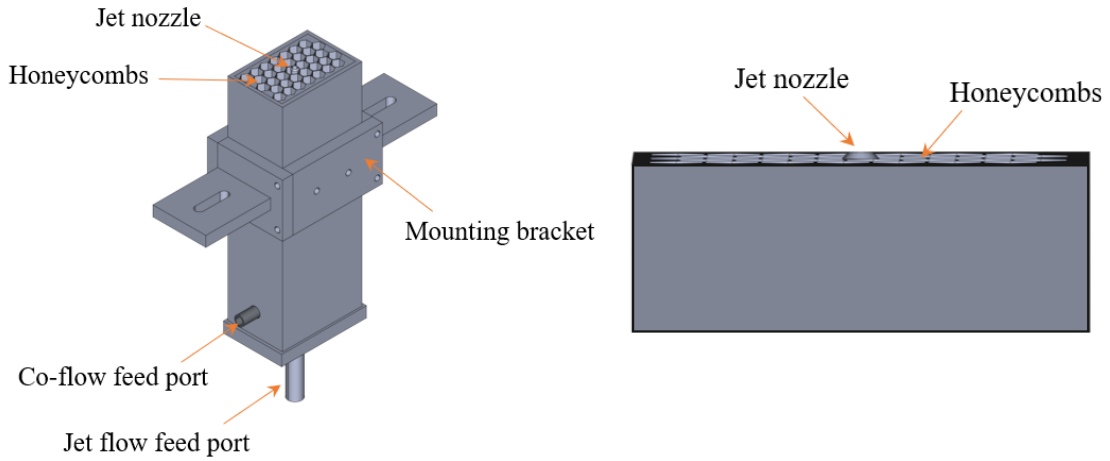

(a) 3D sketch (b) Side view of the nozzle region

Figure 6.1: Rendered representations of the jet with co-flow setup in two views. Supply gas was fed to the central jet and co-flow using three ports, one co-flow port is facing away from the viewer.

A sketch of the complete setup is shown in fig. 6.2. Two lasers were used to illuminate the measurement volume above the jet exit. A double-pulse green laser was operated at 532 nm, and a single-pulse UV laser was operated at either 266 nm

or 355 nm. Details on the selection of the UV wavelength are provided in section 5.2, and the light sources were characterised as reported in section 6.1.1. To match the diameter of all laser beams at 8 mm, a custom Galilean telescope was added to the green beam path. Using a dichroic mirror, the green and UV laser beams were spatially overlapped and passed through a circular aperture to remove outer beam regions with low laser fluence before entering the measurement volume. Clearly defined borders of the illuminated volume are beneficial for both tomographic reconstruction and luminescence-based thermometry.

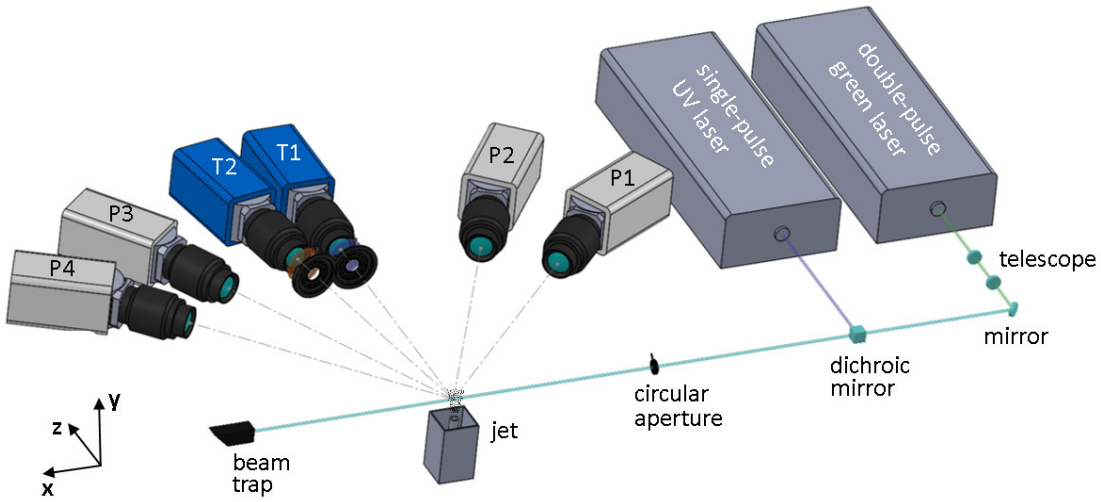

Figure 6.2: Rendered representation of the experimental setup. A gas jet with co-flow was seeded with phosphor particles. Particles were illuminated by two lasers with size-matched beams. A circular aperture was used to remove low-fluence beam edges. Four double-frame cameras P1-4 recorded Mie-scattered green laser light for particle reconstruction and tracking. Two cameras T1-2 recorded particle luminescence emissions excited by a UV laser in two spectral bands determined by the filters mounted in front of these cameras (blue/red disks). External apertures were used with T1-2 to control the depth of field. Reproduced from Stelter et al. 2023 (CC-BY 4.0).

Two imaging subsystems were integrated to produce the measurements. The first subsystem for particle position reconstruction and velocity evaluation consisted of four double-frame cameras P1 to P4 (LaVision Imager Pro X). They were positioned in a common horizontal plane at angles of 51°, 66°, 114°, and 129°, centred on the jet nozzle at a distance of 715 mm, where 0° denotes the forward scattering

direction. These cameras recorded the Mie-scattered light of the particles following green double-pulse illumination. More details on the hardware implementation are provided in section 6.2. The second subsystem consisted of two more cameras, T1 and T2 (LaVision Imager sCMOS), positioned in the same horizontal plane as the other cameras at angles of 89° and 101°. These cameras were equipped with spectral filters to observe the luminescence emission of phosphor particles excited by UV laser illumination in distinct spectral regions. This allowed the calculation of a temperature dependent LIR for every individual particle. External apertures were mounted in front of these cameras to allow control of their depth of field (DoF) without touching the cameras or lenses. More details on the hardware setup and selection for temperature measurements are provided in section 6.3, including the camera arrangement, selection of the imaging sensor technology, spectral filter selection, and control of the DoF. This combined system allowed the recording of single-shot temperature and velocity measurements by using four views of double-frame Mie scattering images from cameras P1-4 and two spectrally separated single-frame images of phosphor luminescence emissions from cameras T1-2. In the following sections, main components of the setup are characterised, and design considerations discussed, to arrive at the shown setup implementation.

6.1.1 Particle illumination

As shown in fig. 6.2, two different solid-state lasers were used to provide the necessary illumination and excitation energy for the measurements. Green laser emissions were scattered by seeded phosphor particles, while UV laser emissions were absorbed to excite luminescence emissions. The light sources used in this work were characterised and consequences for data processing were derived.

Double-pulse green laser

To generate Mie scattering emissions from seeded particles for 3D particle position reconstruction and velocimetry, the 2nd harmonic emission of a double-pulsed flashlamp-pumped Nd:YAG laser (Quantel Q-smart 850 Twins) was used at 532 nm. This system combines two laser heads, each operating at 10 Hz, with a pulse

duration of 6 ns. The raw beam of approximately 6 mm in diameter was enlarged using a custom-built Galilean telescope, as shown in fig. 6.3. This telescope is built using two spherical lenses of focal lengths −50 mm (Thorlabs LC1715-A) and 75 mm (Thorlabs LA1608-A), respectively, which were positioned on a common axis at a distance of 25 mm from each other. To minimise energy losses from the beam due to reflections on lens surfaces, both lenses were equipped with anti-reflective coatings. The lenses were mounted in lens tubes and fixated using retention rings. This telescope magnifies an input beam by a factor of 1.5, while maintaining its collimation.

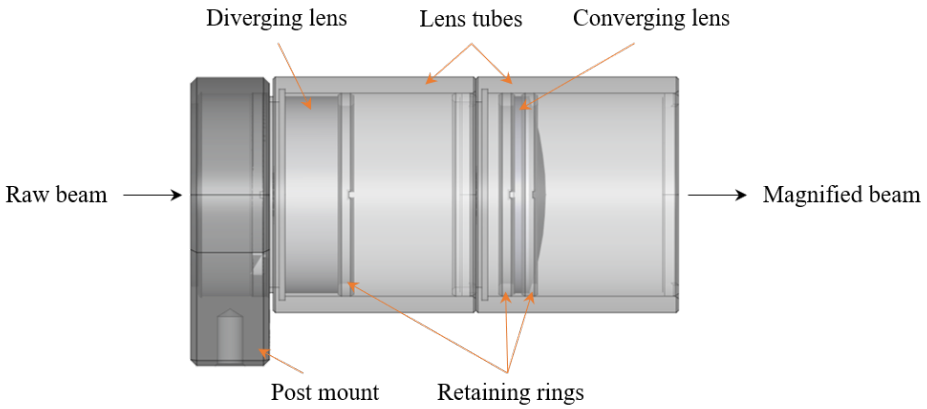

Figure 6.3: Galilean telescope to expand the beam of the green double-pulse laser to match the UV laser beam. Transparency was added to the outer lens tubes for visualisation purposes. CAD files for individual components were obtained from (Thorlabs, Inc. 2025).

For a successful tomographic reconstruction of a particle's position within the illuminated measurement volume, it must have been imaged by all four cameras P1 to P4. The imaged particle signal intensity is proportional to the amount of Mie-scattered light. As the Mie scattering intensity scales with the irradiating laser fluence, a uniform value above an absolute minimum within the measurement volume was desirable. For low particle seeding densities, the attenuation of the laser beam owing to light scattered away by particles while travelling through the length of the measurement volume is negligible. Hence, the main source of fluence variations within the measurement volume stems from the laser beam profile itself. An ideal laser emits a TEM_{00} beam with a Gaussian beam profile. By removing the low-intensity outer regions of such a beam, efficient volumetric illumination

is possible. To check the actual laser beam profiles produced by both green laser heads, a beam sampling camera (Gentec Electro-Optics Beamage-4M) was used. The laser beam profiles for both laser heads were recorded with and without the telescope in the beam path. Without the telescope, the near and far fields at 30 cm and 5 m after the laser output port were imaged. After adding the telescope, the beam profile was imaged at the measurement volume centre, 4 m after the laser output port. The laser was operated at pulse energies of 60 mJ during the recording of the beam profiles monitored using a pyroelectric power meter (Coherent LabMax Top with J-50MB-YAG sensor). For both laser heads, the standard deviation of measured laser pulse energies over 100 single-shot measurements was below 4 %. The recorded beam profiles are shown in fig. 6.4.

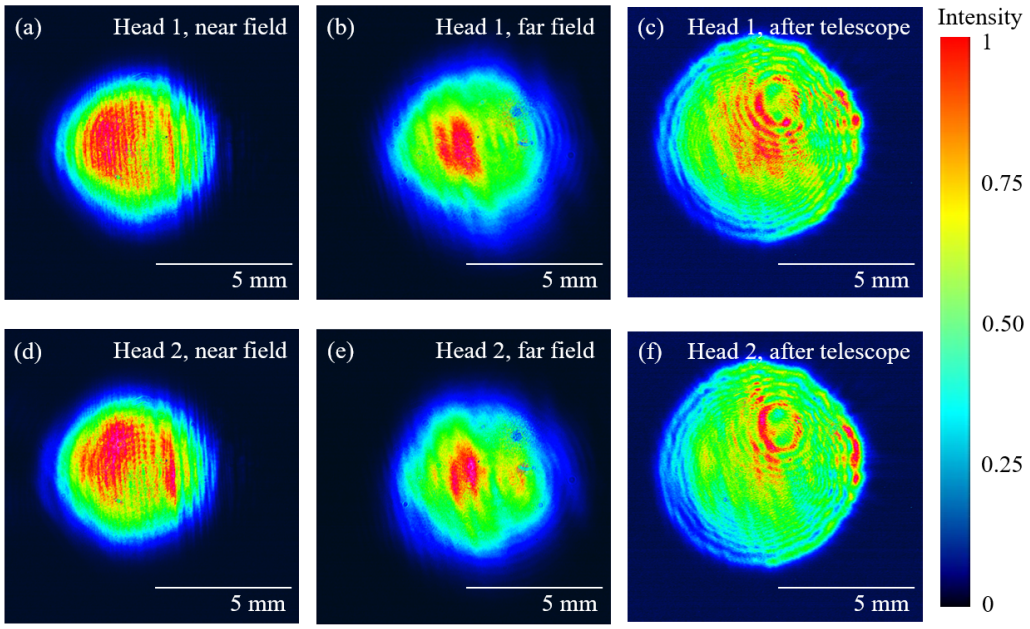

Figure 6.4: Normalised beam profiles emitted by double-pulse green laser heads recorded in near (a, d) and far field (b, e), and in the measurement volume after telescope and 8 mm beam aperture (c, f).

For both laser heads, the near-field laser beam profiles were highly circular with an ellipticity of 96.5 % and 93.7 % for heads one and two, respectively. The diameters of both beams were virtually identical with 5.85 mm and 5.87 mm, calculated using the D86 diameter definition in the near field. In the far field, these diameters increased to 6.67 mm and 6.29 mm, respectively, owing to beam divergence. Fitting

a Gaussian function to the laser beam profiles and using the R^2 value as measure for the goodness of fit supports the visual impression that the beam deviates from a perfect Gaussian intensity distribution, yielding values of 0.74 in the near field to 0.83 in the far field. After passing through the telescope and the beam aperture, the beam profiles are circular with a D86 diameter of 7.87 mm, matching the set diameter of the aperture of 8 mm, and clearly defined beam edges. While the lower intensity towards the left border of the beams was indicated already in the far field profiles, the overall quality and similarity of the beams was good.

Similar beam cross-sections of both laser heads were complemented by a similar power output for the same Q-switch delay, as shown in fig. 6.5. The maximum power outputs achieved with this laser were 388 mJ/cm^2 and 395 mJ/cm^2 for laser heads one and two, respectively. This allowed the illumination of a volumetric measurement region while maintaining sufficient scattering signal levels for sub-micrometre particle imaging.

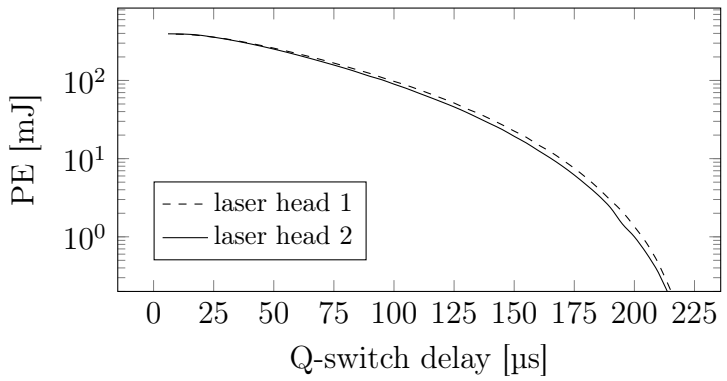

Figure 6.5: Pulse energies of the green double-pulse laser for both laser heads.

Single-pulse UV laser

To excite a luminescence response from seeded phosphor particles, they have to be supplied with excitation energy. For zinc oxide (ZnO), as the phosphor chosen in this thesis, light of both 266 nm and 355 nm can be used (cf. section 5.2). This corresponds to the 4$^{\text{th}}$ and 3$^{\text{rd}}$ harmonics of common Nd:YAG lasers, respectively. Here, a Quantel YG981E was used to provide the necessary UV beam. This laser has a maximum pulse energy of 1600 mJ at 1064 nm and operates at a fixed repetition

rate of 10 Hz. The laser itself was equipped with an internal 2nd harmonic generator (SHG), allowing output of pure 1064 nm (Nd:YAG fundamental wavelength), pure 532 nm (2nd harmonic), or a mix of 1064 nm and 532 nm, depending on the internal configuration of the laser. 3rd and 4th harmonic generation was facilitated using external harmonic generators. Generally, harmonic generation includes transferring the energy of multiple photons at identical or different wavelengths in a parametric nonlinear process to emit a photon of higher energy or shorter wavelength (Boyd 2008). Nonlinear optical crystals made from birefringent materials such as potassium dihydrogen phosphate (KDP) or deuterated potassium dihydrogen phosphate (DKDP) are commonly used to generate harmonics from Nd:YAG lasers. If the power of the input beams to the crystal, their polarisation with respect to the crystal's principal plane, crystal temperature, cut angle, material, and angle relative to the beam path match at conditions specific to the desired frequency mixing process, phase matching is achieved, and a harmonic beam is generated (Eichler 2018).

To obtain 355 nm, sum-frequency mixing using 532 nm of the laser-internal SHG and the residual fundamental emission at 1064 nm was performed. The internal SHG was tuned out of its optimum angle to increase the fraction of the residual infrared emission. The mixed-wavelength beam was then directed through a temperature-controlled crystal made from deuterated potassium dihydrogen phosphate (DKDP, Eksma DKDP-403). This crystal was carefully aligned with the laser beam to achieve type-two phase matching with the horizontally polarised fundamental and the vertically polarised 2nd harmonic (Guha 2017). After the DKDP crystal, the laser beam contained a mix of fundamental, 2nd, and 3rd harmonic wavelengths. To maintain only the 3rd harmonic, a Pellin–Broca prism (Pellin et al. 1899) was used to disperse the different wavelengths and dump all but the 355 nm emission.

To access 266 nm, a process similar to that described above was used. However, the internal SHG of the laser was tuned to emit the maximum of 532 nm radiation and then passed through a potassium dihydrogen phosphate crystal (KDP, Eksma KDP-402) to generate the desired 266 nm radiation through sum-frequency generation with type-one phase matching (Guha 2017). Residuals of other harmonics were stripped using a combination of the added prism and beam dumps, as described

above, before the cleaned UV beam was used to excite phosphor luminescence emissions.

For a laser generating a UV beam, a homogeneous beam profile is particularly important for at least two reasons. First, the wavelength conversion process described above is nonlinear, with higher conversion efficiencies for higher input laser power (Eichler 2018). Hence, fluence differences across the laser beam cross-section in the input beam to the (D)KDP crystal are amplified by conversion to UV. Second, ZnO exhibits a cross-dependency of the emitted luminescence on the excitation laser fluence. Therefore, inhomogeneities in the UV laser beam fluence translate to uncertainties in the measured temperatures (Abram et al. 2015).

To access the fluence homogeneity within the UV laser beams, the beam sampling camera was optionally equipped with a UV converter to allow imaging in the UV spectral region (Gentec Electro-Optics BSF23R23N), or a colour camera was used to image paper fluorescence excited by the UV beam. For the 3$^{\text{rd}}$ harmonic generation, the beam profiles of the input 2$^{\text{nd}}$ harmonic and output 3$^{\text{rd}}$ harmonic beam are shown in fig. 6.6. All profiles were recorded in the near field, 30 cm, after the laser output port. The 3$^{\text{rd}}$ harmonic beam was imaged using the beam-sampling camera with and without the UV converter. Compared to the near-field beam profiles of the double-pulse green laser presented above, the 2$^{\text{nd}}$ harmonic beam profile in fig. 6.6a appeared to be degraded. The intensity maximum was not clearly positioned in the centre of the beam, and a high-intensity zone was present at the lower beam edge. Considering this input beam, the 3$^{\text{rd}}$ harmonic beam profile imaged using the UV converter, as depicted in fig. 6.6b, appears surprisingly smooth. Not only does the UV converter act as a telescope, minifying the imaged beam diameter by a factor of 1.4, it also acts as a strong spatial filter. Within the UV converter, a phosphor disk is used to convert irradiating UV light to visible light that is imaged by the camera. The resulting beam profile is not suitable for investigations of fluence homogeneity. This becomes apparent when comparing it to the profile recorded under identical conditions but without the UV converter, as shown in fig. 6.6c. This profile shows a much clearer correspondence with the input beam to the DKDP crystal in fig. 6.6a, with a D86 beam diameter of 9.36 mm. In addition, a clear correspondence between high-intensity regions in the 532 nm and 355 nm beams is observed.

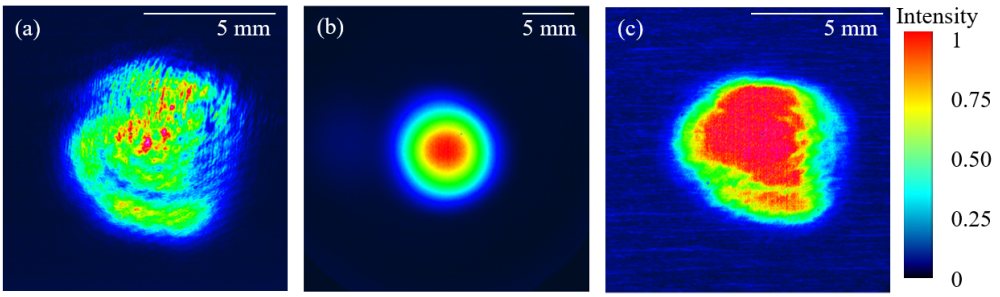

Figure 6.6: Normalised laser beam profiles for the 2nd and 3rd harmonics of the Quantel YG981E. Profile (a) appears degraded compared to the beams from the double-pulse laser presented above (fig. 6.4). Imaging the 3rd harmonic beam using the UV converter leads to a minified and biased beam profile (b) compared to the actual profile (c).

Because the UV converter lead to strongly biased images of the laser beam profiles, it was not used for imaging the 4th harmonic beam at 266 nm. Instead, this beam was shot at a white piece of paper to excite its fluorescence, which was then imaged by a colour camera from behind the paper. Two beam sampling windows were used to reflect only a fraction of the original beam onto the paper, and the linearity of the paper response to the laser radiation was tested. Hence, the recorded beam profile images provided a qualitative view of the fluence homogeneity in the beam cross-section. The green beam as input to the KDP crystal stems from the same laser as above in fig. 6.6, but its cavity mirrors were tuned differently. While no high-intensity region at the lower edge of the laser beam profile is visible, a similar region is present at the top of the beam profile in fig. 6.7a. In addition, a diagonal stripe pattern was superimposed on the beam profile. After an analysis of the internal components of the laser, these stripes were attributed to a corresponding crystal surface defect of the SHG. This was confirmed by qualitatively comparing the 266 nm beam profile after the KDP crystal in fig. 6.7b with the green beam profile input to it (fig. 6.7a). As no timely replacement of the SHG was possible, resulting fluence inhomogeneities were dealt with in data processing by applying a flat field correction (FFC, section 6.4).

Knowledge of the available UV laser fluence was important when working with ZnO as phosphor for at least two reasons, following investigations by Abram et al. 2015. First, the luminescence signal emitted by ZnO scales with the excitation

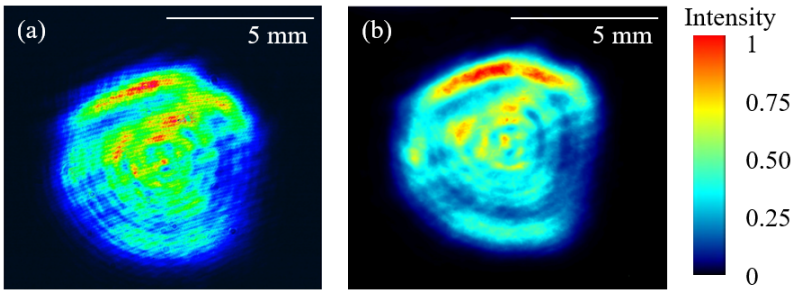

Figure 6.7: Normalised beam profiles of the 2nd and 4th harmonics generated using the Quantel YG981E laser showing good qualitative match.

laser fluence until a threshold of approximately 10 mJ/cm^2 is reached. Second, the spectrum of ZnO is not only influenced by temperature changes but also depends on the excitation laser fluence if it is below 50 mJ/cm^2 (saturation threshold). Hence, a minimum fluence of the excitation laser beam had to be maintained to prevent high-temperature uncertainties due to fluence variations. Therefore, the pulse energy and pulse-to-pulse stability of the laser were measured for both 355 nm and 266 nm, as presented below in fig. 6.8. For the 3rd harmonic, the pulse energy was tested until 157 mJ at a Q-switch delay of 320 µs, whereas for the 4th harmonic, a maximum of 105 mJ could be achieved at a Q-switch delay of 300 µs. Assuming a homogeneous flat-top beam profile, these pulse energies would correspond to 228 mJ/cm^2 and 153 mJ/cm^2, respectively. Even when considering the non-homogeneous beam profiles of the actual UV beams, most of their cross-sections were above the saturation threshold for ZnO. As the pulse-to-pulse variations of pulse energies were below 4 %, a flat field correction within the beam cross-section was an effective measure to correct the measured LIRs, as presented below in section 6.4.

In conclusion, the double-pulse beam used for particle reconstruction and velocimetry was size-matched with the single-pulse UV beam used for phosphor thermometry. The UV beam profiles at both 266 nm and 355 nm showed strong deviations from idealised Gaussian profiles and required a flat field correction of the measurement data, as detailed later in section 6.4, while the beam profiles of the green double-pulse laser were much more Gaussian.

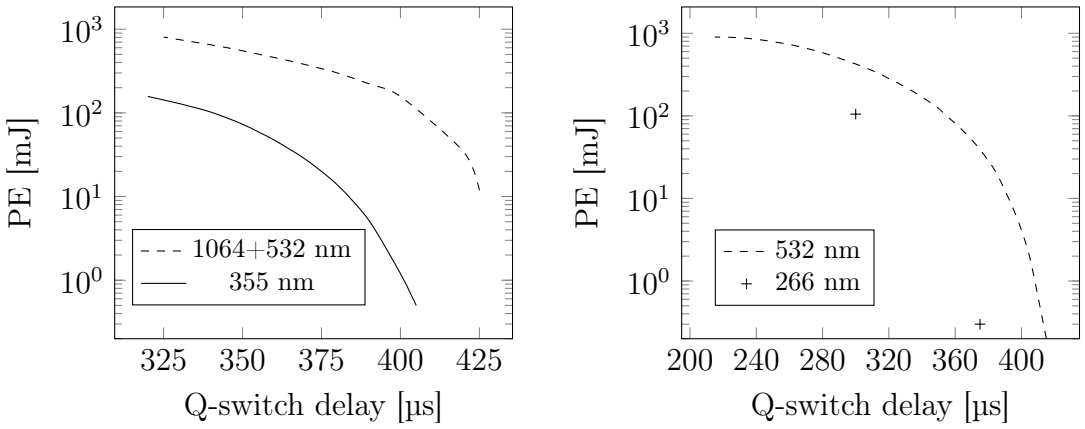

(a) 3rd harmonic generation (b) 4th harmonic generation

Figure 6.8: Pulse energies (PE) measured for both the 3rd and 4th harmonic generation, including the input beam power to the (D)KDP crystals depending on the laser Q-switch delay.

6.1.2 Imaging subsystem for flow velocimetry

Mie scattering images of tracer particles were recorded for particle position reconstruction and tracking to facilitate 3D fluid flow velocity measurements. For the tomographic reconstruction described in section 4.2.1, multiple simultaneously captured views of the particle distribution are required. Moreover, particle images should be recorded in focus, regardless of their position within the volume, to provide high-intensity image maxima for reliable particle image detection. To allow for 3D tracking of the reconstructed particle positions, two Mie scattering images were recorded in quick succession using double-frame cameras (LaVision DaVis Imager Pro X) matching the double-pulse laser characterised in section 6.1.1. Below, details of the macroscopic imaging of small particles are discussed before delving into details of the implemented camera setup.

Imaging small particles

Mie scattering is a type of elastic light scattering in which the particle diameter is on the same order of magnitude as the scattered light wavelength (Hecht 2017). Here, we used (sub-)micron ZnO particles (section 5.2) as flow tracers and a double-pulse

laser operated at 532 nm as the scattering light source. As shown by simulations of the angular distribution of scattering intensity for 1 µm particles in fig. 6.9 using an implementation by Prahl 2023 and substance properties of ZnO from Samsonov 1973, the scattering signal is highly anisotropic. Most of the scattered light is in the forward scattering direction enclosed in a cone of 50°, while side and back scattering are much weaker. To show its intensity distribution, a linear-scaled polar plot is complemented by a log-scaled line plot of the intensity distribution in fig. 6.9a and fig. 6.9b, respectively.

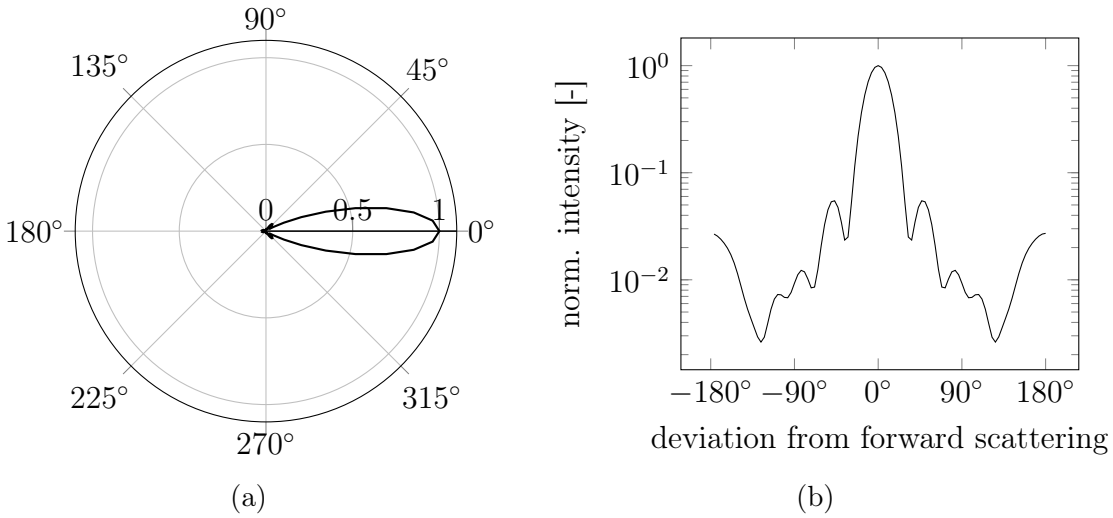

Figure 6.9: Angle-dependent Mie scattering signal of 532 nm light on 1 µm ZnO particles. Signal intensities are normalized to the value in forward scattering direction at 0°, shown as polar plot (a) and log-scaled line plot (b). Data computed using implementation of Prahl 2023.

Apart from the angular distribution of the scattering signal, which affects the positioning of the cameras, the aperture settings of the cameras are important. A change in the lens aperture has two main effects: changing the imaged signal levels and the DoF. The DoF of an imaging system is the distance between the nearest and furthest object in acceptable focus within an image. It increases with decreasing lens aperture diameter or increasing f-number. The f-number N is the ratio of focal length of a lens f and its entrance pupil diameter D (Hecht 2017). Conventionally, the f-number is given as approximate geometric sequence of powers of $\sqrt{2}$ called f-stops, for example $f/1.4$, $f/2.0$, $f/2.8$, ..., $f/16$, $f/22$, $f/32$. For each f-stop up, the amount of light passing through the lens is halved as the

diaphragm opening area is reduced by factor of $\sqrt{2}$.

$$N = \frac{f}{D} \tag{6.2}$$

Besides the signal level, the particle image size has to be considered, too. It depends mainly on four factors (Kähler et al. 2012a) and helps to find a definition for the DoF. The most apparent factor is the geometric image size d_{geom} as image of the particle diameter d_p considering the magnification of the imaging system M as

$$d_{geom} = M d_p. \tag{6.3}$$

The second factor is the diffraction limited particle image size d_{diff} (Olsen et al. 2000) resulting from lens diffraction depending on the f-stop and the wavelength of light λ according to

$$d_{diff} = 2.44 \lambda N (M + 1). \tag{6.4}$$

The third factor stems from defocusing effects when imaging particles at a distance ϵ_Z from the plane of focus of the imaging system. Following Scarano 2013 and Novara 2013, the resulting blur spot diameter d_{blur} can be estimated using eq. 6.5. This effect of blur on the particle image size is especially important for volumetric measurements, where the measurement region is a volume of finite thickness and particles outside the plane of focus will be imaged.

$$d_{blur} \approx \frac{\epsilon_Z M^2}{N}. \tag{6.5}$$

Combining the individual contributions yields the theoretical particle image size

$$d_{img} = \sqrt{d_{geom}^2 + d_{diff}^2 + d_{blur}^2}, \tag{6.6}$$

which can also be expressed in terms of pixels by accounting for the discretization of the particle image space by square pixels of size Δ_{pix} and a minimum particle image size of a single pixel

$$d_{img,pix} = \max(1, \frac{d_{img}}{\Delta_{pix}}). \tag{6.7}$$

Using eqs. 6.3 to 6.6, the theoretical image size for a particle of 1 µm physical diameter was calculated. The assumed magnification of 0.2 matched the measurements presented below in chapter 7. The pixel size for the CCD cameras used was 7.4 µm, and the particle was located 4 mm away from the plane of focus. Focusing the cameras at the centre of the 8 mm diameter beam, this corresponds to the maximum distance that the particles could have to the plane of focus in the present measurements. As shown in fig. 6.10a, the blur spot contribution decreases with increasing lens f-stop. At the same time, the diffraction spot size increases monotonously, resulting in a decreasing particle image size from $f/1.4$ to $f/11$ before diffraction becomes the dominant factor and the particle image size increases again. From fig. 6.10a, it follows that even particles at the perimeter of the measurement volume will be below six pixels in diameter (starting from $f/5.6$), fulfilling the criterion from Raffel et al. 2018 for good particle images for particle based flow velocimetry. Next, the usable DoF was estimated by plugging eqs. 6.3 to 6.5 into eq. 6.6 and solving for ϵ_Z. A maximum allowed particle image size of six pixels in diameter was assumed, in line with the optimum range from Raffel et al. 2018. The distance to the plane of focus was calculated at which the particle image size would exceed these six pixels in diameter. Assuming symmetry of the DoF about the plane of focus, the DoF was approximated as twice the distance. As shown in fig. 6.10b, this depth range increases monotonically with increasing lens f-stop over the evaluated range. If the f-number is further increased, the usable DoF shrinks again owing to the growing diffraction-limited particle image diameter. While this definition might appear contradictory to the definition of the optical focal depth given in other publications, such as Scarano 2013, it is just a different approach. While the cited definition defines the focal depth relative to the lens performance in the plane of focus (which changes with f-stop), the present definition used for fig. 6.10b assumes an absolute criterion of a fixed maximum particle image size to determine the limit of the usable DoF.

In conclusion, a compromise between the available DoF and imaged signal levels must be found for volumetric measurements. The f-stops used for the different cameras are indicated in the following.

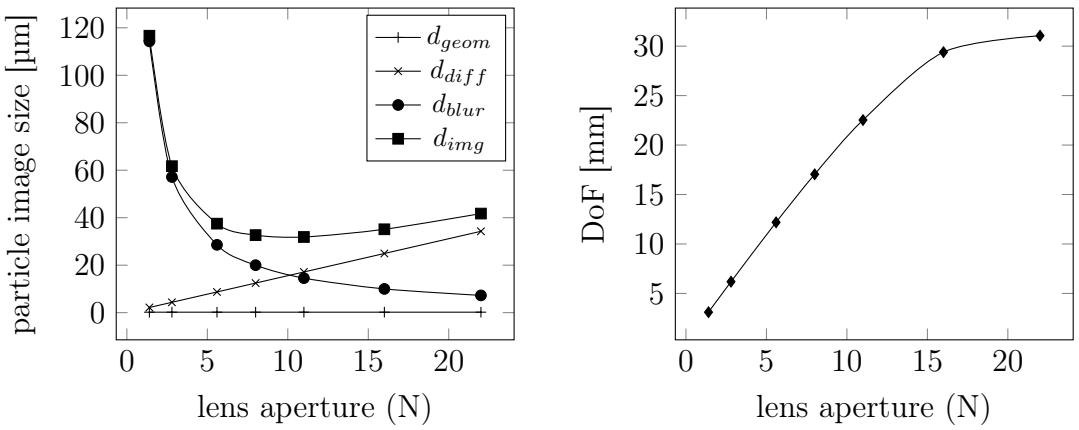

(a) particle image size contributions (b) usable DoF

Figure 6.10: The particle image size for a particle of 1 µm physical diameter at 4 mm from the plane of focus plotted against the lens aperture f-stop (a). In (b) the usable DoF depending on the lens f-stop is shown.

Camera setup

From fig. 6.9 it follows, that the cameras imaging Mie-scattered light should be positioned in forward scattering direction to maximise imaged signal levels. Due to space constraints, this was not possible in the present study. Instead, cameras P1 to P4 (cf. fig. 6.2 on page 62) were placed in the side and backward scattering directions at angles of 51°, 66°, 114°, and 129°. In this way, the scattering signal available for each of these views is comparable in magnitude and the setup angular aperture as the largest angle between different views is large at 78°. Remaining differences in available signal levels per camera were compensated by setting the apertures of the camera lenses of 100 mm focal length to $f/22$ and $f/16$ for cameras P1 and P2 (smaller angles), and cameras P3 and P4 (larger angles), respectively. The angular aperture has a strong influence on the reconstruction quality as it determines the shape of the reconstructed particles and, therefore, the reconstruction error as investigated in Scarano 2013. As shown in fig. 6.2 (page 62), the cameras were placed in a linear viewing configuration, where all cameras were located in a common horizontal plane with their lens optical axes centred on the jet nozzle exit. Other viewing configurations, such as a cross-like configuration, offer a slightly higher reconstruction quality as investigated using synthetic data in Scarano 2013

and Thomas et al. 2014 at the expense of a more complex setup. Considering the angular aperture of the presented system is 78°, the expected difference in reconstruction quality for the implemented linear camera setup compared to a cross-like camera setup is below 2 %. As the current particle image seeding densities were below 0.01 ppp, a linear camera setup was sufficient.

As cameras P1 to P4 were placed at angles other than 90° to the measurement volume, their planes of focus did not align with the largest dimension of the measurement volume, as defined by the laser propagation direction. In standard camera setups, the plane of focus is defined by the image sensor plane. This would limit the measurement volume size in the present case, as shown schematically considering two cameras in fig. 6.11. Only the volume where the DoF of all cameras overlap could be used for tomographic particle position reconstruction due to strong particle image blur outside of it.

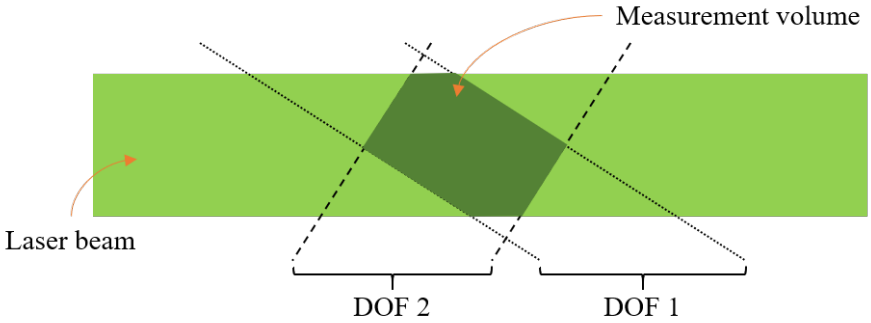

Figure 6.11: Measurement volume as determined by the intersection of a laser beam and the depth of field (DoF) of two cameras.

This means that not only the absolute DoF as controlled by the lens aperture is important when designing a tomographic camera system, but also its orientation relative to the object plane, that is, the largest dimension of the measurement volume. Following the Scheimpflug principle (Merklinger 1993), the DoF plane can be aligned with the object plane if the lens and image sensor planes are rotated against each other to fulfil the Scheimpflug criterion. In other words, the object, lens, and image sensor planes must meet in a single line. A 2D representation of this is shown in fig. 6.12, where the planes become lines intersecting at a point. To

tilt the lens against the camera body at an angle, Scheimpflug adapters (LaVision Scheimpflug mount V3) were used with cameras P1 to P4.

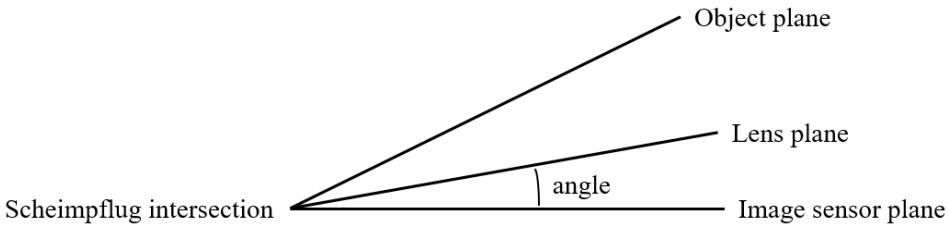

Figure 6.12: Simplified 2D representation of the Scheimpflug principle, matching the image, lens, and object planes in a single point by adjusting the angle between image sensor and lens planes.

In conclusion, double-frame image quartets of particle Mie scattering were recorded from different views. These recordings were processed as described in section 6.2 to obtain the particle positions and velocities.

6.1.3 Imaging subsystem for flow thermometry

In-flow temperature measurements using the developed measurement technique were based on the imaged luminescence emissions of seeded thermographic phosphor tracer particles. In this thesis, a ratiometric thermometry approach was used (cf. section 3.2.3). To record particle luminescence emissions in two spectral channels, two cameras were equipped with spectral filters to limit the spectral range observed with each camera. Below, a characterisation of the thermometry subsystem is provided. Different imaging sensor technologies and camera arrangements were investigated, spectral filters used with these cameras were selected using simulations, and the use of external apertures to control the DoF of these cameras is described.

Imaging sensor technology

As the luminescence cross-section of the phosphor particles is orders of magnitude lower than their scattering cross-section, the available signal levels for the luminescence images are also much lower (Stelter et al. 2023). A crucial measure of image quality in this regard is the signal-to-noise ratio (SNR). It compares the

imaged signal levels with the noise added by the camera. If the SNR is too low, the relative influence of noise becomes large and degrades the LIR and later the temperature precision, which are based on the imaged signal. The SNR could be increased by increasing the imaged signal levels or by reducing the noise. On the one hand, the imaged signal level was maximised by widely opening the lens apertures for luminescence imaging cameras. On the other hand, the noise level could be influenced by the choice of the image sensor technology or camera.

Two image sensor technologies were available: charge-coupled devices (CCD) and scientific complementary metal-oxide-semiconductor (sCMOS) sensors implemented in LaVision Imager Pro X and Imager sCMOS cameras, respectively. Both technologies consist of 2D pixel arrays, where each pixel has a photoactive area (photodiode) and irradiating photons are converted to an electrical charge. In CCD sensors, the charge of individual pixels is transferred to serial registers for analogue-to-digital conversion, while parts of the readout electronics are integrated into each pixel for sCMOS sensors (Saha 2015).

Some key performance indicators when comparing different image sensors or cameras are their quantum efficiencies and noise contributions. The quantum efficiency (QE) is the ratio of irradiating photons on the photoactive sensor area to the generated electrons. Higher values are better and are scaled between 0 and 100 %. For the available cameras, the QE is compared in fig. 6.13 as published by the manufacturer (LaVision 2018; LaVision 2023). For both cameras, it peaks at approximately 60 % but at different wavelengths. While the Imager Pro X is listed as being sensitive from 300 nm, QE data is only available from 400 nm. Compared to the emission spectrum at room temperature of ZnO ranging from 370 nm to 440 nm, both cameras offer good coverage of the signal.

The image noise of the cameras can be split into random and fixed pattern noise. Random noise consists of three main components. First, read noise is generated by the electric circuitry required to run and read the image sensor. Second, dark noise is due to thermally excited electrons in the pixel photodiodes, as the sensors are operated at temperatures above 0 K. Finally, shot noise is caused by the stochastic detection of discrete photons interacting with the photodiode material. While readout and dark noise are camera properties, shot noise is related to the imaged

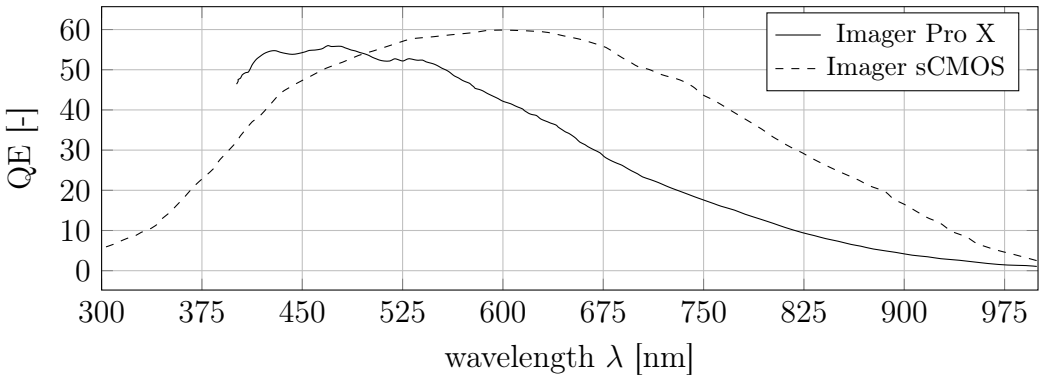

Figure 6.13: Quantum efficiency (QE) of available cameras for luminescence imaging as provided by the manufacturer (LaVision 2018; LaVision 2023).

Table 6.1: Important technical data for selecting luminescence imaging cameras. Reproduced from (LaVision 2018; LaVision 2023).

	Unit	Imager Pro X	Imager sCMOS
Sensor resolution	*pixel*	1600 × 1200	2560 × 2160
Pixel size	μm	7.4	6.5
Readout noise (rms)	e^-	10	1.4
Dark noise (rms)	$e^-/pixel/s$	0.01	0.5

signal and scales with the number of photons hitting a pixel N as $\sqrt{N}$. Fixed pattern noise is constant across recorded frames and stems from pixel differences or defects, known as hot or dark pixels.

Important technical data to compare the performance of the cameras for luminescence imaging are listed in table 6.1. Both cameras offer high-resolution image sensors with large individual pixels. The main difference between the two cameras is their noise characteristics. While the Imager Pro X offers very low dark noise, it suffers from high read noise. For the present application, the exposure time of the cameras was in the millisecond to microsecond range. Hence, dark noise is irrelevant (below 0.02 e^-). The strength of the Imager sCMOS is its low read noise. For the CCD-based Imager Pro X camera, hardware binning can reduce the relative read-noise contribution by pooling the recorded signal from multiple pixels before readout. In this way, pixel bins are formed where the relative readout noise drops by a factor of 16 for $8x2$ binning at the expense of spatial resolution.

Imaging experiments were performed to compare the real-world performance of both cameras in imaging low-intensity phosphor luminescence emissions. The ZnO particles were seeded in a nitrogen flow at room temperature. A UV laser beam at 266 nm and a diameter of 8 mm was used to excite the luminescence emission of the particles. Both cameras were equipped with 85 mm focal length lenses with apertures set to $f/1.4$ and mounted 387-11 nm interference filters (Edmund Optics 84-094) to image only phosphor luminescence emissions. Example images at similar magnifications of 0.18 (CCD) and 0.2 (sCMOS) are shown in fig. 6.14. While the sCMOS camera operated at native resolution the CCD image was binned $8\times8\,\text{pixel}^2$ ($8\times2\,\text{pixel}^2$ hardware, rest software). Orange lines indicate the height of the laser beam in the images. The difference in spatial resolution between particle images recorded by both cameras is striking. In Imager Pro X recordings, particle images started to overlap if more than a few particles were present in the laser beam. Out-of-focus particles created an elevated background signal and could not be recognised as individual particles. This limited the maximum usable particle seeding density and reduced the SNR, deteriorating the temperature precision. In comparison, the Imager sCMOS showed smaller particle images, resolving orders of magnitude more particles within the laser beam against a uniform background. At the same time the peak intensities in the sCMOS image were lower than in the CCD recordings, which highlights the challenging image data evaluation for thermometry based on individual particle images. Based on these results, the sCMOS-based Imager sCMOS cameras were selected for phosphor luminescence imaging in the thermometry subsystem.

To further characterise the selected sCMOS cameras for luminescence imaging, the true image noise was calculated using dark images. These dark images were recorded by covering the camera lenses with lens caps to prevent any light from entering. For later phosphor thermometry measurements, the cameras were set to an exposure time of 35 ms and operated at a slow scan-sensor readout speed of 95.3 MHz in rolling shutter mode with double inside-out sensor readout and no software image filters. Using these settings, sets of 100 single-shot images were recorded and the image-to-image standard deviation of each pixel is calculated as realistic measure of true camera noise for the present settings. As a result, both sCMOS cameras performed close to the manufacturer's specifications of $1.4\,\text{e}^-$

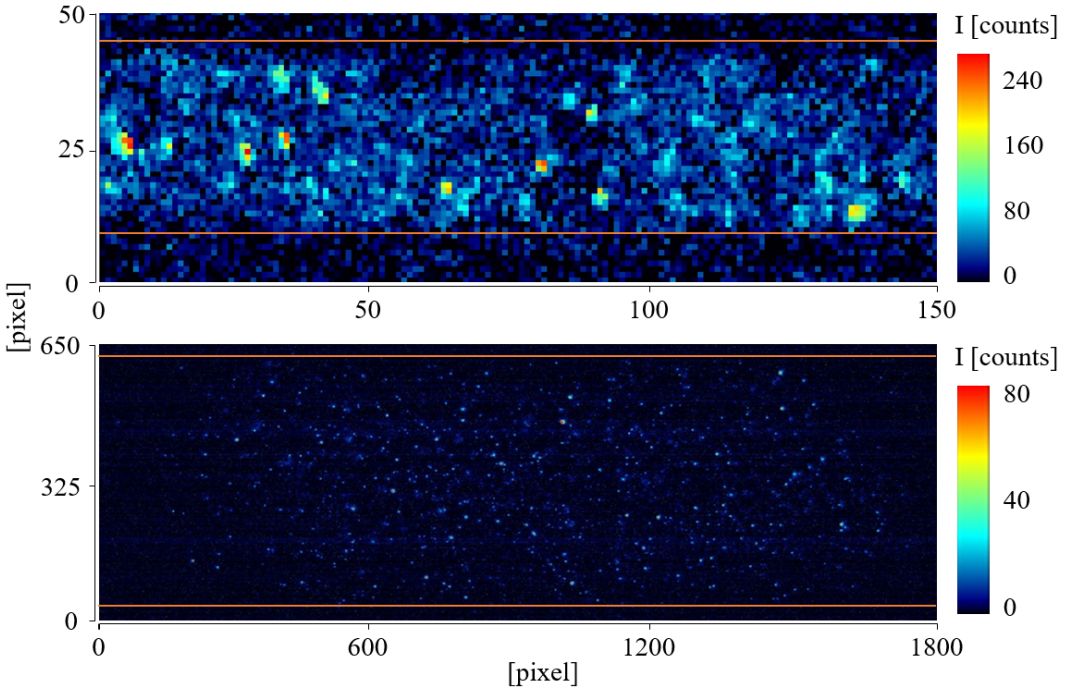

Figure 6.14: ZnO particles imaged by Imager Pro X (top) and Imager sCMOS (bottom) cameras. The Imager Pro X was $8 \times 8\,\mathrm{pixel}^2$ binned while the Imager sCMOS operated at native resolution. Orange lines indicate bounds of laser beam passing from right to left.

(rms) readout noise with actually measured $1.42\,\mathrm{e}^-$ (rms) and $1.45\,\mathrm{e}^-$ (rms) for cameras T1 and T2, respectively. Considering the analogue-to-digital converter factor of $0.45\,\mathrm{e}^-$/count, this results in an image noise of approximately 3 count. This underpins that the readout noise is the dominant noise factor for short-exposure recordings used within the present thesis for 3D flow temperature measurements and that the noise floor for the sCMOS cameras is very low.

A special kind of noise in sCMOS cameras is due to a memory effect (Rhodes et al. 2014). After recording a static scene with high irradiance on the sensor with short exposure times ($< 10\,\mathrm{ms}$) over the course of several minutes, the signature of the image can be embedded in subsequent readout cycles of the sensor. This effect is visualised below in fig. 6.15. When calibration target images were recorded using sCMOS cameras, high image intensity was desired to record target image patterns with high contrast for later corner or edge detection algorithms to work properly in preparation of camera calibration. Such an image is shown in fig. 6.15a. During

following luminescence particle image recordings for flow thermometry, the imaged signal levels were much lower and relatively long exposure times of 35 ms were used (cf. section 6.1.4). Hence, trapped charges from the calibration target recording would be readout together with particle images, creating a strong dark noise offset in previously bright regions of the target image. Processing meaningful particle temperature information from such images would be impossible. This is visualised in fig. 6.15b where dark images were recorded after target image recordings with a lens cap blocking any light from entering the lens. While the camera could not see the target through the capped lens, the image still showed the target pattern owing to the memory effect (Rhodes et al. 2014). While the charge depleted naturally by waiting for several days, a quicker reset was possible as well. By turning the cameras off and exposing them for 5 min with a high-intensity uniform light source, the charge was freed, and the sensor noise returned to nominal values, as shown by dark images recorded after the reset procedure in fig. 6.15c. This sensor reset was required after each target image set recording before starting to capture in low-light conditions. While a chessboard target was used to show the memory effect, a dot-pattern target was used to calibrate the cameras (cf. section 6.1.5).

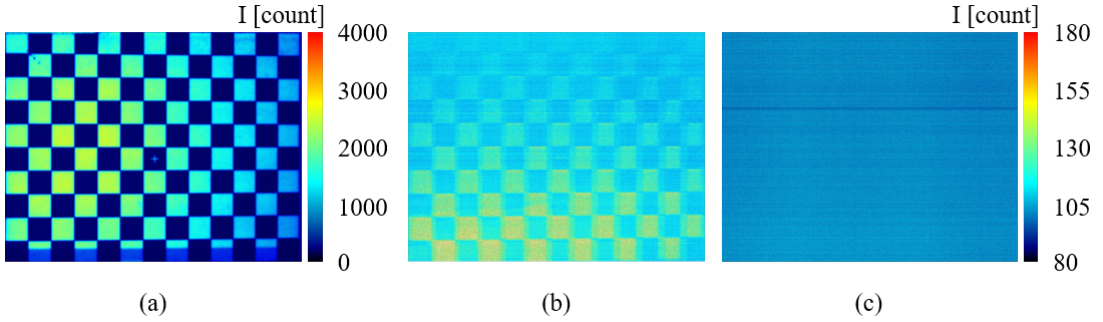

Figure 6.15: Exposing a sCMOS sensor to a static scene with high image intensities (a) creates regions of elevated dark current visible in dark images (b). After a reset procedure, the image noise is homogeneous at nominal values with little dark signal non uniformities (c).

Spectral filter selection

To implement ratiometric phosphor thermometry, two spectrally separated images ('channels') of the seeded phosphor particles must be recorded, as described above

in section 3.2.3. To create such images using the selected camera arrangement of one camera per channel, one can either mount spectral filters in front of each camera or use a dichroic beamsplitter that selectively reflects and transmits light based on its wavelength. To select the filters or dichroic beamsplitter for the present application, two main criteria must be considered as follows from section 3.2.3. First, the imaged signal levels per channel must be sufficiently high as a low SNR limits the achievable LIR precision. Second, the ratio between both channels must be sensitive to temperature. To aid the selection process, simulations were run to test 13 different filters (and beamsplitters) in 15 combinations as summarised in table 6.2.

Table 6.2: Interference filter combinations and dichroic beamsplitters considered as candidates for LIR creation. Interference filters are given as combination of central wavelength (cwl) and bandwidth (bw).

Interference filter combination (cwl-bw) [nm]	Dichroic beamsplitter (manufacturer name)
400-50 / 394-10	Chroma T387lp
425-50 / 387-11	Chroma ZT375rdc
375-50 / 394-10	Semrock FF390-Di01
375-50 / 400-50	Semrock FF389-Di01
375-50 / 425-50	Semrock FF376-Di01
400-50 / 387-11	Omega 400DRLP
400-25 / 387-11	UniBW 392lp (custom)
400-25 / 400-50	

Using simulations, similar to the considerations in Petit et al. 2022, instead of testing all filters in lab saves lots of time and money compared to procuring all filters and testing them in lab experiments. To run these simulations, both luminescence emission spectra of the selected phosphor at different temperatures and spectral characteristics of the imaging system components were needed. For the setup components, the required characteristics were obtained from the respective manufacturers. The emission spectra of ZnO as selected phosphor are available from literature over a temperature range of 293 K to 488 K (Abram et al. 2015). However, these spectra were recorded with ZnO in aggregated powder state which is very different compared to dilute particle dispersions in a fluid phase. This is important as a dependency of the emission spectrum on the state of aggregation

was found in an earlier study (Stelter 2019). This is visualised in fig. 6.16a, where the luminescence emission spectra of ZnO are shown for the same temperature but once recorded from an aggregated powder and once from a dilute liquid dispersion. The emission spectrum recorded from powder is red-shifted compared to the liquid dispersion spectrum, with intensity distribution peaks separated by 7 nm. As the emission and absorption spectra of ZnO overlap in the near UV region (cf. fig. 5.1a on page 50), this shift is attributed to reabsorption of the near UV emissions by adjacent particles, creating the perceived red shift. As the inter-particle distances in dilute liquid dispersions (or when seeded in a gas flow) are much larger compared to an aggregated powder, reabsorption is much less probable for the former. This demonstrates the necessity of using liquid or gas dispersion spectra for the filter selection simulation. It is reasonable to assume that the inter-particle distance in a dilute liquid dispersion of ZnO is similar to the case of a seeded gas flow with low particle image seeding density, as used in the present thesis. Hence, luminescence emission spectra recorded using the spectroscopy setup from (Fond et al. 2019a) in a dilute dispersion of 2 µg/mL of ZnO in distilled water were used for the simulations (available from Stelter 2019). The dispersion was prepared in a fused silica cuvette placed on a combined heating and magnetic stirring plate. This allowed the recording of emission spectra at homogeneous dispersion temperatures between 296 K and 334 °C as plotted in fig. 6.16b.

However, the temperature range targeted in this thesis extends beyond 334 K. To simulate the different filter behaviour up to 460 K, synthetic spectra were created. By evaluating the shift and broadening of the liquid spectra with increasing temperature, an extrapolation of the behaviour to higher temperatures was facilitated. Observed spectral changes were combined with the thermal quenching behaviour of ZnO from Abram et al. 2015 to create artificial emission spectra from 296 K to 460 K. These spectra were then computationally filtered using the optics transmission curves (in case of dichroic beamsplitters also reflectance), while also considering the camera quantum efficiency and lens transmittance. This resulted in an intensity value for each filter or beamsplitter channel. From these intensity values, LIRs were calculated for the interference filter combinations and dichroic beamsplitters listed in table 6.2. Finally, using these ratios for all available temperatures, the normalised LIR sensitivity (eq. 3.4 on page 20) was estimated and normalised to the maximum

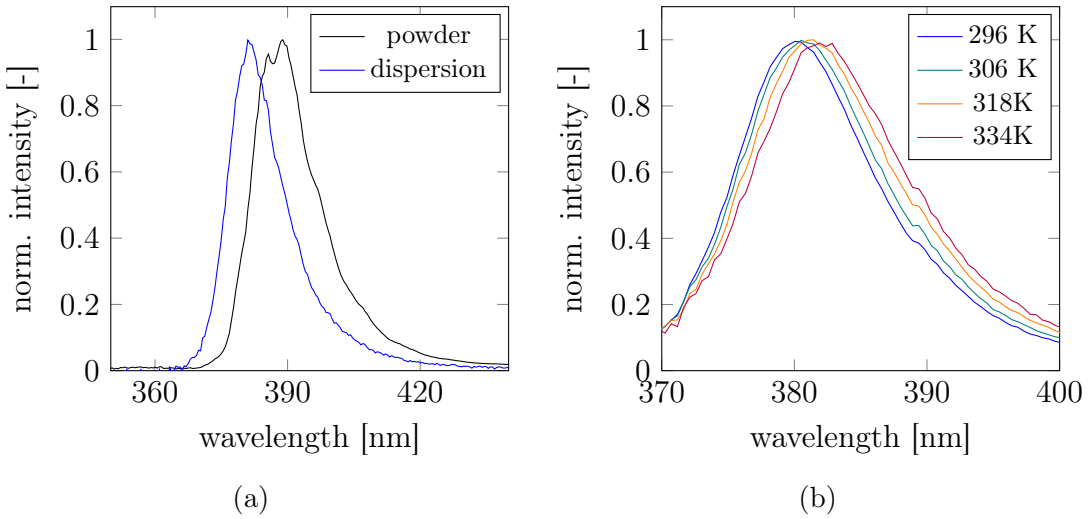

Figure 6.16: Comparison of ZnO emission spectra recorded in powder and dispersed state (a) and recorded in dispersed state at different temperatures. Data reproduced from Stelter 2019.

sensitivity to allow for a quick comparison among filters. Figure 6.17 shows the normalised sensitivities for all interference filter combinations. As beamsplitters introduced strong aberrations to the particle images they could not be used and are therefore not shown here (cf. fig. 6.20 on page 89 below).

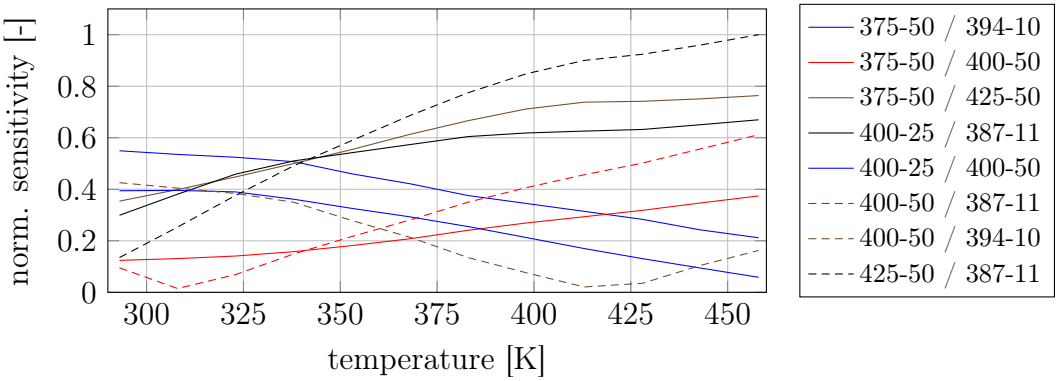

Figure 6.17: Simulated sensitivity of LIR to temperature for different interference filter combinations, normalised to maximum found over all options.

The best filter combination in terms of LIR temperature sensitivity consists of 425-50 nm and 387-11 nm filters, especially at temperatures above 350 K. Absolute signal levels as second criterium are sufficient for ratiometric thermometry, too,

as known already from literature (Abram et al. 2015). The transmission spectra for both filters as publicly available from the manufacturer website are plotted in fig. 6.18 where they are overlaid with simulated ZnO emission spectra at different temperatures.

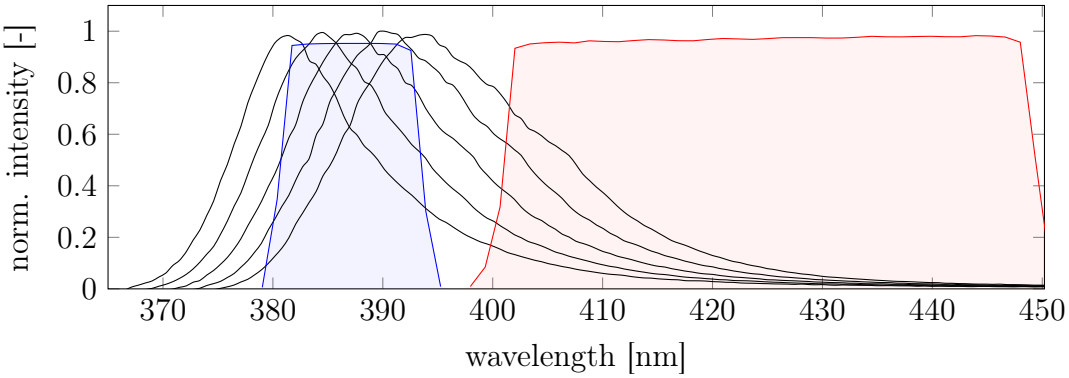

Figure 6.18: Simulated ZnO luminescence emission spectra from 296 K to 460 K with overlaid transmission spectra of the 387-11 nm and 425-50 nm filters normalized to the peak transmission of the latter.

The decision for these filters was additionally backed by the rather equal split of available luminescence signal into both spectral channels, as indicated by a LIR close to unity at ambient temperatures of 296 K. This is desirable as creating a very weak channel would deteriorate the achievable temperature precision (Rothamer et al. 2011). In conclusion, the combination of 425-50 nm and 387-11 nm filters were used in all phosphor thermometry experiments shown in this thesis unless explicitly stated otherwise.

Camera arrangement

To realise two-colour imaging for ratiometric phosphor thermometer measurements, several camera arrangements are conceivable. Five candidates, as reported by Abram et al. 2018 are shown in fig. 6.19. Suitable candidates for the present measurement concept were selected based on usable image sensor space per colour channel, the light throughput to maximise image signal levels, and their robustness to potential anisotropy in luminescence emissions.

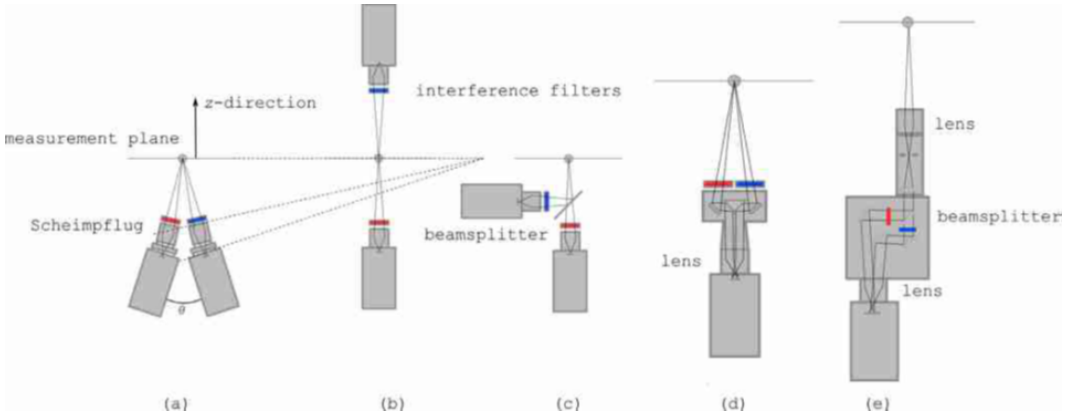

Figure 6.19: Two view camera arrangements for LIR based phosphor thermometry: a) stereo pair, b) opposing view, c) beamsplitter, or d-e) image-doubling optics. Reproduced from Abram et al. 2018 (CC-BY 4.0).

As the measurement volume size is partly determined by the available image sensor size, the entire image sensor of luminescence imaging cameras should be usable per colour channel to maximise the monitored volume size. Hence, imaging configurations (d) and (e), which use image-doubling optics to use half of the sensor for each of the colour channels, are not an ideal fit for the present concept. This is supported by two additional challenges associated with such devices. First, cross-talk between the two images created by image doublers is common, hindering the precise separation of the signals of both colour channels. Second, either owing to the optical setup of these devices or as a measure to reduce the aforementioned crosstalk between the double images, the light throughput is equal to lens apertures of $f/5.6$. Compared to a standard camera lens with an aperture of $f/1.4$ this is an order of magnitude less light throughput, which is unacceptable for low-light applications, such as single-particle phosphor luminescence imaging (Abram et al. 2018).

When using two-colour approaches, a beamsplitter, as in fig. 6.19c, is normally used to create nearly identical optical paths for two cameras imaging a phosphor particle distribution. The angular dependence of the Mie-scattered signal is well known (cf. section 6.2), but this has not been investigated for phosphor luminescence emissions. Hence, systems sharing similar views between two colour channels were preferred to mitigate potential anisotropy of luminescence emissions, and

configuration fig. 6.19b was not deemed to be a good candidate for the present concept. Instead, a stereo camera setup as in fig. 6.19a and a single-view two-camera setup using a beamsplitter as in fig. 6.19c were selected for practical evaluation, and luminescence particle images were recorded using both to facilitate a comparison.

Three different sCMOS camera setups were tested, and the resulting luminescence particle images are shown in fig. 6.20. As a test case, ZnO particles were seeded into a flow of nitrogen at ambient temperatures of 296 K, and luminescence emissions were excited from the particles by a 8 mm laser beam of 266 nm at 58 mJ per pulse. Among the three tested systems were two one-view systems in which the cameras were arranged at 90° to each other, and different beamsplitters were used to provide them with nearly identical views of the particle distribution. First, a broadband beamsplitter with a signal splitting ratio of 50:50 between reflection and transmission was tested. The camera lenses were additionally equipped with 387-11 nm and 425-50 nm bandpass filters in transmission and reflection, respectively, to allow for two-colour ratiometric imaging. Particle images recorded using this setup showed strong aberrations in the form of astigmatism and halo-like areas around imaged particles, where the imaged intensity was elevated compared to the average background signal, as shown in fig. 6.20a. As the available beamsplitter (Edmund Optics 46-642) was only 1 mm, astigmatism is attributed to a lack of surface flatness and potential deformation. This could stem from inherent surface non-uniformities or mechanical deformation of the beamsplitter by mounting mechanics. Next, a custom-manufactured dichroic beamsplitter was tested. The camera in transmission was equipped with a 400-50 nm bandpass filter (Edmund Optics 84-793) while the camera in reflection position was equipped with a Schott BG64 coloured glass filter and a 532 nm notch filter (Edmund Optics 86-130) to remove unwanted laser and background signals. As the beamsplitter's substrate was 5 mm thick, it was much more rigid than the previously tested broadband beamsplitter. Luminescence particle images recorded by the camera in the reflection channel showed profound halo-like aberrations around individual particle images, as shown in fig. 6.20b. These findings regarding image quality deterioration are in line with the findings of Xuan 2023 who also investigated two-camera image setups using different beamsplitters. Finally, the sCMOS cameras were placed in a stereo camera setup with one camera at 90° and the other at 80° relative to the laser beam

propagation direction. Here, the cameras were equipped with 387-11 nm (90°) and 425-50 nm (80°) filters. As shown in fig. 6.20c, images recorded by these cameras did not show strong aberrations and the recorded signal levels were higher due to the lack of multiple optical filters compared to the former two setups.

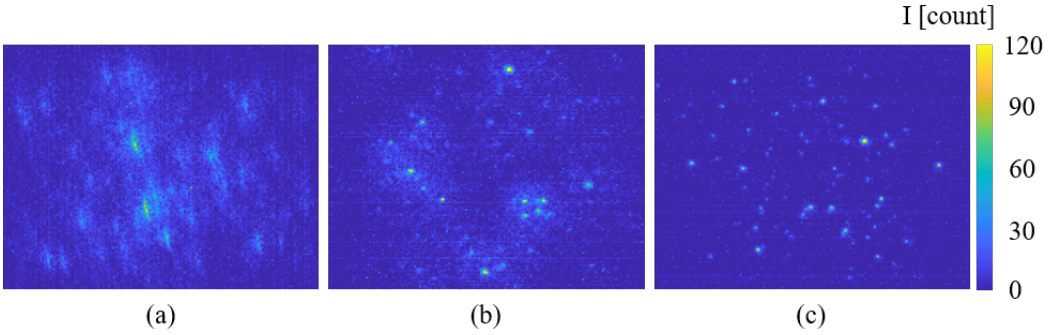

Figure 6.20: Luminescence particle images recorded by sCMOS cameras using different imaging configurations: (a) 50:50 broadband beamsplitter, (b) dichroic beamsplitter, and (c) two-view system.

In conclusion, particle images recorded using any available beamsplitter did not satisfy the image quality requirements needed for single particle based phosphor thermometry measurements. Therefore, the cameras of the thermometry subsystem were placed in a stereo arrangement. By keeping the stereo angle between the cameras as small as possible, the influence of potential anisotropic effects of the luminescence emissions of phosphor particles was minimised.

Depth of field control

For luminescence recordings, imaged signal levels had to be maximised while for calibration target image recordings, the DoF had to be maximised. This translated to opposing requirements for camera lens aperture settings for these steps of every 3D measurement using the developed technique. For luminescence particle recordings, the apertures should be opened as wide as possible to collect as much of the relatively weak phosphor luminescence emission on the camera image sensor. However, for target image recordings, the signal is less of a concern and the lens apertures should be closed to record in-focus images of the target at every

in-depth position of the measurement volume instead. This ensures reliable and precise detection of target markers in the images by contrast-driven edge detection algorithms. As before, it was not allowed to move the cameras between the target and particle image recordings, so the internal apertures of the lenses could not be used. Instead, circular external apertures were placed directly in front and centred in the entrance pupil of the camera lenses but mounted on independent supports to prevent physical contact. This allowed adjustment of the effective aperture for the cameras at any time.

The effect of using these external apertures during target image recording is shown in fig. 6.21. Two images of the same dot target placed 8 mm away from the plane of focus are shown. In fig. 6.21a, the camera lens aperture was set to $f/1.4$ and the external aperture was opened completely to 50 mm. The resulting image shows strong blur. In fig. 6.21b, the external aperture was set to an opening of only 7 mm, leading to an in-focus image of the target markers.

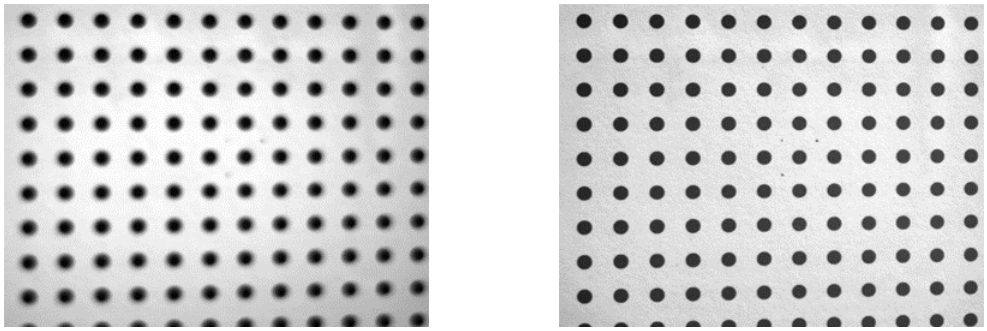

(a) (b)

Figure 6.21: Calibration target images recorded with sCMOS camera and external aperture set to diameter of (a) 50 mm and (b) 7 mm.

Out of focus luminescence particle imaging

Imaging particles distributed within a volume using cameras with open lens apertures and a fast lens is associated with some challenges, mainly caused by image blur as an out-of-focus effect. For the current setup, this impacted the luminescence imaging cameras. Their point spread function (PSF) was strongly dependent on the position of the imaged object relative to the plane of focus. This is visualised using

the 2D sketch in fig. 6.22. Three particles, A, B, and C, are positioned at different locations within a measurement volume. Particles A and C are centred within the depth of the measurement volume along the z-axis of the world coordinate system, coinciding with the plane of focus of all cameras. Here, only two of the P-cameras imaging Mie-scattered light of particles with stopped down apertures are shown. Both T-cameras had completely open apertures. As a result, all three particles were imaged in focus by the P-cameras, visualised by the three intensity peaks of equal height and low spread formed on each of their sensors. For the T-cameras, however, for particle B, an out-of-focus image is created, characterised by a reduced peak intensity and a much larger spread of the particle image.

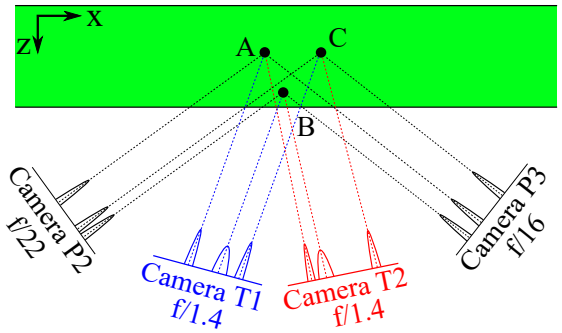

Figure 6.22: Schematic comparing Mie scattering and luminescence particle imaging of three particles A, B, and C at different locations within the measurement volume shown in green.

If we considered only non-overlapping particle images as usable, because only their luminescence signals could be processed straightforwardly, then the expanded diameter of the out-of-focus particle images sets an upper boundary for the maximum possible particle image seeding density. Increasing the number of physical particles per unit volume increases the particle image seeding density until the overlap between individual particle images becomes so severe that the number of usable samples starts to decrease.

To find the optimum seeding density corresponding to the largest number of usable particle image samples, simulated particle distributions and corresponding camera images were used. Using a Monte Carlo approach, random 3D particle distributions were generated within a domain of $7 \times 7 \times 7\,\mathrm{mm}^3$, and the corresponding Mie scattering and luminescence camera images were generated. Three different apertures

of $f/1.4$, $f/2.0$, and $f/2.8$ were considered for luminescence imaging, and $f/16$ was used for the Mie scattering counterpart. Particle distributions and artificial camera images were computed for a range of particle image seeding densities between 0.001 and 0.1 ppp, samples of which are shown in fig. 6.23. The particle image size was calculated using the eqs. 6.3 to 6.7 introduced above. Images fig. 6.23a and c show 50×50 pixel regions of simulated luminescence camera images. The corresponding Mie scattering images are shown in subfigures b and d. For the luminescence images, the dependence of particle image size on the position of the particle within the volume is striking. Two particles are highlighted in red. Particle A was located within the plane of focus of the camera, while particle B was located at the border of the simulated measurement volume. As the aperture of the luminescence camera was opened to $f/1.4$, the minimal particle image size is smaller than in the corresponding Mie images, as the diffraction-limited particle image diameter scales with aperture f-number, as shown above in fig. 6.10a. In comparison, the particle sizes in the Mie scattering images were almost constant for all particles owing to the stopped-down camera aperture. For low particle image seeding densities of 0.001 ppp (subfigures a and b), no overlap of adjacent particle images was found. Even for seeding densities ten times higher, overlapping particle images were rare (subfigures c and d).

Increasing the particle quantity within the volume would lead to increasing overlap between individual particle images. Reducing the blur spot diameter in the luminescence images would reduce its likeliness, as individual particle images would cover less image space. This was simulated in fig. 6.24, where simulated particle distributions at 0.03 ppp are shown as imaged by an sCMOS camera with the lens stopped down to $f/2.8$ (a) and the corresponding Mie scattering image with an aperture of $f/16$ (b). While the maximum image diameter per particle was in fact considerably reduced from 9.2 to 4.6 pixel, there were still many overlapping particles. This was further quantified below by evaluating the computed camera images of many random particle distributions.

By evaluating and averaging the results of 100 simulations, the graphs in fig. 6.25 were generated. The number of usable particle image samples S_u, the ratio of separable non-overlapping particle images R_s and the corresponding source density N_S in the luminescence camera images are plotted and compared to the particle

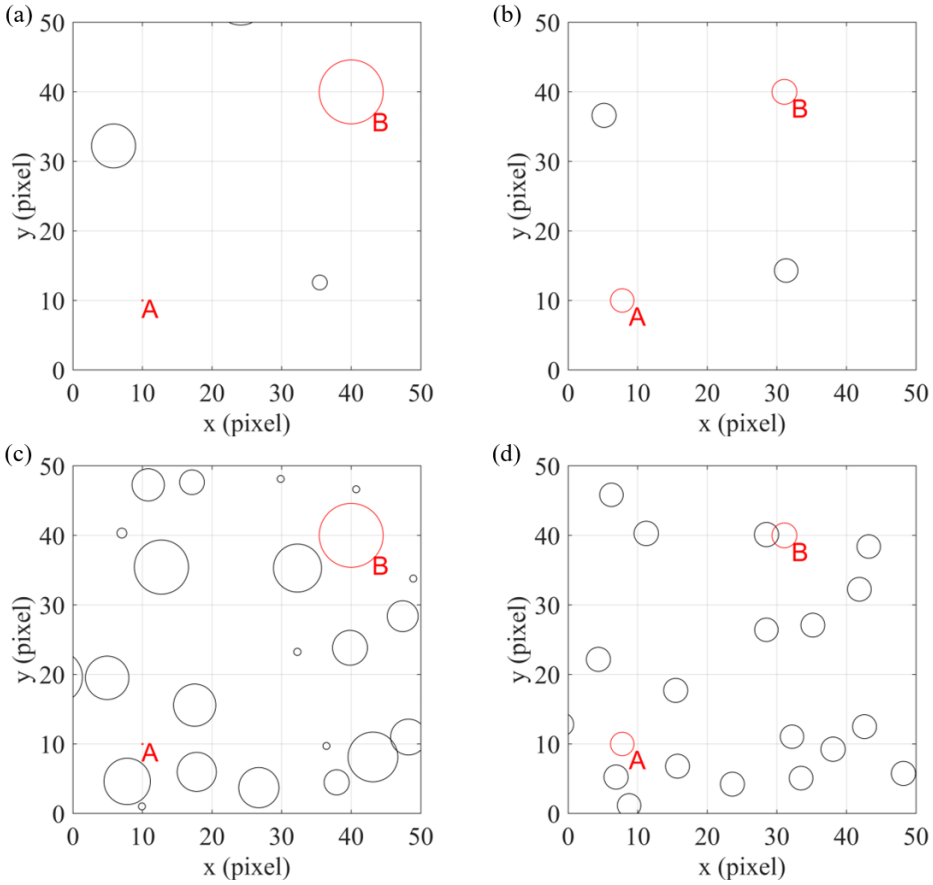

Figure 6.23: Simulated luminescence (a, c) and Mie scattering (b, d) camera images for particle seeding densities of 0.001 ppp (top) and 0.01 (bottom) and apertures of $f/1.4$ (luminescence) and $f/16$ (Mie scattering). Particles A and B in red are located in the plane of focus and at the boundary of the measurement volume, respectively.

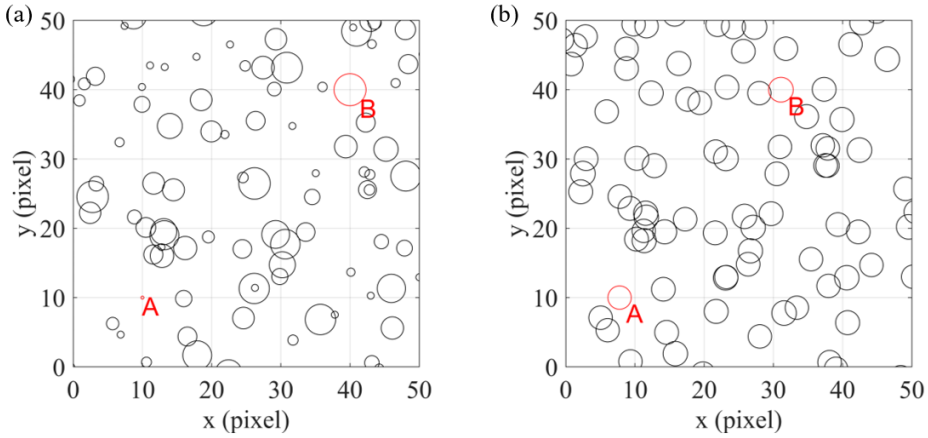

Figure 6.24: Simulated luminescence (a) and Mie scattering (b) camera images for a particle seeding density of 0.03 ppp and camera apertures of $f/2.8$ (luminescence) and $f/16$ (Mie scattering). Particles A and B in red are located in the plane of focus and at the boundary of the measurement volume, respectively.

image seeding density n_{ppp}. Following Scarano 2013, N_S is an alternative measure to n_{ppp} that considers the particle image size in pixel space $d_{img,pix}$ as

$$N_S = \frac{\pi d_{img,pix} n_{ppp}}{4}. \tag{6.8}$$

This measure is especially useful if the particle image size is not constant, as in the case of luminescence camera images, owing to blur. For each data point, the average of 100 simulations was taken. Increasing the number of simulations to 1000, the result values changed by only 0.8 % which did not justify the much longer processing time.

As expected from the increasing probability of overlapping particle images with increasing particle image seeding density n_{ppp}, the ratio of separable non-overlapping particle images R_s decreased steadily for all aperture settings, as shown in fig. 6.25a.Here, particle images were considered to overlap as soon as they touched. For completely opened apertures, the ratio approached zero from 0.05 ppp. Combining this ratio with the absolute number of particles yields fig. 6.25b, which shows the number of usable samples S_u. A clear peak is visible that shifts with larger f-numbers towards higher particle image seeding densities. In addition, the maximum sample

number increased with the lens f-number. While the particle image seeding density provides a good idea of how many particles are imaged, the source density is especially useful for describing luminescence imaging. As it is a measure of the fraction of the image sensor space covered by particle images, it is more robust than the bare particle number per image, as it considers the varying particle image size in the luminescence images. It is plotted in fig. 6.25c, where it becomes clear that the available sensor space is filled completely when using fully open apertures and approaching 0.1 ppp. Based on these results, the optimal particle image seeding density appears to be 0.13 ppp for fully open apertures.

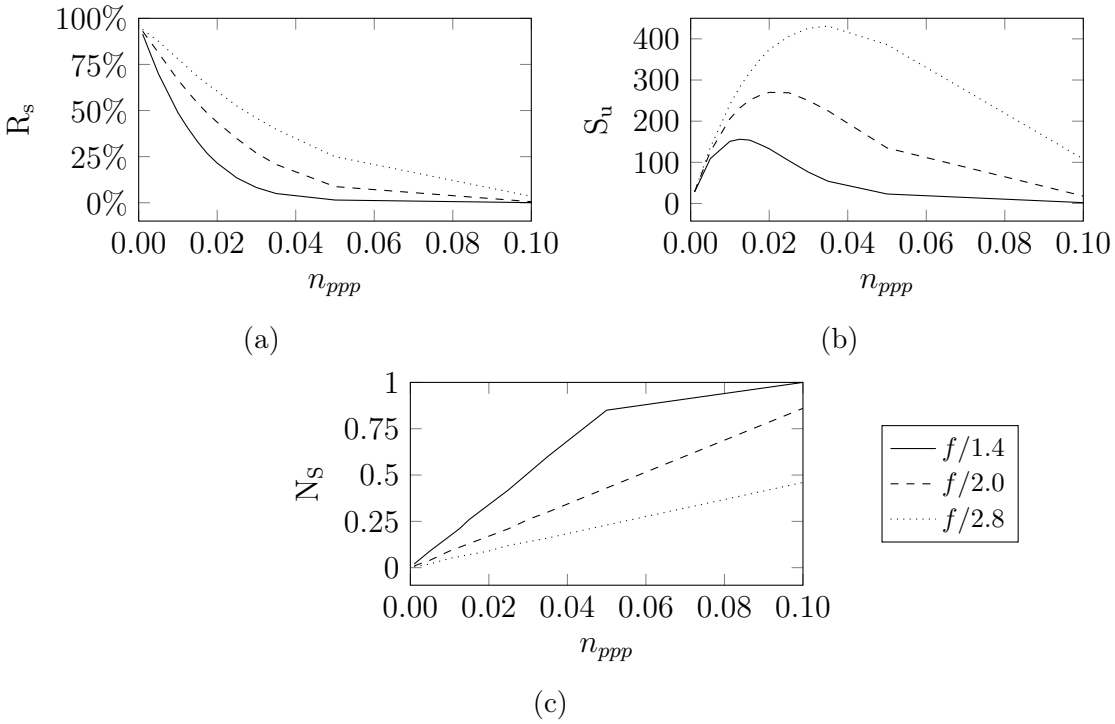

Figure 6.25: Influence of particle image seeding density n_{ppp} on (a) the fraction of usable particle images, (b) the absolute number of usable particle images, and (c) the source density.

Closing the lens apertures of luminescence imaging cameras would have been an option to measure at higher particle image seeding densities. This would enable more temperature and velocity samples per unit flow volume. However, the amount of light passing through the camera lens is halved for each full f-stop, which is critical for low-light applications. To investigate the feasibility of closing the lens

aperture to $f/2.0$ or $f/2.8$ from an image signal standpoint, images of seeded ZnO tracer particles under 266 nm illumination with a 8 mm laser beam at 210 mJ/cm^2 were recorded and imaged signal levels were compared. Examples of luminescent particle images are shown in fig. 6.26. The background signal was removed by subtracting the minimum pixel intensity over 100 single-shots. The decreasing particle image signal level with increasing f-number is reflected in the changing colour bar limits of the subfigures. At $f/2.8$ in fig. 6.26c, the few visible particle images start to dissolve in the remaining image background and noise. Not only is the peak intensity reduced, but the lower-intensity particle image borders also disappear into the background. This makes particle image segmentation increasingly challenging, and less signal is available for temperature inference, reducing the SNR, and inevitably the temperature precision (Rothamer et al. 2011).

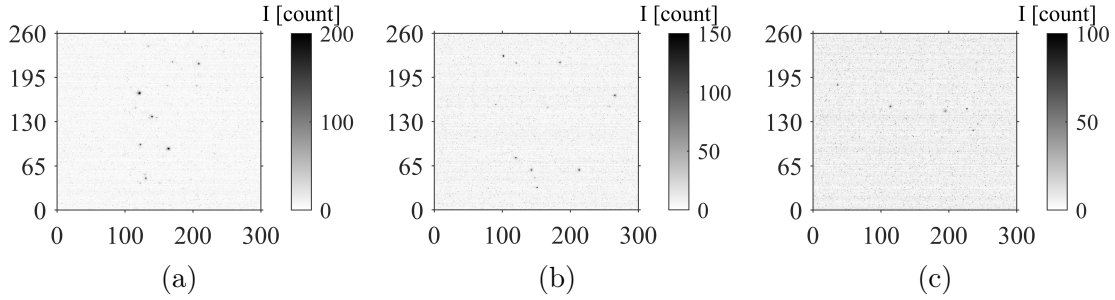

Figure 6.26: ZnO luminescence particle images recorded by a camera through a 387-11 nm filter and apertures of $f/1.4$ (a), $f/2.0$ (b), and $f/2.8$ (c).

In conclusion, an aperture setting of $f/1.4$ was selected for cameras T1 and T2, to maximise the imaged luminescence signal levels and improve the temperature precision at the expense of the number of measurements per unit volume. The estimated particle image seeding density limit is in line with the minimum line of sight (MinLOS) algorithm's capabilities, that was implemented for the present chapter (Michaelis et al. 2010).

6.1.4 Timing

Precise timing and synchronisation of all hardware devices are crucial when performing measurements using multiple lasers and cameras. Here, these devices were

grouped in two subsystems. One subsystem for the acquisition of Mie scattering images utilising four double-frame cameras and a green double-pulse laser, and a second subsystem for luminescence imaging featuring two cameras and a single-pulse UV laser. A central programmable timing unit (PTU) was used as master clock to send TTL trigger signals to all hardware components.

The overall timing is summarised in fig. 6.27. To record Mie scattering images, the green laser pulses were synchronised with the double-frame P-camera exposure times. Note that only the first exposure time can be controlled for these interline-transfer CCD cameras, and the second frame exposure is in the millisecond range, determined only by the camera frame rate. The first frame exposure was set to 5 µs and started 3 µs before the first green laser pulse to centre the pulse within the camera exposure temporally. The delay between both green laser pulses was adjusted to ensure an average particle displacement of 9 pixel within the Mie scattering images, considering the camera magnification, pixel size, and flow speed. To record luminescence images with the lowest noise level possible, the sCMOS T-cameras were operated in rolling shutter mode. In this mode, the image sensor pixel rows are read out one after the other, as shown in fig. 6.27. Commonly, this leads to spatial aliasing effects in the image if imaging fast-moving objects. These effects would degrade the image quality, and the luminescence information would not be recorded simultaneously across the whole field of view. However, tests revealed that a common exposure time for all pixel rows could be achieved if the overall camera exposure time was sufficiently long. For the present implementation, an exposure time of 35 ms lead to a common exposure time of all image sensor pixel rows of 5 ms. By starting the T-camera exposure 32 ms before the UV laser pulse, the laser pulse arrived in the middle of this exposure. Even if the actual camera exposure time was multiple milliseconds, the effective exposure time was determined by the luminescence decay time of the phosphor or UV laser pulse duration, whichever was longer. For the present implementation using ZnO tracer particles, the UV laser pulse duration of 10 ns was longer than the phosphor luminescence decay time (Rodnyi et al. 2011). Owing to this very short effective exposure, even fast particle movements were imaged without motion blur.

In conclusion, six images of the particle distribution were synchronously recorded at the first laser pulse time using four Mie scattering and two luminescence imaging

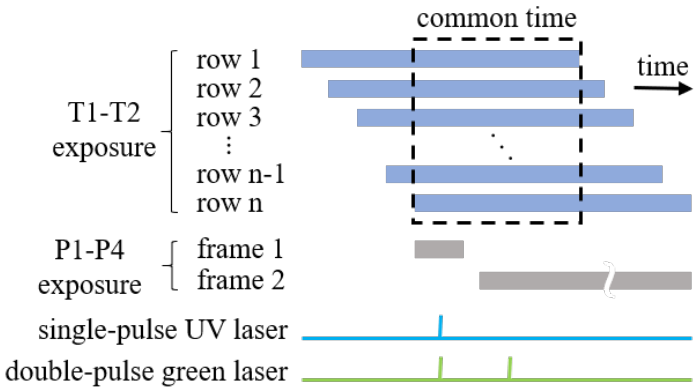

Figure 6.27: Schematic showing relative timing of camera exposures and laser light pulses. Double-frame exposures of cameras P1 to P4 were synchronised with the green laser pulses, and the common exposure of all sensor rows of cameras T1 and T2 were in sync with the UV laser pulse. Adapted from Stelter et al. 2023 (CC-BY 4.0).

cameras. At the second laser pulse time, another Mie scattering image quartet was recorded. Both image sets together form a single-shot measurement of the particle velocity and temperature. Owing to the cameras used, a measurement frequency of 5 Hz was the maximum possible, although this could, in principle, be increased to the megahertz range if faster cameras and sufficiently powerful lasers were available as explored in the outlook (chapter 9).

6.1.5 Joined camera calibration

To enable the merging of temperature and velocity information contributed by two imaging subsystems, all cameras must be mapped to the same 3D coordinate system by deriving suitable camera models (cf. section 4.1). As introduced in section 4.1.2, these can be obtained from a process called camera calibration relying on calibration target plates. By placing these plates at different locations within the field of view of all cameras and simultaneously recording images of it with all six cameras, pinhole camera calibration models (cf. section 4.1.1) can be computed. In the following, the manufacturing of a calibration target, its illumination, and the process suitable for joined calibration of Mie scattering and luminescence imaging

cameras is described. After these prerequisites, the most suitable camera calibration model is identified.

Target manufacturing

The physical design of the calibration target results from the task of presenting well-defined points at precise positions to the cameras to facilitate their calibration. These points must be easily captured automatically. One way to achieve this is to print a regular pattern of calibration marks with high contrast in a 2D plane. Two different marker patterns were tested for this thesis: a black and white chessboard pattern (cf. fig. 6.15 on page 82) and a dot pattern (cf. fig. 6.21 on page 90). While the chessboard worked well, using dots proved to be advantageous due to the robust detection of dots' centres of gravity even if blur deteriorates the edge contrast between dot and background, if the target was imaged slightly out of focus. For all 3D measurements presented in this thesis, a dot target pattern with 2 mm dots on a $5 \times 5\,\mathrm{mm}^2$ grid was used, as shown below in fig. 6.28b.

To provide target visibility in the UV spectral region, which was necessary to record calibration target images with the UV channel luminescence imaging camera (387-11 nm filter channel), paper was chosen as the front-facing material of the target as it exhibits a strong luminescence emission between 360 and 480 nm (FWHM) under UV excitation (Olmstead et al. 1993; Gong et al. 2013). Using paper as the target material also allowed for uncomplicated in-house production of the target. To ensure that the target marks were printed at accurate positions and true to scale, a custom MATLAB script was created to produce PDF files of the target patterns adapted to the printer resolution of 1200 dots per inch. The laser printer used for target printing was characterised, and the printed target patterns were measured for quality control. In addition to the printer's accuracy, the finished target must be rigid to prevent the target marks from moving during or between individual target image recordings. To achieve this, a steel block of 25 mm thickness with a precision milled front surface was used as the substrate for the paper target. The paper was glued to the steel block using double-sided adhesive tape, producing a robust target with calibration marks in a well-defined 2D plane. To allow for

precise positioning of the calibration target, it was mounted on top of a micrometer translation stage.

Target illumination

In conventional PIV and PTV measurements based on particle Mie scattering recordings in the visible light spectrum, it is most common to use identical cameras and lenses for all views. In these cases, the calibration of the cameras is straightforward, as standard white light sources can be used to illuminate the target surface and images are taken using all cameras. In the present concept, however, two different imaging systems were used. For the Mie scattering subsystem, conventional white light sources could be used to illuminate the physical calibration target and to record high-SNR images. However, this was not possible for the luminescence imaging subsystem, specifically for the camera equipped with a narrow bandpass filter in the UV region (387-11 nm). Commonly available white light sources (LED, halogens, and fluorescent lamps) emit little or no light in the transmission band of this filter. Hence, the SNR of the calibration target recordings would be low even when using the longest camera exposure possible (2 s for the present sCMOS cameras). As any movement of the cameras between calibration target and particle image recording would deteriorate or even invalidate the camera calibration models, it was not possible to remove the spectral filters mounted on the luminescence imaging cameras. Instead, the target had to be either illuminated within the transmission band of the UV bandpass filter or it had to emit light within this spectral range itself. Here, the fluorescent emission of paper following excitation within the UV spectral range was utilised (Olmstead et al. 1993; Gong et al. 2013). While a white LED light was used to illuminate the calibration target for the Mie scattering and visible-range luminescence imaging cameras, a pencil-style mercury vapour lamp (Newport 6035) was used to excite fluorescence from the paper surface of the calibration target for the UV camera. The mercury vapour lamp was chosen for its high-intensity UV emissions, see fig. 6.28, and its ability to illuminate a large area with sufficient homogeneity. The resulting paper fluorescence could be imaged by the UV-facing camera to create high-SNR images, as shown in fig. 6.28b for camera calibration.

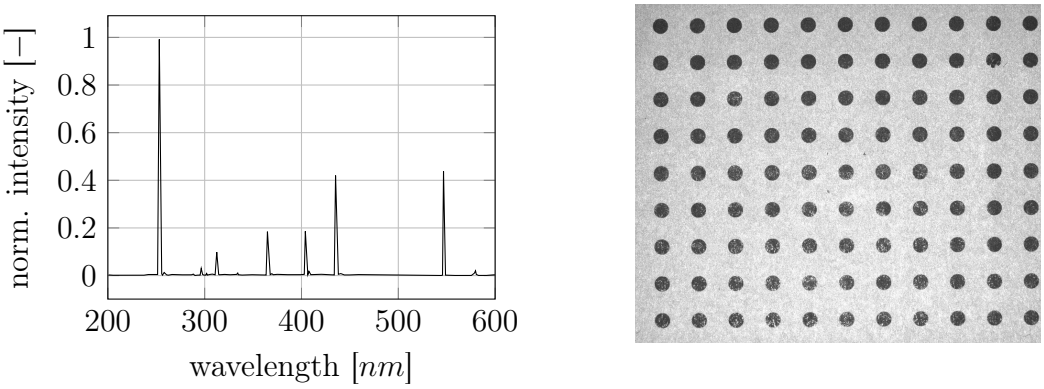

(a) (b)

Figure 6.28: Emission spectra of mercury vapour calibration lamp (a) as provided by the manufacturer (Newport Corporation 2025), used to illuminate the target for imaging with the sCMOS camera fitted with a 387-11 nm filter (b).

Calibration procedure

To record the calibration target images, the target was placed within the measurement volume centred above the jet nozzle exit. Its front surface, showing the calibration marks, was aligned parallel to the laser beams, and its micrometer stage axis was aligned with the optical axis of camera T2. The P-camera apertures were maintained at their f-number settings used for particle image recording($f/16$ and $f/22$). For the T-cameras, the lens apertures were kept at $f/1.4$ but their external apertures were set to diameters of 7 mm and 14 mm for the cameras with 425-50 nm and 387-11 nm filters, respectively. This ensured a sufficient DoF and SNR in the camera images during calibration. The white LED light and the mercury vapour lamp were started and a warm-up period of 5 min was allowed for mercury emissions to stabilise. The target was then moved 8 mm closer to the cameras by adjusting the micrometer stage. Images of the calibration target were recorded with all cameras. Then, the target was moved 2 mm away from the cameras using a micrometre translation stage and images of it were recorded again. This procedure was repeated until images of the calibration target were recorded in 2 mm intervals along the world coordinate system z-axis between -8 and 8 mm. These recordings were the input for computing a pinhole camera-based model of each camera.

Recalling the susceptibility of sCMOS cameras to an image memory effect after exposure to a constant high intensity scene (see fig. 6.15 on page 82), resetting their image sensors was necessary before proceeding with particle image recordings. Therefore, the mercury vapour lamp and luminescence cameras were turned off, and their external apertures opened completely. A white piece of paper was placed in front of the calibration target to reflect the white LED light homogeneously into the T-cameras and reset their sensors (cf. fig. 6.15). After 5 min, the LED light was turned off, the T-cameras turned on again and dark images were recorded using the 35 ms exposure as for subsequent particle image recordings. Successful sensor reset was ensured by evaluating these dark images using a custom MATLAB script before continuing with the measurements.

Camera calibration model selection

To determine if a simple pinhole camera model was sufficient for the present measurement concept or if the Scheimpflug camera model was beneficial (see section 4.1.1 for model details), the models were compared using projection and back-projection errors. The projection error quantifies the accuracy of the 3D world to 2D image mappings facilitated by a camera model by comparing target marker image positions with the projections of corresponding 3D target markers. In contrast, the back-projection error is a measure of the inaccuracy when projecting points from the 2D image coordinate system to the 3D world coordinate system by comparing known 3D marker locations with the back-projected positions within the same world coordinate system $z-$plane (Hartley et al. 2019). Both camera models were calculated using custom solver implementations for either Tsai 1987 and Calluaud et al. 2004 or Cornic et al. 2016 in MATLAB. The same calibration target images were used as inputs.

As tomographic reconstruction of particle locations was based on the P-camera Mie scattering recordings being projected into 3D space, a low back-projection error was of great significance for them. As shown in fig. 6.29a, the Scheimpflug model lead to an error that was on average 27.5 % lower than that of the simple pinhole model. For T-cameras, a low projection error was more important, as reconstructed 3D particle positions were projected into their image space to associate them with

the particle luminescence emissions for thermometry. Here, the obtained mean errors were on average 31 % lower when the Scheimpflug model was used instead of the simple pinhole model.

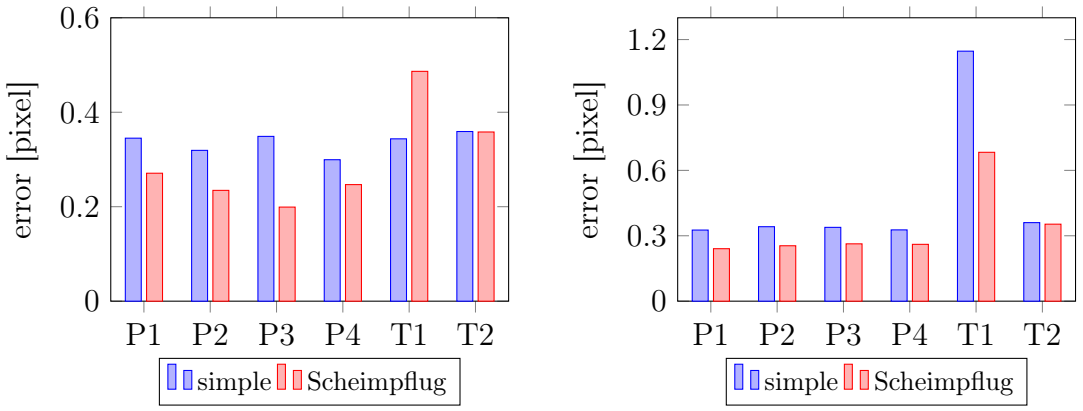

(a) back-projection error (b) projection error

Figure 6.29: Back-projection and projection error for all cameras depending on the target marker image detection and camera calibration algorithm.

Following the error estimations, the Scheimpflug camera model was used for all measurements presented in this chapter. The absolute calibration errors were sufficiently low when working with low particle image seeding densities below 0.01 ppp. More advanced iterative camera calibration algorithms (i.e., volume self-calibration) and their effects on the calibration accuracy and 3D measurement results are explored in section 8.2.

6.2 Mie scattering image data processing

Using the imaging system described above (section 6.1.2), Mie scattering double-frame images of the particle distribution were simultaneously recorded from four different views, using a double-pulse 532 nm laser as light source. After pre-processing these images, 3D particle positions were computed from each double-frame image quartet recorded at the first and second laser pulse times. For this reconstruction, camera models obtained from calibration (section 6.1.5) were used with a tomographic reconstruction algorithm (cf. section 4.2.1) to create one

reconstruction volume per laser pulse time. Finally, 3D velocities were calculated by tracking the reconstructed particles from the first to second frame volumes in the corresponding volume pairs (cf. section 4.3.2). An overview of the workflow for Mie scattering image data processing is provided in fig. 6.30.

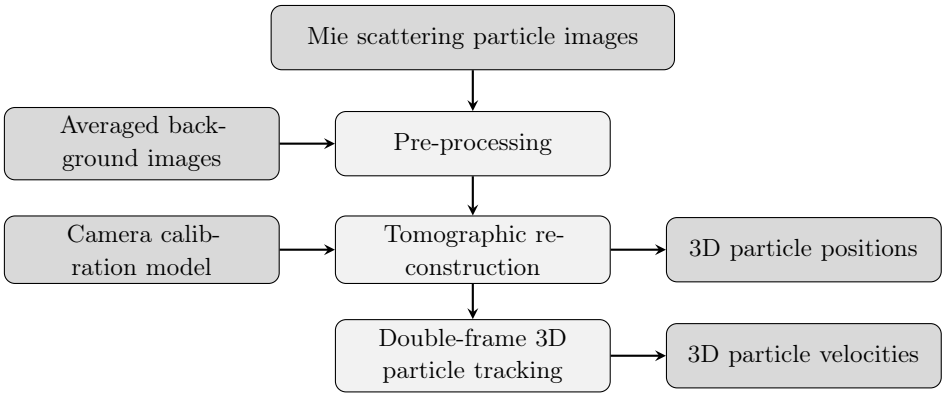

Figure 6.30: Mie scattering image data processing scheme.

6.2.1 Camera image pre-processing

Raw Mie scattering camera images of particles distributed within a flow are subject to noise and a constant image background offset. This offset is added by the camera firmware to prevent negative pixel intensity values from being read from the image sensor owing to noise. Additional background noise may arise from illuminated structures or reflections within the field of view of the camera. Any background signal should be removed prior to tomographic particle reconstruction, as it would result in reconstruction artefacts or prevent the successful reconstruction of actual particles imaged close by.

To remove constant background signals from the camera images, an average background image was subtracted from it pixel by pixel. To acquire this average background image, 100 double-frame image pairs were recorded with the same camera and laser settings as for particle image recordings, but no particles were seeded into the flow. An example of an averaged background image is shown in fig. 6.31a. It was subtracted from raw particle images (fig. 6.31b) to obtain background subtracted versions as plotted in fig. 6.31c. A constant image offset

of approximately 100 counts present prior to background subtraction was removed using this subtraction. Remaining jet nozzle reflections close to the lower border of the cropped camera image were removed by spatial masking, where pixel intensities outside a defined region of interest were set to zero. To retain only the brightest particle images as candidates for the following tomographic reconstruction, a minimum intensity threshold was applied to the camera images. Thereby, all pixel intensities below this threshold (for example 0 counts) were zeroed.

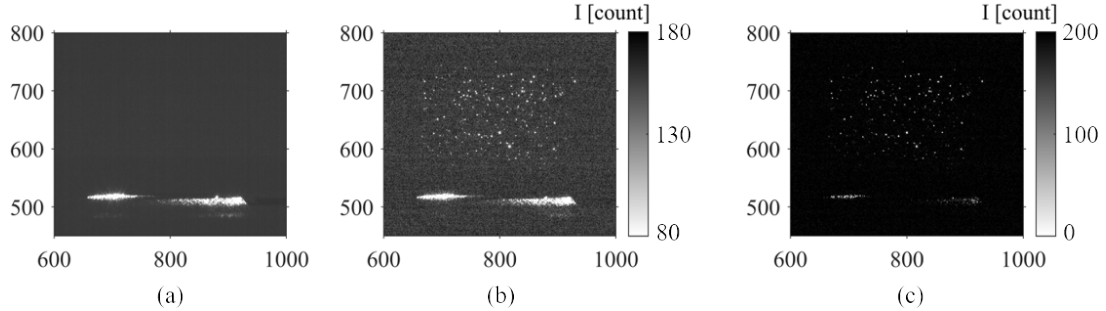

Figure 6.31: Background subtraction from Mie scattering camera images. An average background image (a) is subtracted from raw Mie scattering camera images (b) to remove pixel intensity offsets (c). (a) and (b) share the same colour bar.

To remove higher frequency noise in the camera images, a 2D Gaussian smoothing filter was applied with a square kernel and a standard deviation of 0.5. Then, each camera image was individually normalised to scale pixel intensities between zero and unity. This gave all cameras equal weight in the following reconstruction process even if imaged particle intensities varied. These pre-processed particle images were then passed to the tomographic reconstruction algorithm below.

6.2.2 Tomographic particle position reconstruction

Following the general introduction to tomographic reconstruction in section 4.2.1, the specific implementation and potential challenges related to its application in non-isothermal gas flows are discussed.

Optical tomography in non-isothermal gas flows

Multiple unobstructed views of the particles within the reconstruction volume are required to obtain particle positions from optical tomography (cf. section 4.2.1). Additionally, the properties of the optical path between image sensors and individual particles must be time-invariant. Therefore, the refractive index of the medium through which images are taken is important. While static refractive index changes can be accounted for in the camera calibration, this is not possible if the refractive index within the measurement volume changes over time. As the refractive index of a gas changes with temperature (and pressure), non-isothermal flows can provide challenging environments for tomographic reconstruction, as expressed by the following equation from Shaheen et al. 2023

$$n - 1 = (n_0 - 1)\frac{pT_0}{p_0 T}. \tag{6.9}$$

Here, n is the refractive index at temperature T and pressure p relative to a known refractive index n_0 at reference conditions T_0 and p_0. As only far-subsonic free streams were investigated in this thesis, there was no significant pressure difference within the flow. However, temperature differences could lead to difficulties in the reconstruction process if the light rays were deflected strong enough between particles and image sensors. To assess this, the change in the refractive index of air between 296 K ($n_0 = 1.000273$, Voronin et al. 2017) and 453 K was calculated as the highest temperature investigated. As it is below 0.1 %, a strong deflection of the light rays was not expected. To verify this conclusion a practical test was run with the setup shown in fig. 6.32, where a USAF 1951 1X target was placed 8.5 mm behind the jet nozzle within the field of view of camera P4.

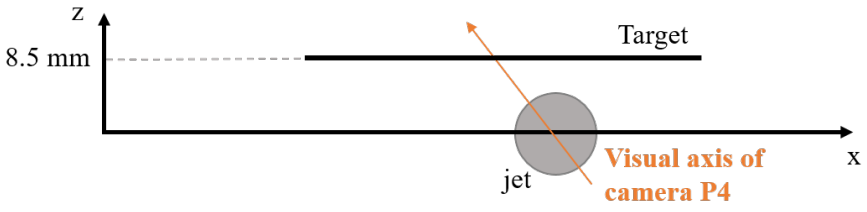

Figure 6.32: Setup sketch for accessing the impact of refractive index change with temperature in top-down view.

If the refractive index of the gas between camera and target changed, the imaged position of target marks would change. The USAF target was chosen for this test as the small-scale patterns on its surface could be monitored for any displacement. While the actual measurement volume in later demonstration experiments ended at $z = 4\,\mathrm{mm}$, the target was placed at more than double the distance from the jet centre to amplify any perceived displacement of target marks for aided detection. Camera P4 was focused on the target, and images of the target were recorded without any gas flow to provide a baseline reference. Images of the target were then captured with a jet of air emerging from the nozzle at four different temperatures, ranging from room temperature to 563 K at a Reynolds number of 4600.

After image recording, a cross-correlation algorithm was applied to the recordings of different flow conditions to quantify any shift in the image position of target features. Comparing the target images with and without gas flow at room temperature, as expected no image displacement was found. To access the influence of a non-isothermal gas flow, target recordings with room-temperature gas flow versus 383 K, 473 K, and 563 K were processed. The cross-correlation algorithm revealed average displacements of target images from 0.12 pixel over 0.17 pixel to finally 0.21 pixel for the investigated temperatures. As shown in vector fields averaged over 25 single-shots each in fig. 6.33, the direction of image displacement was consistent from fig. 6.33a to c with increasing temperature. In addition, the displacement within each frame was approximately constant. The standard deviation of displacements computed from single-shots was 0.018 pixels on average, indicating no strong differences in refractive index over time within the observed region.

While the displacement of target images as a result of temperature-induced refractive index changes in air was measurable,its magnitude - a small fraction of a pixel - was exaggerated in this test, as noted above. Hence, the practical effect on optical tomography results produced within this thesis was negligible. In the following, the implemented reconstruction algorithm and its application to particle Mie scattering recordings are discussed.

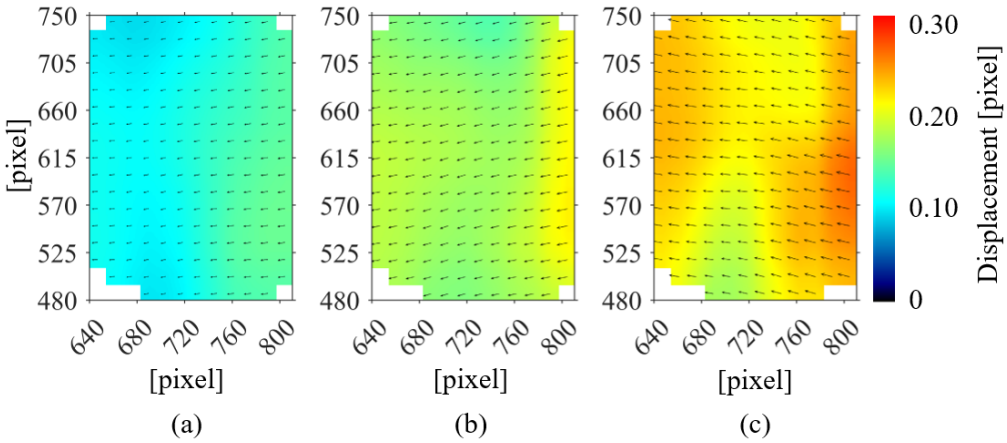

Figure 6.33: Average cross-correlation results for target images recorded through gas jets at (a) 383 K, (b) 473 K, and (c) 563 K versus room temperature. Background color indicates displacement magnitude.

Algorithm implementation and application

For tomographic reconstruction (cf. section 4.2.1) of 3D particle positions from Mie scattering particle images, a custom implementation of the MinLOS algorithm proposed by Putze et al. 2008 and H.-G. Maas et al. 2009 was used. This computationally efficient tomographic reconstruction algorithm showed good performance on synthetic and real experimental data up to particle seeding densities of 0.02 ppp (Michaelis et al. 2010). To prepare the reconstruction domain, the measurement volume above the nozzle exit (fig. 6.34a) was discretised into 13 million cubic voxels of 41 µm edge length, as determined from the camera pixel size of 7.4 µm and an image magnification of 0.18.

Each voxel was assigned an initial intensity of one that was minimised using the MinLOS algorithm using the Mie scattering camera images. For each camera P1-4, the mapping function resulting from camera calibration was loaded and the centre coordinates of each voxel were projected into the camera image space. Its current intensity was compared with the Gaussian weighted intensity of the $3 \times 3\,\text{pixel}^2$ neighbourhood in the camera images (Thomas et al. 2014). The voxel intensity was then updated with the minimum of its current value and the detected image intensity. After cycling through all voxels in all camera views for a given double-frame single-shot recording, the reconstruction domain was filled with many

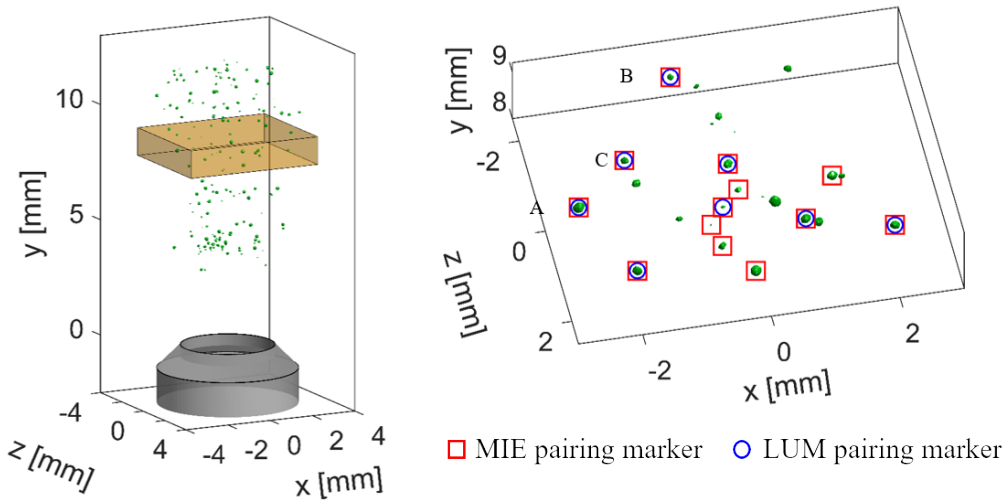

(a) (b)

Figure 6.34: Particle intensities reconstructed in a gas jet are shown above a nozzle representation as green isosurfaces in (a) and (b). The sub-volume indicated as an orange box in (a) is shown in detail in (b). Adapted from Stelter et al. 2023 (CC-BY 4.0).

voxels either at near zero intensity, representing void space, or non-zero intensity, where either a particle was recognised by all cameras or noise survived the preceding filtering steps.

To make the reconstruction process more robust against interference from image noise, the recorded camera images were idealised before using them for reconstruction. This was achieved by replacing raw particle images with uniform intensity blobs as follows. Regional intensity maxima were detected in the pre-processed (section 6.2.1) Mie scattering camera images as patches of 8-connected pixels with higher intensity than their neighbours. The centre of gravity of these pixel patches was used as initial guess for individual particle image centres. To determine their location with sub-pixel precision, an $11 \times 11\,\text{pixel}^2$ window was extracted from the pre-processed camera image centred on the guessed position. A generalised 2D Gaussian function was fitted to these windows to model the spatial intensity distribution $I(x, y)$. The fit function shown in eq. 6.10 accounts for the elliptical shape of these particle images and rotation against the pixel axes (Stelter et al. 2023).

$$
\begin{aligned}
I(x,y) = & I_0 \exp\Bigg(-\Big(\frac{\cos^2\theta}{2\sigma_x^2} + \frac{\sin^2\theta}{2\sigma_y^2}\Big)(x-x_0)^2 \\
& + \Big(\frac{\sin 2\theta}{2\sigma_x^2} - \frac{\sin 2\theta}{2\sigma_y^2}\Big)(x-x_0)(y-y_0) \\
& - \Big(\frac{\sin^2\theta}{2\sigma_x^2} + \frac{\cos^2\theta}{2\sigma_y^2}\Big)(y-y_0)^2 \Bigg)
\end{aligned}
\tag{6.10}
$$

From the fit result, the peak positions x_0 and y_0 were extracted and used to correct the initial centre-of-gravity image position x and y. Further fit parameters include the rotation against the pixel axes Θ, the width of the fit along its major and minor axes σ_x and σ_y, and the peak intensity I_0. The refined particle image locations were treated as particle candidates, as indicated by green rectangles in the Mie scattering camera images of the reconstruction volume shown in fig. 6.35. Then, uniform artificial particle images were created at their sub-pixel position. These particle images had uniform peak intensity and an intensity profile described by a 2D Gaussian distribution with 3 pixel diameter. Using a Gaussian function to model their image intensity distribution is suitable as these cameras recorded diffraction-limited particle images, where the intensity distribution follows an Airy disk distribution.

To prepare extraction of 3D particle positions from the reconstruction domain filled with intensity values, each xy-plane slice was filtered using a 2D Gaussian smoothing filter. This reduced noise in the volume while also accounting for the anisotropic shape of reconstructed particles (elongated along z-axis, cf. Scarano 2013). To separate noise from reconstructed particles, an intensity threshold was applied to the smoothed reconstruction domain, and any voxel intensity below it was zeroed. The 3D position of individual particles was then extracted with sub-voxel accuracy as weighted centroid of 26-connected voxel regions (green isosurfaces in fig. 6.34).

Once the particle positions were extracted from the tomographic reconstruction results, they were associated with particle image candidates in 2D camera image space of cameras P1-4. To facilitate this 3D to 2D mapping, the mapping functions

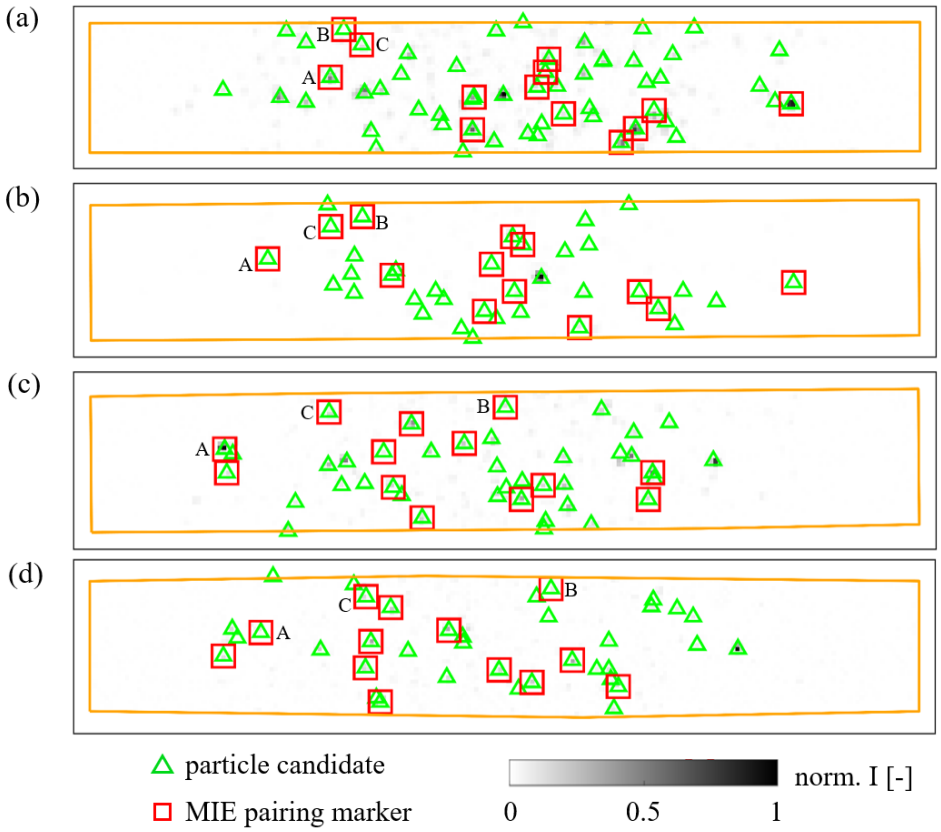

Figure 6.35: Mie scattering images of the sub-volume shown in fig. 6.34, whose projected limits are drawn in orange. Green markers indicate particle image candidates, red markers indicate successful pairing with reconstructed particles. Adapted from Stelter et al. 2023 (CC-BY 4.0).

from camera calibration were used again to project obtained 3D particle positions to each camera's image space. For each camera, the Euclidean distance between the projected position and particle image candidates (intensity maxima) was evaluated. Pairing between both was considered successful if the distance was below 2 pixels, as indicated by the red square marks in fig. 6.35. The pairing distance accounts for inaccuracies in the camera models obtained from the calibration and position reconstruction schemes. If multiple particle image candidates were found within this threshold, the reconstructed particle position was discarded due to ambiguity. At low particle seeding densities, the probability for this is generally low as the average distance between projected particle positions and paired particle image centres was 0.77 pixels, while the average distance between individual particle

image candidates within the same camera image was 7.58 pixels. Reconstructed particles were retained for further processing only if pairing to particle images in all Mie scattering cameras was successful. Such a correspondence is shown for three particles labelled A, B, and C in fig. 6.35 and fig. 6.34.

In conclusion, two particle-filled volumes were reconstructed for each double-frame Mie scattering image recording, originating from the four first- and second-frame recordings acquired during the first and second green laser pulse, respectively. Luminescence camera images were not included in the reconstruction process as only single-frame recordings were available, and the particle position-dependent image blur spot diameter would add extra complexity to the reconstruction scheme. It should be noted that this blur spot diameter encodes additional information on particle in-depth positions and could be used by more advanced algorithms, as presented in section 8.3 and section 8.4.

6.2.3 Particle tracking

The 3D velocity of individual particles was computed using a custom double-frame particle tracking algorithm using the volume pairs reconstructed in the preceding section 6.2.2 as input. To obtain the velocities of the particles, their 3D displacement between the first and second frame volumes was evaluated and divided by the inter-pulse time between the first and second green laser pulses. While the general background for particle tracking velocimetry (PTV) was provided in section 4.3.2, the specific implementation used in the present work is described in this subsection.

An initial estimate for individual particle displacements was obtained by performing a multi-pass cross-correlation on ensemble volume pairs (Meinhart et al. 2000; Kováts et al. 2020). This yielded the time-averaged velocity field of the flow. Individual particle displacements were then computed by shifting each particle from a first frame volume by the local guess from ensemble cross-correlation, before searching for the nearest neighbour around this predicted location in the second-frame volume. If the Euclidean distance between both was below 2 voxels, pairing was established. If more than one candidate was found within this distance, the

particle was discarded to minimise the likelihood of false pairing events due to ambiguity. This naive approach for double-frame PTV was enabled by the dominant streamwise velocity component of the free jet and low particle seeding density in the present measurements. This is supported by the particle spacing displacement ratio p_{sd} introduced by Malik et al. 1993

$$p_{sd} = \frac{\Delta_o}{u\Delta t}. \tag{6.11}$$

This relates the mean spacing between particles Δ_o to the mean displacement of particles defined by their velocity u and the time between both laser pulses or double-frame images of the particles Δt. For the measurements shown within this thesis, the inter-particle distance regularly exceeded 500 µm compared to bulk velocities on the order of 30 m/s and a time delay between both green laser pulses of 12 µs. Hence, p_{sd} exceeded unity for the presented measurements, enabling tracking by relatively easy means without sacrificing accuracy (Barker et al. 2011).

As a result, the 3D velocities of individual reconstructed particles were available. In section 8.3, a more sophisticated reconstruction algorithm was introduced to cope with higher particle seeding densities during reconstruction, and section 8.4 added an iterative particle tracking algorithm. Below, the particle velocities are augmented by corresponding particle temperatures by evaluating luminescence imaging camera recordings to obtain joined temperature and velocity measurements.

6.3 Phosphor luminescence image data processing

Once 3D particle positions and velocities were computed, the luminescence images of the same tracer particles were processed to obtain their LIRs. Using calibration, these were converted to particle temperatures. An overview of the processing scheme is shown in fig. 6.36. As for the processing of Mie scattering camera images, this included pre-processing the luminescence camera images (section 6.3.1) using background subtraction. This enabled subsequent particle image detection and localisation (section 6.3.2), mapping with 3D reconstruction results (section 6.3.3), and segmentation of individual particle images from the luminescence camera

recordings (section 6.3.4). Once particles images were segmented from images of both cameras T1 and T2, the imaged signals were integrated. From these intensity values, temperature dependent LIR values were computed, flat field corrected (section 6.4), and finally converted to temperature values using a calibration function (section 6.5).

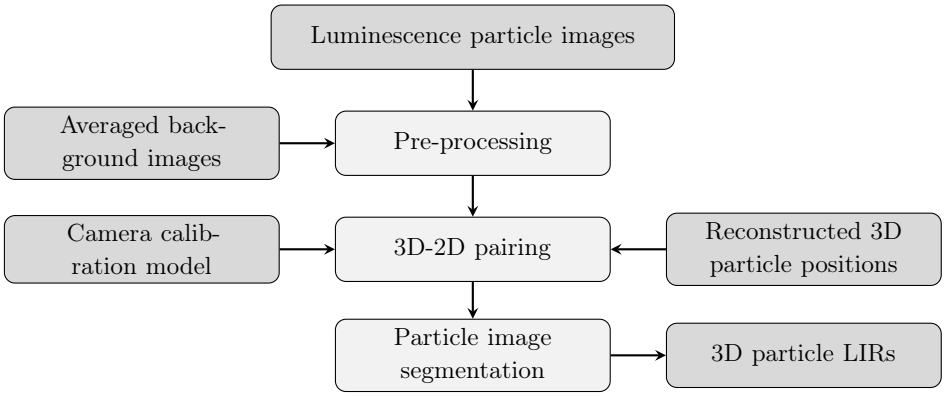

Figure 6.36: Luminescence image data processing scheme. LIRs were converted to temperature using a calibration obtained in section 6.5.

6.3.1 Camera image pre-processing

As for the Mie scattering camera images in section 6.2.1, the raw luminescence images from cameras T1 and T2 had to be pre-processed prior to deeper analysis. This was limited to the subtraction of an average background image to remove constant pixel intensity offsets. No smoothing or image normalisation was applied, as the absolute signal levels are important for a precise evaluation of the luminescence signal imaged per particle.

6.3.2 Particle image detection and localisation

After background subtraction, particle image candidates were detected within the camera images. Three different approaches were tested for this purpose. First, a global threshold was used to binarize the images. Pixels with intensities below the threshold were set to zero, and pixels above the threshold were set to one.

While this was straightforward, individual particle images had a wide variance of peak intensities owing to the particle position-dependent blur in the luminescence recordings. Hence, a global threshold to binarise the images was not suitable as it either detected only in-focus particles with high peak intensities (high threshold value) or it was prone to detect noise as particle image candidates (low threshold value).

Second, a combination of local maxima detection and gradient search algorithm was tested as introduced by Xuan et al. 2023. Local maxima were detected first as pixels with higher intensity than their eight neighbours. Then, isolated high-intensity pixels as generated from noise were detected and removed. Finally, the intensity gradient to neighbouring pixels was calculated to detect the extent of each particle image. Once the gradient dropped below a threshold, the algorithm terminated. As this algorithm relied on intensity differences between neighbouring pixels rather than on absolute intensities, it was insensitive to the inevitable tradeoff faced when using the global intensity threshold described above. However, the algorithm implementation from Xuan et al. 2023 was optimised for particle images without strong image blur. Therefore, it was challenging to detect low-intensity particle images where the total signal was spread over many pixels and the intensity gradients between neighbouring pixels were low.

An algorithm not susceptible to this was found with the *imregionalmax* algorithm implemented in MATLAB. It detects 8-connected pixel patches where pixel intensities are higher than for their neighbours. It was combined with a minimum pixel intensity filter to effectively reject pixels below the noise floor, preventing noisy pixels from being detected as particle image candidates. This combination provided a computationally efficient and reliable detection of individual particle images independent of image blur or absolute particle image peak intensity.

As for the processing of Mie scattering particle images, the position of the centroid pixel of these regional maxima was only used as an initial guess. Particle image positions were computed with sub-pixel accuracy by applying the 2D Gaussian fit introduced in eq. 6.10 to an $11 \times 11\,\text{pixels}^2$ area centred on the guessed position. The fitted peak location was used to correct the initial position guess. Particle image centres detected in this way are plotted as green markers in fig. 6.37, where

luminescence camera images are shown corresponding to the sub-volume plotted above in fig. 6.34b.

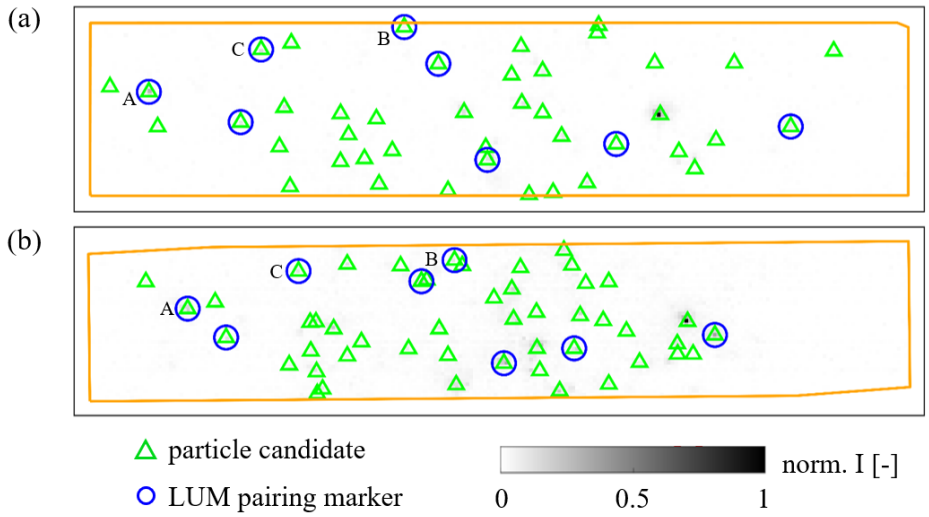

Figure 6.37: Luminescence (LUM) images of cameras T1 (a) and T2 (b) of the sub-volume shown in fig. 6.34b, orange lines denote projected volume limits. Markers indicate particle image candidates and their successful pairing with reconstructed particles. Adapted from Stelter et al. 2023 (CC-BY 4.0).

6.3.3 Pairing with reconstructed particles

To allow a later association of individual particle temperatures with corresponding velocity results, a mapping between reconstructed 3D particle positions from Mie scattering recordings and luminescence particle images had to be established. The process is analogous to the pairing process described above for Mie scattering image data in section 6.2.2. For each single-shot recording, reconstructed 3D particle locations were loaded and projected into the luminescence camera image space using the mapping functions obtained from camera calibration. A maximum Euclidean distance of 3 pixels was allowed between 2D particle candidates and projected positions of reconstructed particles. If an image candidate was found within this distance, pairing was established, as indicated by the blue markers in fig. 6.37. If more than one candidate was found, no pairing was established,

and the particle was discarded from further processing to prevent issues related to ambiguous pairing. For the present data at low seeding density, the average distance for successfully paired particles was 0.94 pixels, while the average distance between individual particle image candidates was much larger at 12.05 pixels. After this step, correspondence between 2D image and 3D object space was established for the luminescence recordings. Only particles where this pairing was successful were kept for further processing.

Comparing fig. 6.35 and fig. 6.37, it is noticed that about twice as many particles were paired for Mie scattering than for luminescence image recordings. This is directly related to a difference of one order of magnitude between scattering and luminescence image signal levels, stemming from the scattering and luminescence cross-sections of the particles. This made it much more difficult to detect particles in luminescence camera images, which was further complicated by stronger particle position-dependent blur and aberrations.

6.3.4 Particle image segmentation and signal integration

To obtain temperature information from individual particles using the present approach of phosphor thermometry with spectral LIR, it was necessary to evaluate the imaged signal of every particle in two different spectral regions. Here, two cameras, T1 and T2, were used to record images of the same particles in two distinct spectral regions, facilitated by filters mounted on the lenses of these cameras. After identifying the centre of an individual particle image in the camera images and associating it with the 3D particle obtained in the previous subsection, the imaged luminescence signal of each particle had to be found. This was performed using image segmentation, where the pixels belonging to an individual particle image were identified. Different segmentation approaches were tested, including naive square and circular pixel masks as well as more elaborate fit-based masks.

First, two naive masks were considered. The most straightforward implementation of a pixel mask was selecting an $n \times n$ pixel^2 region around the particle image centre location. However, it is intuitive that the shape of the PSF of a particle imaged close to the diffraction limit will not be square but rather circular. Hence, this mask

did not provide accurate segmentation results. Instead, a circular mask with a fixed size was implemented initially. While allowing segmentation of the particle images, its fixed size was not compatible with the particle position-dependent blur spot diameter. An adaptive mask was needed to deal with particle images of variable diameters.

As the intensity distribution of macroscopic images of microscopic particles can be modelled using a 2D Gaussian distribution (Xuan 2023; Xuan et al. 2023), it can be used as basis for a segmentation algorithm. The implementation was straightforward. Each particle image was fitted with the flexible 2D general Gaussian function introduced above in eq. 6.10. The size parameters σ_x and σ_y adapt automatically to the size of the luminescence image while allowing for an elliptical shape of the image, and the rotation of the image against the image pixel axes are also accounted for by the angle θ. The pixels that comprise the individual particle images were selected by evaluating the fit and taking all pixels where the fit was above 5 % of its maximum value I_0. Masks resulting from this approach are shown below in fig. 6.38.

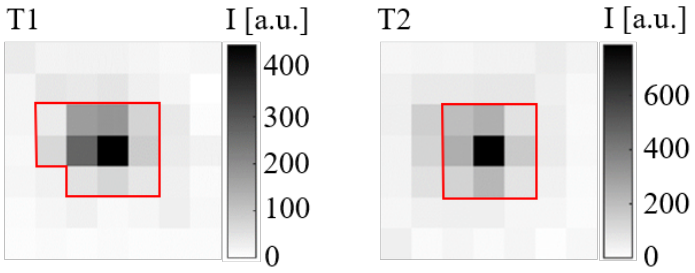

Figure 6.38: Particle luminescence image pair recorded with cameras T1 and T2. Red bounding box marks adaptive mask from Gaussian fit. Adapted from Stelter et al. 2023 (CC-BY 4.0).

To prevent bad fit results and pairing errors from impacting further processing, two filters were implemented based on the fit results. The first filter evaluated the coefficient of determination R^2 of the Gaussian fit as a measure of the goodness of the fit (T. Zhang 2025). Assuming I_i as the imaged intensity of pixel i and $\hat{I}_i$ as

its intensity predicted by the fit, the R^2 of the fit is calculated as

$$R^2 = 1 - \frac{\sum_{i=1}^{n}(I_i - \hat{I}_i)^2}{\sum_{i=1}^{n}(I_i - \bar{I})^2} \tag{6.12}$$

where $\bar{I}$ is the mean intensity of n observed pixel intensity values

$$\bar{I} = \frac{1}{n}\sum_{i=1}^{n} I_i. \tag{6.13}$$

The coefficient of determination takes values between 0 and 1, where 1 indicates a perfect prediction of measured data by the fit. The particle is retained only if the R^2 exceeds a set threshold. This was aimed at detecting very poor fit results by selecting rather low threshold of for example 0.5. The second filter compares the average spread of the particle image along the mayor and minor axis of the fit result $\bar{\sigma} = (\sigma_x + \sigma_y)/2$ between cameras T1 and T2. For the same physical particle, the imaged particle size in both cameras should be similar as the imaging system and setup (camera, lens, magnification) were virtually identical. Hence, if a particle appeared small in one camera and large in the other camera, false pairing between the object and image space might have occurred. This would result in an incorrect LIR, as the imaged luminescence signals in the paired particle images would not correspond to each other. Particles that did not fulfil any of the filter criteria were discarded.

For all surviving particles, the imaged luminescence signal was found by summing the intensity of all masked pixels. The LIR was then computed for individual particles by dividing the summed signal in one spectral channel by the equivalent signal in the second spectral channel. Here, the signal recorded by camera T2 was divided by the signal imaged by camera T1, corresponding to 425-50 nm and 387-11 nm spectral channels, respectively. Before converting the LIRs to temperature, a flat field correction was applied.

6.4 2D flat field correction

Before proceeding with the conversion of the computed LIRs to temperature, a flat field correction (FFC) was applied. It is a standard measure in 2D phosphor thermometry measurements (cf. section 3.3.4 in Abram et al. 2018) and should be adapted for 3D measurements. Recalling the cross-dependency of ZnO's luminescence emission spectrum on the excitation laser fluence (section 5.2) and the beam profiles of the UV laser (figs. 6.6 to 6.7 on pages 69 to 70), a FFC was mandatory in the present work. Formally, the dependency of the LIR φ on the particle temperature T and excitation laser fluence F at particle locations x, y, z in the measurement volume can be expressed as

$$\varphi = \varphi(x, y, z, T, F). \tag{6.14}$$

Following Abram et al. 2015, it is possible to separate the individual dependencies according to

$$\varphi(x, y, z, T, F) = \alpha(x, y, z)\beta(T)\gamma(F(x, y, z)), \tag{6.15}$$

where α denotes the spatial collection non-uniformity owing to angular effects for the interference filters mounted on the luminescence imaging cameras, β describes the temperature dependency of the LIR, and γ denotes the local fluence cross-dependency of the LIR. While the temperature is location dependent, this is not mentioned explicitly in the equation for better legibility.

It is then possible to correct for the influence of laser fluence variations by normalising each measured LIR with a LIR value obtained under isothermal conditions at a reference temperature, which includes a correction for α and γ

$$\varphi_n = \frac{\varphi(x, y, z, T, F)}{\varphi(x, y, z, T_{ref}, F)} = \frac{\alpha(x, y, z)\beta(T)\gamma(F(x, y, z))}{\alpha(x, y, z)\beta(T_{ref})\gamma(F(x, y, z))} = \frac{\beta(T)}{\beta(T_{ref})}. \tag{6.16}$$

Because this normalised LIR is only dependent on temperature, a single calibration curve can be used to convert it to temperature without knowing the absolute laser fluence at every point in the measurement volume (Abram et al. 2015).

Obtaining a 3D correction map required dedicated measurements in an isothermal

flow. The laser fluence and imaging conditions must match the measurements that should be corrected. Because the particle seeding density was low and a collimated light source (laser) was used for luminescence excitation, the laser fluence did not change along the laser propagation direction (world coordinate system x-axis). As the luminescence imaging cameras were also far from the measurement volume compared to its width in the camera field of view, the angle of collection was small (approximately 1°). Hence, the angular non-uniformities of the interference filter transmission wavelengths were treated as negligible. This eliminated *alpha* and the x-location dependency of the FFC. This allowed a simplification of the FFC process, as only the fluence inhomogeneities within the laser beam cross-section had to be corrected using a 2D correction map

$$\varphi(x, y, z, T_{ref}, F) \approx \varphi(y, z, T_{ref}, F). \tag{6.17}$$

Such a map is shown in fig. 6.39a, created by combining 3D LIR results from several single-shot measurements and collapsing them along the x-axis. The scattered data was binned to 29 × 15 rectangular windows in the yz-plane, each representing 300 × 450 µm^2 of object space and starting 4 mm above the jet nozzle exit. Every window was assigned the average LIR of all contained particles after values deviating more than 3σ from the respective average ratio were removed, rejecting 1.5 % of 2900 available samples. Windows with less than five measurements were removed. The raw correction value map was interpolated using the *smoothn* algorithm (Garcia 2010b; Garcia 2010a) to create a continuous map, as shown in fig. 6.39b.

This map reflects the laser fluence inhomogeneity within the beam cross-section and provides a correction value for arbitrary particle positions. This was used to correct the data presented in section 6.5 and chapter 7.

6.5 In-situ phosphor thermometry calibration

To convert flat field corrected LIRs to temperatures, a calibration function was required. It was obtained from 3D *in situ* calibration measurements performed in a heated jet of nitrogen at four known jet nozzle exit temperatures ranging from 295 K

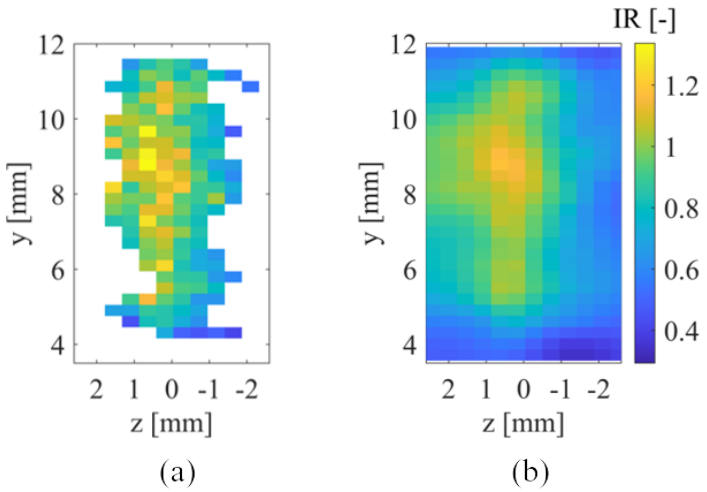

Figure 6.39: Raw (a) and interpolated (b) correction maps computed from 3D measurements in an isothermal flow. Adapted from Stelter et al. 2023 (CC-BY 4.0).

to 438 K with the inline camera setup from fig. 6.2 on page 62. A jet nozzle with a diameter of 9.5 mm was used to create a comparably large potential core region, where quasi-isothermal conditions could be achieved. The jet flow was surrounded by a co-flow at ambient temperature of 300 K. Only the jet flow was seeded with ZnO particles, and 3D LIR maps were computed from combined Mie scattering and luminescence camera images using the processing described in sections 6.2 to 6.4. To excite phosphor luminescence from seeded ZnO particles, a 10 mm diameter beam of a 266 nm laser at 130 mJ/cm^2 was used. To ensure that measurements were taken in the potential core region of the jet, the measurement volume was started close to the jet nozzle exit at a distance of only 2 mm. The radial extent of the quasi-isothermal region in the jet was assessed from a temperature profile measured with a 0.5 mm type K thermocouple. It was moved through the nozzle cross-section using a micrometer translation stage at a distance of 4 mm along the volume x-axis (laser propagation direction). The flow was set to a nozzle exit temperature of 383 K, and the Reynolds number was 4600 for the 3D calibration measurements. The resulting temperature profile of the rotationally symmetric flow is shown in fig. 6.40. Within a radius of 2 mm around the jet centre, the measured temperature differs by less than 1 % from the set nozzle exit temperature. Calibration data were sampled from this region.

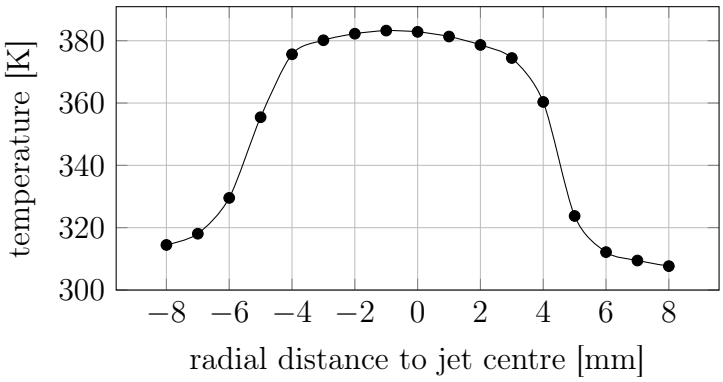

Figure 6.40: Temperature profile of calibration jet at set nozzle exit temperature of 383 K measured using a 0.5 mm thermocouple 4 mm above the nozzle.

The gas flow heater was a metal pipe wrapped with a flexible heating wrap. This heating wrap was controlled using a PID controller (Fuji Electric PXR4) with the heater temperature as the control variable. It was measured using a 0.5 mm type-K thermocouple at the interface between outer pipe wall and heating wrap close to the nozzle exit. Owing to this design, the pipe wall temperature exceeded the gas flow temperature during heated operation. Hence, the gas flow temperatures measured using another 0.5 mm thermocouple at the nozzle exit could be biased by heat radiation of the hot pipe walls. This would result in an erroneous temperature calibration of the heater and phosphor thermometry. To quantify the influence of radiation, an estimation based on an equilibrium approach for heat transfer to the thermocouple through convection from the gas and radiation from the tube walls was performed. Convective heat transfer was solved using the Churchill-Bernstein equation (Churchill et al. 1977). For radiation, it was assumed that the temperature at the inner and outer pipe walls were identical for this thin-walled steel pipe. This provided the worst-case estimate of the radiative heat transfer. The resulting bias of measured gas flow temperature was generally low, ranging from 0.1 K to 0.5 K depending on the ratio of gas temperature to nozzle wall temperature.

As the particle images were taken over several minutes, the stability, and repeatability of the gas flow heater operation was important. After each increase in the heater temperature set point, it overshot the new set point initially and reached a steady state after approximately 10 min. As the calibration data were acquired in increasing temperature steps, a minimum wait of 10 min was required after each heater set-point adjustment before recording the next set of calibration data. Once

the stabilisation time passed, the expected nozzle exit temperature of the gas flow was reached with excellent repeatability. Even over multiple days the difference in measured gas flow nozzle exit temperature was at maximum 0.5 K.

Once the reliability of the setup was established, calibration measurements were conducted at four different temperatures. Resulting 3D LIR maps are shown in fig. 6.41. Each map represents the combined result of multiple single-shot measurements to provide more samples for fitting the calibration function, thereby reducing the calibration uncertainty. Every point in these maps corresponds to an individual reconstructed particle coloured according to its LIR. For every temperature, between 250 and 1050 particles were available. The average particle LIR increased monotonically with temperature, as expected from the emission spectra and filter transmission curves presented in section 5.2. At the perimeter of the jet, lower LIRs were measured than in the centre for fig. 6.41c and d. This is due to the mixing of the heated jet flow with the unseeded, unheated, and slower co-flow in a shear layer.

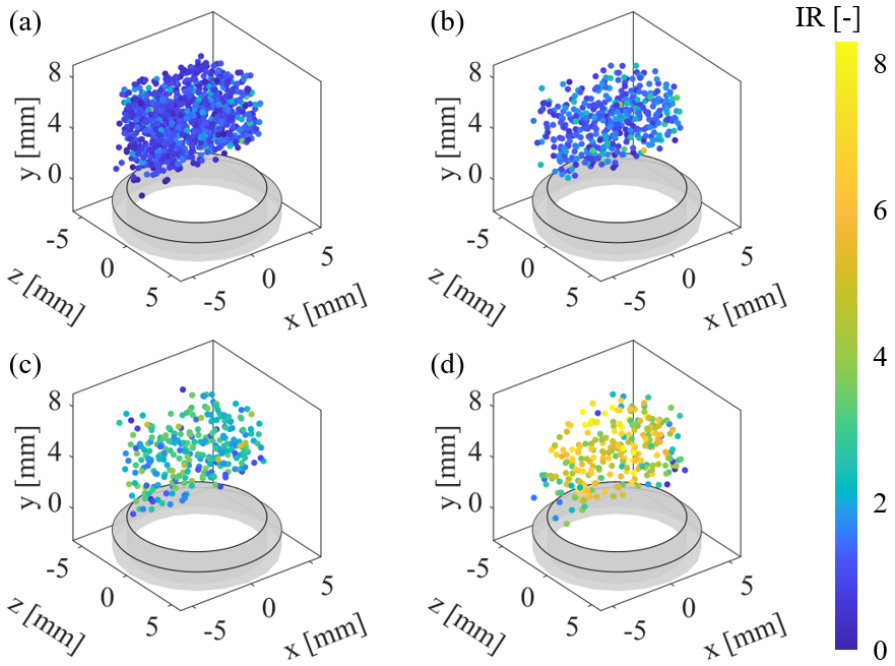

Figure 6.41: 3D particle distributions in false colours indicating LIRs computed at jet flow core temperatures of 295 K (a), 338 K (b), 383 K (c), and 438 K (d). Adapted from Stelter et al. 2023 (CC-BY 4.0).

From each 3D LIR map, the average LIR within the 4 mm diameter potential core region was computed as indicated by the blue markers in fig. 6.42. Following Abram et al. 2015, the power-law

$$\varphi(T) = p_1 + p_2 T^{p_3} \tag{6.18}$$

was fitted to these points to model the relationship between particle temperature and LIR. This yielded the calibration function for the conversion of any LIR to its corresponding temperature value, shown as a dashed line in fig. 6.42.

As later measurements in gas flows were performed using both 266 nm and 355 nm lasers for excitation of phosphor luminescence signals, the calibration function was also checked for applicability to such data. For this, a two-point recalibration was added. Two sets of calibration data were recorded under 355 nm excitation at 299 K and 422 K. The calibration curve in fig. 6.42 was normalised to the average LIR in the jet core region at 299 K, and the validity of the approach was checked using the equivalent LIR at 422 K. As the latter was well within the uncertainty of the original calibration function from 266 nm excitation, the normalised calibration function was used with recordings under 355 nm excitation. Finally, the normalised sensitivity of the LIR was calculated according to eq. 3.4 (page 20) as derivative of the power-law fit normalised by the momentary LIR, reaching more than 1 %/K over a wide temperature range.

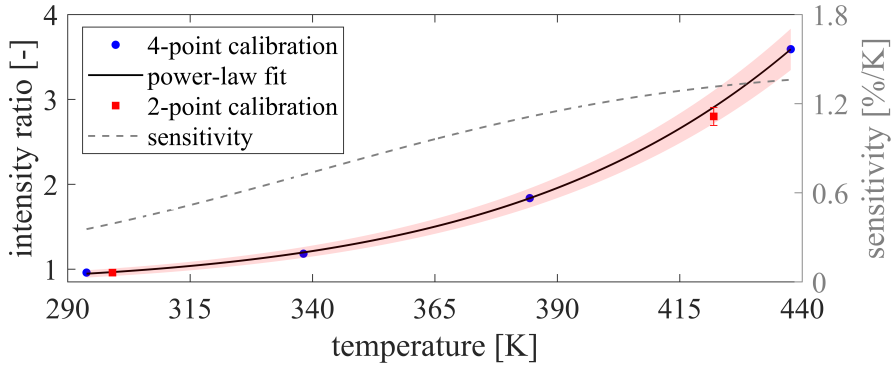

Figure 6.42: Temperature calibration function fitted to four-point calibration data (266 nm excitation), re-normalized to two-point calibration (355 nm excitation). Red area and error bars indicate 2σ standard error of measured LIRs. Adapted from Stelter et al. 2023 (CC-BY 4.0).

With the calibration function at hand, 3D temperature values could be derived from computed LIRs to augment the 3D velocity information from particle tracking yielding simultaneous measurements of temperature distributions and velocity fields. Such measurements are demonstrated in the next chapter within a smaller-diameter heated turbulent gas jet, embedded in a slower and much cooler co-flow.

Chapter 7

Demonstration in a non-isothermal turbulent gas jet

The practicality of the measurement system implemented in the previous chapter was demonstrated by performing simultaneous temperature and velocity measurements in a heated turbulent gas jet embedded in a co-flow at ambient temperature. The parameters of the demonstration experiment (**section 7.1**) and obtained results (**section 7.2**) are discussed below. Both single-shot and cumulative time-averaged measurement results are provided. From the results, a clear path for further improvements is derived, which are implemented in the following **chapter 8**. This chapter is based on and extends the findings of an earlier publication by the author (Stelter et al. 2023).

7.1 Experimental parameters

A nozzle with a circular cross-section of 4 mm diameter was used to provide a jet flow. Nitrogen was used for the jet and air for the co-flow, but air could be used for both flows without impacting the performance of the concept. To achieve a Reynolds number of 4600 for the jet flow at a nozzle exit temperature of 433 K, the bulk velocity was set to 34 m/s. Compared to the jet flow, the co-flow was at an ambient temperature of 300 K and a much lower bulk velocity of 0.2 m/s, which created a shear layer between the jet and the co-flow. Both flows were seeded

with (sub-)micron ZnO particles selected in section 5.2. The linear camera setup presented in section 6.1 was used for the present measurements. To illuminate the measurement volume of 8 mm in diameter, the circular beams of the double-pulse green and single-pulse UV lasers were overlapped in both time and space domains. The measurement volume started at 4 mm (1 nozzle diameter) above the nozzle. The pulse energy of the green beams was adjusted to provide a fluence of 95 mJ/cm^2 each, while the 355 nm UV laser exceeded the critical excitation fluence threshold of 60 mJ/cm^2 (cf. section 5.2) with 280 mJ/cm^2. At a camera image magnification of 0.2, the time delay between both green laser pulses was set to 9 µs to allow for a particle image displacement on the order of 9 pixel. Single-shot and time-averaged cumulative results are shown and discussed in section 7.2.

7.2 Results and discussion

Single-shot results derived from an individual set of four double-frame particle Mie scattering (cameras P1-4) and two single-frame luminescence camera images (cameras T1-2) are shown in fig. 7.1. As it was very challenging to achieve consistent seeding between jet and co-flow, results for a small sub-volume centred above the jet nozzle are shown to focus on the most interesting part of the flow. The co-flow was practically free of particles in the presented results. Within a volume of 74 mm^3, 33 individual particles were reconstructed and tracked between double-frames, and temperature results were derived. Below, each of these particles is coloured in false colours to represent either its temperature (fig. 7.1a,c) or its streamwise velocity (fig. 7.1b,d). As expected, particles close to the central axis of the jet exhibited the highest temperature and velocity values. Particles close to the nozzle exit, corresponding to the origin of the coordinate system, were up to 25 % faster than the bulk velocity, while indicating temperatures close to the nozzle exit temperature. If the co-flow could have been seeded equally to the jet flow, more than 350 individual samples of flow temperature and velocity would have been available for the single-shot measurement. Assuming the availability of more powerful UV laser light sources, the measurement volume could be expanded along the y-axis to fill the entire camera field of view. This would result in 1200 individual

particles per single-shot measurement, even at the low particle seeding density of the presented results. It should be noted that the size of the measurement volume was currently limited by the UV laser power available for this demonstration, rather than limitations of the measurement concept itself.

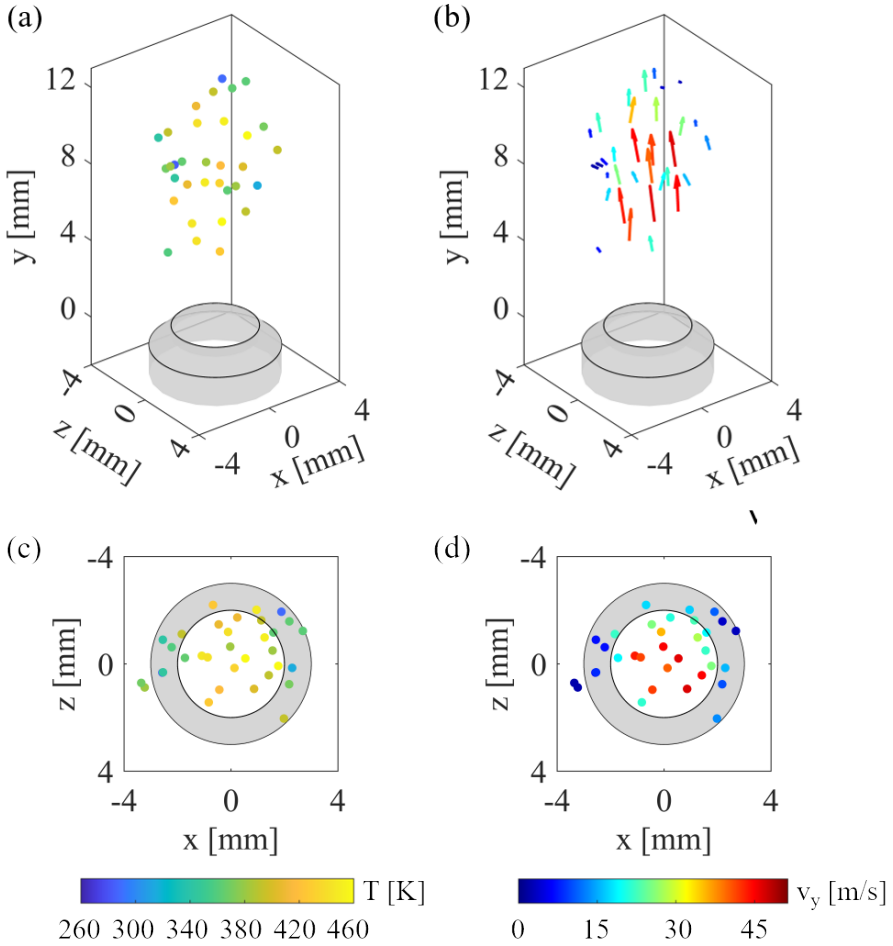

Figure 7.1: Single-shot result of 3D temperature and velocity of particles within a non-isothermal turbulent jet flow. Adapted from Stelter et al. 2023 (CC-BY 4.0).

In addition to instantaneous single-shot results, it is also possible to derive time-averaged cumulative results by combining multiple single-shot results. This is shown in fig. 7.2, where 3100 individual temperature-velocity measurements were distributed in a volume of 213 mm^3, resulting in spatially dense measurements with 14.6 particles/mm^3. Temperature results are presented in fig. 7.2a, c, and e, where individual particles are coloured according to their temperature from

phosphor thermometry. The 3D scatter plot shows only particles with a negative z-axis position (indicated by the green bounding box) to allow insights into the hot core of the jet flow. Particles with a high temperature close to the nozzle exit temperature were grouped in the core region. In the outer region of the flow, particle temperatures were reduced owing to thermal mixing with colder gas from the co-flow region. The radial symmetry of the jet is visible in the xz-plane and ry-projection plots, where r indicates the radial distance of the particle from the jet centre axis. The corresponding velocity results for the same particles are shown in fig. 7.2b, d, and f. Here, the particles are coloured according to the dominating axial velocity component. The velocity distribution was similar to that of the temperature field, but the results were less noisy. The shear layer between the hot and fast jet core region and the colder and much slower co-flow region is clearly visible at a radial distance of 1.9 to 2 mm. Both the temperature and velocity results were produced without any post-processing filters applied. The velocity results suggest a core region of the jet with a diameter of 2.5 mm, where the particle velocities were almost constant. To estimate the uncertainty of the technique in the present first implementation, the root mean squared deviation of particle temperature and velocity from the respective average value is calculated in this region. This results in uncertainties of 27.4 K and 4.5 m/s or 6 % and 10.2 % relative to the computed mean values. As these estimates also include inherent fluctuations of these quantities in the turbulent jet flow, they are worst-case estimates.

7.2.1 Velocity profile

To validate the provided velocity measurements, the time-averaged velocity profile was compared to the theoretical velocity profile of a turbulent gas jet predicted by the $1/7^{\text{th}}$ power law, as proposed by Chant 2005. For this comparison, the particles from the cumulative results shown in fig. 7.2 were binned using their radial distance from the jet centre axis using bins of 0.5 mm and 33 % overlap. These measured velocities are shown in fig. 7.3, complemented with error bars indicating one standard deviation of the mean in black. Piecewise linear interpolation between individual measurement points allows visualisation of the estimated velocity profile.

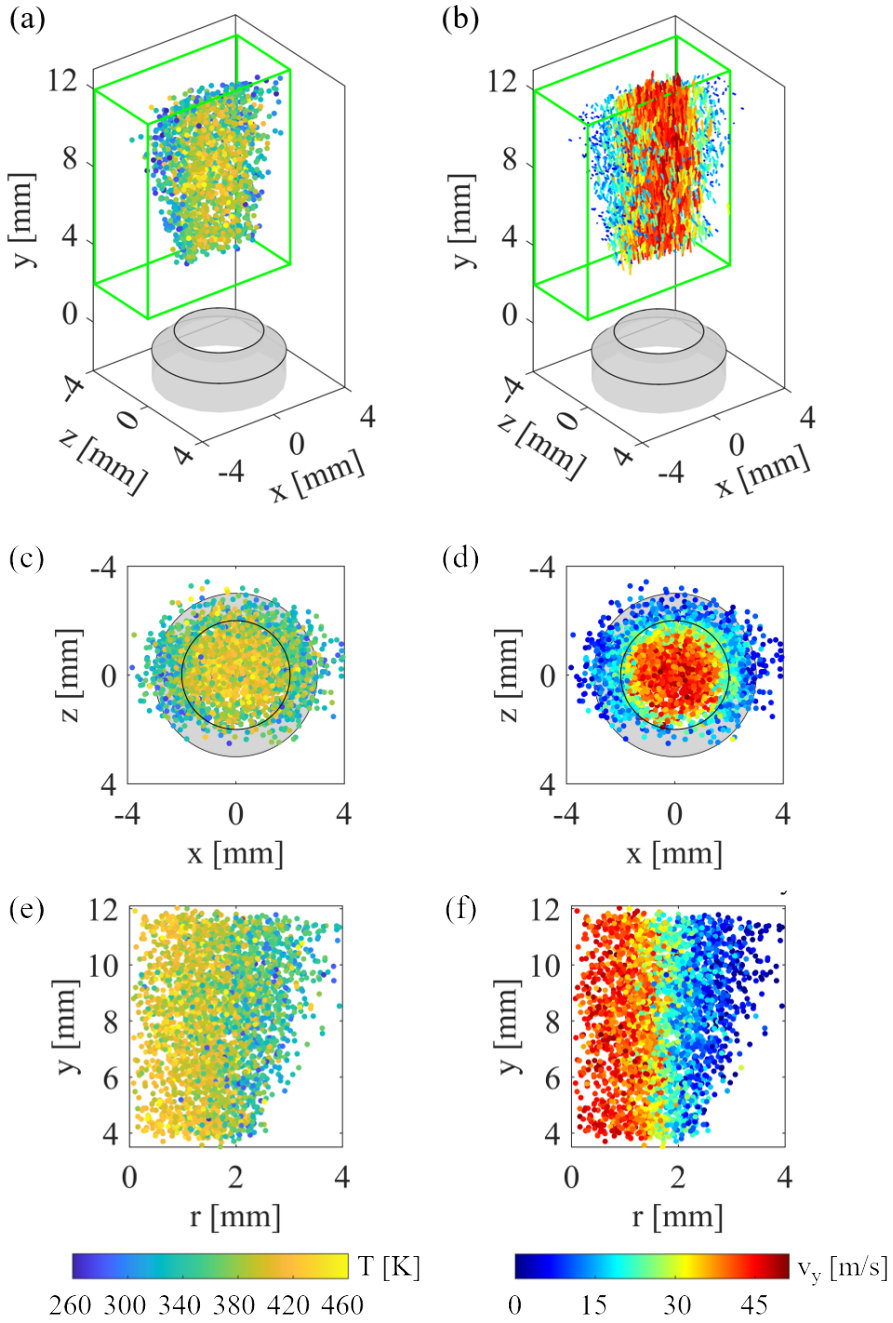

Figure 7.2: Cumulative results of 3D temperature and velocity distributions within a non-isothermal turbulent jet. Adapted from Stelter et al. 2023 (CC-BY 4.0).

Following Chant 2005, the theoretical velocity profile is given by

$$v(r) = v_{\max} \left(1 - \frac{r}{R}\right)^{1/n} \tag{7.1}$$

where r is the radial distance from the jet centreline, R is the diameter of the jet nozzle, and the maximum flow velocity $v_{\max}$ is approximately 22 % higher than the bulk velocity. While the power law exponent n is a function of the Reynolds number, $n = 7$ was found to be suitable for a wide range of fully developed turbulent pipe flows (Salama 2021). The theoretical profile is shown as a red line in fig. 7.3. Within the radius of the jet nozzle ($r \leq 2\,\mathrm{mm}$), good agreement between the measured average velocities from the double-frame particle tracking velocimetry (PTV) and the theoretical prediction was achieved. The difference in centreline velocity is 6 % which is fine considering the simple PTV scheme (section 6.2.3), entrainment of surrounding gas into the jet, and potential uncertainties in the model equation. At $r > 2\,\mathrm{mm}$, the theoretical and measured velocity profiles show large differences. Although the theoretical velocity profile drops steeply to 0 m/s at the inner wall of the jet nozzle, this is not the case for a real jet.

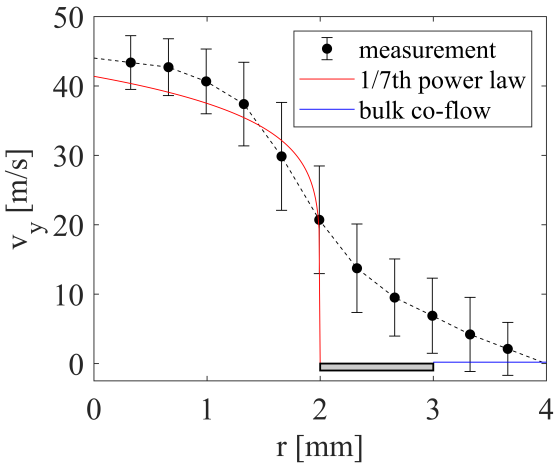

Figure 7.3: Axial velocity profile comparison between measurement and theory. Adapted from Stelter et al. 2023 (CC-BY 4.0).

While the measured velocities show a strong decrease in that region, too, the velocities dropped towards the co-flow velocity instead. This is explained by the no-slip condition imposed on the theoretical profile by the $1/7^{\text{th}}$ power law, opposed to a shear layer between the jet and co-flow for the real flow, as the free jet is not confined by a solid wall after leaving the nozzle.

7.2.2 Temperature profile

The separation of the potential core of the jet and its surroundings was also visible in the temperature results, as shown by the temperature histograms in fig. 7.4. In fig. 7.4a, the temperatures measured for particles within and outside the central 2.5 mm potential core region proposed above are plotted. The temperature distributions in both parts of the flow show a clear separation, with the core region reflecting temperatures close to the set temperature of 433 K and the co-flow at much lower temperatures. The fact that the actual potential jet core might be even smaller than 2.5 mm is suggested by fig. 7.4b, where the temperature distributions within even smaller regions of 0.5 mm and 1.5 mm are compared to the 2.5 mm diameter region. While the sample number drastically decreased when considering only particles with gradually decreasing distance to the jet centreline, the peak temperature of the histograms clearly shifts from 395 K for the largest diameter to 415 K for the smallest diameter.

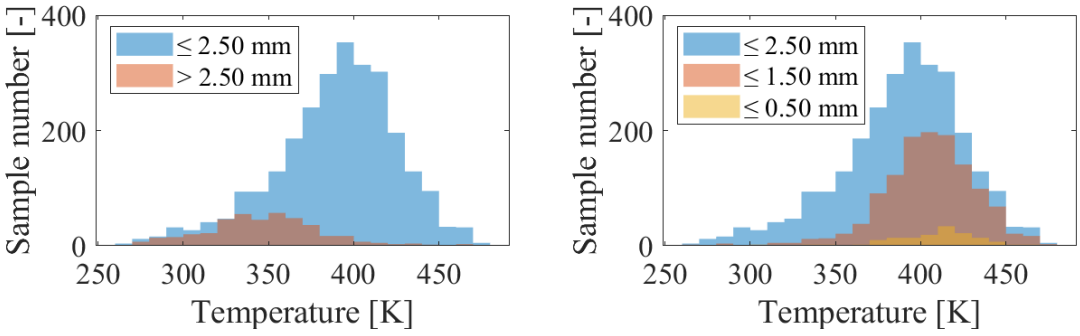

Figure 7.4: Temperature histograms (a) within and outside a potential core region of the flow and (b) for different sizes of central core regions.

7.2.3 Temperature uncertainty

To further improve the implementation of the measurement concept in terms of temperature precision, it is important to understand the sources of uncertainty. As phosphor thermometry using individual particle images is a low-light application, signal is at a premium and often a limiting factor in fluid phosphor thermometry

measurements (Lawrence et al. 2013; Jenkins et al. 2012; Lipzig et al. 2013). To quantify the effect of the overall low signal levels, the model introduced in section 3.2.3 (eq. 3.7, page 21) was used. Considering an average integrated intensity of 650 counts and particle image size of 22 pixel obtained from isothermal measurements, the signal limited luminescence intensity ratio (LIR) precision was estimated as 8.75 %. Using the normalised LIR sensitivity at ambient temperature (fig. 6.42, page 125), this translates to approximately 20 K or 73 % of the measured temperature precision.

A reduction in this initial temperature uncertainty was desired to improve the performance of the developed measurement concept. The possibility for improvement is highlighted by a study from Abram et al. 2015. There, fluid thermometry results obtained with ZnO using the LIR approach are demonstrated with a ratio precision of 2.5 % or 6 K of signal limited temperature precision. The key difference between their study and the present work are the imaged luminescence signal levels. In Abram et al. 2015, the luminescence signal of multiple particles within evaluation windows was combined whereas the present study relied on luminescence emissions of individual phosphor particles. This highlights the tradeoff between spatial resolution and temperature precision and the importance of high luminescence image signal levels. Ways to increase them are explored below.

As ZnO was used within its saturation regime (UV laser fluence $\geq 250\,\mathrm{mJ/cm^2}$), the number of emitted photons from luminescence could not be increased any further by increasing the excitation laser fluence. However, the collection of emitted photons could be improved by increasing the solid angle that the luminescence particles subtend at the cameras T1 and T2, for example, by moving the cameras closer to the measurement volume. Switching to another phosphor with higher per-particle luminescence emission would also be an option, although other parameters such as the luminescence lifetime and particle size must be considered.

Even at the present state, the limited luminescence image signal levels did not explain the entire uncertainty. About one quarter of it must stem from other effects. It was attributed to erroneous pairing, particle image segmentation errors, and potential differences in particle-to-particle luminescence emissions. False pairing could occur between both luminescence imaging cameras and between 3D positions

obtained from Mie scattering camera images and the luminescence imaging cameras. The probability of both scales with the error in the camera calibration models. To reduce this error an advanced camera calibration scheme was integrated in the next chapter (see section 8.2). Particle image segmentation errors were addressed by the implementation and benchmarking of eight different schemes for this task in section 8.5. While the presence of multiple particle images within the fitting window for a single particle was possible and could have impacted the derived LIR, it was not very likely to happen considering the low particle image seeding densities. As long as multiple particle images would not overlap with one another, they could be processed using the more advanced segmentation schemes anyway. While measures were taken to reduce the dust load within the lab, some dust particles could have been entrained into the investigated free jet. If detected by the measurement system, their LIR would have deviated from the expected range and therefore falsified LIR statistics. This could be countered by setting LIR thresholds to prevent individual extreme LIR values from degrading the statistical results. Finally, physical luminescence emission differences between individual phosphor particles are more difficult to investigate. Some insights have been gained for another phosphor BAM:Eu^{2+} in Ojo et al. 2015; Fond et al. 2015 where little differences between particle emissions have been found. While this might be taken as indicative, with ZnO a different phosphor was selected for the present thesis, warranting a separate investigation.

7.2.4 Seeding stability

As mentioned above, achieving stable seeding of solid particles in a gas flow is a challenging task. The stability of particle seeding was assessed by evaluating the particle image seeding density and source density for individual single-shots measurements of an exemplary camera image time-series. Both measures were calculated separately for the Mie scattering and luminescence camera groups. In fig. 7.5, the average particle seeding density and source density for all cameras in both groups are plotted per individual single-shot recording. One can clearly see the variation in the number of particles imaged per single-shot in fig. 7.5a. The predicted limit of 0.013 ppp from fig. 6.25b (page 95) is never exceeded; therefore,

the probability of particle image overlap was low. While the qualitative trend is similar for both Mie scattering and luminescence image recordings, the perceived seeding density was always higher for the Mie scattering recordings. This can also be visualised on a single-shot basis. While in fig. 7.1 and fig. 7.2 only those particles were plotted where both temperature and velocity results were available, in fig. 7.6, particle locations from one single-shot recording are shown where either of both was available. While velocity information was available for 100 particles, only for 30 of them a temperature value could be determined, too.

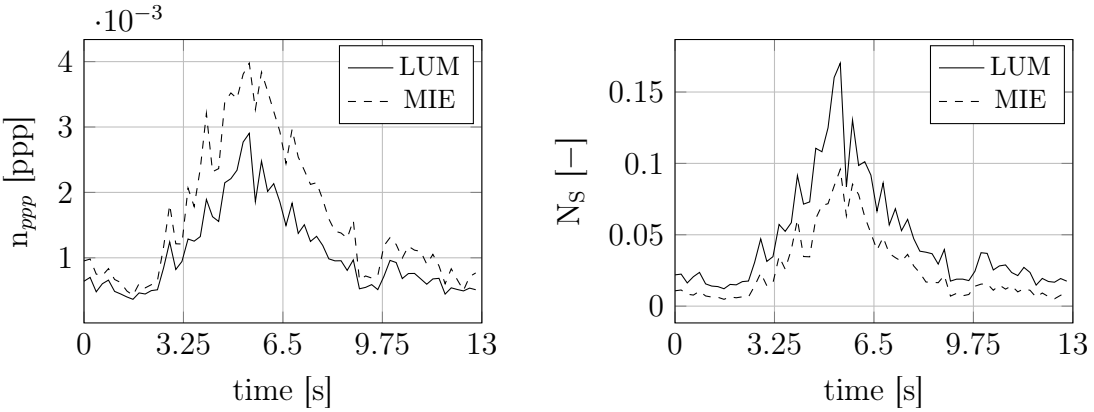

Figure 7.5: Particle image seeding density n_{ppp} (a) and source density N_S (b) evaluated from time-series of Mie scattering and luminescence camera images.

The larger number of velocities compared to temperature samples is due to overall higher imaged signal levels in the scattering views (i.e. brighter particle images, better SNR) as well as better detectability of individual particle images due to a more consistent particle image size and peak intensity between individual Mie scattering particle images.

Owing to the particle position-dependent blur in luminescence recordings, particle images were more challenging to detect, and some dim particle images could not be detected at all in the luminescence recordings. The effect of image blur in the luminescence recordings resonates with the source density plotted in fig. 7.5b. While the number of particles imaged per single-shot was higher in Mie scattering images, peaking at 0.004 ppp compared to 0.003 ppp for the luminescence image equivalent (fig. 7.5a), the fraction of camera image area covered by them was

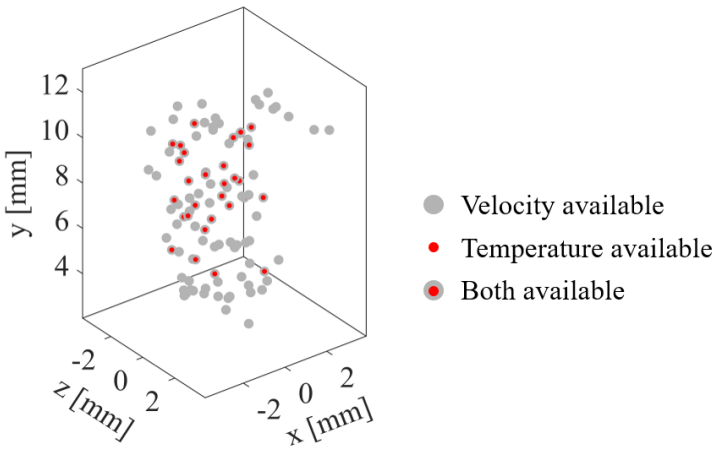

Figure 7.6: Particle locations obtained from an individual single-shot recording where either temperature, velocity, or both were available.

larger in luminescence recordings (fig. 7.5b). Even at these low particle seeding levels, up to 17 % of the available luminescence camera image space was covered by particle images. Focusing the comparison on particle image and source densities for either luminescence or Mie scattering recordings, one sees a qualitative agreement between the trend in both measures. However, the stability over time is low, as expressed by the intermediate peak between 3 s and 9.5 s and high normalised standard deviations of approximately 60 % of the *ppp*-distributions. After an initial decline in the particle seeding at the beginning of the time-series recording, the particle powder bed was moved by slightly shaking or knocking the seeder. This lead to a strong increase in seeding, which declined equally rapidly. The single-shot measurement plotted in fig. 7.1 was recorded slightly after the n_{ppp} peak at 6 s.

7.2.5 Particle image size

While the 3D temperature and velocity results presented above are encouraging and prove the practical applicability of the conceived measurement concept, a higher number of tracer particles per unit volume from individual single-shot measurements was desirable. Two main factors limited this: the ability to reconstruct densely seeded particle distributions and the delimitation of individual particle images in luminescence camera recordings. The former was solved by including state

of the art camera calibration and particle triangulation algorithms (sections 8.2 to 8.4), while the latter was investigated above in section 6.1.3 (fig. 6.25), resulting in a prediction of a maximum particle image seeding density of 0.013 ppp. This estimation was based on predictions for blur spot diameter-limited luminescence particle images. These predictions could now be compared against the actual measured particle image sizes. These were derived by utilising the 2D Gaussian fits (eq. 6.10) used for luminescence image segmentation. The particle size was then estimated as $2(\sigma_x + \sigma_y)$, which is equal to four times the average spread of the fitted Gaussian function along its major and minor axes (Stelter et al. 2023). Compared to the predicted maximum luminescence particle image size of 18 pixel (equal to 117 µm), the particle image size measured in this way reached its maximum at 6 pixel for particles at the border of the measurement volume, as shown in fig. 7.7a. Considering this, the maximum seeding density was estimated again using the Monte Carlo simulation approach, as above for fig. 6.25b (page 95). Because the luminescence particle images were smaller than initially predicted, the maximum usable seeding density was shifted from 0.013 ppp to 0.022 ppp, as summarised in fig. 7.7b, matching the estimation from Stelter et al. 2023.

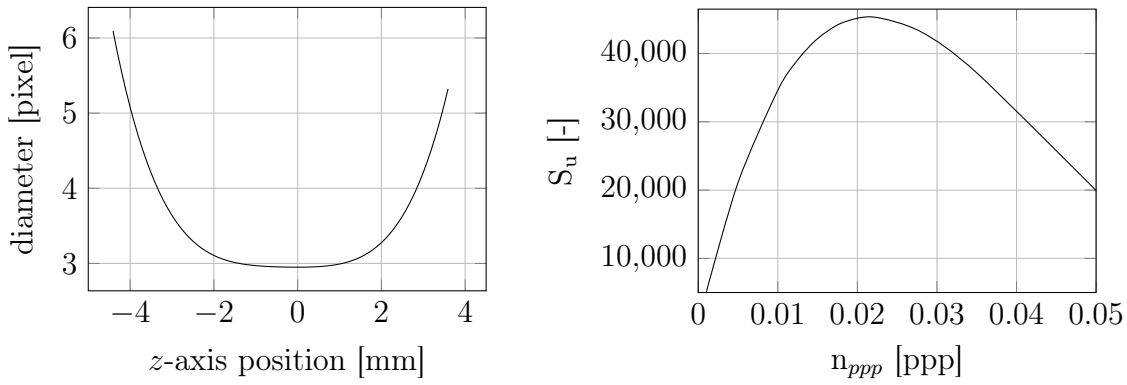

(a) (b)

Figure 7.7: Measured luminescence particle image diameter versus particle in-depth position within the measurement volume (a), and its impact on the predicted maximum seeding density (b). Adapted from Stelter et al. 2023 (CC-BY 4.0).

To investigate the difference between the predicted and measured particle image sizes, the optical measurement system was evaluated again. While the assumptions in the above sections regarding the approximation of the particle image diameter

were correct, the filters used with the luminescence imaging cameras were neglected in that model. These filters had a diameter of 50 mm compared to the bare camera lens entrance pupil of 77 mm. Hence, the filters acted as additional external aperture equal to an imaginary f-number of $f/1.7$. This accounts for approximately half the difference between the predicted and actually measured particle image sizes for particles 4 mm away from the plane of focus. The remaining difference is attributed to uncertainties in the approximation of the blur spot diameter (eq. 6.5, page 73).

Overall, the results presented in this chapter demonstrated the measurement concept's applicability to practical measurements in turbulent non-isothermal gas flows. The adjusted prediction of the particle image seeding density limit paves the way for improvements in terms of sample number per single-shot measurement, by processing camera images with higher particle image seeding densities. Using more advanced algorithms for camera calibration, 3D particle position reconstruction, particle tracking, and luminescence image segmentation will also increase the number of particle samples retrieved from identical image data. These advanced algorithms were implemented in the following chapter, and their effect on the results was quantified by re-processing the raw data obtained in the current chapter.

Chapter 8

Advanced processing schemes

In this chapter, more advanced algorithms are introduced for processing raw particle image data. This marks a general switch from single-pass algorithms to iterative successors. After outlining the overall scheme and camera image pre-processing in **section 8.1**, target image based camera calibration models were refined using volume self-calibration (VSC) (**section 8.2**). In addition to camera models with very low errors, the iterative VSC process returns the optical transfer function for all six cameras. This is a prerequisite for the implementation of iterative particle reconstruction (IPR) as a replacement for the previously used minimum line of sight (MinLOS) reconstruction in **section 8.3**. To reliably track individual particle movement in 3D space at higher particle seeding densities, the former double-frame particle tracking velocimetry (PTV) algorithm with an initial guess from ensemble cross-correlation was replaced with two-pulse Shake-The-Box (TP-STB), as described in **section 8.4**. Multiple image segmentation schemes were investigated in **section 8.5** to improve the accuracy of computing the luminescence signal imaged for every particle by cameras T1 and T2, to allow a more precise luminescence intensity ratio (LIR) calculation and improved thermometry results. In preparation for measurements at higher particle image seeding densities, the former 2D flat field correction (FFC) is expanded to 3D in **section 8.6**. To illustrate the combined impact of the overall advanced processing scheme, the same raw data as in chapter 7 was processed, and differences in the results were quantified in **section 8.7**.

The improved processing is summarised in fig. 8.1 and fig. 8.2. The former provides an overview of the first part of the processing, where pre-processed Mie scattering and luminescence particle images were used to refine initial target image-based camera calibration models using VSC.

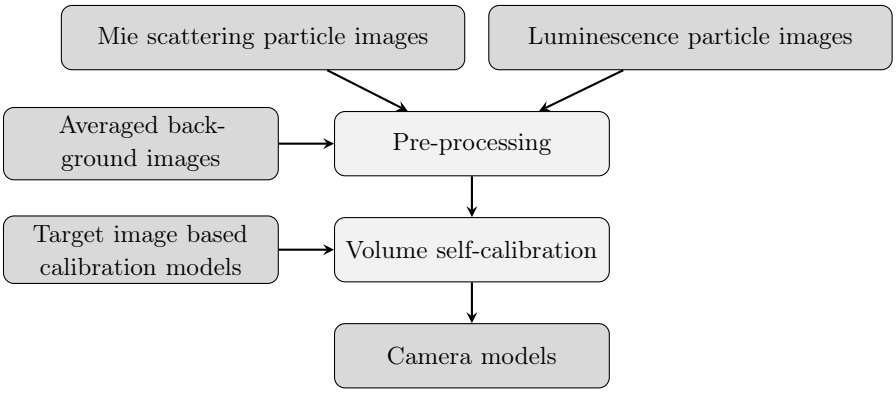

Figure 8.1: Processing scheme to obtain joined camera calibration for Mie scattering and luminescence imaging cameras using volume self-calibration.

Figure 8.2 describes the processing of the pre-processed Mie scattering and luminescence camera images to obtain simultaneous velocity and temperature results. Once VSC is completed, 3D particle positions are reconstructed using iterative triangulation with IPR. From there, the left leg of fig. 8.2 produces 3D velocities using TP-STB, while the right leg uses the 3D positions and adds temperature information to it, employing more advanced image segmentation schemes.

The following sections describe the individual steps in more details. This starts with pre-processing raw camera recordings to reduce image noise, increase particle image SNR, and equalise intensity levels across recordings of different cameras.

8.1 Camera image pre-processing

Similar to section 6.2.1, raw particle images were pre-processed to aid following evaluations. As here both Mie scattering and luminescence particle camera images were used to refine an initial camera calibration based on calibration target images, both kinds of camera recordings had to be pre-processed to aid the VSC. For this,

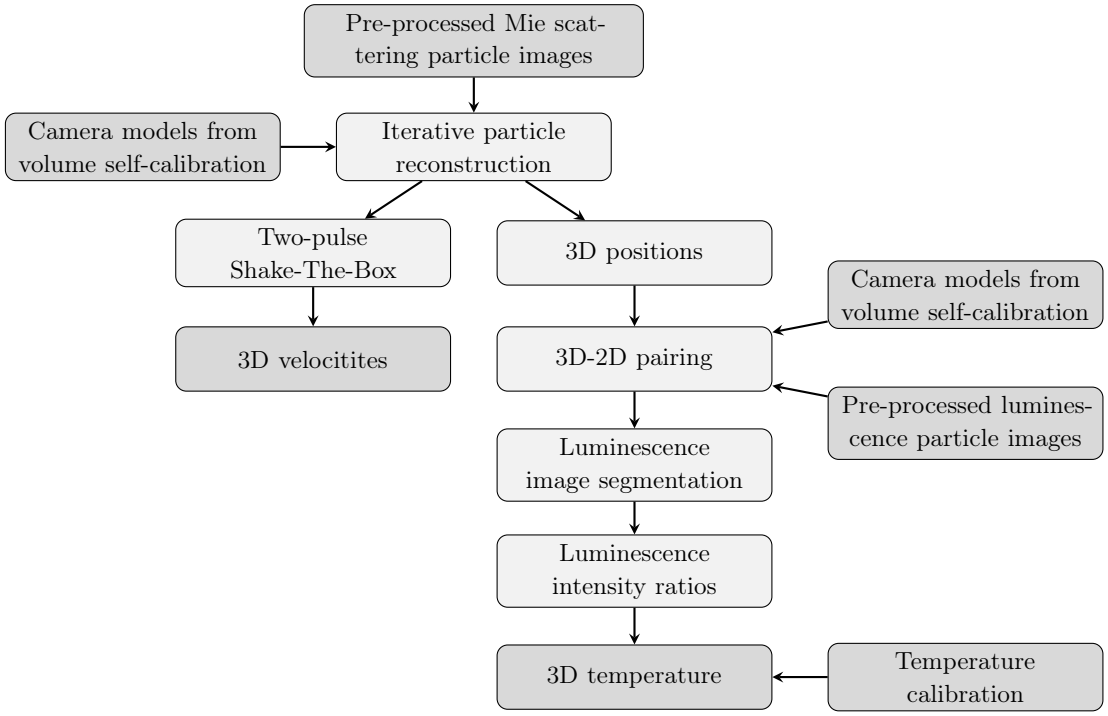

Figure 8.2: Advanced processing scheme to obtain 3D velocity and temperature information on a per-particle basis.

an average background image was subtracted from each individual particle camera image recording. As the VSC process is sensitive to residual image noise, remaining background signal was removed by subtracting the minimum pixel intensity over 11 consecutive camera images (temporal filter), followed by subtraction of the minimum pixel intensity found within a sliding $40{\times}40\,\text{pixel}^2$ window in each image (spatial filter). A spatial mask was then applied, retaining only parts of the camera images filled with the particle images. To reduce remaining high-frequency noise, a 2D Gaussian filter was applied. Its strength was determined by the width of the Gaussian function σ. As the luminescence recordings had a lower SNR than their Mie scattering counterparts, they were more prone to noise and the filter strength was therefore higher for them with $\sigma = 1.6$ pixel compared to $\sigma = 1.2$ pixel for the latter recordings. Usually, a very low intensity background signal remained that was removed by subtracting a constant value of 7 to 14 counts from each image. In the last step, the pixel intensities were multiplied by a factor adapted for each camera to ensure identical average particle image intensities across all cameras.

The pre-processed luminescence and Mie scattering particle camera images were then passed to VSC to refine initial target image-based camera models.

8.2 Camera calibration with volume self-calibration

As introduced in section 4.1.3, VSC is an optimisation technique for camera calibration models. As such, it requires an initial calibration model for each camera that is subsequently refined using particle images recorded by the same cameras. Here, initial pinhole-based models were obtained for each camera P1-4 and T1-2 from target images, as detailed in section 6.1.5, before VSC was applied to compute a correction field adding to the original camera models.

To quantify the impact of VSC on the camera calibration model accuracy, the calibration errors from the pure target image-based legacy calibration from section 6.1.5 and the present VSC are plotted in fig. 8.3a. Both the maximum and average calibration errors are given across all six cameras. Note that the computation of the calibration error differed slightly for the target image-based calibration and VSC. For the former, the projection error (Hartley et al. 2019) was calculated as the Euclidean distance in image space between projections of target markers and their imaged position, whereas for VSC, the disparity (Wieneke 2008) was calculated between the projection of reconstructed particle positions and their image positions. The first VSC iteration noticeably reduced the maximum calibration error encountered in all cameras. For the second VSC iteration, the calibrated measurement volume was split from one global volume into $2 \times 2 \times 1$ sub-volumes to allow for a more fine-grained correction of the potential inaccuracies of the pinhole model across the field of view of all cameras (cf. section 4.1.3). This explains the intermediate increase in the detected errors in this step. The effectiveness of VSC was underlined by the very low calibration errors achieved after the third VSC iteration, culminating in an average (maximum) calibration error of 0.02 pixel (0.04 pixel).

The effect of such low calibration errors is illustrated in fig. 8.3b. The detected Euclidean distance between projections of reconstructed 3D particle locations

and detected particle image centres in both luminescence camera image spaces was computed. As detailed in section 6.3.3, a low distance is desirable for the association of particle position and velocity information from Mie scattering images and later temperature information derived from luminescence image recordings. The provided histograms visualise this distance for both cameras T1 and T2 using the final camera calibration resulting from VSC. For both cameras, the histograms peak between 1 and 2 pixel, mitigating ambiguity when pairing the 3D information with 2D particle images in luminescence camera image space, which would arise if multiple image intensity maxima (i.e. pairing candidates in image space) were in proximity of a projected 3D location from reconstruction. This is a prerequisite for measurements at high particle seeding densities, where the 2D interparticle distance will decline sharply.

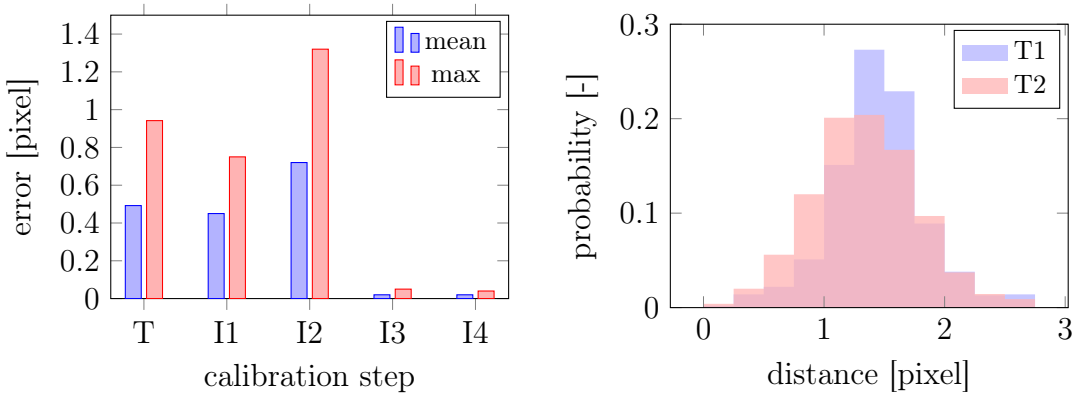

Figure 8.3: Evolution of camera calibration errors from an initial Scheimpflug calibration model over four VSC iterations (a), and the impact of improved camera calibration parameters on the mapping distance between projections of reconstructed 3D positions and intensity maxima in the luminescence camera images (b).

Most commonly, a global VSC is employed. As described above, it uses reconstructed 3D particle positions from several single-shot recordings to calculate the average disparity over time within each sub-volume. While this allows gathering reconstructed particle locations and their disparities over multiple single-shots, to improve the statistical stability of the estimated average disparity, it also implies that the camera setup is completely static. Any movement of the cameras between the recording of

the particle images used for the VSC process and other particle images would result in increased calibration errors. The same is true for target image-based camera calibration models, where any movement of the cameras between the recording of target and particle images would result in a degradation of the camera model, negatively impacting the reconstruction and reprojection accuracies. Even if the cameras were properly mounted, active cooling elements are regularly required within the cameras to maintain low temperature of the image sensor to limit image noise. They cause vibrations in the cameras, causing their views to shift slightly from image to image. This slightly decalibrates the cameras over time, as their views differ compared to the calibration target images (relevant for decalibrating the initial perspective calibration) and also from particle to particle image (relevant for decalibrating the global VSC). These vibrations are visualised in fig. 8.4, where the global disparity of all six cameras is plotted per single-shot over a time-series of 65 single-shots that were not used for the derivation of the global VSC. While the resulting disparities are sufficiently low to not invalidate the calibration, a negative effect on the reconstruction accuracy cannot be ruled out. As described in section 4.1.3, this can be compensated by applying a single-shot-based VSC in addition to the global VSC. Using a single (sub-)volume per image, frame-to-frame camera vibrations are detected and corrected if the particle seeding density is high enough to allow for a reliable disparity estimation from individual single-shot recordings. This is a unique advantage of VSC over legacy target image-based camera calibration. As the final step of a VSC process is the calibration of the particle image optical transfer function (Schanz et al. 2012), this can be included in advanced reconstruction algorithms introduced in section 8.3.

In summary, using VSC reduces the camera calibration errors by one order of magnitude compared with the original Scheimpflug model by computing a correction field from combined Mie scattering and luminescence particle images. If the seeding density is sufficient, even vibrations of the cameras between the recording of individual single-shots can be compensated by applying a secondary VSC in addition to a global VSC and was applied whenever possible. This paves the way for measurements at higher particle image seeding densities.

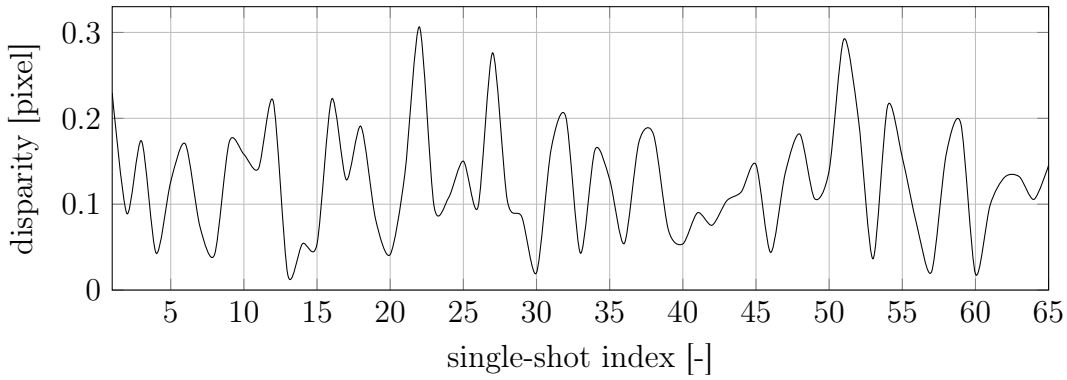

Figure 8.4: Variations in average disparity computed from time-series of individual single-shots not used for computation of global VSC.

8.3 Iterative particle position reconstruction

Once improved camera calibration models were available from VSC in the preceding section, particle positions could be reconstructed. In section 6.2.2, an in-house implementation of the MinLOS algorithm was used to provide individual 3D particle locations from particle Mie scattering camera images using a single-pass tomographic reconstruction scheme. For higher particle seeding densities, a more advanced algorithm was desired. Hence, IPR (cf. section 4.2.2) was introduced for data processing. As shown in fig. 8.2 (page 143), the optimised camera calibration from VSC and the pre-processed Mie scattering particle images served as input to the IPR algorithm. Using IPR marked not only a switch from a single-pass to a multi-pass algorithm to obtain 3D particle positions, but also a switch from tomography to triangulation. As detailed in section 4.2.2, this iterative algorithm can suppress reconstruction artefacts (ghost particles) and is more computationally efficient than tomographic algorithms. Here, its impact on the presented concept for joined 3D temperature and velocity measurements was quantified.

A key parameter for IPR is the number of inner- and outer-loop executions (cf. fig. 4.6 on page 36). In fig. 8.5, the number of particles reconstructed from the same image data as for the previous results (section 7.2) is plotted versus the number of IPR iterations. For simplicity, the same number of inner (position adjustment) and outer (adding particle candidates) loop iterations was set, and other processing parameters were fixed to see the influence of the iteration count on recovered 3D

particle positions. These other parameters included the particle position shaking distance of 0.2 voxel and weak particle removal threshold of 10 % of the average reconstructed particle intensity. If the reconstructed particle positions were closer than 1 voxel or the triangulation error exceeded 2 voxel, they got removed to suppress ghost particles. Note that here, the number of reconstructed particles was used as an intermediate performance metric for the final number of 3D temperature and velocity measurement points. Focusing on fig. 8.5, the superiority of the combination of VSC with IPR over MinLOS was immediately apparent. Even if the IPR algorithm was set to a single iteration, which effectively forced non-iterative triangulation, five times more particles were successfully reconstructed. After five IPR iterations, the number of reconstructed particles was doubled again, reaching 1135 particles instead of 94 particles (average of both frames). Increasing the iteration count further than 10 iterations did not lead to any gain or loss of particles (fluctuations ±4 %). It was noted that more particles were reconstructed from the second Mie scattering image quartet of cameras P1-4 than from the first one (corresponding to the first and second time steps or frames of the double-frame recordings). This was due to different particle visibility in both frames of this single-shot measurement caused by fluctuations in the green laser power output of both laser heads.

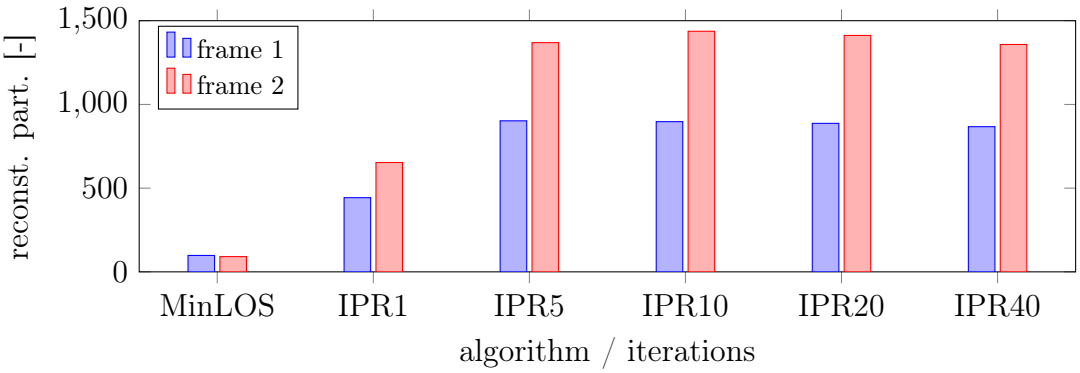

Figure 8.5: Number of reconstructed 3D particle positions for the same single-shot image data depending on the reconstruction algorithm used (MinLOS/IPR) and the number of IPR iterations (1 to 40). Particle numbers are reported separately for first and second time step.

The reconstructed particle positions resulting from 10 IPR iterations for both time steps are plotted in fig. 8.6. Comparing them with the results from MinLOS plotted

in fig. 6.34 on page 109, a greater number of reconstructed particles is both visually apparent and reflected in the numbers of 897/1437 instead of 98/91 particles for the first/second time step, respectively. As IPR triangulates particle locations rather than reconstructing volumetric intensities as done by MinLOS tomography, it directly returns point positions in 3D space. Hence, the particle positions in fig. 8.6 were plotted artificially large to be visible to the reader compared to the isosurfaces of reconstructed intensity plotted in fig. 6.34.

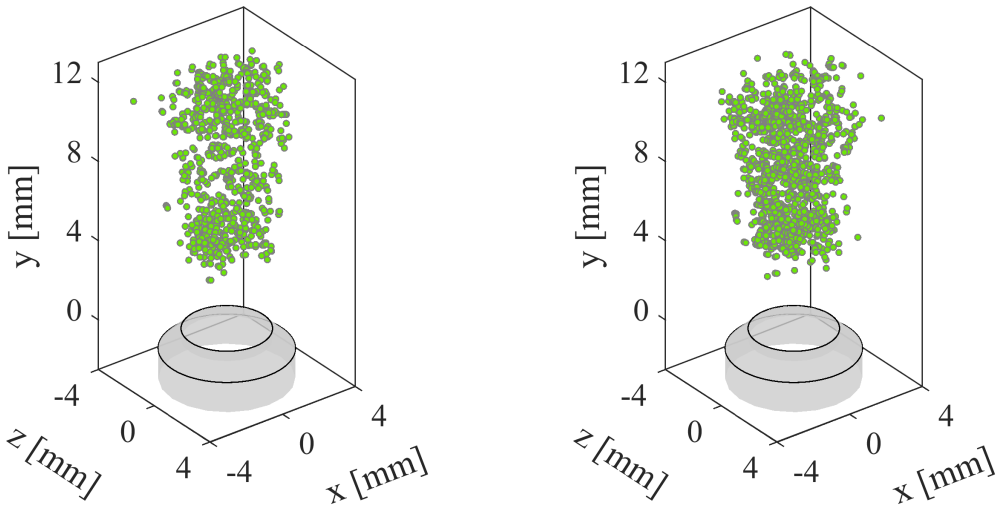

Figure 8.6: Particle positions reconstructed from (a) first and (b) second frame Mie scattering camera image quartets using IPR. For (a) the same image raw data as for fig. 6.34 (page 109) was processed.

Adding to the much higher count of reconstructed particles, the reconstruction time per double-frame recording (i.e. two volumes) with 10 IPR iterations was only 3 s compared to 90 s using the MinLOS implementation on the same workstation computer. Considering that approximately 2000 images were recorded in a typical campaign of experiments, this translated to a processing time for the reconstruction of particle positions of a mere 3.5 h compared to 100 h before. The reduced processing time presents a practical advantage as it (a) allowed a faster turnover from recording data in experiments to obtaining results, and (b) allowed for a much quicker optimisation of several processing parameters as the effect on the results became visible much faster.

In conclusion, IPR provided a significantly higher number of reconstructed particles in a much shorter amount of time than the MinLOS implementation used to process the same image raw data in chapter 6. IPR takes advantage of the improved camera calibration models from VSC and an iterative triangulation approach that enables successful reconstruction of 3D particle positions at higher particle image seeding densities, where MinLOS algorithms reportedly fail to provide meaningful results (Michaelis et al. 2010).

8.4 Two-pulse Shake-The-Box particle tracking

Following the left leg of the processing scheme (fig. 8.2 on page 143), particle velocities were obtained by tracking reconstructed particle positions between corresponding 3D reconstruction results from IPR for the first and second Mie scattering double-frame time and dividing the displacement by the time delay between both green laser pulses. In section 6.2.3, a non-iterative in-house developed particle-tracking algorithm with an initial displacement guess from 3D ensemble cross-correlation was implemented and used for this task. Although it worked reasonably well for low particle seeding densities and allowed a demonstration of the concept, it would reach limits once the particle seeding density was increased or flows with a less predictable velocity field were investigated. In these cases, the instantaneous velocity fields would deviate strongly from the average velocity field obtained from ensemble cross-correlation, rendering the naive nearest neighbour pairing error-prone. As an advanced replacement, the recently developed TP-STB (cf. section 4.3.3 and Novara et al. 2023) was used, which marked a switch from a single- to a multi-pass algorithm, as for camera calibration and 3D reconstruction with VSC and IPR before. While the reader is referred to section 4.3.3 for more details on the TP-STB algorithm, here the influence of several parameters on the obtained 3D velocity results were investigated. As TP-STB is deeply integrated with IPR, the processing parameters and values discussed for IPR in the preceding section applied to the IPR executions within TP-STB as well. In addition to these parameters, the number of tracking iterations and an optional guess for the velocity field govern the algorithmic behaviour of TP-STB. For each tracking iteration, IPR was executed

with the specified number of inner and outer iterations.

The effect of the number of tracking iterations per single-shot recording was evaluated below. Although a larger number of iterations could lead to more particles being tracked successfully, this also increased the processing time. As we have seen with IPR above, there might be a number of iterations after which the results no longer change. The same single-shot data as for IPR and section 7.2 were processed with TP-STB tracking iteration counts of 1 (forces non-iterative operation), 5, 10, and 20 while monitoring the number of retrieved velocity tracks. The resulting number of tracks is plotted in fig. 8.7 and compared to the number of tracked particles from single-pass PTV. The switch from PTV to TP-STB resulted in a 12-fold increase in tracked particles, even for a single-pass of TP-STB. This improvement stemmed not only from tracking with TP-STB, but also the improved camera calibration with VSC and a higher number of reconstructed particles using IPR contributed to the improvement. Allowing a multi-pass operation with five iterations of TP-STB increased the number of tracks by another 16 %. Increasing the number of iterations further did not yield substantial gains (changes between 5, 10, and 20 iterations <1 %), as the true number of tracks had been tracked already. As the processing time increased linearly with the number of TP-STB tracking iterations, a setting higher than 10 seemed excessive with the present data. The tracking overhead per single-shot recording was also small, with 7 s, totalling a processing time of 13 s per single-shot (twice IPR plus TP-STB per single-shot).

Comparing the number of tracked particles from TP-STB to the number of 3D particle positions obtained from IPR above, about half of the reconstructed particles were successfully tracked. Besides limitations in the tracking itself, this could result from a spatial mismatch of volumes illuminated by the first and second green laser pulse or from ghost particles that could not be tracked over time. The overlap of both green beams was ensured by recording double-frame Mie scattering recordings with a very short time delay between both green laser pulses of 4 µs. Applying a 2D cross-correlation algorithm on these images yielded the degree of beam overlap encoded in the correlation peak value. If the beam overlap was perfect, a correlation value of 1 would indicate that both camera images were identical. Due to slight differences in the laser beam profiles and residual misalignment correlation peak values of 0.85 to 0.9 were found for the present data. This left ghost particles as

explanation for the remaining difference in reconstructed and tracked particles. By reducing the allowed triangulation error during IPR processing, the number of ghost particles could be reduced (Wieneke 2008; Wieneke 2012), which might be especially valuable once camera recordings with higher particle image seeding density will be evaluated.

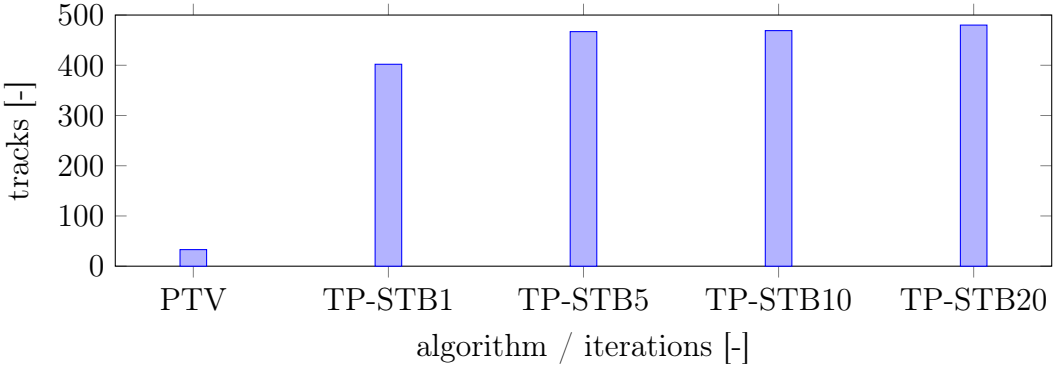

Figure 8.7: Number of particle tracks depending on algorithm and iteration count.

The processing time of 7 s per single-shot for TP-STB compared to 85 s using the PTV implementation. The speed-determining step for PTV was the multi-pass cross-correlation to obtain the initial displacement guess for the initialisation of the tracking algorithm. Such a guess is not strictly needed for TP-STB, but could be added. In general, TP-STB relies on the minimisation of a cost function to find the most likely match between particles of the first and second time steps (Novara et al. 2023). As detailed in section 4.3.3, a global displacement guess or velocity predictor

$$P = [\bar{v}_x \pm v'_x | \bar{v}_y \pm v'_y | \bar{v}_z \pm v'_z] \tag{8.1}$$

could be provided to aid TP-STB in the pairing process, by restricting the search area for pairing partners within the second frame volume (Novara et al. 2022). For this, the expected mean $\bar{v}_i$ and fluctuation v'_i velocity components in $i = x, y, z$ direction are used. Therewith, this predictor acts as a filter as it limits the range of valid velocity results. This is useful if the flow is characterised by a rather stable time-averaged velocity profile with fluctuations in a limited range. As this is the case for the investigated turbulent jet flow, three different predictors were evaluated by repeatedly processing the same raw data from above: First, a zero-mean predictor was investigated ($P_1 = [0 \pm 25 | 0 \pm 50 | 0 \pm 25]\ m/s$). The conveyed information

was limited to the velocity fluctuation magnitude and a preference for the y-axis velocity component. The absolute limit of 50 m/s was easily obtained from the bulk velocity of the jet flow and the $1/7^{\text{th}}$ power law, as demonstrated in section 7.2 (fig. 7.3). The second predictor acknowledged that negative axial velocities were rather unlikely in the present jet flow, but large fluctuations were expected in this turbulent jet flow. The velocity estimate in the non-axial directions was limited to 75 % of the streamwise component with zero mean ($P_2 = [0 \pm 25.5|34 \pm 34|0 \pm 25.5]$ m/s). Finally, the velocity boundaries were tightened by allowing only 50 % of the axial velocity as fluctuation in v_x and v_z ($P_3 = [0 \pm 17|34 \pm 34|0 \pm 17]$ m/s). The velocity results for all three parameter sets were compared with respect to the retained number of tracks (fig. 8.8a), measured mean absolute velocity, and histograms for the axial velocity component (fig. 8.8b).

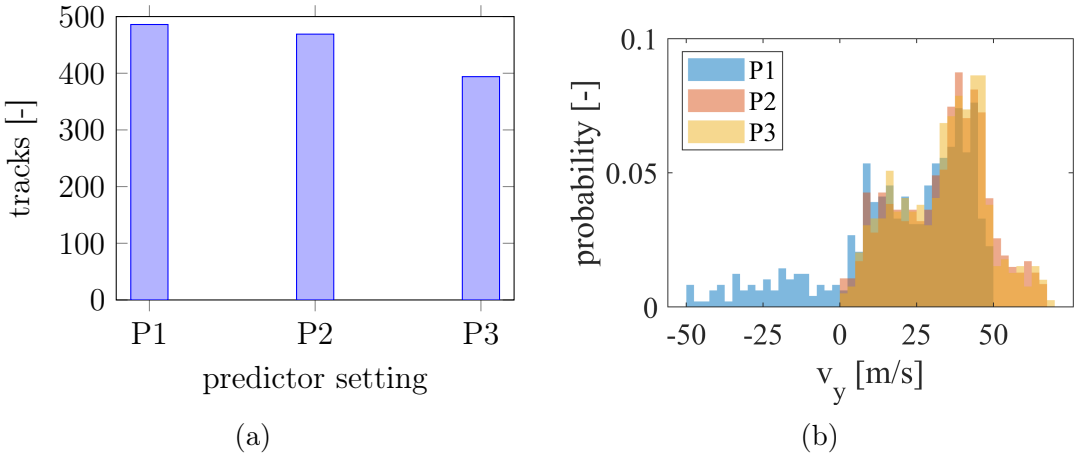

Figure 8.8: Computed number of tracks (a) and histogram of axial velocity component (b) depending on selected velocity predictor.

Comparing the results for different velocity predictors in fig. 8.8a, the number of computed particle velocity tracks decreased as the limits of the velocity predictor became stricter. This was expected, as the predictor bounds present limits for the allowed velocities. This is apparent in the axial velocity histogram in fig. 8.8b, where the maximum velocity was clipped at 50 m/s, corresponding to the spread of P_1. However, a larger sample size is not necessarily better. If it results from overly wide velocity predictor boundaries, a number of 'ghost tracks' might appear as result of false particle pairing between the first and second time steps. This was the case for $P1$ where many of the tracks with high negative axial velocity

were found in the potential core region of the jet. While recirculation and vortices in the shear layer between jet and co-flow could lead to negative axial velocities, their appearance within the potential core of the jet is very unlikely. The velocity distribution and average absolute velocities for P_2 and P_3 were very similar with only 4 % difference. Considering the higher sample count for $P2$, it was selected for the present evaluations. The average velocity measured using P_2 was 35.85 m/s, which is within 5 % of the bulk velocity computed from the gas flow rate and nozzle diameter (34 m/s).

To reject spurious vectors from the velocity results, a 3D median filter was applied. For this filter, the absolute velocity deviation of every track to its n neighbours was computed. Then, this deviation was compared to the deviations found for its n neighbours. If the difference exceeded m times the standard deviation from the deviation of its n neighbours, the track was rejected. With $m = 3$ only strongly deviating particles were removed which was important in this turbulent flow. In laminar flows, smaller values for m might be justified. The effect of the median filter on the instantaneous velocity field of the single-shot recorded under non-isothermal flow conditions (shown in fig. 7.1, fig. 8.6) is plotted in fig. 8.9. Only 18 out of 469 particles were removed by applying the median filter. Three of these particles with very high velocities were removed in the outer region of the flow (marked by arrows). For all following results, a median filter with $m = 3$ was applied.

It was clear that using TP-STB in conjunction with VSC and IPR lead to a much higher velocity sample count based on the single-shot results presented above. To check the validity of the new velocities, the time-averaged axial velocity profile was computed and compared to the prediction from the $1/7^{\text{th}}$ power law (Chant 2005), as done for PTV validation above. To obtain a good estimate for the time-averaged velocity profile, the same raw camera image data as for the cumulative results in fig. 7.2 were processed with TP-STB. Compared to 3100 individual particle measurements retrieved using legacy processing, a whopping 29600 measurements were extracted using the advanced algorithms. These measurements were binned according to their radial distance from the jet axis using the same scheme as for fig. 7.3 on page 132 (0.5 mm bin width, 33 % overlap). To obtain the continuous velocity profile plotted in fig. 8.10, a cubic Hermite spline was fitted to the median velocity computed for each bin. Error bars indicate the 1σ standard deviation

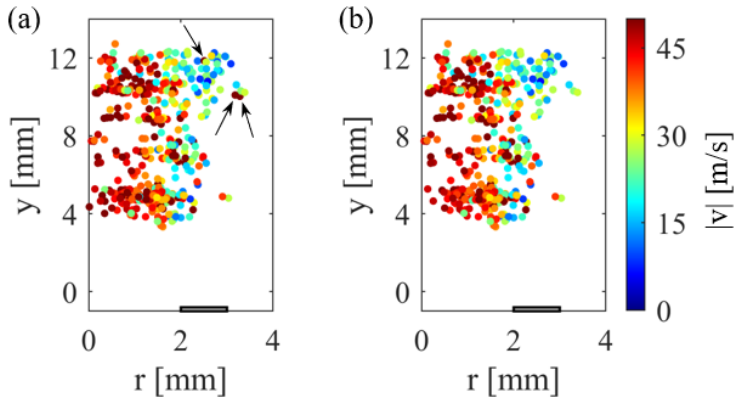

Figure 8.9: Particles tracked in a single-shot measurement without (a) and with (b) applied median filter in radial distance from jet axis versus distance from the jet nozzle plot. Colour indicates absolute velocities. The jet nozzle pipe is indicated at the bottom in gray, and black arrows mark three out of 18 velocity measurements removed by the filter.

variation of measured velocities within each bin. A good match between measured and predicted velocity profiles was achieved for r <2 mm (within the inner radius of the jet nozzle). As gas from the co-flow was entrained into the free jet flow once it left the nozzle, velocities higher than those predicted for an enclosed pipe flow were expected. This was supported by the TP-STB results, which were above but within 1σ from the theoretical predictions. The shear layer between the jet and co-flow is reflected in the large variations in the measured velocities in the region $1.5 < r < 2.5$mm. Beyond the shear layer, the measured velocities declined towards co-flow bulk velocity. These results were in good agreement with those previously obtained from the double-frame PTV implementation (cf. fig. 7.3 on page 132), supporting the validity of the TP-STB results.

After establishing the validity of velocity results from TP-STB by exploiting the predictable average velocity field of this jet flow, coherent 3D flow structures were investigated. While scattered results from TP-STB are free from spatial averaging and allow measurement of the flow velocity at the exact same location as the temperature, several measures in fluid mechanics are well-defined for grid-based data only. Hence, the scattered data from TP-STB might be binned to regular grid points to access commonly used measures such as vorticity (Guyon et al. 2015) or the Q criterion (Jeong et al. 1995). To bin the data to a regular grid, the spacing

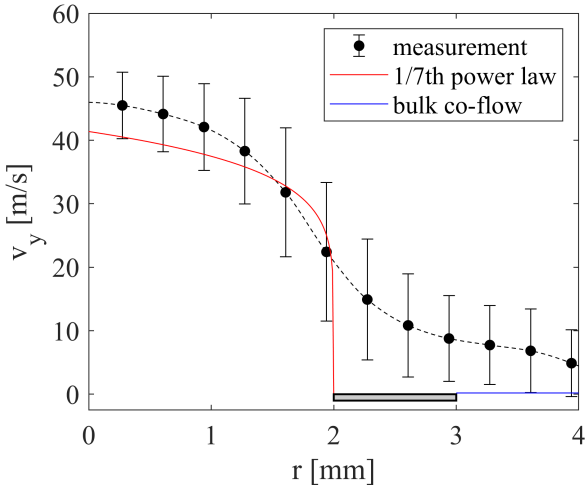

Figure 8.10: Axial velocity profile derived from cumulative TP-STB processing compared to predictions from $1/7^{\text{th}}$ power law for turbulent pipe flows. Error bars for one standard deviation of measured velocities, nozzle pipe wall and bulk co-flow velocities are indicated. Modelled after fig. 7.3.

of the grid must be determined first. The grid spacing is a critical parameter, as it determines the spatial resolution of the binned velocity field and of all derived quantities. A limiting factor for the minimal grid spacing is the requirement to have at least n tracks within the sub-volume with a radius of i voxels around each grid node. Otherwise, the binned grid data would have discontinuities. Even though the number of tracks retrieved from individual single-shot measurements had increased dramatically compared to the initial demonstration in chapter 7, the current seeding density limits the resolution for instantaneous grid data to a minimum of 80 voxel ($i = 40$). Using an overlap of 75 % between adjacent binning sub-volumes, similar to the window overlap in (2D-)PIV, the effective grid spacing was reduced to 20 voxel or 0.6 mm. For this demonstration, the minimum number of tracks within each binning sub-volume was set to $n = 1$. If multiple tracks were found within a sub-volume, their contributions to the grid node value were weighted according to the distance to it using a Gaussian weighted average (LaVision 2025). Once the data were binned, a deeper analysis was possible. Here, 3D isosurfaces of instantaneous absolute velocity are shown in fig. 8.11. As expected, the enclosed volume close to the jet axis decreased with increasing velocity boundary value. These isosurfaces highlight the importance of instantaneous 3D measurements for

investigations of turbulent flows, as these clearly show 3D features and a loss of rotational symmetry about the jet axis for instantaneous measurements.

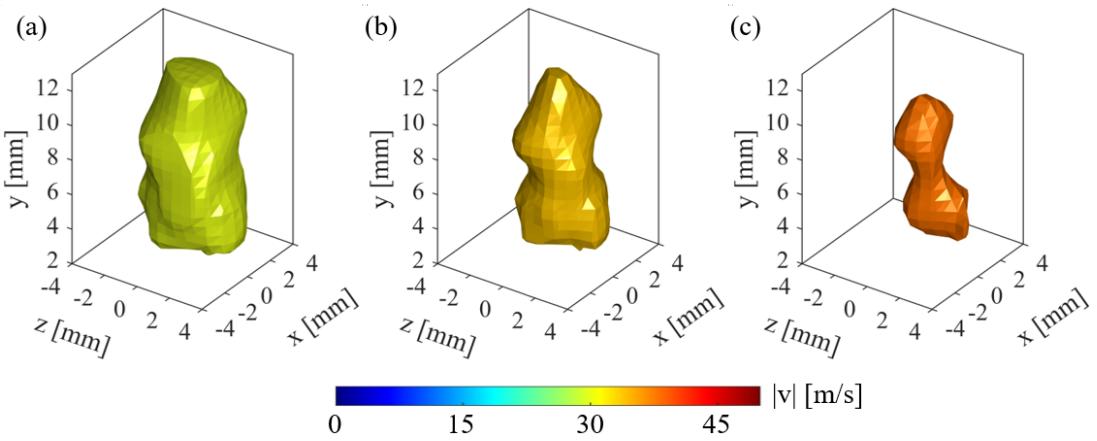

Figure 8.11: 3D isosurfaces from single-shot TP-STB results enclosing flow regions with velocities above 30 m/s (a), 34 m/s (b), and 38 m/s (c).

In conclusion, introducing TP-STB as a replacement for the double-frame PTV with an initial guess from ensemble cross-correlation and subsequent nearest neighbour pairing resulted in a substantial enhancement of 3D particle velocity samples (tracks) that were extracted from the same camera images that have been used for the initial demonstration in chapter 7 (page 127 et seqq.). The larger number of tracks retrieved per single-shot measurement allowed a deeper analysis of 3D flow structures while being in good agreement with time-averaged data from legacy processing. As a quality of life improvement, the combined 3D reconstruction and tracking time was an order of magnitude lower than for the legacy implementation, allowing for a faster turnover time of experiments. The following sections discuss the combination of the 3D position and velocity information of individual particles with temperature values, which were also obtained using improved algorithms (cf. the right leg of fig. 8.2).

8.5 Luminescence particle image segmentation

Following the right leg of the processing flow chart in fig. 8.2, the 3D particle locations reconstructed using IPR were projected onto the corresponding pre-

processed images of cameras T1 and T2 using the camera models resulting from VSC (section 8.2). These projections were then paired with 2D luminescence images in cameras T1 and T2 (local intensity maxima), analogous to section 6.3.3. As established in section 8.2 (fig. 8.3b), the matching certainty between 3D and 2D space was improved by using VSC and IPR for camera calibration and 3D reconstruction. This reduced not only the likelihood of false pairing of 3D and 2D particle information, but also reduced the likelihood of false pairing between both luminescence imaging camera recordings. The subsequent segmentation of the imaged luminescence signal from the background-subtracted camera images of T1 and T2 remained a critical step on the way to temperature information. In section 6.3.4, a 2D Gaussian fit was introduced to generate pixel masks for segmentation. Using this segmentation scheme required the presumption that the intensity distribution of individual luminescence particle images followed a 2D Gaussian distribution. While this is generally true for diffraction-limited macroscopic imaging of microscopic particles (Hecht 2017), the discretisation of the image into pixels of finite size had to be considered. While the study from Xuan et al. 2023 reports high $R^2 = 0.9$ for their 2D Gaussian fits of images from micrometer SMP:Sn^{2+} and ZnO particles, for the data evaluated in Stelter et al. 2023 the R^2 values of ZnO particle image fits show a broader distribution, as shown below in fig. 8.12. This difference was attributed to several factors. First, the data in Xuan et al. 2023 were recorded from a 2D laser sheet instead of a 3D volume, reducing the influence of high-frequency noise in the images originating from imaging particles overlapping in volume depth (z-axis) and out-of-focus image blur. Second, the magnification of the imaging system was much higher than in the present work (0.6 vs 0.2) while the minimum camera lens aperture was smaller ($f/2$ vs. $f/1.4$). Hence, the diffraction-limited diameter in the present work was three times smaller than that in Xuan et al. 2023, equal to a quarter of a pixel.

Therefore, while many particles were fitted nicely using the 2D Gaussian distribution with 86.6 % of particle images having an R^2 of above 0.8 in camera T1 (64.5 % in T2), 4.5 % (6.8 %) were below $R^2 = 0.6$. This suggested that a 2D Gaussian function might not be ideal to describe the present luminescence particle images and that camera T2 was more prone to producing images with strong aberrations, that could not be fitted with the Gaussian function. While one could reject particle samples

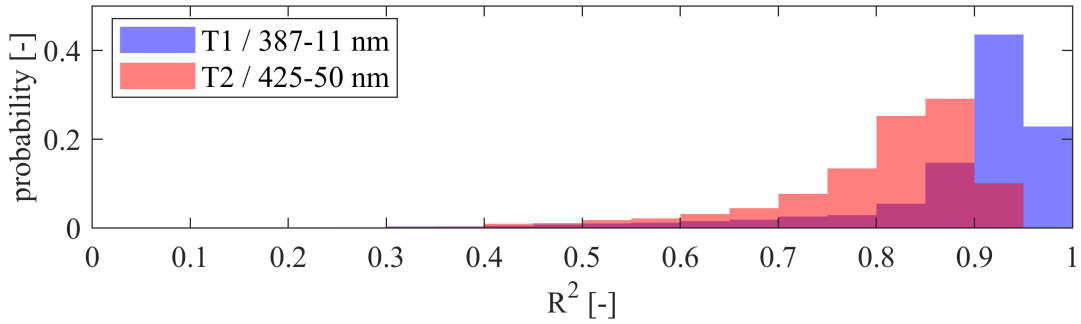

Figure 8.12: Histograms of R^2 values obtained from the rotated 2D Gaussian fit (eq. 6.10 on page 110) for individual luminescence particle images from recordings of both cameras T1 and T2.

where the fit results in R^2 values below some threshold, objectively determining a *good enough* threshold value of R^2 is not straightforward, and the number of samples should be kept as high as possible. Hence, other image segmentation and signal integration schemes were explored that either do not impose *a priori* assumptions about the particle image shape (i.e. do not require a Gaussian shape) or work together with the Gaussian fit by trying to eliminate interferences such as from hot pixels or adjacent particle images by acting as a pre-mask before deriving the Gaussian fit. An overview of the eight luminescence image signal integration schemes is provided in table 8.1. These schemes were grouped into single-stage schemes (SiSt) and dual-stage schemes (DuSt), depending on whether a pre-mask was used. For all SiSt, the imaged luminescence signal was directly computed using the primary mask, whereas for DuSt variants, the primary mask was used to select the pixel area to which a 2D Gaussian function was fitted to generate the final secondary mask. Furthermore, the segmentation algorithms have been divided into two types. The first type were Gaussian-fit-based algorithms. The second type were region growing algorithms (RGA) (Pal et al. 1993), including a gradient search (GS) and active contour (AC) segmentation algorithm. Details on these algorithms are provided below. After segmentation, the luminescence intensity per particle was integrated in one of two ways: The signal was either calculated as in Stelter et al. 2023 by summing the masked pixel intensities or the obtained fit function was integrated numerically. In total, five different segmentation schemes were implemented as a combination of Gaussian fit and region-growing algorithms. For every fit-based segmentation scheme, the signal was integrated in two ways,

resulting in eight signal integration schemes presented in table 8.1.

Table 8.1: Overview of luminescence image segmentation and signal integration schemes for LIR calculation.

Tag	Primary mask	Secondary mask	Intensity integration
SiSt1	2D Gauss fit	-	Pixel sum
SiSt2	2D Gauss fit	-	Fit integration
SiSt3	RGA GS	-	Pixel sum
SiSt4	RGA AC	-	Pixel sum
DuSt1	RGA GS	2D Gauss fit	Pixel sum
DuSt2	RGA GS	2D Gauss fit	Fit integration
DuSt3	RGA AC	2D Gauss fit	Pixel sum
DuSt4	RGA AC	2D Gauss fit	Fit integration

As an alternative to the 2D Gaussian fit, two region growing algorithms were implemented as they do not impose any assumption on the shape of individual particle images. The first variant (RGA GS), developed together with Senarathna 2023, works based on intensity gradients within a subwindow. This sub-window is extracted from the camera images as a 25×25 pixel window centred on a detected particle image to serve as the processing domain for the segmentation algorithm. Within this domain, the core of the particle image is detected to serve as the starting point for the region-growing algorithm. All pixels close to the centre of the domain that are above 30 % of the maximum pixel intensity are selected as core. This core is then grown by comparing the intensity gradient from each pixel in the core boundary to each 8-connected neighbour pixel outside the core. If the gradient is negative and the candidate pixel intensity is above the stopping threshold, the candidate pixel is added to the core. The stopping threshold was set as the average background pixel intensity (background = all pixels in the domain not contained in the masked area) plus one standard deviation of the background pixel intensity. This threshold is adapted every time a new pixel is added to the mask, and the process is repeated until the mask is no longer growing. The second region-growing algorithm (RGA AC) works not based on image gradients but minimises an energy equation between the fore- (particle) and background parts of the 25×25 pixel processing domain, as described in detail in Chan et al. 2001. As both region-growing algorithms use a different principle to expand their region

boundaries, implementing and comparing both seemed fit.

In fig. 8.13 a sample particle image is shown with masks generated using all five segmentation schemes. The background-subtracted particle image before segmentation is shown in fig. 8.13a. Another close-by particle image is visible in the upper border of the shown window. All segmentation schemes excluded this secondary particle image (fig. 8.13b-f) but produced slightly different masks.

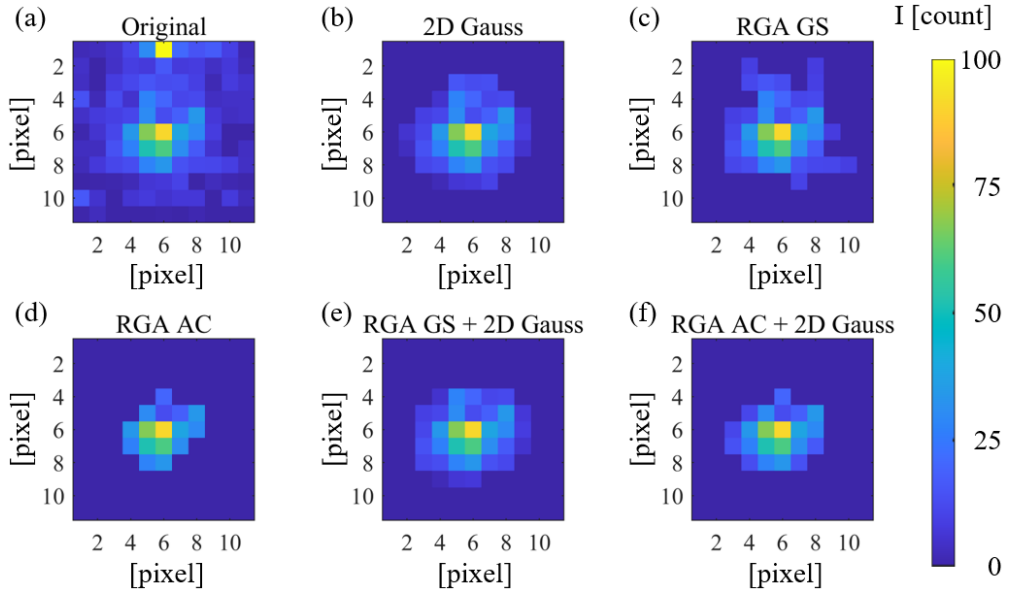

Figure 8.13: Particle luminescence image recorded by camera T1, after background subtraction (a) and segmentation using five schemes (b-f).

To compare the performance of all schemes, 3D data recorded in an isothermal flow were used. The luminescence signal was segmented and integrated using all eight schemes shown above in table 8.1. Then, the normalised LIR uncertainty was calculated as the standard deviation of the LIR normalised to the mean LIR of each scheme. To provide a quick qualitative comparison among the schemes, the resulting values were normalised to the uncertainty from the best-performing scheme and plotted in blue in fig. 8.14. The lowest normalised LIR uncertainty was achieved using the DuSt2 scheme, a dual-stage scheme consisting of a pre-mask from RGA GS and a secondary mask from a 2D Gauss fit, where the signal was obtained by integrating the fit function rather than summing the masked pixel intensities. Compared to the previously used SiSt1 scheme (chapter 7, Stelter et al.

2023), the estimated uncertainty was halved. Using the RGA algorithms for fitting without a secondary mask (SiSt3 and 4) was not promising, as the uncertainty was doubled for them again compared to scheme SiSt1. On average, the dual-stage schemes result in 2.4 times lower uncertainty than the single-stage schemes. In addition to the LIR precision, a high number of samples was still desirable. Hence, the number of particle image samples where the segmentation and luminescence signal integration using a given scheme was successful was counted and plotted in fig. 8.14 as red bars. On average, 1460 particles were available per scheme, with a minimum of 1342 particles for DuSt1 and 2, and a maximum of 1660 particles for SiSt4.

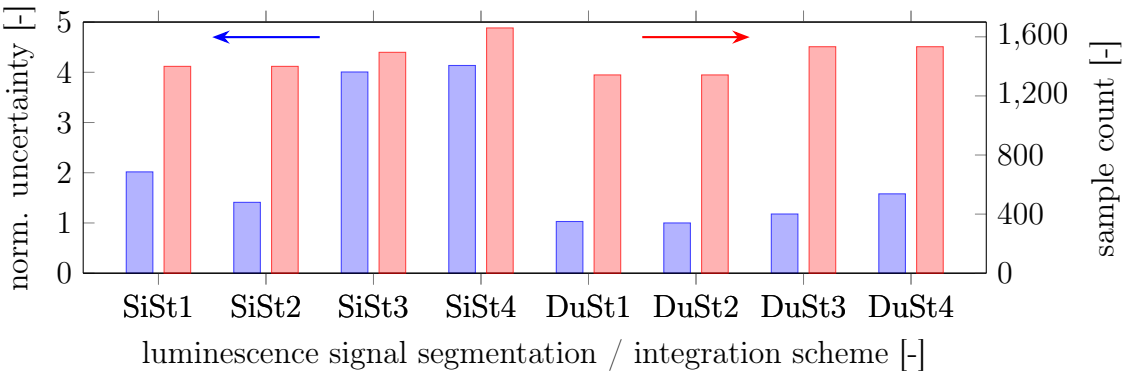

Figure 8.14: LIR uncertainty (blue bars) obtained using eight image segmentation and signal integration schemes (cf. table 8.1 on page 160) normalised to the best performing scheme (DuSt2) and number of temperature and velocity samples retained per scheme (red bars).

In summary, eight schemes for segmenting and integrating imaged luminescence signals were presented and evaluated in this section. The best performing scheme in terms of LIR precision was DuSt2, while the highest number of samples were available with the single-stage region growing algorithms SiSt3 and SiSt4.

8.6 3D flat field correction

While the assumptions about a small angle of collection of the cameras as in section 6.4 were valid for evaluations in this chapter, the aim is to measure in

larger measurement volumes. As this would increase the angle of collection, the assumption of negligible angular effects of the interference filters might no longer hold. To compensate for these effects, a 3D flat-field correction was introduced. This allows to estimate the collection non-uniformity α in combination with the LIR fluence dependence γ following eq. 6.15 (page 120).

A 3D correction map can be obtained in at least three ways. First, the measurement volume could be divided into small sub-volumes, similar to tomographic reconstruction (section 6.2.2). Using image data recorded in an isothermal flow, the average LIR within each sub-volume would be calculated to directly obtain a true 3D correction map. However, a vast amount of data would be needed to provide sufficient particle samples per sub-volume for a stable average LIR estimation. To reduce the required particle sample count, the existing 2D FFC in the yz-plane (laser beam cross-section) could be combined with another 2D FFC in the xy-plane (camera field of view). This would be straightforward to implement but might lead to an overcorrection along the y-axis, as this axis would be part of both planar corrections. Another approach, that circumvents this potential issue, was to combine the existing yz-plane correction with an x-axis correction as follows.

To obtain the 3D correction map, a 2D correction map was computed first in the yz-plane, as described in section 6.4. Compared to the preceding chapter, the number of available particle samples increased from 2900 to more than 13500 thanks to the improved algorithms introduced above. This allowed refinement of the calculation grid for the 2D FFC map to 28×28 cells. Hence, the resolution of the correction map shown in fig. 8.15(a) was increased by 80 % compared to fig. 6.39 (page 122). At the same time, the uncertainty in the average LIR calculated per grid cell was below 3 % for most of the 2D correction map, as shown in fig. 8.15(b). If the uncertainty exceeded 10 %, the cell was removed from the FFC map. Only very few cells at the border of the illuminated area were removed this way. Finally, the yz-plane correction map was smoothed, and gaps were interpolated using the *smoothn* algorithm (Garcia 2010b; Garcia 2010a) to provide a continuous correction map (fig. 8.15(c)). To augment the 2D FFC, an x-axis dependent correction value was computed. For this, the x-axis extent of the measurement volume was discretised into six bins, and the average LIR within each of these bins was computed from the contained particle samples. Applying the same selection

rules as for the computation of the yz-plane correction map yielded a distribution of correction values, as plotted in fig. 8.16a. While the detected variation of the average LIR along the x-axis was low, it was measurable, indicating the need for a correction in this dimension of the measurement volume as well.

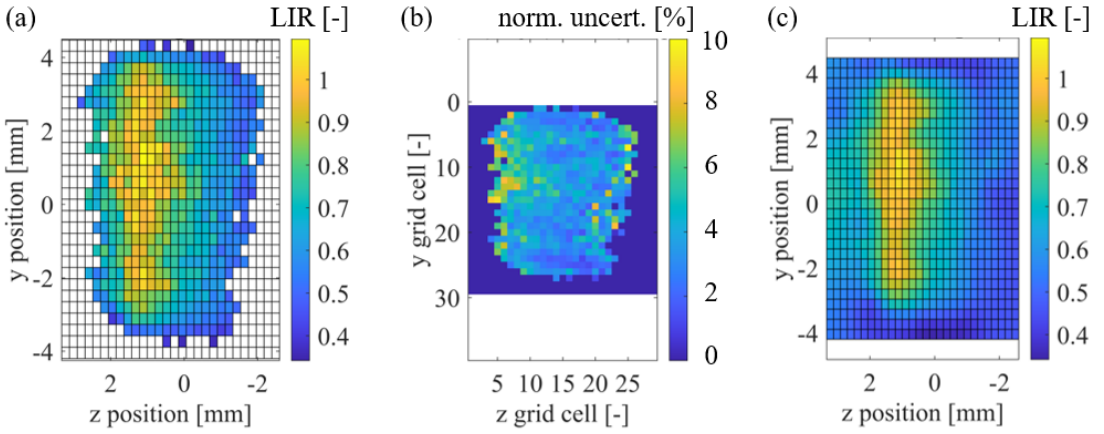

Figure 8.15: Average LIR per grid cell in yz-plane (a), normalised uncertainty per grid cell (b), and (c) interpolated correction map.

To apply the 3D correction, first, the values of the yz-plane and x-axis correction maps were interpolated at the location of the particle whose LIR should be corrected. Then, the product of the xy-plane and x-axis correction values was computed and normalised using the average LIR to prevent large alterations in the average LIR distribution by the FFC application. Finally, the raw LIR was divided by the normalised product to produce the corrected LIR. The effect of this 3D FFC is shown in fig. 8.16b, where the LIR histograms of isothermal data are plotted before and after FFC. After FFC, the distribution was noticeably narrower, and the LIR distribution was concentrated on the average LIR.

The combination of two separate low-dimensional corrections to create a combined 3D correction was advantageous for the present technique, as it reduced the number of required particles per unit volume to obtain a reliable estimate for the correction map values. Compared to a 2D FFC in yz-plane, the 3D FFC improved the LIR precision by just 3.5 % which underlined the limited influence of angular collection non-uniformities for the present data. It should be noted that separate FFC maps must be computed for each luminescence image segmentation and signal integration

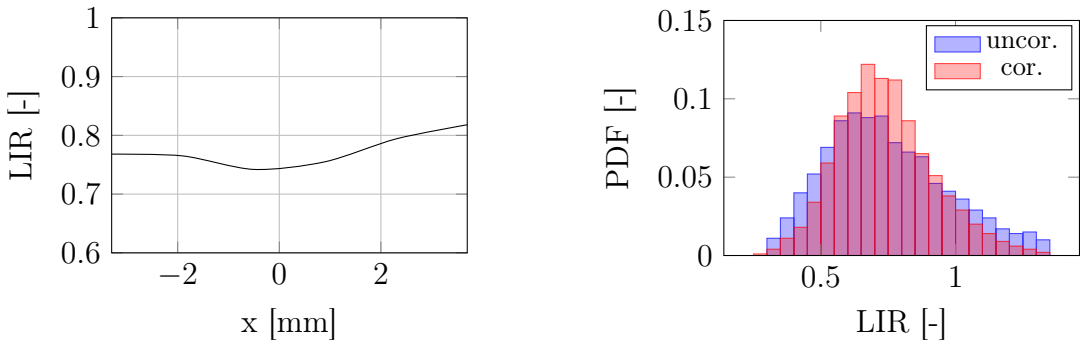

(a) (b)

Figure 8.16: Correction factor as average LIR per bin along the x-axis (a) and probability density functions of LIR (b) obtained from isothermal data at ambient temperature of 300 K before and after correction.

scheme (cf. table 8.1 on page 160). Here, the results for the DuSt2 scheme were shown exemplarily, as it was deemed most promising in the preceding section.

8.7 Effect on non-isothermal turbulent gas jet measurements

After advanced algorithms for camera calibration (section 8.2), 3D reconstruction of particle positions (section 8.3), 3D particle tracking for velocimetry (section 8.4) had been implemented, a 3D flat field correction (section 8.6) was added, and luminescence signal integration schemes (section 8.5) were improved, the effect on joined 3D temperature and velocity results was accessed below. As the impact of the individual algorithmic improvements had already been assessed in the respective sections, here the focus was on the impact on the joint temperature and velocity results. This concludes the right leg of fig. 8.2 with the derivation of a new temperature calibration scheme and its use for the conversion of LIR values computed for every individual particle to temperature. For the rest of this chapter, the same raw data as evaluated for chapter 7 were evaluated to allow for a direct comparison of the results.

As the luminescence signal segmentation and integration schemes introduced in

section 8.5 altered the absolute LIR derived from camera T1 and T2 images for each phosphor particle, the calibration function for conversion of LIR values to temperatures had to be adapted. The same strategy as in Stelter et al. 2023 was applied for this. The average LIR was calculated from the image data recorded in an isothermal flow at ambient temperatures of 300 K. The previous calibration function from section 6.5 was then normalised to this value. As the luminescence signal was now obtained in eight different ways, this process was repeated for each luminescence signal segmentation and integration scheme, resulting in eight slightly different power-law fit calibration functions. For details on the process, refer to section 6.5 and Stelter et al. 2023.

Using the combination of advanced processing algorithms, the number of individual particle samples with valid temperature and velocity results was increased by a factor of 2.2, from 3100 particles in section 7.2 to more than 6950 particles or 34 particles/mm^3 (considering a particle filled volume of 205 mm^3), depending on the luminescence image segmentation and signal integration scheme. The cumulative results for the DuSt2 scheme are presented in fig. 8.17. Only particles at negative z-position are shown to reveal the hot and fast potential core region of the jet. Hence, only approximately half of the available particle samples are plotted here. This scheme was chosen as it was deemed to be the most promising in section 8.5, where it achieved the lowest LIR uncertainty from isothermal results. The results confirmed the expectation regarding the temperature and velocity distributions within the flow. Temperatures and velocities were highest at the centre of the jet and decline with increasing radial distance from it. As the velocity results plotted here are a subset of the data plotted in fig. 8.10, their agreement with the theoretical profile of a turbulent pipe flow has already been established. The validity of the temperature results is supported by the average temperature measured at the jet axis being close to the set temperature of 433 K.

Very few cold particles were detected within the potential core region of the jet (fig. 8.17c). As they were also associated with a high velocity, they were likely examples of measurement errors, as fast particles should originate from the hot jet centre. The relationship between measured particle velocities and temperatures is also visualized in fig. 8.18, where each particle is represented as a cross at a position determined by its measured temperature and velocity. The resulting cloud

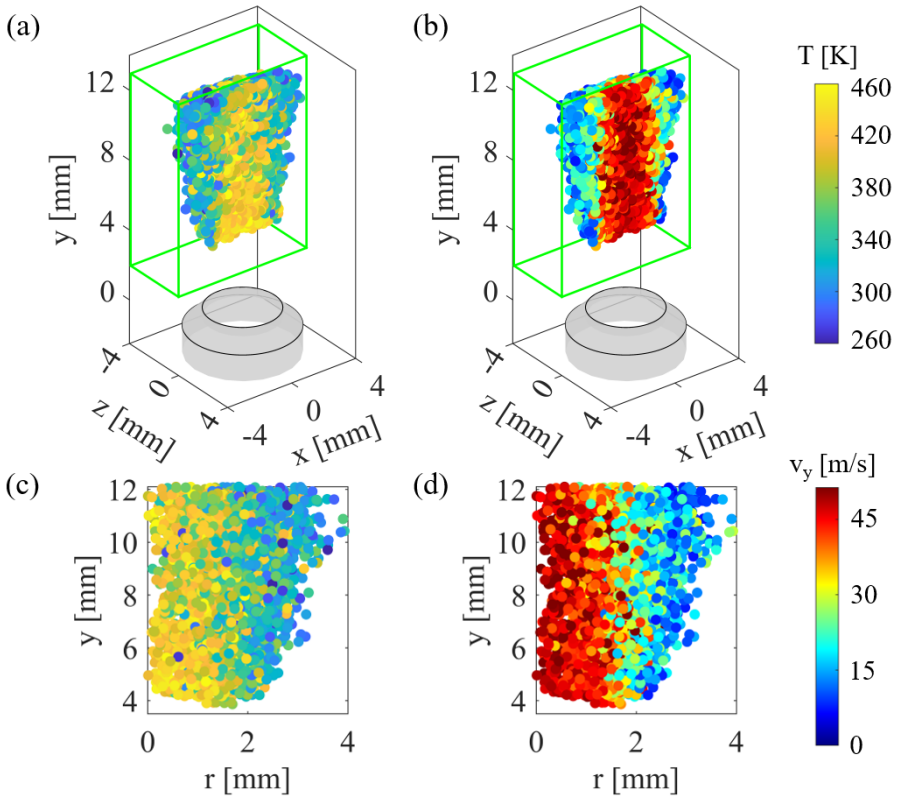

Figure 8.17: Cumulative 3D temperature (a, c) and velocity (b, d) results obtained from the same image data as fig. 7.2 but using advanced algorithms.

of data points suggests the expected relationship of faster particles being hotter, too. At the same time, this plot visualizes the current measurement uncertainty by the spread of the data point cloud, and probable measurement errors considering the isolated crosses far away from the central cloud.

Temperature and velocity uncertainties were quantified analogous to section 7.2 using the root-mean-square variation of both quantities within a 2.5 mm diameter cylindrical region centred on the jet axis. While the measured temperature fluctuations of 28.48 K were almost identical to previous results in section 7.2 (+3.9 %), the measured velocity fluctuations increased to 6.14 m/s (+36.4 %). While the temperature precision was still mainly limited by the available signal level, the measured temperature precision varied between 28.48 K and 33.49 K, depending on the luminescence signal segmentation and integration scheme. In line with findings from section 8.5, scheme DuSt2 resulted in the best precision. The increased

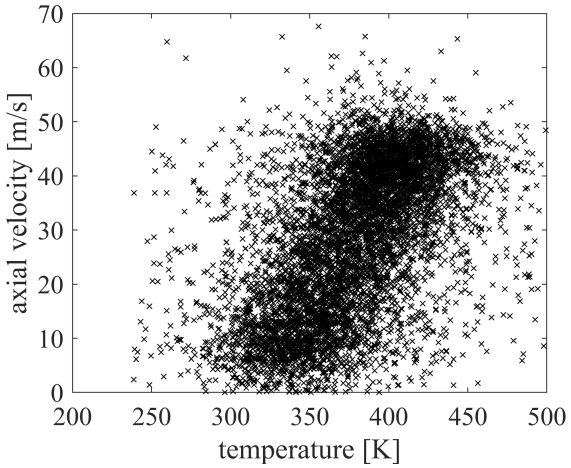

Figure 8.18: Particle velocities plotted against particle temperatures to illustrate the relationship between both quantities.

measured velocity precision could either be indicative of TP-STB being able to better measure physical velocity variations or of adding extra noise. A comparative study of our 3D-PTV algorithm and TP-STB using artificial particle distributions, where the true particle displacement is known as ground truth, could clarify this, similar to the TP- and TR-STB comparison in Novara et al. 2023.

A direct comparison of cumulative results obtained from the same image raw data using either the initial (chapter 7) or advanced processing pipeline (this chapter) is provided in fig. 8.19. Temperature and velocity results are plotted side-by-side in xz-plane plots as if looking down onto the jet nozzle. Results from chapter 7 are plotted on the left and results from the current chapter are plotted on the right. Results obtained using both the earlier processing schemes and the advanced algorithms resolve the expected time-averaged temperature and velocity profiles. In both cases the temperature results were more noisy than the velocity results. Results from the more advanced processing introduced in this chapter showed a more narrow potential core region of the jet in both temperature and velocity results. Velocity results showed a more fine-grained profile with a group of highest velocities in the centre close to 48 m/s that was not resolved by the legacy processing. The more narrow potential core region resulting from advanced processing also explains the difference in velocity precision between legacy and advanced processing. For the latter, a smaller potential core diameter could be used for estimation of temperature and velocity precision which would lead to favourable numbers. For

the present thesis however, the same potential core diameter was used to compare identical flow regions across different processing schemes.

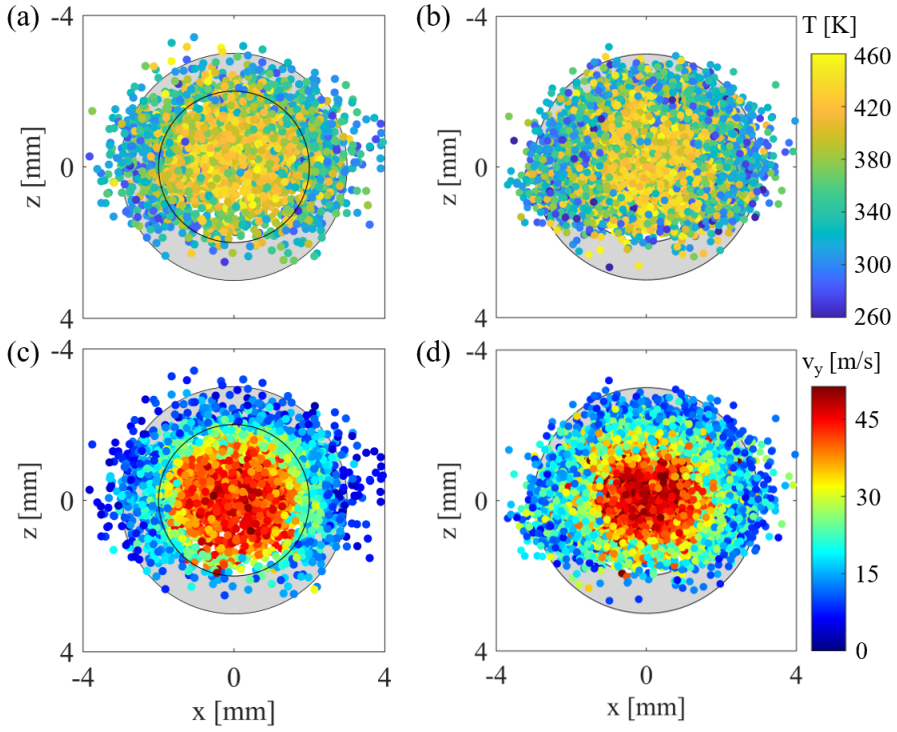

Figure 8.19: Cumulative temperature (a, b) and velocity (c, d) results obtained from the same image data, either using the processing pipelines of chapter 7 (a, c) or the current chapter (b, d).

The single-shot results also reflect the advantage of using advanced processing algorithms for image data evaluation. From the same single-shot image data as for fig. 7.1 (page 129), up to 54 particle samples (+63 %) were obtained in a volume of 89 mm^3, corresponding to a median inter-particle spacing of 900 µm. To maintain consistency with cumulative results shown in fig. 8.17, the single-shot result shown in fig. 8.20 was also computed using the DuSt2 scheme, even though the increase in particle number was below average for this scheme for this particular single-shot.

As for the cumulative data, a direct comparison of single-shot results obtained from the same image raw data using the initial and improved processing pipeline is facilitated in fig. 8.21. Temperature and velocity results are plotted side-by-side in ry-plots (radial distance from jet centre axis vs. distance from nozzle exit). Results from chapter 7 are plotted on the left and results from the current chapter

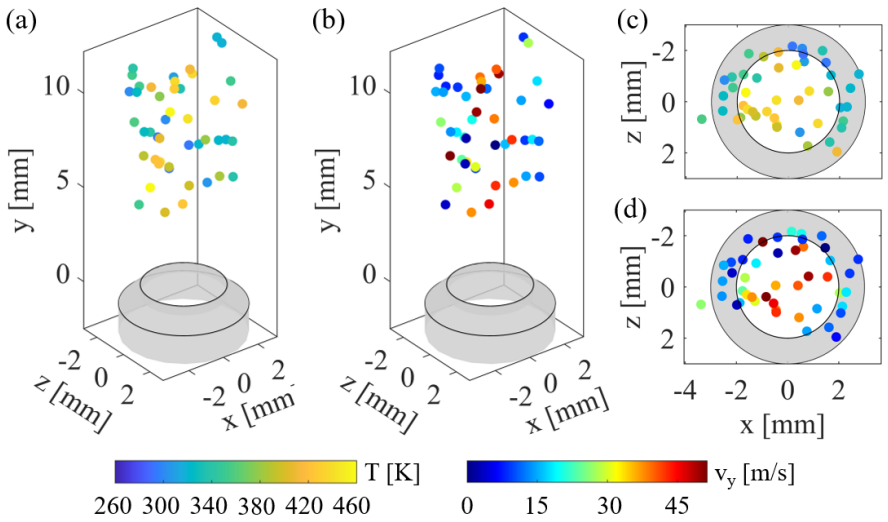

Figure 8.20: 3D temperature (a, c) and velocity (b, d) results obtained from the same single-shot image data as fig. 7.1 using advanced algorithms.

are plotted on the right. While the higher number of samples obtained using the advanced algorithms is apparent the samples are differently distributed within the measurement volume. While the results obtained from processing in chapter 7 are more spread along the r-axis, processing with the more advanced algorithms lead to a more even sample distribution along the y-axis. The same individual particle sample was rarely identified by both processing pipelines though. On its own, both sets of results seem valid as hotter and faster samples are grouped towards the jet central axis. If a certain particle sample could be evaluated was determined to a large extent by the particle image segmentation scheme. This was found when comparing single-shot results obtained from the same image data but using different segmentation schemes introduced in section 8.5. In fig. 8.21, the used segmentation schemes differ as DuSt2 was found to result in the best LIR precision with the advanced processing pipeline while SiSt1 was used before. See table 8.1 on page 160 for an overview of the segmentation schemes. A detailed analysis of the influence of the particle image segmentation scheme on retaining individual particle samples is an opportunity for further research.

Both the cumulative and single-shot results confirmed earlier findings and expectations from theory. Hot and fast particles were clustered within the jet flow region above the nozzle outlet. Comparing the joined temperature and velocity results to the pure velocity results obtained using TP-STB in section 8.4, temperature

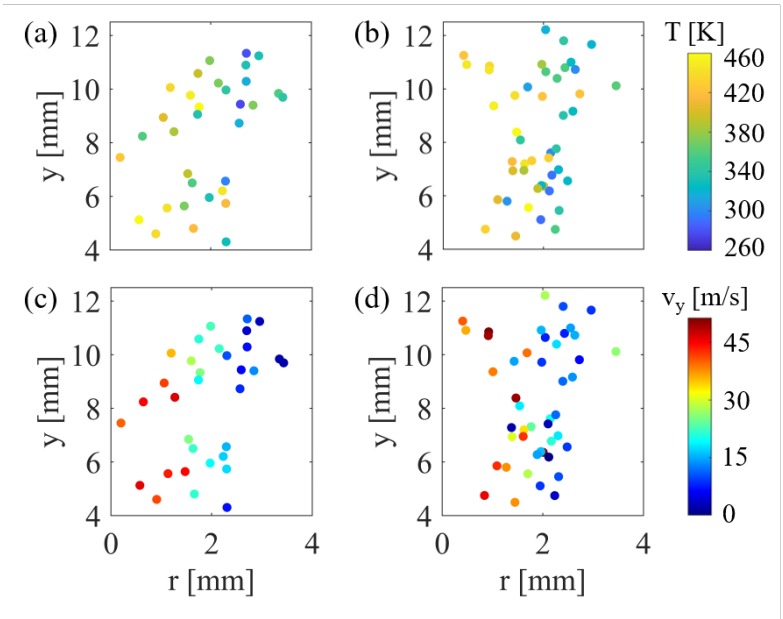

Figure 8.21: Temperature (a, b) and velocity (c, d) results obtained from the same single-shot image data, either using the processing pipelines of chapter 7 (a, c) or the current chapter (b, d).

information was available only for a subset of the particles. As discussed in section 6.1.3, this was due to the much lower luminescence cross-section compared to the Mie scattering cross-section of the seeded phosphor particles, resulting in reduced visibility of the particles within the luminescence camera recordings. This was confirmed by tracking the number of particles during processing: For 26 % of the particles tracked in 3D space using TP-STB, a corresponding luminescence particle image candidate was found. For 89.9 % of these candidates, the image segmentation process was successful. Hence, for 23 % of the particles that could be tracked in 3D initially, a temperature result could be obtained as well.

After the demonstration of the measurement concept in chapter 6, this chapter focused on the improvement of the data processing. This was achieved by including advanced algorithms for many aspects of image data evaluation. The effect of every algorithmic improvement on the results was quantified by comparing new results to those in chapter 6. On average 2.2-times more combined temperature and velocity samples could be obtained using the improved processing in total. After this highlights the potential of the developed measurement concept, the next chapter provides a summary of the present work and an outlook for future works.

Chapter 9

Conclusions and outlook

In this thesis, a technique for simultaneous and instantaneous 3D temperature and velocity measurements in fluid flows based on seeded luminescent tracer particles was developed and demonstrated in a turbulent heated gas jet. Both quantities were obtained from individual tracer particles by exploiting camera images of Mie scattering and luminescence emissions recorded from multiple views. In this final chapter, the measurement concept development, including its initial implementation and algorithmic improvements, are summarised in **section 9.1**. Subsequently, further works to improve the system performance in terms of temperature precision and temporal and spatial resolution are discussed in **section 9.2**, expanding the number of flow quantities accessible from its results, and a wake flow is proposed as the next object of investigation.

9.1 Summary of the work

In the developed measurement concept, thermographic phosphor particles were seeded into a flow as temperature and velocity tracers. For the present implementation, zinc oxide (ZnO) particles have been chosen for their bright luminescence emission, their temperature sensitivity in the targeted range of approximately 290 K to 500 K, and a suitable particle size. Within the flow, these particles were illuminated using spatially overlapped emissions of a double-pulse green laser at 532 nm and a single-pulse UV laser at either 266 nm or 355 nm. Mie-scattered

green light was recorded from four different views by double-frame CCD cameras. Phosphor luminescence emissions were excited by UV light and recorded in two spectral regions using two low-noise and high-resolution sCMOS cameras. Following a joined calibration of all six cameras, 3D particle positions were reconstructed from the double-frame Mie scattering recordings, resulting in 3D particle positions at the first and second Mie scattering double-frame times. By tracking individual particles between these time steps, their displacement was obtained and converted to instantaneous 3D velocity vectors using the known time delay between both green laser pulses. Individual particle images were also detected and segmented from the luminescence camera images. From image pixel intensities, the luminescence emissions imaged for each particle were computed. Particle images were paired between both sCMOS camera recordings using the joined camera calibration and emissions were associated with 3D positions obtained from Mie scattering images. As the luminescence images in both sCMOS cameras were spectrally separated, a temperature dependent luminescence intensity ratio was calculated for each particle. Using a calibration function obtained from dedicated 3D intensity ratio measurements using the implemented system, these intensity ratios were converted to temperatures. As both the single-frame luminescence and double-frame Mie scattering images were recorded simultaneously, discrete temperature and velocity values were obtained at each particle location.

First demonstration measurements in a heated turbulent gas jet surrounded by a slower co-flow at ambient temperature resulted in initial single-shot results of 33 particles distributed over a volume of 74 mm^3 (median inter-particle distance 990 µm). Multiple instantaneous measurements were accumulated in post-processing to create dense time-averaged results of 14.6 particles/mm^3 or 3100 particles in a measurement volume of 213 mm^3. Time-averaged temperature and velocity profiles obtained from these results were rotationally symmetric, as expected for the present jet flow. The measured time-averaged velocity profile was validated by a comparison to the theoretical velocity profile for a turbulent pipe flow and resolves the thin shear layer between the jet and co-flow. The temperature profiles showed a similar symmetry, but the results were more noisy, mainly attributed to luminescence signal levels being an order of magnitude lower than the Mie scattering signals. Temperature and velocity precision were approximated from the temperature and

velocity results in the potential core region in the centre of the jet as 27.4 K and 4.5 m/s or 6 % and 10.2 % of the measured average values, respectively. As these numbers included turbulent fluctuations of both measured quantities within the flow, they were considered worst-case estimates. In summary, the results proved the applicability of the developed measurement technique for research on turbulent gas flows. In the following, key development steps and assessments leading to these results are described before concluding on improvements obtained by substituting the initially used algorithms with more advanced successors.

Key developments for initial implementation

As the developed concept relies on seeded particles to measure the gas temperature and velocity, the particles must be in equilibrium with the surrounding gas to represent its state and motion truthfully. Velocity and temperature response times were calculated for three different phosphor samples after gaining insights into their size distribution using SEM imaging. Particles with a volume equivalent diameter of 600 µm were identified as the best option with temperature and velocity response times of about 2 µs and 5 µs, respectively. As the selected phosphor can be excited using both 266 nm and 355 nm lasers, the effect of excitation wavelength on obtained luminescence image signals was evaluated. The results showed that 355 nm excitation leads to stronger luminescence emissions, in line with the excitation spectrum and findings from the literature (Abram et al. 2016). This was followed by characterisation of the available lasers as a smooth and ideally top-hat beam profile would be advantageous for both 3D reconstruction and phosphor luminescence. While the green beams showed a close to Gaussian beam profile, the UV beam profile was noticeably degraded. This required a 2D flat-field correction to compensate for excitation fluence cross-dependencies of the emission spectrum of ZnO.

As the macroscopic imaging of microscopic particles followed different optimisation criteria for reconstruction and phosphor thermometry, two subsystems were conceived. For 3D reconstruction and tracking, diffraction-limited images of particles located at arbitrary locations within the volume were desired. This required stopped-down camera lenses to provide a large camera depth of field (DoF), which

severely limited the amount of light passing through the lenses, that was countered by increased green laser pulse energies. A four-view, four-camera system for imaging particle Mie scattering was implemented. For thermometry, one order of magnitude weaker luminescence emissions of individual particles were imaged using a two-view, two-camera setup. Widely open apertures were mandatory to maintain sufficient image signal levels, resulting in a shallow DoF and particle position-dependent image diameters. This required an adaptive segmentation of individual particle images to obtain the image intensity for each particle for thermometry, which was implemented initially using a generalised Gaussian fit approach.

To ensure a large DoF during calibration target image recording, external apertures with adjustable iris diameters were placed in front of the luminescence imaging cameras. Due to the spectral filters mounted on these cameras, the calibration target needed near-UV visibility in addition to the visible spectrum. A custom manufactured paper target illuminated by a white LED and a mercury lamp fulfilled these criteria.

To select the specific spectral filters used for the two luminescence imaging channels, simulations of 15 combinations of 13 filter and beamsplitter candidates were performed. The already used (Abram et al. 2015; Abram et al. 2016) combination of 387-11 nm and 425-50 nm filters was found to be the optimum, based on a combination of the available signal level and predicted luminescence intensity ratio (LIR) temperature sensitivity. The LIR approach was selected for the presented implementation of the concept, as it allowed instantaneous 2D luminescence image recordings without motion blur, given the short luminescence lifetime of the selected phosphor ZnO of below 1 ns. If slower flows were to be investigated, a phosphor with a lifetime of a few microseconds could be used together with a one-camera double-frame (Abram et al. 2020) or time-resolved intensity ratio (Omrane et al. 2002), potentially simplifying the setup by using only a single camera for phosphor thermometry.

In the present thesis, CCD and sCMOS cameras were compared for luminescence particle image recording. While the available CCD cameras had a slightly better quantum efficiency in the relevant spectral near-UV region, the sCMOS cameras had a sevenfold lower readout noise, allowing low-noise and high-resolution luminescence

imaging without pixel binning. To achieve the lowest noise level possible with the present sCMOS cameras, a custom timing scheme was employed, where the cameras operated in rolling shutter mode while recording quasi-global shutter mode images. To counter the susceptibility of these cameras to an image memory effect that increased dark noise after recording high intensity calibration target images, a sensor reset was performed before recording particle images.

After these developments allowed the initial implementation of the concept and demonstration experiments discussed above, more advanced algorithms were introduced for many parts of the data processing, and their effect on the results of the demonstration experiment was quantified, as summarised below.

Influence of algorithmic improvements

The initial camera calibration using calibration target images only was complemented by a particle-image-based volume self-calibration. This reduced the calibration error from an initial 0.5 pixel to below 0.05 pixel and allowed for compensation of shot-to-shot camera vibrations. Together with the substitution of the original non-iterative minimum line of sight (MinLOS) tomographic reconstruction by triangulation with iterative particle reconstruction (IPR), the number of particles reconstructed from the same set of single-shot camera images were increased by a factor of 10 while being 30 times faster. Not only did this benefit the presented demonstration with low particle image seeding densities, but it also paved the way for applications of the technique at higher particle seeding levels. To track particles between double-frame recordings and compute 3D velocities for every particle, an original double-frame 3D particle tracking velocimetry algorithm using an initial guess from ensemble cross-correlation and nearest neighbour logic for pairing was replaced by the iterative two-pulse Shake-The-Box (TP-STB) algorithm. This resulted in 12 times more successfully tracked particles than before while reducing the computation time to $1/6^{\text{th}}$. As TP-STB does not rely on *a priori* knowledge of the flow field or an initial guess, this made investigations in more complex flows without a stable time-averaged velocity field accessible for the developed measurement concept.

For luminescence image processing, the particle image segmentation schemes for luminescence intensity integration from camera images and the flat field correction were improved. The initial single-stage particle image segmentation scheme using a generalised 2D Gaussian fit was improved by exploring eight different schemes in total. A two-stage scheme using a region growing algorithm to create a pre-mask with a subsequent 2D Gaussian fit for final segmentation was found to retrieve 2.2 times more particles with temperature information while maintaining the original temperature precision. In general, the two-stage segmentation schemes performed, on average, noticeably better than the single-stage equivalents. Note that this improvement included the aforementioned algorithmic enhancements, too. Finally, a 3D flat field correction (FFC) was implemented to replace the initial 2D FFC. Instead of correcting the measured intensity ratios only within the laser beam cross-section plane, a correction along the laser propagation axis was included. While the LIR precision was only improved by 3.5 % by using the 3D FFC instead of a 2D correction, it becomes mandatory if a larger part of the camera field of view will be utilised for measurements, owing to non-negligible variations in the spectral filter angular collection efficiency.

The final result of this thesis is a validated measurement concept and implementation capable of joined 3D temperature and velocity measurements in turbulent gas flows over a wide range of temperatures and flow velocities using macroscopic images of individual microscopic particles. By using other phosphor materials as flow tracers, it can be adapted to the respective flow and measurement task. Further work will concentrate on improving the temperature precision, extracting more information from the flow, enhancing the spatial and temporal resolution of the measurements, and investigating different flows of technical and scientific interest.

9.2 Further works

In this section, enhancements and applications of the developed measurement technique are suggested. While the current measurement number density allows already insights into 3D flows, increasing the number of measurements per unit volume is always desirable. This could be achieved by retrieving more measurement

points from camera image recordings at the current seeding density and/or by increasing the particle image seeding density in the raw camera image data. In addition to a higher measurement number density, a further improved temperature precision would allow resolving smaller temperature differences. These aims could be achieved by a more elaborate camera setup of the velocimetry subsystem in conjunction with an optimisation of the luminescence imaging subsystem. Two ways are suggested to investigate the effect of these improvements. Either by performing measurements in the heated turbulent jet used in this thesis or in a more complex flow. While the jet would allow a direct side-by-side comparison to the measurement results presented in thesis, it might be worthwhile to test the technique in a more challenging flow, such as a non-isothermal vortex street downstream of a heated cylinder.

Other areas for improvement lie in the utilisation of more temporal information. By extending the developed measurement system with a second green double-pulse laser, flow acceleration and derived quantities would become accessible using multi-pulse STB. Pursuing this idea further, two options for implementation of completely time-resolved measurements using high-speed systems are discussed below.

Finally, by making the 3D temperature distribution within the flow available together with the velocity field, it would be possible to expand data assimilation schemes to non-isothermal flows.

Mie scattering camera setup

The current setup implementation features an inline camera setup to provide four Mie scattering views for 3D reconstruction of particle positions and tracking for velocimetry, similar to the setup arrangement in Ghaemi et al. 2011 and compliant with the system angular aperture recommendations ($40° < \beta < 80°$) of Elsinga et al. 2006. It has the advantage of straightforward assembly and relatively easy adjustment of lens tilt adapters to comply with the Scheimpflug condition. However, as pointed out in Scarano 2013, arranging the four views in a 2D cross-like setup results in up to 10 % higher reconstruction quality based on numerical simulations. Moving the cameras to a 2D arrangement also reduces the angle spanned by the

outermost cameras within the horizontal plane. As the angular distribution of Mie scattering signal intensity is highly anisotropic relative to the laser propagation direction, this would result in more homogeneous image signal intensities in all four Mie scattering views. As particles must be seen in at least three of the four views to be reconstructed by (TP-)STB (in all four views for tomographic reconstruction with MinLOS) (Schanz et al. 2016), this is expected to lead to a higher particle image seeding density and, therefore, sample numbers from the same number of physical particles seeded into the measurement volume.

Luminescence imaging optimisation

The signal levels in luminescence particle images have a great impact on achievable temperature precision and number of temperature samples. If particles are not visible in both cameras used to calculate the temperature dependent LIR, they cannot be processed. If the signal level is too low, the signal-to-noise ratio (SNR) deteriorates the temperature precision. Hence, increasing the luminescence image signal levels has great potential. For the same phosphor particles and illumination strength, the imaged signal levels depend on the distance of the cameras to the measurement volume, spectral transmissivity of the optical filter and lens, optical filter diameter, lens aperture, and camera quantum efficiency.

Standard optical filters as used in this thesis are regularly available in sizes up to 50 mm in diameter. As the 85 mm focal length $f/1.4$ lens has a larger entrance pupil, such filters act as an extra aperture, reducing the signal levels by about one third. Hence, procuring spectral filters with diameters matching the lens entrance pupil will directly increase the image SNR.

Alternatively, one could exploit the aperture-like effect of the present filters. As they increase the camera DoF, the distance between cameras and measurement volume could be reduced without too much overlap of adjacent particle images. This would strongly increase imaged signal levels, as the solid angle particles subtend at the cameras scales with the square of the distance.

In this thesis, the optimal spectral filter combination was evaluated using signal level and temperature sensitivity simulations. These were based on the spectral filters available at that point. Recently, new filters such as the Semrock FF01-386/23-25 were presented, which could be a suitable replacement for the 387-11 nm filter, as the central wavelength is almost identical, but the bandwidth is doubled without overlapping with the second 425-50 nm channel. As the near-UV channel becomes weaker at higher temperatures, this bears potential for improved image SNR and an extension of the upper temperature limit. This would boost the signal levels especially at increased temperatures in the weaker near-UV channel. However, the effect on the temperature sensitivity must be investigated. Finally, sCMOS camera technology continues to advance, and to date, cameras with back-illuminated sCMOS sensors reach quantum efficiencies twice as high as those used for the present implementation. As the imaged signal levels scale linearly with quantum efficiency, any improvement would have an immediate impact on the image SNR.

In combination, the above-mentioned measures could lead to more than a fourfold increase in imaged signal levels (2x from camera quantum efficiency, 1.25x from improved near-UV filter, 1.75x from reducing the camera-to-flow distance to 75 % of its current value), reducing the signal limited LIR uncertainty to 4 %. Considering the current normalised temperature sensitivity, this would translate to a temperature precision on the order of 10 K. This highlights the great potential that lies in increasing the luminescence image signal levels by optimising the luminescence imaging setup.

Wake flow investigation

After demonstrating the developed technique in a non-isothermal turbulent gas jet, it could be beneficial to investigate an arguably more complex flow, to test the capability and potential current limits of the technique.

Vortex streets downstream of (heated) bluff bodies are such flows where multiple shear layers interact with each other and the periodic flow motion creates significant pressure swings normal to the main flow direction which may induce vibrations and

noise (Williamson 1996). This lead to a great research interest in these flows which remains since decades (Berger et al. 1972; Steenhoven et al. 2003) and revealed the 3D nature of vortex shedding processes (Scarano et al. 2009). Instead of having a rather stable average flow and temperature field, suitable for the initial validations of the technique, they show periodic fluctuations that are more difficult to predict and also influence each other (Kieft et al. 2002; Kieft et al. 2003). Hence, such flows would arguably profit even more from simultaneous temperature and velocity measurements than cylindrical gas jets. Thus far, time-resolved 2D measurements of flow temperature and velocity have been reported in the literature, such as for the vortex street after a heated cylinder (Abram et al. 2013). These measurements allowed detailed insights into the temporal evolution of the thermal flow field, but cannot capture the entire 3D behaviour of the flow (W. J. P. M. Maas et al. 2003). Therefore, an investigation using the developed measurement technique is suggested.

Multi-pulse Shake-The-Box

With the presented measurement concept, instantaneous 3D temperature and velocity measurements were already obtained. Accessing more flow quantities from individual measurements is generally desirable because it allows further insight into the flow. One such flow characteristic is acceleration, which provides information regarding the temporal dynamics of the flow. One approach to access the instantaneous acceleration at individual particle locations is the recently developed multi-pulse Shake-The-Box scheme (Novara et al. 2016). It relies on two sets of double-frame particle images with optimised timing between the recordings (Fenelon et al. 2023). The unique advantage is that no high-speed lasers or cameras are necessary to measure acceleration which makes it more accessible. Two double-pulse (green) lasers are required with either of three proposed imaging schemes (Novara et al. 2019). The first two imaging schemes utilise two separate tomographic camera setups, where the laser beams are either separated using different polarisations (Novara et al. 2016) or a specific timing scheme (Novara et al. 2018). Using the polarisation-based approach would be challenged by the currently employed non-spherical phosphor tracer particles and the larger angular

aperture of the camera setup, which conflicts with the preservation of scattered light polarisation (Novara et al. 2019). The second, timing-based approach requires special framing-optimised exposure cameras (Geisler 2014) that allow a short second frame exposure that is not possible with standard double-frame cameras, but are not widely available. The third and arguably most attractive approach for adoption to combined temperature measurements uses only one tomographic imaging system consisting of double-frame cameras, as implemented in the present thesis. To create two sets of double-frame images, a double-frame double-exposure scheme is used, where each frame is exposed twice. In Novara et al. 2019 this approach was successfully applied to a turbulent boundary flow investigation at particle image seeding densities of 0.024 ppp and 0.046 ppp, which would be in line with particle image seeding densities used or targeted in the present thesis.

To adopt multi-pulse STB for the measurement concept developed in this thesis requires only the addition of a second green double-pulse laser. This would result in velocity and acceleration information from double-exposed double-frame images of particle Mie scattering and simultaneously temperature information using the temperature subsystem developed in this thesis. Combined, this information could be used to augment existing data assimilation schemes to produce dense and instantaneous 3D pressure field results.

High-speed imaging

Expanding on the idea of utilising temporal information to retrieve more information about the investigated flow, one could introduce high-speed imaging for velocity and possibly temperature measurements. The advantages of high-speed recording are twofold. First, replacing the double-frame and low-speed tomographic imaging system for Mie scattering with a high-speed system consisting of four high-speed cameras and a high-speed green laser would allow access to the temporal velocity field over extended periods of time. This would benefit the reconstruction process, as ghost particles 'move' erratically over time and do not follow clear trajectories as physical particles do, thus allowing their removal. This is one of the key advantages of the initial implementation of TR-STB designed for time-resolved

measurements (Schanz et al. 2013; Schanz et al. 2014). Second, by obtaining the spatial and temporal derivatives of the 3D velocity field, combined with temperature information at lower rate, allows the determination of instantaneous pressure and density fields - potentially in conjunction with non-isothermal data assimilation as explored below, as solving the Navier-Stokes equations to describe Newtonian fluid flows becomes possible even for non-isothermal flows (Durst 2010). This highlights already the attractiveness of combining high-speed velocity measurements with low-speed temperature measurements using the thermometry subsystem developed in this thesis.

This could be taken a step further by also implementing high-speed thermometry. While this is conceptually clear, current technology might impose limitations. The presently used phosphor ZnO has a very low luminescence lifetime in the (sub-) nanosecond range. Hence, it would be suitable for recordings even at megahertz rates, but the sensitivity and noise level of current high-speed cameras are not on par with low-speed sCMOS cameras. Therefore, the single-shot temperature precision would be expected to be worse than for the measurements presented in this thesis. In addition, volumetric UV illumination at multiple kilohertz rates and pulse energies exceeding 100 mJ would be needed to ensure a sufficient laser fluence. While this is possible using recently developed pulse-burst systems (Slipchenko et al. 2021), they are not commonly found in research institutions. Therefore, the previously discussed combination of high-speed velocimetry with low-speed thermometry might be the currently more viable option.

Non-isothermal data assimilation

In recent years, sophisticated data assimilation (DA) techniques for flow research combined the strengths of numerical simulations and experimentally acquired data. Recent examples include VIC+ (Schneiders and Scarano 2016; Jeon et al. 2018), VIC# (Jeon et al. 2022), FlowFit (Godbersen, Gesemann et al. 2024), and sequential DA (He et al. 2022), that generally rely on the (inviscid) incompressible Navier Stokes equations. As an example, the approach from Jeon et al. 2022 allowed the retrieval of accurate velocity, acceleration, and pressure fields from time-resolved

particle tracks obtained using TR-STB at a particle image seeding density of 0.037 ppp. Only velocity measurements are required as input data which makes these DA schemes accessible once time-resolved velocity data with sufficient spatial resolution is available. However, this also makes their application to non-isothermal flows challenging as they assume constant density. As the presently developed measurement technique provides 3D temperature information together with flow velocity, the density field included in the Navier-Stokes equation becomes accessible. Hence, the expansion of existing DA techniques to non-isothermal flows is within reach as discussed already in above paragraphs on the adoption of multi-pulse STB and high-speed measurements.

Bibliography

Abdullah, N., Abu Talib, A. R., Jaafar, A. A., Mohd Salleh, M. A. and Chong, W. T. (2010). 'The basics and issues of Thermochromic Liquid Crystal Calibrations'. *Exp Therm Fluid Sci* 34, 1089–1121. DOI: 10.1016/j.expthermflusci.2010.03.011.

Abram, C., Sander, T., Straußwald, M., Zigan, L. and Pfitzner, M. (2022). 'Applications Of Thermographic Particle Image Velocimetry To Film Cooling Flow Experiments In A Closed Loop Wind Tunnel'. *Proceedings of the International Symposium on the Application of Laser and Imaging Techniques to Fluid Mechanics* 20, 1–20. DOI: 10.55037/lxlaser.20th.182.

Abram, C. (2014). 'High repetition rate temperature and velocity imaging in turbulent flows using thermographic phosphors'. PhD thesis. Imperial College London.

Abram, C., Fond, B., Heyes, A. L. and Beyrau, F. (2013). 'High-speed planar thermometry and velocimetry using thermographic phosphor particles'. *Appl Phys B* 111, 155–160. DOI: 10.1007/s00340-013-5411-8.

Abram, C., Fond, B. and Beyrau, F. (2015). 'High-precision flow temperature imaging using ZnO thermographic phosphor tracer particles'. *Opt Express* 23, 19453. DOI: 10.1364/oe.23.019453.

Abram, C., Fond, B. and Beyrau, F. (2018). 'Temperature measurement techniques for gas and liquid flows using thermographic phosphor tracer particles'. *Prog Energy Combust Sci* 64, 93–156. DOI: 10.1016/j.pecs.2017.09.001.

Abram, C., Panjikkaran, I. W., Ogugua, S. N. and Fond, B. (2020). 'ScVO4:Bi3+ thermographic phosphor particles for fluid temperature imaging with sub-°C precision'. *Opt Lett* 45, 3893. DOI: 10.1364/ol.392088.

Abram, C., Pougin, M. and Beyrau, F. (2016). 'Temperature field measurements in liquids using ZnO thermographic phosphor tracer particles'. *Exp Fluids* 57. DOI: 10.1007/s00348-016-2200-2.

Adrian, R. J. (1991). 'Particle-Imaging Techniques for Experimental Fluid Mechanics'. *Annu Rev Fluid Mech* 23, 261–304. DOI: 10.1146/annurev.fl.23.010191.001401.

Albani, J. R. (2004). *Structure and dynamics of macromolecules. Absorption and fluorescence studies*. 1st ed. Amsterdam ; Elsevier. 414 pp. ISBN: 9780080474489.

Aldén, M., Omrane, A., Richter, M. and Särner, G. (2011). 'Thermographic phosphors for thermometry: A survey of combustion applications'. *Prog Energy Combust Sci* 37, 422–461. DOI: 10.1016/j.pecs.2010.07.001.

Allison, S. W. and Gillies, G. T. (1997). 'Remote thermometry with thermographic phosphors: Instrumentation and applications'. *Rev Sci Instrum* 68, 2615–2650. DOI: 10.1063/1.1148174.

Atkinson, C. and Soria, J. (2009). 'An efficient simultaneous reconstruction technique for tomographic particle image velocimetry'. *Exp Fluids* 47, 553–568. DOI: 10.1007/s00348-009-0728-0.

Bai, B. et al. (2024). 'Temperature-induced luminescence enhancement and quenching behavior of Eu3+ in Lu2(WO4)3 phosphors'. *Mater Res Bull* 169, 112502. DOI: 10.1016/j.materresbull.2023.112502.

Barker, D., Lifflander, J., Arya, A. and Zhang, Y. (2011). 'A parallel algorithm for 3D particle tracking and Lagrangian trajectory reconstruction'. *Meas Sci Technol* 23, 025301. DOI: 10.1088/0957-0233/23/2/025301.

Bäuerle, B., Hoffmann, F., Behrendt, F. and Warnatz, J. (1994). 'Detection of hot spots in the end gas of an internal combustion engine using two-dimensional lif

of formaldehyde'. *International Symposium on Combustion* 25, 135–141. DOI: 10.1016/s0082-0784(06)80637-5.

Berger, E. and Wille, R. (1972). 'Periodic Flow Phenomena'. *Annu Rev Fluid Mech* 4, 313–340. DOI: 10.1146/annurev.fl.04.010172.001525.

Beshears, D. L., Capps, G. J., Cates, M. R., Simmons, C. M. and Schwenterly, S. W. (1990). *Laser-induced fluorescence of phosphors for remote cryogenic thermometry*. Tech. rep. Oak Ridge National Lab.

Böhm, B., Heeger, C., Gordon, R. L. and Dreizler, A. (2010). 'New Perspectives on Turbulent Combustion: Multi-Parameter High-Speed Planar Laser Diagnostics'. *Flow Turbul Combust* 86, 313–341. DOI: 10.1007/s10494-010-9291-2.

Bohnet, M. and Ullmann, F., eds. (2003). *Ullmann's encyclopedia of industrial chemistry*. 6., completely revised ed. Weinheim: Wiley-VCH. ISBN: 3527303855.

Boyd, R. W. (2008). *Nonlinear optics*. 3rd ed. Burlington, MA: Academic Press. 1613 pp. ISBN: 0080569595.

Bradley, L. C. (1953). 'A Temperature-Sensitive Phosphor Used to Measure Surface Temperatures in Aerodynamics'. *Rev Sci Instrum* 24, 219–220. DOI: 10.1063/1.1770668.

Bray, K. (Jan. 1979). 'The interaction between turbulence and combustion'. *International Symposium on Combustion* 17, 223–233. DOI: 10.1016/s0082-0784(79)80024-7.

Bronkhorst High-Tech B.V. (2025). *Fluidat*. URL: https://www.fluidat.com/default.asp (visited on 22/05/2025).

Brübach, J., Hage, M., Janicka, J. and Dreizler, A. (2009). 'Simultaneous phosphor and CARS thermometry at the wall–gas interface within a combustor'. *Proc Combust Inst* 32, 855–861. DOI: 10.1016/j.proci.2008.05.017.

Brübach, J., Pflitsch, C., Dreizler, A. and Atakan, B. (2013). 'On surface temperature measurements with thermographic phosphors: A review'. *Prog Energy Combust Sci* 39, 37–60. DOI: 10.1016/j.pecs.2012.06.001.

Brücker, C. (1997). '3D scanning PIV applied to an air flow in a motored engine using digital high-speed video'. *Meas Sci Technol* 8, 1480–1492. DOI: 10.1088/0957-0233/8/12/011.

Burch, J. and Tokarski, J. (1968). 'Production of Multiple Beam Fringes from Photographic Scatterers'. *Optica Acta: Int J Opt* 15, 101–111. DOI: 10.1080/713818071.

Byrne, C. (2009). 'Block-iterative algorithms'. *Int Trans Oper Res* 16, 427–463. DOI: 10.1111/j.1475-3995.2008.00683.x.

Cai, T., Khodsiani, M., Hallak, B., Abram, C., Beyrau, F. and Specht, E. (2021). 'Phosphor thermometry at the surface of single reacting large-diameter spherical coke particles to characterise combustion for packed bed furnaces'. *Proc Combust Inst* 38, 4225–4232. DOI: 10.1016/j.proci.2020.06.174.

Cai, T., Peng, D., Liu, Y. Z., Zhao, X. F. and Kim, K. C. (2017). 'A novel lifetime-based phosphor thermography using three-gate scheme and a low frame-rate camera'. *Exp Therm Fluid Sci* 80, 53–60. DOI: 10.1016/j.expthermflusci.2016.08.017.

Calluaud, D. and David, L. (2004). 'Stereoscopic particle image velocimetry measurements of the flow around a surface-mounted block'. *Exp Fluids* 36, 53–61. DOI: 10.1007/s00348-003-0628-7.

Cardwell, N. D., Vlachos, P. P. and Thole, K. A. (2011). 'A multi-parametric particle-pairing algorithm for particle tracking in single and multiphase flows'. *Meas Sci Technol* 22, 105406. DOI: 10.1088/0957-0233/22/10/105406.

Censor, Y. and Segman, J. (1987). 'On Block-Iterative Entropy Maximization'. *J Inf Opt Sci* 8, 275–291. DOI: 10.1080/02522667.1987.10698894.

Champagnat, F., Cornic, P., Cheminet, A., Leclaire, B., Besnerais, G. L. and Plyer, A. (2014). 'Tomographic PIV: particles versus blobs'. *Meas Sci Technol* 25, 084002. DOI: 10.1088/0957-0233/25/8/084002.

Chan, T. F. and Vese, L. A. (2001). 'Active contours without edges'. *IEEE Trans Image Process* 10, 266–277. DOI: 10.1109/83.902291.

Chant, L. J. D. (2005). 'The venerable 1/7th power law turbulent velocity profile: a classical nonlinear boundary value problem solution and its relationship to stochastic processes'. *Appl Math Comp* 161, 463–474. DOI: 10.1016/j.amc.2003.12.109.

Chen, N., Wang, C. and Heidrich, W. (2021). 'Snapshot Space–Time Holographic 3D Particle Tracking Velocimetry'. *Laser Photon Rev* 15. DOI: 10.1002/lpor.202100008.

Churchill, S. W. and Bernstein, M. (1977). 'A Correlating Equation for Forced Convection From Gases and Liquids to a Circular Cylinder in Crossflow'. *ASME J Heat Mass Transf* 99, 300–306. DOI: 10.1115/1.3450685.

Cierpka, C. and Kähler, C. J. (2012). 'Cross-correlation or tracking - comparison and discussion'. *16th International Symposium on Application of Laser Techniques to Fluid Mechanics*.

Cocco, R. and Chew, J. W. (2023). '50 years of Geldart classification'. *Powder Tech* 428, 118861. DOI: 10.1016/j.powtec.2023.118861.

Cornic, P., Illoul, C., Cheminet, A., Besnerais, G. L., Champagnat, F., Sant, Y. L. and Leclaire, B. (2016). 'Another look at volume self-calibration: calibration and self-calibration within a pinhole model of Scheimpflug cameras'. *Meas Sci Technol* 27, 094004. DOI: 10.1088/0957-0233/27/9/094004.

Cornic, P., Leclaire, B., Champagnat, F., Besnerais, G. L., Cheminet, A., Illoul, C. and Losfeld, G. (2020). 'Double-frame tomographic PTV at high seeding densities'. *Exp Fluids* 61. DOI: 10.1007/s00348-019-2859-2.

Corrsin, S. (1943). *Investigation of flow in an axially symmetrical heated jet of air*. Tech. rep. National Advisory Committee for aeronautics. eprint: https://ntrs.nasa.gov/api/citations/19930090930/downloads/19930090930.pdf.

Coudert, S. J. M. and Schon, J.-P. (2001). 'Back-projection algorithm with misalignment corrections for 2D3C stereoscopic PIV'. *Meas Sci Technol* 12, 1371–1381. DOI: 10.1088/0957-0233/12/9/301.

Crimaldi, J. P. (2008). 'Planar laser induced fluorescence in aqueous flows'. *Exp Fluids* 44, 851–863. DOI: 10.1007/s00348-008-0496-2.

Cruyningen, I. van, Lozano, A. and Hanson, R. K. (1990). 'Quantitative imaging of concentration by planar laser-induced fluorescence'. *Exp Fluids* 10, 41–49. DOI: 10.1007/bf00187871.

Dabiri, D. (2020). *Particle tracking velocimetry*. Ed. by C. Pecora. Bristol, UK: IOP Publishing. 1 p. ISBN: 9780750322010.

Delbracio, M., Musé, P., Almansa, A. and Morel, J.-M. (2011). 'The Non-parametric Sub-pixel Local Point Spread Function Estimation Is a Well Posed Problem'. *Int J Comput Vis* 96, 175–194. DOI: 10.1007/s11263-011-0460-0.

Deng, Z., König, J. and Cierpka, C. (2022). 'A combined velocity and temperature measurement with an LED and a low-speed camera'. *Meas Sci Technol* 33, 115301. DOI: 10.1088/1361-6501/ac82da.

Dinkelacker, F., Schäfer, M., Ketterle, W., Wolfrum, J., Stolz, W. and Köhler, J. (Sept. 1992). 'Determination of the third velocity component with PTA using an intensity graded light sheet'. *Exp Fluids* 13, 357–359. DOI: 10.1007/bf00209511.

Dinkelacker, F., Pfadler, S. and Leipertz, A. (2009). 'Laser Diagnostics for the Model Development in Turbulent Premixed Flames'. *Z Phys Chem* 223, 481–502. DOI: 10.1524/zpch.2009.6041.

Doh, D. H., Lee, C. J., Cho, G. R. and Moon, K. R. (2012). 'Performances of Volume-PTV and Tomo-PIV'. *Open J Fluid Dyn* 02, 368–374. DOI: 10.4236/ojfd.2012.24a047.

Doll, U., Burow, E., Stockhausen, G. and Willert, C. (2016). 'Methods to improve pressure, temperature and velocity accuracies of filtered Rayleigh scattering measurements in gaseous flows'. *Meas Sci Technol* 27, 125204. DOI: 10.1088/0957-0233/27/12/125204.

Doll, U., Röhle, I., Dues, M. and Kapulla, R. (2022). 'Time-resolved multi-parameter flow diagnostics by filtered Rayleigh scattering: system design through multi-

objective optimisation'. *Meas Sci Technol* 33, 105204. DOI: 10.1088/1361-6501/ac7cca.

Dorenbos, P. (2005). 'Thermal quenching of Eu2+5d–4f luminescence in inorganic compounds'. *J Phys Condens Matter* 17, 8103–8111. DOI: 10.1088/0953-8984/17/50/027.

Durst, F. (2010). *Fluid mechanics. An introduction to the theory of fluid flows*. Berlin: Springer. 723 pp. ISBN: 9783642090486.

Dyer, T. M. (1979). 'Rayleigh Scattering Measurements of Time-Resolved Concentration in a Turbulent Propane Jet'. *AIAA Journal* 17, 912–914. DOI: 10.2514/3.61247.

Eichler, H.-J. (2018). *Lasers. Basics, advances and applications*. Ed. by J. Eichler and O. Lux. Springer Series in Optical Sciences. Cham: Springer. 1507 pp. ISBN: 9783319998954.

Elliott, G. S., Glumac, N., Carter, C. D. and Nejad, A. S. (1997). 'Two-Dimensional Temperature Field Measurements Using a Molecular Filter Based Technique'. *Combust Sci Technol* 125, 351–369. DOI: 10.1080/00102209708935663.

Elliott, G. S. and Samimy, M. (1990). 'Compressibility effects in free shear layers'. *Phys Fluids* 2, 1231–1240. DOI: 10.1063/1.857816.

Elsinga, G. E., Scarano, F., Wieneke, B. and Oudheusden, B. W. van (2006). 'Tomographic particle image velocimetry'. *Exp Fluids* 41, 933–947. DOI: 10.1007/s00348-006-0212-z.

Fan, L., Vena, P., Savard, B., Xuan, G. and Fond, B. (2021). 'High-resolution velocimetry technique based on the decaying streaks of phosphor particles'. *Opt Lett* 46, 641. DOI: 10.1364/ol.416121.

Fenelon, M. R., Zhang, Y. and Cattafesta, L. N. (2023). 'Optimized Timing Schemes for Multi-Pulse Shake-the-Box Particle Tracking Velocimetry'. *AIAA SCITECH 2023 Forum*. AIAA. DOI: 10.2514/6.2023-0634.

Fond, B., Abram, C., Pougin, M. and Beyrau, F. (2019a). 'Characterisation of dispersed phosphor particles for quantitative photoluminescence measurements'. *Opt Mater* 89, 615–622. DOI: 10.1016/j.optmat.2019.01.011.

Fond, B. (2014). 'Simultaneous temperature and velocity imaging in turbulent flows using thermographic phosphor tracer particles'. PhD thesis. Imperial College London.

Fond, B., Abram, C. and Beyrau, F. (2015). 'Characterisation of the luminescence properties of BAM:Eu2+ particles as a tracer for thermographic particle image velocimetry'. *Appl Phys B* 121, 495–509. DOI: 10.1007/s00340-015-6261-3.

Fond, B., Abram, C., Heyes, A. L., Kempf, A. M. and Beyrau, F. (2012). 'Simultaneous temperature, mixture fraction and velocity imaging in turbulent flows using thermographic phosphor tracer particles'. *Opt Express* 20, 22118. DOI: 10.1364/oe.20.022118.

Fond, B., Abram, C., Pougin, M. and Beyrau, F. (2019b). 'Investigation of the tin-doped phosphor (Sr,Mg)3(PO4)2:Sn2+ for fluid temperature measurements'. *Opt Mater Express* 9, 802. DOI: 10.1364/ome.9.000802.

Fond, B., Xiao, C.-N., T'Joen, C., Henkes, R., Veenstra, P., Wachem, B. G. M. van and Beyrau, F. (2018). 'Investigation of a highly underexpanded jet with real gas effects confined in a channel: flow field measurements'. *Exp Fluids* 59. DOI: 10.1007/s00348-018-2614-0.

Forkey, J., Finkelstein, N., Lempert, W. and Miles, R. (1996). 'Demonstration and characterization of filtered Rayleigh scattering for planar velocity measurements'. *AIAA Journal* 34, 442–448. DOI: 10.2514/3.13087.

Fournel, T., Lavest, J.-M., Coudert, S. and Collange, F. (2004). 'Self-Calibration of PIV Video-Cameras in Scheimpflug Condition'. *Particle Image Velocimetry: Recent Improvements*. Springer Berlin Heidelberg, 391–405. ISBN: 9783642187957. DOI: 10.1007/978-3-642-18795-7_28.

Fuchs, T., Hain, R. and Kähler, C. J. (2016). 'Double-frame 3D-PTV using a tomographic predictor'. *Exp Fluids* 57. DOI: 10.1007/s00348-016-2247-0.

Garcia, D. (2010a). 'A fast all-in-one method for automated post-processing of PIV data'. *Exp Fluids* 50, 1247–1259. DOI: 10.1007/s00348-010-0985-y.

– (2010b). 'Robust smoothing of gridded data in one and higher dimensions with missing values'. *Comp Stat Data Analysis* 54, 1167–1178. DOI: 10.1016/j.csda.2009.09.020.

Geisler, R. (2014). 'A fast double shutter system for CCD image sensors'. *Meas Sci Technol* 25, 025404. DOI: 10.1088/0957-0233/25/2/025404.

Geldart, D. (1973). 'Types of gas fluidization'. *Powder Tech* 7, 285–292. DOI: 10.1016/0032-5910(73)80037-3.

Ghaemi, S. and Scarano, F. (2011). 'Counter-hairpin vortices in the turbulent wake of a sharp trailing edge'. *J Fluid Mech* 689, 317–356. DOI: 10.1017/jfm.2011.431.

Glass, M. and Kennedy, I. M. (1977). 'An improved seeding method for high temperature laser doppler velocimetry'. *Combust Flame* 29, 333–335. DOI: 10.1016/0010-2180(77)90124-9.

Godbersen, P., Gesemann, S., Schanz, D. and Schröder, A. (2024). 'FlowFit3: Efficient Data Assimilation Of LPT Measurements'. *Proceedings of the International Symposium on the Application of Laser and Imaging Techniques to Fluid Mechanics* 21, 1–14. DOI: 10.55037/lxlaser.21st.216.

Godbersen, P., Schanz, D. and Schröder, A. (2024). 'Peak-CNN: improved particle image localization using single-stage CNNs'. *Exp Fluids* 65. DOI: 10.1007/s00348-024-03884-z.

Gomez, M., Yant, B. W., Slipchenko, M. N., Braun, A. M., Rancilio, Z. D., Meyer, T. R. and Roy, S. (2023). 'Four-dimensional laser-induced fluorescence and tomography of liquids'. *Int J Multiphase Flow* 166, 104501. DOI: 10.1016/j.ijmultiphaseflow.2023.104501.

Gong, Y., Andelman, T., Neumark, G. F., O'Brien, S. and Kuskovsky, I. L. (2007). 'Origin of defect-related green emission from ZnO nanoparticles: effect of surface modification'. *Nanoscale Res Lett* 2. DOI: 10.1007/s11671-007-9064-6.

Gong, Y., Tan, Y., Mei, J., Zhang, Y., Yuan, W., Zhang, Y., Sun, J. and Tang, B. Z. (2013). 'Room temperature phosphorescence from natural products: Crystallization matters'. *Sci China Chem* 56, 1178–1182. DOI: 10.1007/s11426-013-4923-8.

Gordon, R., Bender, R. and Herman, G. T. (1970). 'Algebraic Reconstruction Techniques (ART) for three-dimensional electron microscopy and X-ray photography'. *J Theor Biol* 29, 471–481. DOI: 10.1016/0022-5193(70)90109-8.

Ground, C. R., Hunt, R. L. and Hunt, G. J. (2023). 'Quantitative gas property measurements by filtered Rayleigh scattering: a review'. *Meas Sci Technol* 34, 092001. DOI: 10.1088/1361-6501/acd40b.

Guha, S. (2017). *Laser beam propagation in nonlinear optical media*. Ed. by L. P. Gonzalez. First issued in paperback. Boca Raton: Routledge. 311 pp. ISBN: 9781439866382.

Gulati, G. K., Gulati, L. K. and Kumar, S. (2021). 'Recent progress in multi-stimulable photochromic oxazines with their wide-ranging applications'. *Dyes Pigm* 192, 109445. DOI: 10.1016/j.dyepig.2021.109445.

Gupta, M., Mahajan, V. K., Mehta, K. S. and Chauhan, P. S. (2014). 'Zinc Therapy in Dermatology: A Review'. *Dermatol Res Pract* 2014, 1–11. DOI: 10.1155/2014/709152.

Guyon, E., Hulin, J.-P., Petit, L. and Mitescu, C. (2015). 'Vorticity, Vortex Dynamics and Rotating Flows'. *Physical Hydrodynamics, 2nd Edn.* Oxford University Press, 210–276. DOI: 10.1093/acprof:oso/9780198702443.003.0007.

Halls, B. R., Hsu, P. S., Roy, S., Meyer, T. R. and Gord, J. R. (2018). 'Two-color volumetric laser-induced fluorescence for 3D OH and temperature fields in turbulent reacting flows'. *Opt Lett* 43, 2961. DOI: 10.1364/ol.43.002961.

Hanson, R. K. (1988). 'Planar laser-induced fluorescence imaging'. *J Quant Spectrosc Radiat Transf* 40, 343–362. DOI: 10.1016/0022-4073(88)90125-2.

Hara, S., Tsukahara, T. and Kawaguchi, Y. (Dec. 2020). 'Turbulent transport dissimilarity with modulated turbulence structure in channel flow of viscoelastic

fluid'. *Int J Heat Fluid Flow* 86, 108739. DOI: 10.1016/j.ijheatfluidflow.2020.108739.

Hartley, R. and Sturm, P. (1997). 'Triangulation'. *Comput Vis Image Underst* 68, 146–157. DOI: 10.1006/cviu.1997.0547.

Hartley, R. and Zisserman, A. (2019). *Multiple View Geometry in Computer Vision 2ed.* Cambridge University Press. 672 pp. ISBN: 0521540518.

Haynes, W. M. and Lide, D. R., eds. (2010). *CRC handbook of chemistry and physics. A ready-reference book of chemical and physical data.* 91. ed., 2010 - 2011. Boca Raton, Fla. [u.a.]: CRC Press. ISBN: 9781439820773.

He, C., Wang, P., Liu, Y. and Gan, L. (2022). 'Flow Enhancement of Tomographic Particle Image Velocimetry Measurements Using Sequential Data Assimilation'. *Phys Fluids* 34. DOI: 10.1063/5.0082460.

Hecht, E. (2017). *Optics.* 5 ed/fifth edition, global edition. Boston: Pearson. 722 pp. ISBN: 9781292096933.

Herman, G. T. and Lent, A. (1976). 'Iterative reconstruction algorithms'. *Computers in Biology and Medicine* 6, 273–294. DOI: 10.1016/0010-4825(76)90066-4.

Hiller, W., Koch, S., Kowalewski, T. and Stella, F. (1993). 'Onset of natural convection in a cube'. *Int J Heat Mass Transf* 36, 3251–3263. DOI: 10.1016/0017-9310(93)90008-t.

Hoffman, D., Münch, K.-U. and Leipertz, A. (Apr. 1996). 'Two-dimensional temperature determination in sooting flames by filtered Rayleigh scattering'. *Opt Lett* 21, 525. DOI: 10.1364/ol.21.000525.

Jahn, T., Schanz, D. and Schröder, A. (2021). 'Advanced iterative particle reconstruction for Lagrangian particle tracking'. *Exp Fluids* 62. DOI: 10.1007/s00348-021-03276-7.

Jenkins, T., Wu, F. and Turner, K. (2012). 'On the Development of Flow Thermometry Imaging for High Temperatures Using Thermographic Phosphors'. *50th AIAA Aerospace Sciences Meeting including the New Horizons Forum and Aerospace Exposition.* AIAA. DOI: 10.2514/6.2012-405.

Jeon, Y. J., Schneiders, J. F. G., Müller, M., Michaelis, D. and Wieneke, B. (2018). '4D flow field reconstruction from particle tracks by VIC+ with additional constraints and multigrid approximation'. en. *18th International Symposium on Flow Visualization*. ETH Zurich. DOI: 10.3929/ETHZ-B-000279199.

Jeon, Y. J., Müller, M. and Michaelis, D. (2022). 'Fine scale reconstruction (VIC#) by implementing additional constraints and coarse-grid approximation into VIC+'. *Exp Fluids* 63. DOI: 10.1007/s00348-022-03422-9.

Jeong, J. and Hussain, F. (1995). 'On the identification of a vortex'. *J Fluid Mech* 285, 69–94. DOI: 10.1017/s0022112095000462.

Jiao, S. J., Zhang, Z. Z., Lu, Y. M., Shen, D. Z., Yao, B., Zhang, J. Y., Li, B. H., Zhao, D. X., Fan, X. W. and Tang, Z. K. (2006). 'ZnO p-n junction light-emitting diodes fabricated on sapphire substrates'. *Appl Phys Lett* 88. DOI: 10.1063/1.2166686.

Kähler, C. J., Scholz, U. and Ortmanns, J. (2006). 'Wall-shear-stress and near-wall turbulence measurements up to single pixel resolution by means of long-distance micro-PIV'. *Exp Fluids* 41, 327–341. DOI: 10.1007/s00348-006-0167-0.

Kähler, C. J., Scharnowski, S. and Cierpka, C. (2012a). 'On the resolution limit of digital particle image velocimetry'. *Exp Fluids* 52, 1629–1639. DOI: 10.1007/s00348-012-1280-x.

– (2012b). 'On the uncertainty of digital PIV and PTV near walls'. *Exp Fluids* 52, 1641–1656. DOI: 10.1007/s00348-012-1307-3.

Kaiser, W. (2011). *Kunststoffchemie für Ingenieure. Von der Synthese bis zur Anwendung*. 3. Auflage. Hanser eLibrary. München: Hanser Verlag. 575 pp. ISBN: 9783446430471.

Kashanj, S. and Nobes, D. S. (2023). 'Application of 4D two-colour LIF to explore the temperature field of laterally confined turbulent Rayleigh-Bénard convection'. *Exp Fluids* 64. DOI: 10.1007/s00348-023-03589-9.

Käufer, T. and Cierpka, C. (2023). 'Volumetric Lagrangian temperature and velocity measurements with thermochromic liquid crystals'. *Meas Sci Technol* 35, 035301. DOI: 10.1088/1361-6501/ad16d1.

Khodsiani, M., Beyrau, F. and Fond, B. (2024). 'Dual-phosphor thermometry to probe the flame particle interaction in a model packed bed'. *LACSEA 2024 Optica Sensing Congress*.

Kieft, R. N., Rindt, C. C. M. and Steenhoven, A. A. van (2002). 'Heat induced transition of a stable vortex street'. *Int J Heat Mass Transf* 45, 2739–2753. DOI: 10.1016/s0017-9310(01)00356-8.

Kieft, R. N., Rindt, C. C. M., Steenhoven, A. A. van and Heijst, G. J. F. van (2003). 'On the wake structure behind a heated horizontal cylinder in cross-flow'. *J Fluid Mech* 486, 189–211. DOI: 10.1017/s0022112003004567.

Kim, H., Westerweel, J. and Elsinga, G. E. (2012). 'Comparison of Tomo-PIV and 3D-PTV for microfluidic flows'. *Meas Sci Technol* 24, 024007. DOI: 10.1088/0957-0233/24/2/024007.

Kim, M. and Yoda, M. (2010). 'Dual-tracer fluorescence thermometry measurements in a heated channel'. *Exp Fluids* 49, 257–266. DOI: 10.1007/s00348-010-0853-9.

Kimura, I. and Takamori, T. (1987). 'Image processing of flow around a circular cylinder by using correlation technique'. *Flow visualization IV; Proceedings of the Fourth International Symposium*. Paris.

Kimura, I., Takamori, T., Yamauchi, H., Ozawa, M., Takenaka, N. and Sakaguchi, T. (1988). 'Simultaneous measurement of flow and temperature fields based on color image information. Application to visualized images of thermal stratification by liquid crystal.' *J flow vis soc Japan* 8, 185–188. DOI: 10.3154/jvs1981.8.185.

Kissel, T., Baum, E., Dreizler, A. and Brübach, J. (2009). 'Two-dimensional thermographic phosphor thermometry using a CMOS high speed camera system'. *Appl Phys B* 96, 731–734. DOI: 10.1007/s00340-009-3626-5.

Klingshirn, C. (2007). 'ZnO: Material, Physics and Applications'. *ChemPhysChem* 8, 782–803. DOI: 10.1002/cphc.200700002.

Kohse-Höinghaus, K. and Jeffries, J. B., eds. (2002). *Applied combustion diagnostics*. Combustion : an international series. New York, NY: Taylor and Francis. 705 pp. ISBN: 1560329386.

Kováts, P., Martins, F. J. W. A., Mansour, M., Thévenin, D. and Zähringer, K. (2020). 'Tomographic PIV measurements and RANS simulations of secondary flows inside a horizontally positioned helically coiled tube'. *Exp Fluids* 61. DOI: 10.1007/s00348-020-02950-6.

Krug, D., Holzner, M., Lüthi, B., Wolf, M., Tsinober, A. and Kinzelbach, W. (2014). 'A combined scanning PTV/LIF technique to simultaneously measure the full velocity gradient tensor and the 3D density field'. *Meas Sci Technol* 25, 065301. DOI: 10.1088/0957-0233/25/6/065301.

Labergue, A., Deprédurand, V., Delconte, A., Castanet, G. and Lemoine, F. (2010). 'New insight into two-color LIF thermometry applied to temperature measurements of droplets'. *Exp Fluids* 49, 547–556. DOI: 10.1007/s00348-010-0828-x.

Lamarche, F. and Leroy, C. (1990). 'Evaluation of the volume of intersection of a sphere with a cylinder by elliptic integrals'. *Comp Phys Comm* 59, 359–369. DOI: 10.1016/0010-4655(90)90184-3.

LaVision (2018). *Imager sCMOS*.

– (2023). *Imager pro plus and Imager pro X*.

– (2025). *DaVis 11: FlowMaster Shake-the-Box (4D PTV)*. Comp. software. Anna-Vandenhoeck-Ring 19, D-37081 Göttingen: LaVision GmbH.

Lawrence, M., Zhao, H. and Ganippa, L. (2013). 'Gas phase thermometry of hot turbulent jets using laser induced phosphorescence'. *Opt Express* 21, 12260. DOI: 10.1364/oe.21.012260.

Le Dimet, F.-X. and Talagrand, O. (Jan. 1986). 'Variational algorithms for analysis and assimilation of meteorological observations: theoretical aspects'. *Tellus A: Dyn Meteorol and Oceanography* 38, 97. DOI: 10.3402/tellusa.v38i2.11706.

Lei, P., Yang, H., Yin, Z. and Shan, F. (2025). 'Ghost particle suppression multiplicative algebraic reconstruction technique for tomographic PIV'. *Exp Fluids* 66. DOI: 10.1007/s00348-024-03935-5.

Lemos, M. J. de (2012). 'Turbulent Momentum Transport'. *Turbulence in Porous Media*. Elsevier, 33–53. ISBN: 9780080982410. DOI: 10.1016/b978-0-08-098241-0.00004-8.

Li, X.-B., Hao, X.-Y., Zhang, H.-N., Zhang, W.-H. and Li, F.-C. (2023). 'Review on multi-parameter simultaneous measurement techniques for multiphase flow – Part A: Velocity and temperature/pressure'. *Measurement* 223, 113710. DOI: 10.1016/j.measurement.2023.113710.

Lipzig, J. P. J. van, Yu, M., Dam, N. J., Luijten, C. C. M. and Goey, L. P. H. de (2013). 'Gas-phase thermometry in a high-pressure cell using BaMgAl10O17:Eu as a thermographic phosphor'. *Appl Phys B* 111, 469–481. DOI: 10.1007/s00340-013-5360-2.

Liu, C., Gao, Y., Tian, S. and Dong, X. (2018). 'Rortex—A new vortex vector definition and vorticity tensor and vector decompositions'. *Phys Fluids* 30. DOI: 10.1063/1.5023001.

Liu, S., An, Z. and Zhou, B. (2023). 'Optical multiplexing of upconversion in nanoparticles towards emerging applications'. *Chem Eng J* 452, 139649. DOI: 10.1016/j.cej.2022.139649.

Liu, T., Sullivan, J. P., Asai, K., Klein, C. and Egami, Y. (2021). *Pressure and Temperature Sensitive Paints*. Springer International Publishing. ISBN: 9783030680565. DOI: 10.1007/978-3-030-68056-5.

López Bonilla, J., Beyrau, F. and Fond, B. (2024). 'Sub-°C-precision temperature imaging using phase-shift luminescence thermometry'. *Meas Sci Technol* 36, 015204. DOI: 10.1088/1361-6501/ad846b.

Louhichi, H., Fournel, T., Lavest, J. M. and Aissia, H. B. (2007). 'Self-calibration of Scheimpflug cameras: an easy protocol'. *Meas Sci Technol* 18, 2616–2622. DOI: 10.1088/0957-0233/18/8/037.

Lynch, K. P. and Scarano, F. (2015). 'An efficient and accurate approach to MTE-MART for time-resolved tomographic PIV'. *Exp Fluids* 56. DOI: 10.1007/s00348-015-1934-6.

Maas, H. G., Gruen, A. and Papantoniou, D. (1993). 'Particle tracking velocimetry in three-dimensional flows'. *Exp Fluids* 15, 133–146. DOI: 10.1007/bf00190953.

Maas, H.-G., Westfeld, P., Putze, T., Botkjaer, N., Kitzhofer, J. and Brücker, C. (2009). 'Photogrammetric techniques in multi-camera tomographic PIV'. *8th International Symposium on Particle Image Velocimetry*.

Maas, W. J. P. M., Rindt, C. C. M. and Steenhoven, A. A. van (2003). 'The influence of heat on the 3D-transition of the von Kármán vortex street'. *Int J Heat Mass Transf* 46, 3069–3081. DOI: 10.1016/s0017-9310(03)00076-0.

Makhov, V. N., Uvarova, T. V., Kirm, M. and Vielhauer, S. (2016). 'Thermal quenching of luminescence of BaY2F8 crystals activated with Er3+ and Tm3+ ions'. *Bulletin of the Lebedev Physics Institute* 43, 348–351. DOI: 10.3103/s1068335616120022.

Malik, N. A., Dracos, T. and Papantoniou, D. A. (1993). 'Particle tracking velocimetry in three-dimensional flows: Part II: Particle tracking'. *Exp Fluids* 15–15, 279–294. DOI: 10.1007/bf00223406.

Mann, J., Ott, S. and Andersen, J. S. (1999). *Experimental study of relative, turbulent diffusion*. Tech. rep. Forskningscenter Risoe.

Martin, D. and Thorpe, S. J. (June 2012). 'Experiments on Combustor Effusion Cooling Under Conditions of Very High Free-Stream Turbulence'. *Volume 4: Heat Transfer, Parts A and B*. GT2012. ASME. DOI: 10.1115/gt2012-68863.

Martins, F. J. W. A., Foucaut, J.-M., Thomas, L., Azevedo, L. F. A. and Stanislas, M. (2015). 'Volume reconstruction optimization for tomo-PIV algorithms applied to experimental data'. *Meas Sci Technol* 26, 085202. DOI: 10.1088/0957-0233/26/8/085202.

Massing, J., Kaden, D., Kähler, C. J. and Cierpka, C. (2016). 'Luminescent two-color tracer particles for simultaneous velocity and temperature measurements

in microfluidics'. *Meas Sci Technol* 27, 115301. DOI: 10.1088/0957-0233/27/11/115301.

Massing, J., Kähler, C. J. and Cierpka, C. (2018). 'A volumetric temperature and velocity measurement technique for microfluidics based on luminescence lifetime imaging'. *Exp Fluids* 59. DOI: 10.1007/s00348-018-2616-y.

McCormack, J. (1981). 'Remote optical measurement of temperature using luminescent materials'. *Electronics Lett* 17, 630–631. DOI: 10.1049/el:19810442.

McManus, T. A. and Sutton, J. A. (2020). 'Simultaneous 2D filtered Rayleigh scattering thermometry and stereoscopic particle image velocimetry measurements in turbulent non-premixed flames'. *Exp Fluids* 61. DOI: 10.1007/s00348-020-02973-z.

Meinhart, C. D., Wereley, S. T. and Santiago, J. G. (2000). 'A PIV Algorithm for Estimating Time-Averaged Velocity Fields'. *Journal of Fluids Engineering* 122, 285–289. DOI: 10.1115/1.483256.

Melling, A. (1997). 'Tracer particles and seeding for particle image velocimetry'. *Meas Sci Technol* 8, 1406–1416. DOI: 10.1088/0957-0233/8/12/005.

Mendieta, A., Fond, B., Dragomirov, P. and Beyrau, F. (2019). 'A delayed gating approach for interference-free ratio-based phosphor thermometry'. *Meas Sci Technol* 30, 074002. DOI: 10.1088/1361-6501/ab1b0c.

Mercier, B., Thomas, L., Tremblais, B. and David, L. (2024). 'A robust pairing method for two-pulse particle tracking velocimetry based on coherent point drift'. *Meas Sci Technol* 35, 065301. DOI: 10.1088/1361-6501/ad2b42.

Merklinger, H. M. (1993). *Focusing the View Camera. A Scientific Way to Focus the View Camera and Estimate Depth of Field*. MacNab Print. ISBN: 9780969502524.

Michaelis, D., Novara, M., Scarano, F. and Wieneke, B. (2010). 'Comparison of volume reconstruction techniques at different particle densities'. *15th International Symposium on Applications of Laser Techniques to Fluid Mechanics*. Lisbon.

Mikheev, A. V. and Zubtsov, V. M. (2008). 'Enhanced particle-tracking velocimetry (EPTV) with a combined two-component pair-matching algorithm'. *Meas Sci Technol* 19, 085401. DOI: 10.1088/0957-0233/19/8/085401.

Miles, R. and Lempert, W. (1990). 'Two-dimensional measurement of density, velocity, and temperature in turbulent high-speed air flows by UV rayleigh scattering'. *Appl Phys B* 51, 1–7. DOI: 10.1007/bf00332317.

Miles, R., Lempert, W. and Forkey, J. (2001). 'Laser Rayleigh scattering'. *Meas Sci Technol* 12, R33–R51. DOI: 10.1088/0957-0233/12/5/201.

Mitchnick, M. A., Fairhurst, D. and Pinnell, S. R. (1999). 'Microfine zinc oxide (Z-Cote) as a photostable UVA/UVB sunblock agent'. *J Am Acad Dermatol* 40, 85–90. DOI: 10.1016/s0190-9622(99)70532-3.

Mons, V., Marquet, O., Leclaire, B., Cornic, P. and Champagnat, F. (2022). 'Dense velocity, pressure and Eulerian acceleration fields from single-instant scattered velocities through Navier-Stokes-based data assimilation'. *Meas Sci Technol* 33, 124004. DOI: 10.1088/1361-6501/ac8dac.

Most, D., Dinkelacker, F. and Leipertz, A. (2002). 'Direct determination of the turbulent flux by simultaneous application of filtered rayleigh scattering thermometry and particle image velocimetry'. *Proc Combust Inst* 29, 2669–2677. DOI: 10.1016/s1540-7489(02)80325-x.

Most, D. and Leipertz, A. (2001). 'Simultaneous two-dimensional flow velocity and gas temperature measurements by use of a combined particle image velocimetry and filtered Rayleigh scattering technique'. *Appl Opt* 40, 5379. DOI: 10.1364/ao.40.005379.

Mytton, D. (Feb. 2021). 'Data centre water consumption'. *npj Clean Water* 4. DOI: 10.1038/s41545-021-00101-w.

Natrajan, V. K. and Christensen, K. T. (2008). 'Two-color laser-induced fluorescent thermometry for microfluidic systems'. *Meas Sci Technol* 20, 015401. DOI: 10.1088/0957-0233/20/1/015401.

Neal, N. J., Jordan, J. and Rothamer, D. (2013). 'Simultaneous Measurements of In-Cylinder Temperature and Velocity Distribution in a Small-Bore Diesel Engine Using Thermographic Phosphors'. *SAE Int J Engines* 6, 300–318. DOI: 10.4271/2013-01-0562.

Newport Corporation (2025). *Spectral Calibration Lamp, Hg (Ar)*. URL: https://www.newport.com/p/6035 (visited on 22/05/2025).

Nieuwstadt, F. T. M., Westerweel, J. and Boersma, B. J. (2016). *Turbulence*. Springer International Publishing. DOI: 10.1007/978-3-319-31599-7.

Nilsson, S., Feuk, H. and Richter, M. (2023). 'High temperature thermographic phosphors YAG:Tm;Li and YAG:Dy in reduced oxygen environments'. *J Lumin* 256, 119645. DOI: 10.1016/j.jlumin.2022.119645.

Novara, M., Schanz, D. and Schröder, A. (2023). 'Two-Pulse 3D particle tracking with Shake-The-Box'. *Exp Fluids* 64. DOI: 10.1007/s00348-023-03634-7.

Novara, M. (2013). 'Advances in tomographic PIV'. PhD thesis. TU Delft.

Novara, M., Batenburg, K. J. and Scarano, F. (2010). 'Motion tracking-enhanced MART for tomographic PIV'. *Meas Sci Technol* 21, 035401. DOI: 10.1088/0957-0233/21/3/035401.

Novara, M., Schanz, D., Geisler, R., Gesemann, S., Voss, C. and Schröder, A. (2019). 'Multi-exposed recordings for 3D Lagrangian particle tracking with Multi-Pulse Shake-The-Box'. *Exp Fluids* 60. DOI: 10.1007/s00348-019-2692-7.

Novara, M., Schanz, D., Geisler, R. and Schröder, A. (2018). 'Applications of multi-pulse shake-the-box 3D Lagrangian particle tracking to single- and multi-exposed recordings'. *18th International Symposium on Flow Visualization*. ETH Zurich. DOI: 10.3929/ETHZ-B-000279181.

Novara, M., Schanz, D., Reuther, N., Kähler, C. J. and Schröder, A. (2016). 'Lagrangian 3D particle tracking in high-speed flows: Shake-The-Box for multi-pulse systems'. *Exp Fluids* 57. DOI: 10.1007/s00348-016-2216-7.

Novara, M., Schanz, D. and Schröder, A. (2022). 'Shake-The-Box 3D particle tracking for two-pulse recordings'. *20th International Symposium on the Application of Laser and Imaging Techniques to Fluid Mechanics*.

Ojo, A. O., Fond, B., Abram, C., Wachem, B. G. M. V., Heyes, A. L. and Beyrau, F. (2017). 'Thermographic laser Doppler velocimetry using the phase-shifted luminescence of BAM:Eu2+ phosphor particles for thermometry'. *Opt Express* 25, 11833. DOI: 10.1364/oe.25.011833.

Ojo, A. O., Fond, B., Wachem, B. G. M. V., Heyes, A. L. and Beyrau, F. (2015). 'Thermographic laser Doppler velocimetry'. *Opt Lett* 40, 4759. DOI: 10.1364/ol.40.004759.

Olmstead, J. A. and Gray, D. G. (1993). 'Fluorescence emission from mechanical pulp sheets'. *J Photochem Photobiol A: Chemistry* 73, 59–65. DOI: 10.1016/1010-6030(93)80033-6.

Olsen, M. G. and Adrian, R. J. (2000). 'Out-of-focus effects on particle image visibility and correlation in microscopic particle image velocimetry'. *Exp Fluids* 29, S166–S174. DOI: 10.1007/s003480070018.

Omrane, A., Petersson, P., Aldén, M. and Linne, M. A. (2008). 'Simultaneous 2D flow velocity and gas temperature measurements using thermographic phosphors'. *Appl Phys B* 92, 99–102. DOI: 10.1007/s00340-008-3051-1.

Omrane, A., Ossler, F. and Aldén, M. (2002). 'Two-dimensional surface temperature measurements of burning materials'. *Proc Combust Inst* 29, 2653–2659. DOI: 10.1016/s1540-7489(02)80323-6.

Ouellette, N. T., Xu, H. and Bodenschatz, E. (2005). 'A quantitative study of three-dimensional Lagrangian particle tracking algorithms'. *Exp Fluids* 40, 301–313. DOI: 10.1007/s00348-005-0068-7.

Özgür, Ü., Alivov, Y. I., Liu, C., Teke, A., Reshchikov, M. A., Doğan, S., Avrutin, V., Cho, S.-J. and Morkoç, H. (2005). 'A comprehensive review of ZnO materials and devices'. *J Appl Phys* 98. DOI: 10.1063/1.1992666.

Pal, N. R. and Pal, S. K. (1993). 'A review on image segmentation techniques'. *Pattern Recognition* 26, 1277–1294. DOI: 10.1016/0031-3203(93)90135-j.

Pasinato, H. (Feb. 2011). 'Velocity and temperature dissimilarity in fully developed turbulent channel and plane Couette flows'. *Int J Heat Fluid Flow* 32, 11–25. DOI: 10.1016/j.ijheatfluidflow.2010.10.003.

Patil, S., Gorges, C., Lòpez Bonilla, J., Stelter, M., Beyrau, F. and Wachem, B. van (2023). 'Experimental and numerical investigation to elucidate the fluid flow through packed beds with structured particle packings'. *Particuology* 89, 218–237. DOI: 10.1016/j.partic.2023.11.002.

Pellin, P. and Broca, A. (1899). 'A Spectroscope of Fixed Deviation'. *Astrophys J* 10, 337. DOI: 10.1086/140661.

Pereira, F., Stüer, H., Graff, E. C. and Gharib, M. (2006). 'Two-frame 3D particle tracking'. *Meas Sci Technol* 17, 1680–1692. DOI: 10.1088/0957-0233/17/7/006.

Petit, S., Xavier, P., Godard, G. and Grisch, F. (2022). 'Improving the temperature uncertainty of Mg4FGeO6:Mn4+ ratio-based phosphor thermometry by using a multi-objective optimization procedure'. *Appl Phys B* 128. DOI: 10.1007/s00340-021-07733-3.

Pfadler, S., Dinkelacker, F., Beyrau, F. and Leipertz, A. (Aug. 2009). 'High resolution dual-plane stereo-PIV for validation of subgrid scale models in large-eddy simulations of turbulent premixed flames'. *Combust Flame* 156, 1552–1564. DOI: 10.1016/j.combustflame.2009.02.010.

Pitsch, H. G. (2020). *Data Analysis for Direct Numerical Simulations of Turbulent Combustion. From Equation-Based Analysis to Machine Learning*. Ed. by A. Attili. Cham: Springer International Publishing AG. 1294 pp. ISBN: 9783030447182.

Pope, S. B. (2015). *Turbulent flows*. 1. publ., 12. print. Cambridge [u.a.]: Cambridge Univ. Press. 771 pp. ISBN: 9780521598866.

Popovici, E.-J., Muresan, L., Hristea-Simoc, A., Indrea, E., Vasilescu, M., Nazarov, M. and Jeon, D. Y. (2004). 'Synthesis and characterisation of rare earth oxysulph-

ide phosphors. I. Studies on the preparation of Gd2O2S:Tb phosphor by the flux method'. *Opt Mater* 27, 559–565. DOI: 10.1016/j.optmat.2004.07.006.

Prahl, S. (2023). *Mie Scattering*. Version v2.6.3. DOI: 10.5281/zenodo.10087653.

Prasad, A. K. (2000). 'Stereoscopic particle image velocimetry'. *Exp Fluids* 29, 103–116. DOI: 10.1007/s003480000143.

Putze, T. and Maas, H.-G. (2008). '3D determination of very dense particle velocity fields by tomographic reconstruction from four camera views and voxel space tracking'. *International Society for Photogrammetry and Remote Sensing*.

Quarteroni, A. (2022). *Modeling Reality with Mathematics*. Ed. by S. G. Chiossi. 1st ed. Cham: Springer International Publishing AG. 1136 pp. ISBN: 9783030961626.

Raffel, M., Willert, C. E., Scarano, F., Kähler, C. J., Wereley, S. T. and Kompenhans, J. (2018). *Particle Image Velocimetry*. Springer International Publishing. DOI: 10.1007/978-3-319-68852-7.

Rhodes, H. E., Yang, D., Chen, G., Mao, D. and Venezia, V. (2014). 'Negatively charged layer to reduce image memory effect'. English. U.S. pat.

Ribeiro, M. M. and Whitelaw, J. H. (1975). 'Statistical characteristics of a turbulent jet'. *J Fluid Mech* 70, 1–15. DOI: 10.1017/s0022112075001863.

Rodnyi, P. A. and Khodyuk, I. V. (2011). 'Optical and luminescence properties of zinc oxide (Review)'. *Opt Spectrosc* 111, 776–785. DOI: 10.1134/s0030400x11120216.

Ropp, R. C. (2004). *Luminescence and the solid state*. 2nd ed. Studies in inorganic chemistry. Amsterdam ; Elsevier. 711 pp. ISBN: 9780080473239.

– ed. (2010). *The chemistry of artificial lighting devices. Lamps, phosphors, and cathode ray tubes*. Studies in inorganic chemistry. Amsterdam: Elsevier. 664 pp.

Rothamer, D. A. and Jordan, J. (2011). 'Planar imaging thermometry in gaseous flows using upconversion excitation of thermographic phosphors'. *Appl Phys B* 106, 435–444. DOI: 10.1007/s00340-011-4707-9.

Rousseau, G. and Ancey, C. (2020). 'Scanning PIV of turbulent flows over and through rough porous beds using refractive index matching'. *Exp Fluids* 61. DOI: 10.1007/s00348-020-02990-y.

Sadykova, S., Dostiyarov, A., Zhumagulov, M. and Kartjanov, N. (2021). 'Influence of turbulence on the efficiency and reliability of combustion chamber of the gas turbine'. *Therm Sci* 25, 4321–4332. DOI: 10.2298/tsci200831064s.

Saha, S. K. (2015). *High-resolution imaging. Detectors and applications*. Singapore: Pan Stanford Publishing. 1565 pp. ISBN: 9789814613279.

Sakakibara, J. and Adrian, R. J. (1999). 'Whole field measurement of temperature in water using two-color laser induced fluorescence'. *Exp Fluids* 26, 7–15. DOI: 10.1007/s003480050260.

Salama, A. (2021). 'Velocity Profile Representation for Fully Developed Turbulent Flows in Pipes: A Modified Power Law'. *Fluids* 6, 369. DOI: 10.3390/fluids6100369.

Samimy, M. and Lele, S. K. (1991). 'Motion of particles with inertia in a compressible free shear layer'. *Phys Fluids* 3, 1915–1923. DOI: 10.1063/1.857921.

Samsonov, G. V., ed. (1973). *The Oxide Handbook*. Springer US. ISBN: 9781461595977. DOI: 10.1007/978-1-4615-9597-7.

Särner, G., Richter, M. and Aldén, M. (2008). 'Two-dimensional thermometry using temperature-induced line shifts of ZnO:Zn and ZnO:Ga fluorescence'. *Opt Lett* 33, 1327. DOI: 10.1364/ol.33.001327.

Sauter, J. (1926). 'Die Grössenbestimmung der im Gemischnebel von Verbrennungskraftmaschinen vorhandenen Brennstoffteilchen'. *Forschungsarbeiten auf dem Gebiete des Ingenieurwesens*.

Scala, F., ed. (2013). *Fluidized Bed Technologies for Near-zero Emission Combustion and Gasification*. Woodhead Publishing series in energy. Cambridge: Woodhead Publishing Ltd. 11088 pp.

Scarano, F., David, L., Bsibsi, M. and Calluaud, D. (2005). 'S-PIV comparative assessment: image dewarping+misalignment correction and pinhole+geometric back projection'. *Exp Fluids* 39, 257–266. DOI: 10.1007/s00348-005-1000-x.

Scarano, F. (2013). 'Tomographic PIV: principles and practice'. *Meas Sci Technol* 24, 012001. DOI: 10.1088/0957-0233/24/1/012001.

Scarano, F. and Poelma, C. (2009). 'Three-dimensional vorticity patterns of cylinder wakes'. *Exp Fluids* 47. DOI: 10.1007/s00348-009-0629-2.

Schäfer, L. and Schröder, W. (2011). 'Comparison of Holographic and Tomographic Particle-Image Velocimetry Turbulent Channel Flow Measurements'. *J Phys Conf Ser* 318, 022019. DOI: 10.1088/1742-6596/318/2/022019.

Schanz, D., Schröder, A. and Gesemann, S. (2014). ''Shake The Box' - a 4D PTV algorithm: Accurate and ghostless reconstruction of Lagrangian tracks in densely seeded flows'. *17th International Symposium on Allpications of Laser Techniques to Fluid Mechanics*.

Schanz, D., Schröder, A., Gesemann, S., Michaelis, D. and Wieneke, B. (2013). ''Shake The Box': A highly efficient and accurate Tomographic ParticleTracking Velocimetry (TOMO-PTV) method using prediction of particlepositions'. *10th International Symposium on Particle Image Velocimetry*. Delft.

Schanz, D., Gesemann, S. and Schröder, A. (2016). 'Shake-The-Box: Lagrangian particle tracking at high particle image densities'. *Exp Fluids* 57. DOI: 10.1007/s00348-016-2157-1.

Schanz, D., Gesemann, S., Schröder, A., Wieneke, B. and Novara, M. (2012). 'Non-uniform optical transfer functions in particle imaging: calibration and application to tomographic reconstruction'. *Meas Sci Technol* 24, 024009. DOI: 10.1088/0957-0233/24/2/024009.

Schiepel, D., Schmeling, D. and Wagner, C. (2021). 'Simultaneous tomographic particle image velocimetry and thermometry of turbulent Rayleigh–Bénard convection'. *Meas Sci Technol* 32, 095201. DOI: 10.1088/1361-6501/abf095.

Schneiders, J. F. G., Caridi, G. C. A., Sciacchitano, A. and Scarano, F. (2016). 'Large-scale volumetric pressure from tomographic PTV with HFSB tracers'. *Exp Fluids* 57. DOI: 10.1007/s00348-016-2258-x.

Schneiders, J. F. G. and Scarano, F. (2016). 'Dense velocity reconstruction from tomographic PTV with material derivatives'. *Exp Fluids* 57. DOI: 10.1007/s00348-016-2225-6.

Schneiders, J. F. G., Scarano, F. and Elsinga, G. E. (2017). 'Resolving vorticity and dissipation in a turbulent boundary layer by tomographic PTV and VIC+'. *Exp Fluids* 58. DOI: 10.1007/s00348-017-2318-x.

Schreivogel, P., Abram, C., Fond, B., Straußwald, M., Beyrau, F. and Pfitzner, M. (2016). 'Simultaneous kHz-rate temperature and velocity field measurements in the flow emanating from angled and trenched film cooling holes'. *Int J Heat Mass Transf* 103, 390–400. DOI: 10.1016/j.ijheatmasstransfer.2016.06.092.

Schreivogel, P. and Pfitzner, M. (2015). 'Optical convective heat transfer measurements using infrared thermography and frequency domain phosphor thermometry'. *Int J Heat Mass Transf* 82, 299–308. DOI: 10.1016/j.ijheatmasstransfer.2014.11.025.

Schröder, A., Geisler, R., Staack, K., Elsinga, G. E., Scarano, F., Wieneke, B., Henning, A., Poelma, C. and Westerweel, J. (2010). 'Eulerian and Lagrangian views of a turbulent boundary layer flow using time-resolved tomographic PIV'. *Exp Fluids* 50, 1071–1091. DOI: 10.1007/s00348-010-1014-x.

Schröder, A. and Schanz, D. (2022). '3D Lagrangian Particle Tracking in Fluid Mechanics'. *Annu Rev Fluid Mech* 55. DOI: 10.1146/annurev-fluid-031822-041721.

Schulz, C. and Sick, V. (2005). 'Tracer-LIF diagnostics: quantitative measurement of fuel concentration, temperature and fuel/air ratio in practical combustion systems'. *Prog Energy Combust Sci* 31, 75–121. DOI: 10.1016/j.pecs.2004.08.002.

Sciacchitano, A., Leclaire, B. and Schroeder, A. (2021). 'Main results of the first Lagrangian Particle Tracking Challenge'. *14th International Symposium on Particle Image Velocimetry* 1. DOI: 10.18409/ispiv.v1i1.197.

Segura, R., Cierpka, C., Rossi, M., Joseph, S., Bunjes, H. and Kähler, C. J. (2012). 'Non-encapsulated thermo-liquid crystals for digital particle tracking thermography/velocimetry in microfluidics'. *Microfluid Nanofluidics* 14, 445–456. DOI: 10.1007/s10404-012-1063-y.

Segura, R., Rossi, M., Cierpka, C. and Kähler, C. J. (2015). 'Simultaneous three-dimensional temperature and velocity field measurements using astigmatic imaging of non-encapsulated thermo-liquid crystal (TLC) particles'. *Lab Chip* 15, 660–663. DOI: 10.1039/c4lc01268b.

Self, S. A. and Whitelaw, J. H. (1976). 'Laser Anemometry for Combustion Research'. *Combust Sci Technol* 13, 171–197. DOI: 10.1080/00102207608946734.

Senarathna, N. A. C. J. D. (2023). 'Outlier detection and removal in luminescence thermometry data using convolutional neural networks and deep neural networks'. MA thesis. Otto-von-Guericke-University Magdeburg.

Settles, G. S. (2001). *Schlieren and shadowgraph techniques. Visualizing phenomena in transparent media*. Experimental fluid mechanics. Berlin: Springer. 376 pp. ISBN: 9783642566400.

Shafii, M. B., Lum, C. L. and Koochesfahani, M. M. (2009). 'In situ LIF temperature measurements in aqueous ammonium chloride solution during uni-directional solidification'. *Exp Fluids* 48, 651–662. DOI: 10.1007/s00348-009-0758-7.

Shaheen, M. E., Abdelhameed, S. T., Abdelmoniem, N. M., Hashim, H. M., Ghazy, R. A., Abdel Gawad, S. A. and Ghazy, A. R. (2023). 'Determination of the refractive index of air and its variation with temperature and pressure using a Mach–Zehnder interferometer'. *J Opt* 53, 2219–2228. DOI: 10.1007/s12596-023-01486-2.

Shionoya, S., Yen, W. M. and Yamamoto, H., eds. (2006). *Phosphor Handbook*. 2nd ed. The @CRC Press laser and optical science and technology series. Boca Raton: CRC Press. 11053 pp. ISBN: 9781420005233.

Silva, C. M. de, Baidya, R. and Marusic, I. (2012). 'Enhancing Tomo-PIV reconstruction quality by reducing ghost particles'. *Meas Sci Technol* 24, 024010. DOI: 10.1088/0957-0233/24/2/024010.

Slipchenko, M. N., Meyer, T. R. and Roy, S. (2021). 'Advances in burst-mode laser diagnostics for reacting and nonreacting flows'. *Proc Combust Inst* 38, 1533–1560. DOI: 10.1016/j.proci.2020.07.024.

Smith, C. R., Sabatino, D. R. and Praisner, T. J. (2001). 'Temperature sensing with thermochromic liquid crystals'. *Exp Fluids* 30, 190–201. DOI: 10.1007/s003480000154.

Soloff, S. M., Adrian, R. J. and Liu, Z.-C. (1997). 'Distortion compensation for generalized stereoscopic particle image velocimetry'. *Meas Sci Technol* 8, 1441–1454. DOI: 10.1088/0957-0233/8/12/008.

Sposito, A., Heaps, E., Sutton, G., Machin, G., Bernard, R. and Clarke, S. (2021). 'Phosphor thermometry for nuclear decommissioning and waste storage'. *Nucl Eng Des* 375, 111091. DOI: 10.1016/j.nucengdes.2021.111091.

Steenhoven, A. A. van and Rindt, C. C. M. (2003). 'Flow transition behind a heated cylinder'. *Int J Heat Fluid Flow* 24, 322–333. DOI: 10.1016/s0142-727x(03)00023-7.

Stein, H. D. v. and Pfeifer, H. J. (1969). 'A Doppler Difference Method for Velocity Measurements'. *Metrologia* 5, 59–61. DOI: 10.1088/0026-1394/5/2/006.

Steinberg, A. (2023). *Optical Diagnostics for Reacting and Non-Reacting Flows. Theory and Practice*. Ed. by S. Roy. 1st ed. Reston: AIAA. 11343 pp. ISBN: 9781624106330.

Stelter, M. (2019). 'Quantitative photoluminescence measurements of dispersed phosphor paticles to improve optical thermometry in fluids'. MA thesis. Otto-von-Guericke-University Magdeburg.

Stelter, M., Martins, F. J. W. A., Beyrau, F. and Fond, B. (2023). 'Thermographic 3D particle tracking velocimetry for turbulent gas flows'. *Meas Sci Technol* 34, 074008. DOI: 10.1088/1361-6501/acc600.

Straußwald, M., Abram, C., Sander, T., Beyrau, F. and Pfitzner, M. (2020). 'Time-resolved temperature and velocity field measurements in gas turbine film cooling flows with mainstream turbulence'. *Exp Fluids* 62. DOI: 10.1007/s00348-020-03087-2.

Sutton, G., Greenen, A., Roebuck, B. and Machin, G. (2019). 'Imaging phosphor thermometry from T = 20°C to 450°C using the time-domain intensity ratio technique'. *Meas Sci Technol* 30, 044002. DOI: 10.1088/1361-6501/ab04ea.

Takahashi, K. (2007). *Wide Bandgap Semiconductors. Fundamental Properties and Modern Photonic and Electronic Devices*. Ed. by A. Yoshikawa and A. Sandhu. Berlin, Heidelberg: Springer Berlin / Heidelberg. 1482 pp. ISBN: 9783540472353.

Thomas, L., Tremblais, B. and David, L. (2014). 'Optimization of the volume reconstruction for classical Tomo-PIV algorithms (MART, BIMART and SMART): synthetic and experimental studies'. *Meas Sci Technol* 25, 035303. DOI: 10.1088/0957-0233/25/3/035303.

Thomas, L., Vernet, R., Tremblais, B. and Davis, L. (2010). 'Influence of geometric parameters and image preprocessing on tomo-PIV results'. *15th Int Symp on Applications of Laser Techniques to Fluid Mechanics*. Lisbon.

Thorlabs, Inc. (2025). *thorlabs.com*. URL: https://www.thorlabs.com/ (visited on 22/05/2025).

Tropea, C. (2007). *Springer handbook of experimental fluid mechanics*. Berlin: Springer Science+Business Media. ISBN: 9783540302995.

Tsai, R. Y. (1987). 'A versatile camera calibration technique for high-accuracy 3D machine vision metrology using off-the-shelf TV cameras and lenses'. *IEEE J Rob Autom* 3, 323–344. DOI: 10.1109/jra.1987.1087109.

Violato, D. and Scarano, F. (2011). 'Three-dimensional evolution of flow structures in transitional circular and chevron jets'. *Phys Fluids* 23, 124104. DOI: 10.1063/1.3665141.

Virant, M. and Dracos, T. (1997). '3D PTV and its application on Lagrangian motion'. *Meas Sci Technol* 8, 1539–1552. DOI: 10.1088/0957-0233/8/12/017.

Voronin, A. A. and Zheltikov, A. M. (2017). 'The generalized Sellmeier equation for air'. *Sci Rep* 7. DOI: 10.1038/srep46111.

Wachem, B. van, Zastawny, M., Zhao, F. and Mallouppas, G. (2015). 'Modelling of gas–solid turbulent channel flow with non-spherical particles with large Stokes numbers'. *Int J Multiphase Flow* 68, 80–92. DOI: 10.1016/j.ijmultiphaseflow.2014.10.006.

Warhaft, Z. (Jan. 2000). 'Passive Scalars in Turbulent Flows'. *Annu Rev Fluid Mech* 32, 203–240. DOI: 10.1146/annurev.fluid.32.1.203.

Westerweel, J. (1997). 'Fundamentals of digital particle image velocimetry'. *Meas Sci Technol* 8, 1379–1392. DOI: 10.1088/0957-0233/8/12/002.

Wiberg, N. (1995). *Inorganic Chemistry*. Ed. by A. F. Holleman, E. Wiberg and G. Fischer. 102th ed. Berlin/Boston: De Gruyter, Inc. 12190 pp. ISBN: 9783110206845.

Wieneke, B. (2005). 'Stereo-PIV using self-calibration on particle images'. *Exp Fluids* 39, 267–280. DOI: 10.1007/s00348-005-0962-z.

– (2008). 'Volume self-calibration for 3D particle image velocimetry'. *Exp Fluids* 45, 549–556. DOI: 10.1007/s00348-008-0521-5.

– (2012). 'Iterative reconstruction of volumetric particle distribution'. *Meas Sci Technol* 24, 024008. DOI: 10.1088/0957-0233/24/2/024008.

– (2018). 'Improvements for volume self-calibration'. *Meas Sci Technol* 29, 084002. DOI: 10.1088/1361-6501/aacd45.

Willert, C. E. and Gharib, M. (1991). 'Digital particle image velocimetry'. *Exp Fluids* 10, 181–193. DOI: 10.1007/bf00190388.

Willert, C. (1997). 'Stereoscopic digital particle image velocimetry for application in wind tunnel flows'. *Meas Sci Technol* 8, 1465–1479. DOI: 10.1088/0957-0233/8/12/010.

Willert, C. E. (2006). 'Assessment of camera models for use in planar velocimetry calibration'. *Exp Fluids* 41, 135–143. DOI: 10.1007/s00348-006-0165-2.

Williamson, C. H. K. (1996). 'Vortex Dynamics in the Cylinder Wake'. *Annu Rev Fluid Mech* 28, 477–539. DOI: 10.1146/annurev.fl.28.010196.002401.

Witkowski, D., Rothamer, D. A., Lynch, A. and Belovich, V. (2013). 'Measurements of the Temperature and Velocity Fields in a Free Shear Flow between a Vitiated Stream and Clean Air Stream using a Pr:YAG Thermographic Phosphor'. *8th US National Combustion Meeting (Western States Section of the Combustion Institute)*.

Wolf, C. C., Schanz, D., Schwarz, C., Heintz, A., Bosbach, J., Strübing, T. and Schröder, A. (2024). 'Volumetric wake investigation of a free-flying quadcopter using Shake-The-Box Lagrangian particle tracking'. *Exp Fluids* 65. DOI: 10.1007/s00348-024-03880-3.

Worth, N. A. and Nickels, T. B. (2008). 'Acceleration of Tomo-PIV by estimating the initial volume intensity distribution'. *Exp Fluids* 45, 847–856. DOI: 10.1007/s00348-008-0504-6.

Wu, Y., Wang, Q. and Zhao, C. Y. (2021). 'A spatial-temporal algorithm for three-dimensional particle tracking velocimetry using two-view systems'. *Meas Sci Technol* 32, 065011. DOI: 10.1088/1361-6501/abeb43.

Xuan, G. (2023). 'Discrete luminescence particle imaging to determine temperature distributions in highly scattering solid-fluid systems'. PhD thesis. Otto-von-Guericke-University Magdeburg. DOI: 10.25673/116974.

Xuan, G., Fan, L., Beyrau, F. and Fond, B. (2023). 'High spatial resolution fluid thermometry in boundary layers by macroscopic imaging of individual phosphor tracer particles'. *Exp Therm Fluid Sci*, 110977. DOI: 10.1016/j.expthermflusci.2023.110977.

Yap, S. V., Ranson, R. M., Cranton, W. M., Koutsogeorgis, D. C. and Hix, G. B. (2009). 'Temperature dependent characteristics of La2O2S: Ln [Ln=Eu, Tb] with various Ln concentrations over 5–60°C'. *J Lumin* 129, 416–422. DOI: 10.1016/j.jlumin.2008.10.019.

Yin, X.-Q., Tao, W., Zheng, C., Yang, H.-W., He, Q.-Z. and Zhao, H. (2019). 'Analysis and simplification of lens distortion model for the scheimpflug imaging

system calibration'. *Opt Commun* 430, 380–384. DOI: 10.1016/j.optcom.2018.05.086.

Zhang, T. (2025). *An Introduction to Materials Informatics. The Elements of Machine Learning*. 1st ed. 2025. Singapore: Imprint: Springer. 1479137126 pp. ISBN: 9789819979929.

Zhang, Z. (2000). 'A flexible new technique for camera calibration'. *IEEE Transactions on Pattern Analysis and Machine Intelligence* 22, 1330–1334. DOI: 10.1109/34.888718.

Zhang, Z. (1998). 'Determining the Epipolar Geometry and its Uncertainty: A Review'. *Int J Comput Vis* 27, 161–195. DOI: 10.1023/a:1007941100561.

Zhiyin, Y. (Feb. 2015). 'Large-eddy simulation: Past, present and the future'. *Chinese J Aeronaut* 28, 11–24. DOI: 10.1016/j.cja.2014.12.007.

Zhou, K., Grauer, S. J., Schanz, D., Godbersen, P., Schröder, A., Rockstroh, T., Jeon, Y. J. and Wieneke, B. (2024). 'Benchmarking Data Assimilation Algorithms For 3D Lagrangian Particle Tracking'. *Proceedings of the International Symposium on the Application of Laser and Imaging Techniques to Fluid Mechanics* 21, 1–22. DOI: 10.55037/lxlaser.21st.229.

Declaration of honor

I hereby declare that I produced this thesis without prohibited external assistance and that none other than the listed references and tools have been used.

I did not make use of any commercial consultant concerning graduation. A third party did not receive any nonmonetary perquisites neither directly nor indirectly for activities which are connected with the contents of the presented thesis. All sources of information are clearly marked, including my own publications.

In particular I have not consciously:

- Fabricated data or rejected undesired results
- Misused statistical methods with the aim of drawing other conclusions than those warranted by the available data
- Plagiarized data or publications
- Presented the results of other researchers in a distorted way

I do know that violations of copyright may lead to injunction and damage claims of the author and also to prosecution by the law enforcement authorities.

I hereby agree that the thesis may need to be reviewed with an electronic data processing for plagiarism.

This work has not yet been submitted as a doctoral thesis in the same or a similar form in Germany or in any other country. It has not yet been published as a whole.

Magdeburg, 26th May 2025
Moritz Stelter

List of publications

During the doctorate the following works have been published by the candidate.

Journal publications

1. Stelter, M., Martins, F. J. W. A., Beyrau, F., Fond, B. (2023). Thermographic 3D particle tracking velocimetry for turbulent gas flows. *Measurement Science and Technology*, 34, 074008.

2. Patil, S., Gorges, C., Lopez Bonilla, J., Stelter, M., Beyrau, F., van Wachem, B. (2023). Experimental and numerical investigation to elucidate the fluid flow through packed beds with structured particle packings. *Particuology*, 89, 218-237.

Conference proceedings

1. Stelter, M., Beyrau, F., Fond, B. (2024). Towards thermographic Shake-The-Box: Combined three-dimensional flow thermometry and velocimetry using thermographic phosphors, 4^{th} *International Conference on Phosphor Thermometry*, August 26-30, 2024, Budva-Becici, Montenegro.

2. Stelter, M., Martins, F. J. W. A., Beyrau, F., Fond, B. (2023). Thermographic particle tracking velocimetry for three-dimensional temperature and velocity measurements in turbulent gas flows using thermographic phosphor particles,

Gordon Research Seminar on Laser Diagnostics in Energy and Combustion Science, July 8-9, 2023, Newry, USA.

3. Stelter, M., Martins, F. J. W. A., Beyrau, F., Fond, B. (2022). Combined three-dimensional temperature and velocity measurements using thermographic phosphor tracers in turbulent gas flows, *3rd International Conference on Phosphor Thermometry*, July 18-20, 2022, Magdeburg, Germany.

4. Stelter, M., Martins, F. J. W. A., Beyrau, F., Fond, B. (2022). Simultaneous measurements of 3D temperature and velocity fields in gas flows using thermographic phosphor tracer particles, *20th International Symposium on Application of Laser and Imaging Techniques to Fluid Mechanics*, July 11-14, 2022, Lisbon, Portugal.

5. Stelter, M., Martins, F. J. W. A., Beyrau, F., Fond, B. (2021). 3D thermometry and velocimetry in gas flows using thermographic phosphor particles, *GRC Connects: Laser Diagnostics in Energy and Combustion Science*, July 13-14, 2021, held online.

6. Stelter, M., Martins, F. J. W. A., Beyrau, F., Fond, B. (2021). Three-dimensional temperature and velocity measurements in fluids using thermographic phosphor tracer particles, *14th International Symposium on Particle Image Velocimetry — ISPIV 2021*, August 1-5, 2021, Chicago, USA (held online).

7. Stelter, M., Martins, F. J. W. A., Beyrau, F., Fond, B. (2020). 3D temperature and velocity measurements, *2nd International Conference on Phosphor Thermometry*, July 27-29, 2020, Magdeburg, Germany (held online).